

**Unified Approach to
Ship Seakeeping and Maneuvering
by a RANSE Method**

Vom Promotionsausschuss der
Technischen Universität Hamburg-Harburg
zur Erlangung des akademischen Grades
Doktor-Ingenieurin
genehmigte Dissertation

von

Yan Xing-Kaeding

aus China

2006

Unified Approach to Ship Seakeeping and Maneuvering by a RANSE Method

Yan Xing-Kaeding, 1. Auflage, Hamburg: Arbeitsbereiche Schiffbau

Gutachter:

Prof. Dr.-Ing. G. Jensen

Prof. Dr. M. Perić

Prof. Dr.-Ing. Dr.-Ing. E.h. Dr. h.c. E. Lehmann

Prof. Dr.-Ing. T. Rung

Tag der mündlichen Prüfung: 23.01.2006

©Arbeitsbereiche Schiffbau

Technische Universität Hamburg-Harburg

Schwarzenbergstraße 95 C

21073 Hamburg

ISBN 3-89220-634-1

Abstract

In this work, a computational procedure for the prediction of motion of rigid bodies floating in viscous fluids and subjected to currents and waves is presented. The procedure is based on a coupled iterative solution of the equations of motion of a rigid body with up to six Degrees Of Freedom (DOF) and the Reynolds-Averaged Navier-Stokes Equations (RANSE) describing the turbulent fluid flow. The fluid flow is analyzed using a commercial CFD package (Comet) which can use moving grids made of arbitrary polyhedral cells and allows sliding interfaces between fixed and moving grid blocks. The computation of body motion is coupled to the CFD code via user-coding interfaces on the basis of each iteration. A fully-implicit predictor-corrector procedure is employed for the calculation of body motion, taking advantage of the iterative nature of the fluid-flow solver.

The method is used to compute the motion of floating bodies/ships subjected to waves, showing favorable agreement with experiments. Extension to more complex ship maneuvering applications is further conducted, which requires modeling of interaction of ship, its rudder(s) and its propeller(s). With the ship hull and the rudder modeled geometrically and the propeller simulated by a body force model, turning circle and Zigzag maneuvers are performed as examples and the comparison with measurements shows promising agreement.

Acknowledgements

The present thesis is based on the research that I have performed at Institut für Fluidynamik und Schiffstheorie, Technische Universität Hamburg-Harburg.

I wish to record my sincere thanks to Professor Milovan Perić and Professor Gerhard Jensen for their advice, support and encouragement. I thank Professor Eike Lehmann and Professor Thomas Rung for their time in reading the manuscript of this work and in suggesting changes and improvements. My thanks are also due to Professor Heinrich Söding and Professor Stefan Krüger, who have friendly provided support in this research.

A number of colleagues and friends have also provided constant inspiration through special interest in my work. I have greatly benefited from their questions and subsequent discussions. I am grateful to Dr. Eberhard Gerlach, who was always ready and kind whenever help was needed.

Finally, I wish to thank my family for their love, tremendous support and great patience during all these years.

Yan Xing-Kaeding

March 2, 2006

Norderstedt

Contents

Abstract	iii
Acknowledgements	v
Nomenclature	xi
List of Figures	xiii
List of Tables	xxi
1 Introduction	1
1.1 Motivation	1
1.2 Background	2
1.3 Present Contributions	5
1.4 Structure of the Thesis	6
2 Numerical Method	9
2.1 Introduction	9
2.2 Theoretical Basis	9
2.2.1 Fluid Flow	9
2.2.2 Rigid Body Dynamics	15
2.2.3 Coupling of Fluid Flow and Rigid Body Motion	25
2.3 Numerical Implementation	27
2.3.1 Fluid Flow	27
2.3.2 Rigid Body Dynamics	35
2.3.3 Coupling of Fluid Flow and Rigid Body Motion	40
2.4 Initial and Boundary Conditions	43
2.4.1 Initial Conditions	43

2.4.2	Boundary Conditions	44
2.5	Numerical Grids	46
2.5.1	Types of Numerical Grids	48
2.5.2	Grid-Moving Strategies	50
3	Interaction of Flow and Floating-Body	53
3.1	Introduction	53
3.2	Cylinder Water-Entry and Water-Exit	54
3.2.1	Water-Entry of a Horizontal Circular Cylinder	55
3.2.2	Water-Exit of a Horizontal Circular Cylinder	60
3.2.3	Study on Numerical Effects	60
3.3	Wave Generation in Numerical Water Tank	66
3.3.1	Wave Generation by Inlet Boundary Condition	67
3.3.2	Wave Generation by a Flapping Wave-Maker	69
3.4	Motion of Simple Geometry Bodies in Regular Waves	71
3.4.1	Constrained and Free-Floating Rectangular Cylinder in Waves	71
3.4.2	Mid-Ship Section with and without Bilge Keels in Waves	76
3.4.3	Interaction of Two Floating-Bodies in Waves	78
3.5	Motion of a Rectangular Cylinder under Wave Packages	78
3.5.1	Motion under Non-Concentrating Wave Packages	81
3.5.2	Extreme Motion under Concentrating Wave Packages	82
4	Applications to Ship Motion in Waves	91
4.1	Introduction	91
4.2	Wigley Model in Waves	92
4.2.1	Wigley Model in Head Waves	92
4.2.2	Wigley Model in Oblique Waves	93
4.2.3	Effect of Differencing Scheme in Space	94
4.3	RoRo Ship Model in Head Waves	97
5	Interaction of Rudder, Propeller and Ship	103
5.1	Introduction	103

5.2	Modeling of Rudder	104
5.2.1	General Description	104
5.2.2	Computational Domain and Numerical Grid	106
5.2.3	Parameter Study of Rudder Forces in 2D	110
5.2.4	Forces of Rudders without and with Fixed Fins in 3D	114
5.3	Modeling of Propeller	116
5.3.1	Body Force Model for Propeller	116
5.3.2	Determination of Propeller Forces from the Instant Fluid Flow	118
5.3.3	Determination of Thrust by Numerical Self-Propulsion Test	121
5.4	Interaction of Propeller and Rudder	122
5.5	Computation of Rudder Forces behind Ship and Propeller	126
6	Simulation of Ship Motion during Maneuvers	133
6.1	Introduction	133
6.2	Steady Drift Motion of a Container Ship Model	134
6.3	Turning Circle Maneuvers	140
6.3.1	Wigley Model	140
6.3.2	Container Ship Model	140
6.4	Zigzag Maneuvers	146
6.4.1	Zigzag Maneuver of a Wigley Model in Waves	146
6.4.2	Zigzag Maneuver of a Container Ship Model in Calm Water	146
7	Conclusion and Future Work	155
7.1	Conclusion	155
7.2	Future Work	159
A	Derivation of Angular Motion Equation in GS	161
B	HRIC Scheme	165
C	Derivation of Rotation Operator	167

D	RoRo Ship	171
E	CBOX Ship	173
F	Turning Circle Maneuver Test	175
G	Zigzag Maneuver Test	177
	Bibliography	179
	Curriculum Vitae	187

Nomenclature

Roman Symbols

A	[m]	Wave amplitude
A_o	[m ²]	Propeller area
A_R	[m ²]	Rudder disc area
B	[m]	Beam of ship
C_{Th}	[1]	Propeller thrust loading coefficient
D	[m]	Propeller diameter
\mathbf{F}	[N]	Vector of total force on mass center of the body
\mathbf{F}^e	[N]	Vector of effective force on mass center of the body
\mathbf{F}^i	[N]	Vector of impressed force on mass center of the body
\mathbf{F}^q	[N]	Vector of constraining force on mass center of the body
F_n	[1]	Froude number
\mathbf{g}	[m/s ²]	Gravity acceleration vector
\mathbf{I}	[1]	Unit matrix
J	[1]	Propeller advance coefficient
J_T	[-]	Jacobian matrix for translation motion
J_R	[-]	Jacobian matrix for rotation motion
k	[m ² /s ²]	Kinetic energy of turbulent fluctuation per unit mass
k_T	[1]	Propeller thrust coefficient
k_Q	[1]	Propeller torque coefficient
L	[m]	Length of ship
m	[kg]	Mass of body
M_C	[kgm ²]	Matrix of moments of inertia with respect to mass center of the body
\mathbf{m}_C	[Nm]	Resultant moment vector on mass center of the body
\mathbf{n}	[1]	Normal vector of CV face
p	[N/m ²]	Pressure
Q_p	[Nm]	Propeller torque
R	[N]	Ship resistance
R_n	[1]	Reynolds number
S	[m ²]	Closed surface area of CV
\mathbf{T}	[N/m ²]	Viscous stress tensor of fluid
T_p	[N]	Propeller thrust
T_T	[1]	Transformation matrix from BS to GS
T_t	[1]	Rotation operator
t	[s]	Time
V	[m ³]	Volume of CV
u_i	[m/s]	Cartesian component of \mathbf{v}
\mathbf{v}	[m/s]	Velocity vector of fluid
\mathbf{v}_b	[m/s]	Velocity vector of CV face
\mathbf{v}_C	[m/s]	Velocity vector of body
\mathbf{Y}_p	[N]	Propeller side force

Greek Symbols

α	[°]	Angle of attack
β	[°]	Drift angle
β_ϕ	[1]	Blending factor for variable ϕ
Δt	[s]	Time step size
δ_{ij}	[1]	Kronecker delta
δr	[-]	Virtual displacement
ϵ	[m ² /s ³]	Turbulent dissipation rate per unit mass
η	[m]	Water surface elevation
Λ	[1]	Aspect ratio of rudder
λ	[m]	Wave length
μ	[kg/ms]	Dynamic viscosity of fluid
μ_t	[kg/ms]	Eddy viscosity
ω	[1/s]	Wave circular frequency
ϕ	[-]	Intensive scalar quantity
ψ	[°]	Yaw angle
ρ	[kg/m ³]	Density
θ	[°]	Pitch or trim angle
φ	[°]	Roll or heel angle
ξ	[m]	Local coordinate of grid

Acronyms

BS	Body-fixed coordinate System
CDS	Central Differencing Scheme
CFD	Computational Fluid Dynamics
CG	Conjugate Gradient method
CGSTAB	CG Stabilized
CV	Control Volume
DES	Detached Eddy Simulation
DNS	Direct Numerical Simulation
DOF	Degree Of Freedom
HRIC	High Resolution Interface-Capturing scheme
ICCG	Incomplete Cholesky Conjugate Gradient method
IE	Implicit Euler scheme
IS	Intermediate coordinate System
ITTL	Implicit Three Time Level scheme
GM	Metacentric height
GS	Global coordinate System
LES	Large Eddy Simulation
PMM	Planar Motion Mechanism
RANSE	Reynolds Averaged Navier-Stokes Equations
SIMPLE	Semi-Implicit Pressure-Linked Equations
UDS	Upwind Differencing Scheme

List of Figures

2.1	Sequence of rotation.	18
2.2	Motion of the floating body due to the forces acting on the body	26
2.3	The coupled algorithm for flow and body motion.	41
2.4	An example of a stepwise regular grid of a 2D circular cylinder	49
2.5	An example of a surface-fitted grid of a 2D circular cylinder	49
2.6	An example of an overlapping grid of a rectangular cylinder	50
2.7	Examples of moving-grids	51
3.1	Free surface deformation of a neutrally-buoyant cylinder water-entry: simulation (left) and experiment (right).	56
3.2	Numerical grid for the circular cylinder water-entry case.	58
3.3	Velocity vectors and pressure fields of the fluid during the cylinder water-entry.	59
3.4	Time history of the vertical motion (left) and the impact force (right) during the cylinder water-entry.	59
3.5	Free surface deformation of a constant-speed cylinder water-exit: simulation (left) and experiment (right).	61
3.6	Velocity vectors and pressure fields during the cylinder water-exit.	62
3.7	Pressure distribution along the cylinder circumference at different time instants (water-exit).	63
3.8	Computed time history of vertical motion (left) and impact force (right) using three grids (water-entry).	63
3.9	Free surface deformation at $t = 0.330$ s during cylinder water-entry.	64
3.10	Computed vertical motion (left) and impact force (right) during cylinder water-entry using IE and ITTL time integration schemes.	64
3.11	Computed vertical motion (left) and impact force (right) during cylinder water-entry with and without turbulence model.	65
3.12	Pressure distribution on the cylinder surface.	65

3.13	Shear stress distribution on the cylinder surface.	65
3.14	Computed vertical motion (left) and impact force (right) during cylinder water-entry using moving- and fixed-grid methods.	65
3.15	Velocity field of a plane progressive wave and interpolation between water and air.	68
3.16	Computed instantaneous free surface (left) and wave profile comparison in one wavelength (right) for a small amplitude linear wave.	68
3.17	Horizontal velocity component of the fluid particle directly beneath the wave crest (left) and vertical velocity component of the fluid particle at the free surface when $\eta = 0$ (right).	68
3.18	Wave profile for large nonlinear waves.	70
3.19	Comparison of wave profile on grid resolution and time integration scheme.	70
3.20	Wave generation by flapping wave-maker.	72
3.21	Comparison of wave profile for one wavelength.	72
3.22	Horizontal velocity component of the fluid particle directly beneath the wave crest (left) and vertical component of the fluid particle at the free surface when $\eta = 0$ (right).	72
3.23	Computed velocity field for both water and air.	72
3.24	Computed water elevation against time (left) and wave profile at $t = 8.0$ s (right) using IE and ITTL time integration schemes.	73
3.25	Set-up of the constrained motion experiment.	74
3.26	Free surface deformation at $t = 6.82$ s: far view (left) and near view (right).	74
3.27	The experimental photo of the body in constrained motion at $t = 6.82$ s.	75
3.28	Comparison on the angular displacement of the body between computation and experiment (constrained motion).	75
3.29	Computed angular displacement of the body using different time step sizes (constrained motion).	75
3.30	Set-up of the free-floating motion experiment.	77
3.31	Time history of wave elevation at 1.5 m away from the wave-maker (free-floating motion).	77
3.32	Time history of horizontal displacement of the body in waves (free-floating motion).	77
3.33	Time history of vertical displacement of the body in waves (free-floating motion).	77
3.34	Time history of angular displacement of the body in waves (free-floating motion).	77

3.35	Free surface deformation and the position of the 2D mid-ship section at $t = 6.0$ s: without keels (left) and with keels (right).	79
3.36	Horizontal displacement of the free-floating 2D mid-ship section with and without keels.	79
3.37	Vertical displacement of the free-floating 2D mid-ship section with and without keels.	79
3.38	Comparison on the angular displacement of the free-floating 2D mid-ship section with and without keels.	79
3.39	Velocity vector profile around one keel at $t = 8.0$ s.	79
3.40	Initial state of free surface around two floating bodies.	80
3.41	Free surface deformation around two floating bodies at $t = 3.8$ s.	80
3.42	Time history of horizontal distance between two floating bodies.	80
3.43	Time history of horizontal displacement of each floating body.	80
3.44	Time history of vertical displacement of each floating body.	80
3.45	Time history of angular displacement of each floating body.	80
3.46	The grid around two floating bodies at two selected time instants.	81
3.47	Time history of water elevation at two probes: $x = 1.16$ m (left) and $x = 2.66$ m (right).	83
3.48	Comparison on body motion between experiment and computation: horizontal (left), vertical (right) and angular displacement (bottom).	83
3.49	Time history of the angle of the wave-maker.	84
3.50	Time history of water elevation at two probes: $x = 1.65$ m (left) and $x = 2.66$ m (right)	85
3.51	Free-surface deformation and position of the wave-maker and the floating body at four successive time instants.	85
3.52	Comparison on body motion between experiment and computation: horizontal (left), vertical (right) and angular displacement (bottom).	86
3.53	Free-surface shape and body position as observed in the experiment (left) and the computation (right) at $t = 7.2$ s (top) and $t = 7.54$ s (bottom).	86
3.54	Comparison on body motion between experiment and computations using one-domain and overlapping grids: horizontal (left), vertical (right) and angular (bottom) displacement.	88
3.55	Free-surface deformation, body position and overlapping grids at $t = 6.8$ s (left) and at $t = 7.4$ s (right).	88
3.56	Pressure field and overlapping grids at $t = 6.8$ s (left) and at $t = 7.4$ s (right).	89

4.1	Computational grid at the free surface level around the Wigley model (mirrored about the longitudinal plane).	93
4.2	Computed time histories of heave (left) and pitch (right) motions of the Wigley model.	93
4.3	Computed wave patterns of the Wigley model in head waves at four selected time instants.	94
4.4	Computed wave pattern of the Wigley model in oblique waves (170°).	95
4.5	Computed time histories of roll (top), heave (left) and pitch (right) motions of the Wigley model in oblique waves (170°).	95
4.6	Computed time histories of water elevation using UD and CD schemes.	96
4.7	Computed time histories of heave (left) and pitch (right) motions of the Wigley ship using UD and CD schemes.	96
4.8	Computational grid at the free surface level around the RoRo ship.	98
4.9	RoRo ship grid: viewed from stern (left) and bow (right).	99
4.10	Time histories of heave (top) and pitch (bottom) motions of the RoRo ship.	99
4.11	Wetted-surface and the position of the RoRo ship within one wave period.	100
4.12	Computed wave patterns of the RoRo ship at $t = 9.75$ s (left) and $t = 10.20$ s (right).	101
4.13	Dynamic pressure distribution on the RoRo ship surface at two time instants.	101
4.14	Wall shear stress magnitude on the RoRo ship surface at two time instants.	101
4.15	Velocity profile in the longitudinal symmetry plane of the RoRo ship.	102
5.1	Main dimensions of the rudder (Brix [14]).	106
5.2	Computational domain of coarse grid in 2D.	107
5.3	Fine grid in the vicinity of the rudder in 2D.	107
5.4	Computational domain for rudder without fin in 3D.	109
5.5	Grid for rudder with fin in 3D.	109
5.6	Grid for RoRo Ship with two rudders and fins.	110
5.7	Dependency of computed lift and drag coefficients on blending of CD scheme and UD scheme for two turbulence models on coarse and fine 2D grids ($\alpha = 8^\circ$ and $R_n = 2.7 \cdot 10^6$).	111
5.8	Comparison of normalized residuals of turbulence kinetic energy equations using two turbulence models on different grids (2D).	113
5.9	Comparison of normalized residuals of mass equations using two turbulence models on different grids (2D).	113

5.10	Dependency of force coefficients and stall angles on the discretization scheme (2D).	114
5.11	Rudder force coefficients of different Reynolds numbers (2D).	114
5.12	Richardson extrapolation of pressure drag using results from three grids (2D).	115
5.13	Computed force coefficients for rudder without rudder-fin (3D).	116
5.14	Computed force coefficients for rudder with rudder fin (3D).	117
5.15	Body force distribution model for propeller.	119
5.16	Flow through propeller disk.	121
5.17	The coupled algorithm for self-propulsion test.	123
5.18	Rudder and propeller arrangement.	125
5.19	Rudder forces in propeller slipstream ($C_{Th} = 1.94$) and in free stream.	125
5.20	Axial velocity contour at the plane $0.30c$ in front of rudder ($\delta = 10^\circ$).	127
5.21	Pressure distribution on rudder and velocity vectors at two planes $0.30c$ in front of and behind the rudder ($\delta = 10^\circ$).	127
5.22	Comparison of rudder forces behind RoRo ship with experiment.	128
5.23	Axial velocity contours and tangential velocity vectors on the plane $0.3c$ in front of rudders ($\delta = 8^\circ$).	129
5.24	Axial velocity contours and tangential velocity vectors on the plane $0.3c$ in front of rudders ($\delta = 24^\circ$).	129
5.25	Axial velocity contours and tangential velocity vectors on the plane $0.1c$ behind rudders ($\delta = 8^\circ$).	130
5.26	Axial velocity contours and tangential velocity vectors on the plane $0.1c$ behind rudders ($\delta = 24^\circ$).	130
5.27	Pressure distribution on the ship stern and rudder surface, tangential velocity vectors on the propeller plane together with the paths of a few particles starting from the propeller plane ($\delta = 8^\circ$).	131
5.28	Ship-induced wave system at $\delta = 8^\circ$	131
6.1	Rudder and propeller arrangement of the CBOX ship.	136
6.2	Numerical grid of the CBOX ship.	137
6.3	Comparison on the non-dimensional side force (left) and yaw moment (right) on ship hull as a function of drift angles.	137
6.4	Comparison on the non-dimensional roll moment on the ship hull (left) and the non-dimensional transverse force on the rudder (right) as a function of drift angles.	137

6.5	Free surface deformation of CBOX ship under different drift angles (delta of isolines $\Delta\zeta = 5.345 \cdot 10^{-3}$ m).	138
6.6	Dynamic pressure distribution (left) and shear stress (right) of CBOX ship ($\beta = 10^\circ$).	139
6.7	Velocity distribution at $x = -0.45 L$ ($\beta = 10^\circ$): axial velocity contours (left) and tangential velocity vectors together with free surface position (right), viewed from stern.	139
6.8	Turbulent kinetic energy distribution at $x = -0.45 L$ ($\beta = 10^\circ$), viewed from stern.	139
6.9	Numerical grid and boundary conditions for the turning circle maneuver of a Wigley model.	141
6.10	Predefined track (left) and heading (right) of the Wigley model during the turning circle maneuver.	141
6.11	Free surface deformation during a turning circle maneuver of the Wigley model (Delta of isolines $\Delta\zeta = 0.004$ m).	142
6.12	Roll (top), heave (left) and pitch (right) motion of the Wigley model during a turning circle maneuver.	142
6.13	Free surface deformation during a turning circle maneuver of the CBOX ship (Delta of isolines $\Delta\zeta = 5.414 \cdot 10^{-3}$ m).	144
6.14	Yaw rate (left) and absolute velocity (right) for a turning circle maneuver of the CBOX ship.	144
6.15	Dynamic pressure distribution on the ship hull and the rudder at port side (top) and starboard (bottom).	145
6.16	Axial velocity contours with distorted mesh (left) and tangential velocity vectors with free surface position (right) at the cross section $x = -0.45 L$ ($\phi = 2^\circ$), viewed from stern.	145
6.17	Sway and yaw motion (left) and computed wave pattern at $t = 7.0$ s (right) during a 25° Zigzag maneuver of the Wigley hull ($F_n = 0.18$).	146
6.18	Time history of the heading (left) and the track (right) together with the rudder angle of the CBOX ship during the Zigzag maneuver.	149
6.19	Time history of the drift angle (left) and the yaw rate (right) together with the rudder angle of the CBOX ship during the Zigzag maneuver.	150
6.20	Time history of the forward (left) and the transverse (right) displacements together with the rudder angle of the CBOX ship during the Zigzag maneuver.	150
6.21	Time history of the non-dimensional ship speed (left) and the roll angle (right) together with the rudder angle of the CBOX ship during the Zigzag maneuver.	150
6.22	Time history of the propeller thrust (left) and the side force (right) together with the rudder angle of the CBOX ship during the Zigzag maneuver.	151

6.23	Time history of the drag (left) and the lift (right) forces on the rudder together with the rudder angle of the CBOX ship during the Zigzag maneuver. . . .	151
6.24	Time history of the torque on the rudder shaft together with the rudder angle of the CBOX ship during the Zigzag maneuver.	151
6.25	Computed free surface deformation of the CBOX ship at $\psi = 10^\circ$ (left) and $\psi = -10^\circ$ (right) during the Zigzag maneuver.	152
6.26	Dynamic pressure distribution on the ship hull and the rudder surface of the CBOX ship at $\psi = 10^\circ$ during the Zigzag maneuver, viewed from port side (top) and starboard (bottom).	152
6.27	Dynamic pressure distribution on the ship hull and the rudder surface of the CBOX ship at $\psi = -10^\circ$ during the Zigzag maneuver, viewed from port side (top) and starboard (bottom).	153
6.28	Velocity distribution at the cross section $x = -0.45L$ of the CBOX ship at $\psi = 10^\circ$ during the Zigzag maneuver: axial velocity contours (left) and tangential velocity vectors together with the free surface position (right), viewed from stern.	153
6.29	Velocity distribution at the cross section $x = -0.45L$ of the CBOX ship at $\psi = -10^\circ$ during the Zigzag maneuver: axial velocity contours (left) and tangential velocity vectors together with the free surface position (right), viewed from stern.	153
B.1	Normalized Variable Diagram (NVD, see Leonard [51]).	166
C.1	Rotation of vector \mathbf{r}_1 about \mathbf{u}	168
D.1	Transverse sections of RoRo ship.	171
D.2	Profile of RoRo ship.	172
E.1	Transverse sections of CBOX ship.	173
E.2	Profile of CBOX ship.	174
F.1	Turning circle definitions.	176
G.1	Scheme of Zigzag maneuver test.	178

List of Tables

2.1	Values of empirical coefficients in the standard k - ϵ turbulence model	15
2.2	Values of empirical coefficients in the RNG k - ϵ turbulence model	15
2.3	Selected values of under-relaxation factors for the flow solver	43
2.4	Proposed values of under-relaxation factors for the body motion	43
4.1	Dimensions of the RoRo ship model	98
5.1	Dimensions of rudder and fixed fin	116
5.2	Dimensions of the propeller.	124
5.3	Coefficients from the propulsion diagram.	124
6.1	Dimensions of the CBOX ship model	135
6.2	Dimensions of rudders and fixed fins of the CBOX ship	136
6.3	Dimensions of the propeller of the CBOX ship	136
6.4	Coefficients from the propulsion diagram	136
6.5	Computed characteristics of turning circle maneuver of the CBOX ship . .	143
6.6	Comparison of the characteristics of the $10^\circ/10^\circ$ Zigzag maneuver between model test and computation.	149

Chapter 1

Introduction

1.1 Motivation

Model tests in the towing tank have been the most frequently used way to predict the hydrodynamic performance of a new ship. With the increasing demand on ship performance (speed, size, efficiency, environmental impact etc.) and navigational safety, performance-based safety criteria are becoming ever more important. International rules and recommendations have been established. Therefore designers demand the performance of a ship to be assessed at its early design stage. Although model tests will still be indispensable, this calls for prediction tools, which, in principle, should not rely on model test results. The use of *Computational Fluid Dynamics* (CFD) tools is the obvious choice.

As complementary tools to towing tank tests, CFD analyses are used today to study a large variety of ship forms for optimization purpose and to provide a large amount of detailed information on the flow, which can help the designers to improve the performance of a new ship. However, in the long-term objective, the CFD tools should be able to predict the hydrodynamic performance of a ship taking into account all physical phenomena which characterize the flow around a full-scale ship under its real operating conditions. This means a single code would be capable of handling different tasks in the field of ship hydrodynamics, which has conventionally been broken into several areas:

- Resistance
- Propulsion
- Seakeeping
- Maneuvering

Although the so-called *Virtual Towing Tank* (or *Numerical Towing Tank*) based on modern CFD tools has been placed on the agenda of worldwide research groups, the aforementioned ambitious goal has not been achieved yet. The only affordable way to study the coupled complicated problem of ships maneuvering in waves until today is to define a simplified problem and decouple the complex system by either completely ignoring the less important

phenomena or approximating them by other methods or simple corrections. Such a modified problem is set up being as close as possible to the original one. However, maneuverability does not depend on hydrodynamic characteristics of single parts like ship hull, propulsion system and rudder separately. Rather, the ship response to steering inputs is determined by the interaction of these three fundamental components. To better capture this interaction a more general approach is required.

With further development of computer technology, state-of-the-art CFD methods offer the opportunity to study aforementioned different problems in ship hydrodynamics by a unified technique. In this thesis, a coupled method is developed and examined to tackle ship hydrodynamic problems in different areas. Turbulent free-surface flow and flow-induced ship motion are solved simultaneously so that interacting behaviors as mentioned above can be studied by a single code. In other words, an important step towards the long-term objective, the *Numerical Towing Tank*, is taken here. The applicability and the accuracy of the method developed is assessed. To be comparable to the real towing tank, both captured or semi-captured maneuvers and completely free runs of a self-propelled and -steered ship will be performed. The possibility of wave generation in the numerical tank is demonstrated.

1.2 Background

In practice, ship motions in waves are either predicted using experiments or numerical methods based on the potential theory, which assumes an irrotational ideal fluid without viscosity. Motions and waves are mostly linearized (strip method or panel method), or potential flow computations with linearized boundary conditions are combined with non-linear simulations of motions. More advanced simulations use time integration of the equations of motion where the hydrodynamic forces are calculated based on empirical formulae and special calculations for individual force components. This is done for example in SIMBEL (see Pereira [67]), where the hydrodynamic forces on the hull are computed based on a strip theory beforehand for a variety of frequencies and section immersions. An overview of a variety of such methods can be found in Bertram [11]. These methods are considered as fast and robust tools in the design stage because they allow a large number of variants to be analyzed for the purpose of optimization. They are applicable to the assessment of statistical quantities, which can be the only final results in a natural seaway due to its stochastic nature. The motion of a smooth body in waves can be computed using these methods with reasonably good accuracy (especially when empirical corrections are applied). However, they are not suitable for flows, where viscous effects or breaking waves play an important role. Bilge keels, roll damping tanks etc. can be dealt with in the potential theory only with further empirical corrections, which not only decrease the accuracy of the prediction, but are also sometimes expensive because experimental data and experience are required for such corrections. For several practically important cases like ship motions in large amplitude waves, ship response under impact wave load (slamming), ship maneuvering etc., large errors can be introduced by the potential theory assumptions. The need for a numerical tool that can predict the motions and loads in large waves, taking into account viscous effects, turbulence, flow separation and wave-breaking phenomena, is thus obvious.

Ship hydrodynamics computations based on solving the Reynolds-Averaged Navier-

Stokes Equations (RANSE) were initiated in the 1980s, and since then a number of research groups have developed methods for solving viscous flow problems. Computations of viscous turbulent flow around ship without consideration of the free surface have been widely adopted to predict the flow field (especially the wake distribution) and the friction resistance, often employing commercial CFD codes. An acceptable range of accuracy has been achieved for the prediction of friction resistance coefficients, namely error bounds from 1 to 10 %. It has also been applied rather often to compute steady flows around a maneuvering ship to predict hydrodynamic coefficients for the hull, see Cura Hochbaum [19], Ohmori et al. [61] and Nonaka et al. [60]. El Moctar [23] utilized a commercial CFD code to analyze the interaction of ship hull, rudder and propeller. Sato et al. [74] combined hull forces computed by a RANSE code and a mathematical model representing rudder and propeller force to simulate Zigzag maneuvers. Bellevre [9] and Takada et al. [83] used similar methods to simulate the maneuvers of a submarine and the performance of an advanced keel of a racing yacht with horizontal and vertical rudders considering six Degrees Of Freedom (DOF) motion. Unsteady RANSE computations were performed by Ohmori [62] for Planar Motion Mechanism (PMM) motion of a ship using a moving-grid system and by Chen and Huang [17] for a berthing ship in full scale applying a Chimera grid system.

The last decade has seen increasing consideration of free surface deformation in RANSE computations for ships. The breakthrough in ship hydrodynamics was seen at the Tokyo 1994 Workshop (Kodama et al. [44]), where no less than ten methods featured this capacity. Although the earliest numerical method (Marker-and-Cell, MAC) devised for unsteady free surface flow problems was already proposed in 1965 by Harlow and Welch [34], it is mainly used to investigate internal flows, such as sloshing. The first references in ship hydrodynamics are from the mid-eighties, when Miyata et al. [53] introduced their version of the MAC method called TUMMAC. A large number of references to subsequent developments is documented by Larsson [48] and Miyata [56].

Moving grid methods, sometimes called Lagrangian grid methods or interface-tracking methods, see Hirt et al. [35] and [36], are until today the most widely used approach for modeling the free surface in computational ship hydrodynamics, De Bernardis [10]. Examples can be found in Miyata et al. [55], who applied curvilinear grid systems and a finite-volume method to study the free surface flow about a Wigley hull and a HSV A tanker in steady straight course. In such applications, only the water flow is computed and a Lagrangian grid is constructed to be adapted to the instant position of the free surface, which is unknown at the beginning of computation. The limitation of such methods is that they cannot track surfaces that break apart or intersect, which draws a barrier for the method to be applied to problems with large amplitude free surface deformations (e.g. wave breaking) and ship hull with complicated geometry. Despite these shortcomings, moving grid solvers have been considerably improved, and on the Gothenburg 2000 Workshop (Larsson et al. [49]), seven out of 13 CFD solvers with free surface capacities were still using this technique .

The first viscous transient free surface flow computation by a Volume-Of-Fluid (VOF) method appeared more than twenty years ago, see Hirt and Nichols [37]. Many similar methods have been presented since then. The VOF approach has, however, just recently become more widely used in ship hydrodynamics. These methods employ a numerical grid that includes both water and air domain and does not follow the free surface deformation. Some of these methods solve the part of the water flow only (normally ignoring viscosity

of the water); others solve both water and air flow. In the latter methods, the position of the free surface is determined by solving an additional transport equation for the volume fraction of one phase (water or air). Such a method is used in this work. Some examples and a detailed description of the VOF approach can be found in Muzaferija and Perić [58]. The VOF methods have proven to be very suitable to analyze many problems in free-surface ship hydrodynamics such as sloshing, slamming, surface-piercing propellers and large amplitude ship motion in waves.

Early applications of the VOF method analyze flow characteristics around bodies moving with prescribed motion. Arai et al. [4], Schumann [77] and Sames [73] applied such methods for water impact (slamming) problems of two dimensional sections such as wedges, circular cylinders and bow sections. A 3D ship bow water entry was investigated by Muzaferija et al. [57] and Klemt [42]. Also, investigations of radiation and diffraction problems are conducted by applying the VOF techniques. One of the early works was conducted by Kawamura and Miyata [40] for flow around a high-speed ship. Hino [38] and Azcueta et al. [7] and [8] carried out comparative studies on the free surface flow around a ship model with a blunt bow involving breaking waves. Computations of breaking waves were presented by Schumacher [76] for waves behind a submerged hydrofoil and by Caponnetto [15] for flows around a planing hull (spray generation, detachment and reattachment of the water at the chine). Wilson et al. [89] computed diffraction problems of a forced steadily advancing naval combatant in regular head waves. In maneuvering applications, extensive work has also been done for the Series 60 hull form in steady oblique motion with focus on free surface deformation, see Alessandrini and Delhommeau [3], Tahara [82] and Queutey and Visonneau [69]. Their results were compared with experiments published by Longo and Stern [52] with satisfactory agreement.

Since the motion of a floating body is a direct consequence of the flow-induced forces acting on it while at the same time these forces are a function of the body movement itself, the prediction of flow-induced body motion in viscous fluid is a challenging task and requires coupled solution of fluid flow and body motion. One of the first works analyzing the body motion by a free surface RANSE method can be found in Orihara and Miyata [63], where sinkage and trim of semi-planing boats are simulated. Further extension of the work to heel motion of a sailing boat is given in Miyata et al. [54]. Subramani et al. [81] and Orihara [65] predicted flows about a high-speed ship considering sinkage and trim. Orihara and Miyata [64] examined the effectiveness of their RANSE code as a design tool for a hull form with smaller resistance in waves. Dynamic heave and pitch motions of a ship in head waves have been studied by several researchers, see Kinoshita et al. [41], Sato et al. [75], Azcueta [5] and Cura Hochbaum and Vogt [20]. Azcueta [6] simulated the dynamic sinkage and trim of a sailing boat as well as its motion in waves. Recently, Klemt [43] has analyzed a fast conventional passenger ferry advancing in head waves emphasizing on the ship motion and slamming loads on the bow door. So far, to the author's knowledge, this coupled solution technique has not been applied to maneuvering motion of a ship with one exception presented by Akimoto and Miyata [2], where motions of a sailing boat have been predicted. Only the hull has been modeled geometrically. The appendages have been idealized by a wing theory and empirical equations.

Although the conventional codes based on strip theory or panel methods will still be used in the near future for seakeeping and maneuvering applications, the coupled solution

of flow and motion involving RANSE solvers will be useful in investigating problems where the influence of viscous effects or nonlinearities is significant, such as roll motion, slamming, large motion in waves and maneuvering.

1.3 Present Contributions

The present work aims at the application of the coupled solution of RANSE and body motion to seakeeping and maneuvering in waves. On this way, the work pursues mainly three goals:

- 1) Building up a viscous numerical wave tank.
In this tank, small amplitude waves and large amplitude wave packages are generated. The accuracy and the damping-factor of the generated waves are assessed and different methods (e.g. inlet condition and moving non-slip wall) for wave generation are examined.
- 2) Implementing the rigid body dynamics into the existing flow solver.
The method allows for time-accurate simulations of floating bodies in waves, where motions of both 2D simple-geometry bodies and 3D complex-geometry ships are analyzed.
- 3) Extending the method further to more complex ship maneuvering applications.
The aim is to obtain a time-accurate simulation of a whole maneuvering procedure of a self-propelled ship. This requires modeling the interaction of ship, its propeller(s) and its rudder(s). Turning circle and Zigzag maneuvers are performed as examples.

Such analyses have to cover rather long periods of real time to give insight into the maneuvering characteristics. Typically, the whole maneuver has to be simulated, which requires a method with high accuracy for the body motion. Therefore, an accurate rotation operator is implemented in this work whereas previously applied methods, see Azcueta [5] and Klemt [43], do not ensure orthogonality of the body-fixed coordinates.

The first two parts of the present work were begun almost simultaneously under the framework of a BMBF¹ research project ROLL-S² aiming at developing and validating a computational technique for the coupled analysis of viscous flow and flow-induced body motion in waves. The interaction of flow and floating-body without incoming waves is investigated to test the robustness and accuracy of the coupled algorithm, the moving-grid technique for body motion and the prediction of free surface deformation. Test cases such as water entry of a 2D rectangular and circular cylinder etc. are validated and published in Hadžić et al. [30] and Xing-Kaeding et al. [98]. In addition, waves are generated and tested in the viscous numerical tank before the interaction of waves and floating bodies can be analyzed. Two techniques are applied for wave generation in this work, namely by specifying the inlet condition and by simulating the flapping motion of a wave-maker. The latter technique is particularly attractive for validation purpose. Relevant numerical parameters and the

¹German Ministry of Education and Research

²Safety of ships and cargo at large ROLL angle at Sea

required resolution of grids are examined and discussed to achieve an accurate prediction of the wave profile and minimize the wave damping during its propagation.

By combining these two parts, the technique was then ready to be used in prediction of the motion of a floating body in waves. A variety of 2D simple-geometry bodies were first tested in the numerical wave tank subjected to both small amplitude waves and large amplitude wave packages. Correspondingly, experiments were conducted for validation purposes at two water tanks, namely at the Technical University Hamburg-Harburg (TUHH) and the Technical University Berlin (TU Berlin). Due to the very promising agreement in these test cases, see Xing et al. [91]-[92] and Hadžić et al. [30]-[31], the work is extended to applications in three dimensions, which is obviously of main interest in practice. A RoRo vessel running against incoming regular waves at $F_n = 0.22$ was selected as an example and the predicted motion was compared with the model test results, showing satisfactory agreement. The underlying work on ship seakeeping applications was documented in Xing-Kaeding et al. [95]. The first two parts of the work were summarized in the final report of the ROLL-S project, see Hadžić et al. [32].

Since this coupled approach in the present work has demonstrated its robustness and accuracy, the method is further extended to more challenging ship maneuvering applications. The ultimate goal is to perform a transient motion simulation of the whole maneuvering process of a self-propelled ship with its own operating rudder. This requires the modeling of the maneuver organs, e.g. propeller and rudder, and their interaction with the ship in turbulent free surface flow. The rudder is geometrically modeled and surrounded by sliding interfaces to allow rotation of the rudder during computation. The propeller is simulated by applying body forces distributed to a layer of finite-volume cells in the propeller plane for the time being to avoid further complication of the geometry and reduce the computing effort (due to the current limit on computer performance). Before any time-accurate maneuver like turning circle or Zigzag maneuver can be performed, the modeling of the single components, i.e. rudder and propeller, and their interaction between each other has to be validated, see Xing et al. [93] for this basic work. Also, the boundary conditions and moving-grid techniques have to be tested and assessed beforehand. This work was presented on several international conferences, see Xing et al. [94], Xing-Kaeding and Jensen [96]-[97], and Jensen et al. [39].

Building upon this experience, simulations of turning circle and Zigzag maneuvers were performed for self-propelled and -steered ships freely floating at the free surface in the viscous numerical water tank. This kind of simulation – as mentioned in the last section – is yet not common among research groups worldwide. The present work rather belongs to one of the first works applying the coupled technique and a unified approach to different fields of ship hydrodynamics, taking an important step towards the ambitious goal of the *Virtual Towing Tank*.

1.4 Structure of the Thesis

The methodology of the coupled simulation of fluid flow and flow-induced body motion is introduced in Chapter 2. The theoretical basis of flow solver, rigid body dynamics and their coupling procedure is introduced first. Then it is explained how the algorithms for fluid flow, body motion and coupling of both are implemented numerically. In the following section, the

initial and boundary conditions for ship hydrodynamic applications are discussed. Finally, different types of numerical grids applied in this work are outlined and grid-moving strategies adopted in this work are addressed.

Chapter 3 presents a number of two-dimensional test cases of flow and floating body interaction focusing on verification and validation of the numerical method and demonstration of the robustness and reliability of this coupled approach. First, water-entry and -exit of a horizontal circular cylinder are computed with the main concern on accurate predictions of the cylinder motion and the water elevation over time (e.g. jets formation during water-entry). The computational results are compared with experiments, showing good agreement. Especially in terms of the free surface deformation, jet forming, traveling, and collapsing as well as entrapped air bubbles near the cylinder have been captured successfully. Then, waves – both small amplitude regular waves and large amplitude wave packages – are generated and tested in the viscous numerical wave tank. Recommendations of the selection of numerical parameters/schemes and necessary grid resolutions for wave generation are given. Next, the motion of simple-geometry bodies – in both constrained and free motion – is predicted in regular waves. A rectangular cylinder, a mid-ship section with and without keels, and the interaction of two freely floating bodies are computed. The motion of the rectangular cylinder is validated by own experiments. Finally, the large motion of a rectangular cylinder is predicted under large amplitude wave packages, further demonstrating the applicability and reliability of the underlying coupled procedure and the adopted moving-grid strategy.

Chapter 4 extends the method further to 3D problems of predicting the motion of a complex-geometry ship subjected to waves. Incoming waves – both head and oblique waves – are generated in the viscous wave tank. As they travel towards the ship, the resulting ship motion is realized by the underlying moving-grid method, which is proven to be stable and effective. Computational results are compared with available experiments, showing satisfactory agreement. The emphasis of this chapter is to demonstrate the applicability of the present numerical method in studying special problems in seakeeping to reduce the number of expensive model tests in the towing tanks. In addition, robustness, flexibility and accuracy of the coupled method are further examined, which serves as a preliminary step for more complex simulations in ship maneuvering simulations, which will be presented in Chapter 6.

To be capable of predicting ship motions during maneuvering operation, a necessary step beforehand is to model the maneuvering organs like propeller and rudder as well as their interaction with each other and with the ship hull. Three sub-steps are taken in Chapter 5. The first sub-step comprising the first two sections in Chapter 5 deals with rudder and propeller models individually. The rudder is geometrically modeled first in 2D, and then in 3D (without and with rudder fin), and numerical parameters influencing the simulation are discussed. The propeller is modeled by a body force distribution simulating the effect of propeller thrust, torque and side force on the fluid flow. Two methods to determine the total thrust of the propeller are proposed, which are applied later in the maneuvering tests. The second sub-step is to couple the propeller with the rudder and to model their interaction with each other. The rudder forces – both lift and drag forces – increase dramatically due to the rudder's location in the slipstream of the propeller. The axial velocity distribution on the propeller plane becomes less homogenous due to the presence of the rudder. The third sub-step is to assemble the propeller and the rudder in the region of the ship wake so that their

interaction with a hull in captured motion is simulated. The important maneuvering forces – rudder forces behind the propeller and the ship hull – are further examined under different angles of attack, and the comparison with the experimental data shows very satisfactory agreement.

As techniques for modeling individual maneuvering devices and their interaction with the ship hull are examined in Chapter 5, the simulation of motion of a maneuvering ship with appendages is focused on in Chapter 6. The main goal of this chapter is to show how robust, reliable and accurate this coupled method is in applications to such complex maneuvering operations and thus to demonstrate the applicability and flexibility of the unified approach to different problems in ship hydrodynamics. A container ship is selected as example to perform different maneuvers in this chapter. Steady drift motions at a series of drift angles are first computed – with free surface considered – for the fully-equipped container ship to examine the hydrodynamic forces and moments acting on the ship hull and the rudder surfaces and validate them with measurements, which builds up a solid basis for further maneuvering motion simulations. Then, turning circle maneuvers are conducted in the numerical water tank. The Wigley hull – due to its simple geometry – is used to examine the suitability of the boundary conditions and the moving-grid strategies by a semi-captured turning circle test (no rudder is modeled), where roll, heave and pitch motions are free while surge, sway and yaw motions are predefined. The turning circle maneuver of 6-DOF ship motion is then computed for the self-propelled container ship on its own operating rudder. Since no model test result is available for the turning circle maneuver of the container ship, the computed maneuvering characteristics of the ship are compared to the measurements from full scale trials, showing reasonably good agreement. As the last and most challenging application, Zigzag maneuvers are simulated for the Wigley hull and the container ship. A captured 25° Zigzag maneuver of the Wigley hull is conducted against incoming head waves to test the applicability of the boundary conditions. A quite realistic and complex wave pattern can be observed in this simulation. Then, the fully-equipped container ship performs a $10^\circ/10^\circ$ Zigzag maneuver by its own operating rudder. The predicted track, motion and maneuvering characteristics of the ship are compared to available model test measurements, showing promising agreement.

The last chapter summarizes this work, draws conclusions and gives suggestions on future research work.

Chapter 2

Numerical Method

2.1 Introduction

This chapter describes the underlying numerical method for the coupled simulation of fluid flow and the flow-induced body motion. First, the theoretical basis of the flow solver, rigid body dynamics and their coupling algorithm is introduced in section 2.2. In the following, section 2.3 gives the numerical implementation of this coupled procedure. Section 2.4 describes the initial and boundary conditions for ship hydrodynamics applications. In the last section, numerical grids are discussed concerning the different types of grids and grid-moving strategies adopted in this work.

2.2 Theoretical Basis

2.2.1 Fluid Flow

The finite volume method is employed here for computation of incompressible viscous fluid flows with free surface. The solution domain is divided into a finite number of non-overlapping control volumes (CVs). The integral form of conservation equation is applied to each CV (see Eq. 2.1), where piecewise profiles expressing the variation of variables (ϕ) over the CV and its neighboring CVs are used to evaluate the required integrals. If the equations for all CVs are summed up, the conservation equation for the solution domain as a whole can be obtained, since surface integrals over inner CV faces cancel up. This implies that the integral conservation of quantities (ϕ) is exactly satisfied over any group of CVs and, of course, over the whole calculation domain, which makes the finite volume method especially attractive.

The generic conservation equation for a scalar quantity is written in its integral form:

$$\frac{d}{dt} \int_V \rho \phi dV + \int_S \rho \phi (\mathbf{v} - \mathbf{v}_b) \cdot \mathbf{n} dS = \int_S \Gamma \nabla \phi \cdot \mathbf{n} dS + \int_S \mathbf{q}_{\phi,S} \cdot \mathbf{n} dS + \int_V q_{\phi,V} dV, \quad (2.1)$$

where t is time, ρ denotes the density of the fluid, V is the volume of each CV bounded by a closed surface S , \mathbf{v} is the fluid velocity vector whose Cartesian components are u_i , \mathbf{v}_b is the velocity of the CV surface, and \mathbf{n} is the unit vector normal to the CV face and directed outwards. Γ is the diffusion coefficient, $\mathbf{q}_{\phi,S}$ contains portions of the flux vector which are not included in the term $\Gamma \nabla \phi$, and $q_{\phi,V}$ is the volumetric source of the conserved scalar quantity ϕ .

The scalar quantity ϕ can be any conserved *intensive* property (*intensive* property means the property which is independent of the amount of matter considered.). This property can be the unit 1 (for mass conservation), velocity vector \mathbf{v} (for momentum conservation), turbulence quantities like kinetic energy of turbulence or its dissipation rate, enthalpy, or concentration of chemical species. For incompressible flows, the corresponding equations for mass and momentum conservation are expressed below:

$$\frac{d}{dt} \int_V \rho dV + \int_S \rho (\mathbf{v} - \mathbf{v}_b) \cdot \mathbf{n} dS = 0, \quad (2.2)$$

$$\frac{d}{dt} \int_V \rho \mathbf{v} dV + \int_S \rho \mathbf{v} (\mathbf{v} - \mathbf{v}_b) \cdot \mathbf{n} dS = \int_S (\mathbb{T} - p\mathbf{l}) \cdot \mathbf{n} dS + \int_V \rho \mathbf{b} dV. \quad (2.3)$$

In the above equations, \mathbb{T} is the viscous stress tensor, p is the pressure, \mathbf{l} is the unit tensor, and \mathbf{b} represents the body force vector. Only Newtonian fluids are considered here: in Cartesian coordinates the components of the viscous stress tensor τ_{ij} are defined as

$$\tau_{ij} = \mu \left(\frac{\partial u_i}{\partial x_j} + \frac{\partial u_j}{\partial x_i} \right) - \frac{2}{3} \delta_{ij} \mu \nabla \cdot \mathbf{v} \quad (2.4)$$

with μ being the molecular viscosity of the fluid and δ_{ij} the Kronecker delta (1, when $i = j$, otherwise 0).

When the control volume moves or changes its shape, the so-called *space conservation law* (SCL) has to be satisfied. It is expressed by the following relation between the rate of volume change of the CV and the velocities at its faces S :

$$\frac{d}{dt} \int_V dV - \int_S \mathbf{v}_b \cdot \mathbf{n} dS = 0. \quad (2.5)$$

Solutions of continuity and Navier-Stokes equations, Eqs. (2.2) and (2.3), are not easy to obtain because the continuity equation, Eq. (2.2), does not have an independent variable and the pressure p , which appears in the momentum equation, Eq. (2.3), is an extra unknown in addition to the unknown velocity vector. In incompressible flow, the pressure is therefore indirectly determined via the continuity equation, which needs to be treated with special attention, see section 2.3.1 for more details.

Modeling of free surface flows

Methods for computation of free surface flows can be grouped into two broad categories. Interface-tracking methods appeared earlier, where normally only the water flow is computed and numerical grids have to be adapted to the instant position of the free surface. Since the free surface position is normally unknown at the beginning of computation, the complexity of adaptation of the grid to the free surface draws a barrier for the method to be applied to a ship hull with complicated geometry. Furthermore, difficulties of grid adaptation rise dramatically when strong deformations of the free surface (like breaking waves) appear. Another type of method, the so called interface-capturing method, is more suitable to analyze complex wave phenomena and ship geometry, and therefore has been taken in this work. This method treats the continuum as a mixture of two species (water and air) and assumes:

- The mixing of two immiscible species on the molecular level does not take place. So the mass diffusion flux can be set to be zero.
- Two species share the same velocity, pressure and temperature field. This assumption is only relevant in a small part of solution domain where the interface exists since all transport equations are identical as in the case of one-fluid flow where only one fluid is present.

In addition to the conservation equations for mass and momentum, a transport equation for void fraction of the liquid phase c is introduced:

$$\frac{d}{dt} \int_V c \, dV + \int_S c (\mathbf{v} - \mathbf{v}_b) \cdot \mathbf{n} \, dS = 0 . \quad (2.6)$$

Here the void fraction of the liquid phase c is defined as

$$c = \frac{V_l}{V} , \quad (2.7)$$

where V_l denotes the volume occupied by the liquid phase in a CV with the volume V .

The computational domain extends over both water and air phase; the void fraction c is set equal to 1 for CVs filled by water, 0 for CVs filled by air, and between 0 and 1 if one CV is partially filled with one and partially the other fluid. As it is assumed that both fluids share the same velocity and pressure if $0 < c < 1$, both fluids are treated as a single effective fluid whose properties vary in space according to the volume fraction of each phase, i.e. :

$$\rho = \rho_1 c + \rho_2 (1 - c) , \quad \mu = \mu_1 c + \mu_2 (1 - c) , \quad (2.8)$$

where subscripts 1 and 2 denote the two fluids: 1 for water and 2 for air.

No boundary is represented by the interface between two fluids. If surface tension is significant at the interface, it can be treated by a body force in the momentum equation as a function of the volume fraction c , which is achieved by introducing the *continuum surface force* (CSF) model (see Brackbill et al. [12]). In the applications of this work, surface

tension forces are in general small at the free surface and therefore neglected.

Modeling of turbulence

For computations of turbulent flows around ships, the so-called Reynolds Averaged Navier-Stokes equations are solved instead of directly solving the Navier-Stokes equations, although turbulent flows are actually well described by the Navier-Stokes equations. However, the *Direct Numerical Simulation* (DNS), which, as it says, solves the Navier-Stokes equations directly, is of little practical interest since it can only be applied to simple flows of low Reynolds number (R_n) at the current state of computer resources. Another approach is the so-called *Large Eddy Simulation* (LES), in which the large-scale turbulence eddies are directly resolved by the numerical grid while the small-scale turbulence is treated by a turbulence model. This method is in its beginnings of being applied to complex flows in engineering practice, but its computational cost is still too high to be applicable to high R_n flows around ships. An alternative to LES is the *Detached Eddy Simulation* (DES), which could be a good compromise between accuracy and cost. In the DES approach, RANS is used for the attached boundary layer and LES is used for the free shear flow resulting from separation, Travin et al. [85]. To the author's knowledge, this method has not yet been applied to ship flows. The fact that ships have rather complex geometry and turbulent flows around ships usually have high Reynolds number makes the RANS method the only currently available approach.

The RANS equations have the same form as conservation equations for laminar flow, see Eq. (2.2)-(2.3). The only difference is that the variables are now replaced by averaged ones by ensemble averaging (or time averaging if the flow is not transient). Each quantity is replaced by its average and a fluctuation:

$$u_i = \bar{u}_i + u'_i, \quad (2.9)$$

$$\phi = \bar{\phi} + \phi', \quad (2.10)$$

where the overbar denotes the averaged quantity and $'$ denotes the fluctuating part of a variable, which also applies later on.

This poses no problem with the linear terms since averaging any linear term in the conservation equations gives just the identical term for the averaged quantities in the RANS equations, which is the case for the continuity equation. However, for momentum and scalar equations, additional terms result:

$$-\rho \overline{u_i \phi} = -\rho \overline{(\bar{u}_i + u'_i) (\bar{\phi} + \phi')} = -\rho \bar{u}_i \bar{\phi} - \rho \overline{u'_i \phi'}, \quad (2.11)$$

$$-\rho \overline{u_i u_j} = -\rho \overline{(\bar{u}_i + u'_i) (\bar{u}_j + u'_j)} = -\rho \bar{u}_i \bar{u}_j - \rho \overline{u'_i u'_j}, \quad (2.12)$$

The last term of the above equation brings more unknowns than equations available and therefore has to be modeled to close the equation system.

The well-known eddy-viscosity types of turbulence models are selected in this work, which assume an analogy between the turbulent and viscous diffusion and then model the effects of turbulence by introducing turbulent diffusivity terms.

For scalar quantities

$$-\rho \overline{u'_i \phi'} = \Gamma_t \frac{\partial \overline{\phi}}{\partial x_i} \quad (2.13)$$

where Γ_t represents the turbulence diffusivity coefficient.

The terms $-\rho \overline{u'_i u'_j}$, see Eq. (2.12), called as Reynolds stresses, are expressed by a similar form as the viscous stress tensor:

$$-\rho \overline{u'_i u'_j} = \mu_t \left(\frac{\partial \overline{u}_i}{\partial x_j} + \frac{\partial \overline{u}_j}{\partial x_i} \right) - \frac{2}{3} \rho \delta_{ij} k \quad (2.14)$$

where k is the kinetic energy of turbulence

$$k = \frac{1}{2} \overline{u'_i u'_i} , \quad (2.15)$$

δ_{ij} is the Kronecker delta and μ_t is the so-called eddy viscosity.

The dynamic viscosity in the momentum equation, Eq. (2.3), is now replaced by a so-called *effective* viscosity:

$$\mu_{\text{eff}} = \mu + \mu_t . \quad (2.16)$$

k - ϵ turbulence model

The most popular eddy-viscosity model is the standard k - ϵ model (see Launder and Spalding [50]), which will be briefly introduced here.

Since the turbulence/eddy viscosity μ_t is not a material property, it depends on density, velocity (expressed by the square root of kinetic energy of turbulence) and turbulence length scale as expressed below:

$$\mu_t = \rho C_\mu \sqrt{k} L , \quad (2.17)$$

where C_μ is a model parameter. L is the turbulence length scale, which is determined by the turbulence dissipation rate ϵ , and k is the kinetic energy of turbulence as introduced above.

The determination of turbulence length scale L is not obvious. The following relation is assumed following the fact that the rates of construction and destruction of turbulence are in near-balance in the so-called equilibrium turbulent flows:

$$L = \frac{k^{3/2}}{\epsilon} . \quad (2.18)$$

Substituting Eq. (2.18) into Eq. (2.17), the turbulence viscosity μ_t can be rewritten as

$$\mu_t = \rho C_\mu \frac{k^2}{\epsilon} . \quad (2.19)$$

Employing the standard k - ϵ model, the pressure is modified by

$$p_m = p + \frac{2}{3} \rho k . \quad (2.20)$$

The conservation equations for k and ϵ have the same form as for other scalars and can be derived:

$$\frac{d}{dt} \int_V \rho k \, dV + \int_S \rho k (\bar{\mathbf{v}} - \bar{\mathbf{v}}_b) \cdot \mathbf{n} \, dS = \int_S \left(\mu + \frac{\mu_t}{\sigma_k} \right) \nabla k \cdot \mathbf{n} \, dS + \int_V (P_k + P_B - \rho \epsilon) \, dV , \quad (2.21)$$

$$\begin{aligned} \frac{d}{dt} \int_V \rho \epsilon \, dV + \int_S \rho \epsilon (\bar{\mathbf{v}} - \bar{\mathbf{v}}_b) \cdot \mathbf{n} \, dS = \int_S \left(\mu + \frac{\mu_t}{\sigma_\epsilon} \right) \nabla \epsilon \cdot \mathbf{n} \, dS + \\ \int_V \left[C_{\epsilon,1} P_k \frac{\epsilon}{k} - C_{\epsilon,2} \rho \frac{\epsilon^2}{k} + C_{\epsilon,3} \max(P_B, 0) \frac{\epsilon}{k} \right] \, dV, \end{aligned} \quad (2.22)$$

where P_B is due to buoyancy and is neglected here. P_k represents the production of turbulent kinetic energy by shear and is modeled as

$$P_k = -\overline{\rho u'_i u'_j} \frac{\partial \bar{u}_i}{\partial x_j} = \mu_t \left(\frac{\partial \bar{u}_i}{\partial x_j} + \frac{\partial \bar{u}_j}{\partial x_i} \right) \frac{\partial \bar{u}_i}{\partial x_j} , \quad (2.23)$$

The values of the empirical coefficients C_μ , σ_k , $C_{\epsilon,1}$, $C_{\epsilon,2}$, $C_{\epsilon,3}$ and σ_ϵ in the standard k - ϵ turbulence model are given in Table 2.1.

Another turbulence model, the RNG (Renormalization Group) k - ϵ model (see Yakhot and Orzag [99]), has also been tested in this work. This model differs from the standard k - ϵ model in the following two aspects:

- An additional source term for the ϵ equation is introduced, which is associated with the effect of the rate of mean flow distortion on turbulence dissipation rate:

$$S_\epsilon = - \int_V \frac{C_\mu f^3 \left(1 - \frac{f}{C_{\epsilon,5}} \right) \rho \epsilon^2}{1 + C_{\epsilon,6} f^3} \frac{1}{k} \, dV , \quad (2.24)$$

Table 2.1: Values of empirical coefficients in the standard k - ϵ turbulence model

C_μ	$C_{\epsilon,1}$	$C_{\epsilon,2}$	$C_{\epsilon,3}$	σ_k	σ_ϵ
0.09	1.44	1.92	1.44	1.0	1.3

Table 2.2: Values of empirical coefficients in the RNG k - ϵ turbulence model

C_μ	$C_{\epsilon,1}$	$C_{\epsilon,2}$	$C_{\epsilon,3}$	$C_{\epsilon,5}$	$C_{\epsilon,6}$	σ_k	σ_ϵ
0.085	1.42	1.68	1.42	4.38	0.012	0.72	0.72

where

$$f = S \frac{k}{\epsilon}, \quad \text{with } S = \sqrt{2D_{ij}D_{ji}} \text{ and } D_{ij} = \frac{1}{2} \left(\frac{\partial \bar{u}_i}{\partial x_j} + \frac{\partial \bar{u}_j}{\partial x_i} \right). \quad (2.25)$$

$C_{\epsilon,5}$ and $C_{\epsilon,6}$ are empirical parameters given in Table 2.2. This extra term is believed to be important when the dimensionless shear (ratio of turbulent dissipation time scale k/ϵ and the mean flow distortion time scale $1/S$) is large compared with unity.

- The model parameters differ from the standard k - ϵ turbulence model and are given in Table 2.2.

The comparison on the numerical results using the two models will be shown for a rudder profile in section 5.2.3.

2.2.2 Rigid Body Dynamics

Frames of reference

To describe the rigid body motions, the frames of reference to which the motions of the rigid body are referred, are defined here first:

- A global coordinate system (GS) is a non-rotating, non-accelerating Newtonian reference system. It coincides with a space-fixed coordinate system if it is defined as a frame of reference fixed to space, or it can also be a frame of reference moving at a constant velocity with its axes parallel to the space-fixed coordinate system. It is defined here with the XY plane parallel to the undisturbed free surface plane and Z axis pointing upwards for convenience. This frame of reference is taken to describe the RANS equations and to record the position and orientation of the rigid body.
- A body-fixed coordinate system (BS) is set to be originated at the mass center of the body, maintaining the orientation of the body. With respect to a ship, the x-axis is in the longitudinal direction pointing towards the ship bow; the z-axis is set to be upwards pointing to the superstructure of the ship, and y-axis is pointing the port side

following the right-hand rule. This coordinate system is helpful to identify the rigid body orientation and to realize the body motion or constrain certain angular motions of the rigid body.

- An intermediate frame of reference (IS) is defined as a non-rotating Newtonian system with the body mass center as its origin. The angular momentum equations become simpler in this system since the momentum lever of linear momentum vanishes. It is possible to construct the angular momentum equations in such a system because in principle the reference point of the body angular momentum can be chosen in space at random. Though, a good deal of care must be exercised in doing so because it must be considered simultaneously a space-fixed and body-fixed point. In other words, at any instant of time (time ceases to flow), the body can have velocity and acceleration relative to it, but never a displacement. In this way, the velocity and acceleration of the center of mass computed relative to this point are absolute and relative to the GS. This type of reference system was devised by Leonard Euler (see e.g. Kolk [45]) and will be used in this work to compute the velocity and acceleration. As the velocity and acceleration of the body computed in this system – as already mentioned – are absolute and relative to the GS, GS will be referenced later on to coincide with the displacement.

Governing equations of rigid body motion

The governing equations of the motion of a rigid body with six Degrees Of Freedom (DOF) in a Newtonian reference system are:

$$\frac{d(m\mathbf{v}_C)}{dt} = \mathbf{f} . \quad (2.26)$$

$$\frac{d(M_C \cdot \boldsymbol{\omega}_C)}{dt} = \mathbf{m}_C . \quad (2.27)$$

In the above equations, m represents the mass of the body, \mathbf{v}_C is the velocity vector of the center of mass of the body, M_C is the tensor of the moments of inertia of the body, $\boldsymbol{\omega}_C$ is the angular velocity vector of the body, \mathbf{f} is the resultant vector of forces acting on the body, and \mathbf{m}_C represents the moments acting on the body with respect to its center of mass.

Since the mass of the rigid body is supposed to be constant and the moments of inertia of the body keep constant with respect to BS, Eq. (2.26) and Eq. (2.27) can be written as

$$m\dot{\mathbf{v}}_C = \mathbf{f} , \quad (2.28)$$

and

$$\frac{d(M_C \cdot \boldsymbol{\omega}_C)}{dt} = M_C \cdot \frac{d(\boldsymbol{\omega}_C)}{dt} = M_C \cdot \dot{\boldsymbol{\omega}}_C + \boldsymbol{\omega}_C \times M_C \cdot \boldsymbol{\omega}_C = \mathbf{m}_C . \quad (2.29)$$

with respect to the BS.

According to the principle of virtual work, we can set

$$[\delta \mathbf{r}^g]^T \cdot \mathbf{f}^g = [\delta \mathbf{r}]^T \cdot \mathbf{f} , \quad (2.30)$$

$$[\delta \mathbf{r}^g]^T \cdot \mathbf{m}_C^g = [\delta \mathbf{r}]^T \cdot \mathbf{m}_C . \quad (2.31)$$

Here, the superscript g indicates the variables expressed in terms of the GS (or IS), which applies throughout this work. $\delta \mathbf{r}$ denotes an infinitesimal virtual displacement vector. Then, the equations with respect to the GS can be derived (for the derivation, see Appendix A):

$$m \dot{\mathbf{v}}_C^g = \mathbf{f}^g , \quad (2.32)$$

and

$$\mathbf{M}_C^g \cdot \dot{\boldsymbol{\omega}}_C^g + \boldsymbol{\omega}_C^g \times \mathbf{M}_C^g \cdot \boldsymbol{\omega}_C^g = \mathbf{m}_C^g . \quad (2.33)$$

Here, \mathbf{M}_C^g is the tensor of the moments of inertia with respect to the mass center of the body expressed in GS. When the body rotates, \mathbf{M}_C^g is changing; therefore it is updated each time the body position changes by the following expression:

$$\mathbf{M}_C^g = \mathbf{T}_T \cdot \mathbf{M}_C \cdot \mathbf{T}_T^{-1} . \quad (2.34)$$

Here \mathbf{M}_C is the constant moments of inertia with respect to the BS and usually known at the initial stage for a certain rigid body. \mathbf{T}_T stands for the transformation matrix from the BS to the GB (or IS). The columns of \mathbf{T}_T are the unit vectors \mathbf{x} , \mathbf{y} and \mathbf{z} attached to the BS.

Eulerian angles

Once the angular velocities of the body are obtained, the orientation of the body can be determined from the tensor \mathbf{T}_T , whose columns are the unit vectors \mathbf{x} , \mathbf{y} and \mathbf{z} attached to BS. In engineering applications, the interest is in how far the vehicle (body) has been rotated about its own axes (\mathbf{x} , \mathbf{y} and \mathbf{z}) from the space-fixed reference (GS) rather than how far the vehicle should be rotated about the axes in the GS. For instance, one speaks about the roll motion of a ship, indicating how far the ship has been rolled about its own longitudinal axis from a horizontal space reference. This being the case, one would like to rotate one axis system successively about its own axes so that at the end of the third rotation the axis system would be parallel to the expected axis system. Care must be taken to the order of the rotation, since they do not obey the commutative law thereby requiring the sequence of rotations to be kept. Though the sequence is arbitrary, the following one has been taken here to follow the common practice of ship hydrodynamics.

As explained in Fig. 2.1, we rotate first by ψ about \mathbf{Z} , then by θ about \mathbf{Y}' (where \mathbf{Y}' is the new orientation of the \mathbf{Y} -axis brought about by the ψ -rotation), and finally by φ about \mathbf{x} (where \mathbf{x} is the new orientation of the \mathbf{X} -axis brought about by the ψ -rotation and by the

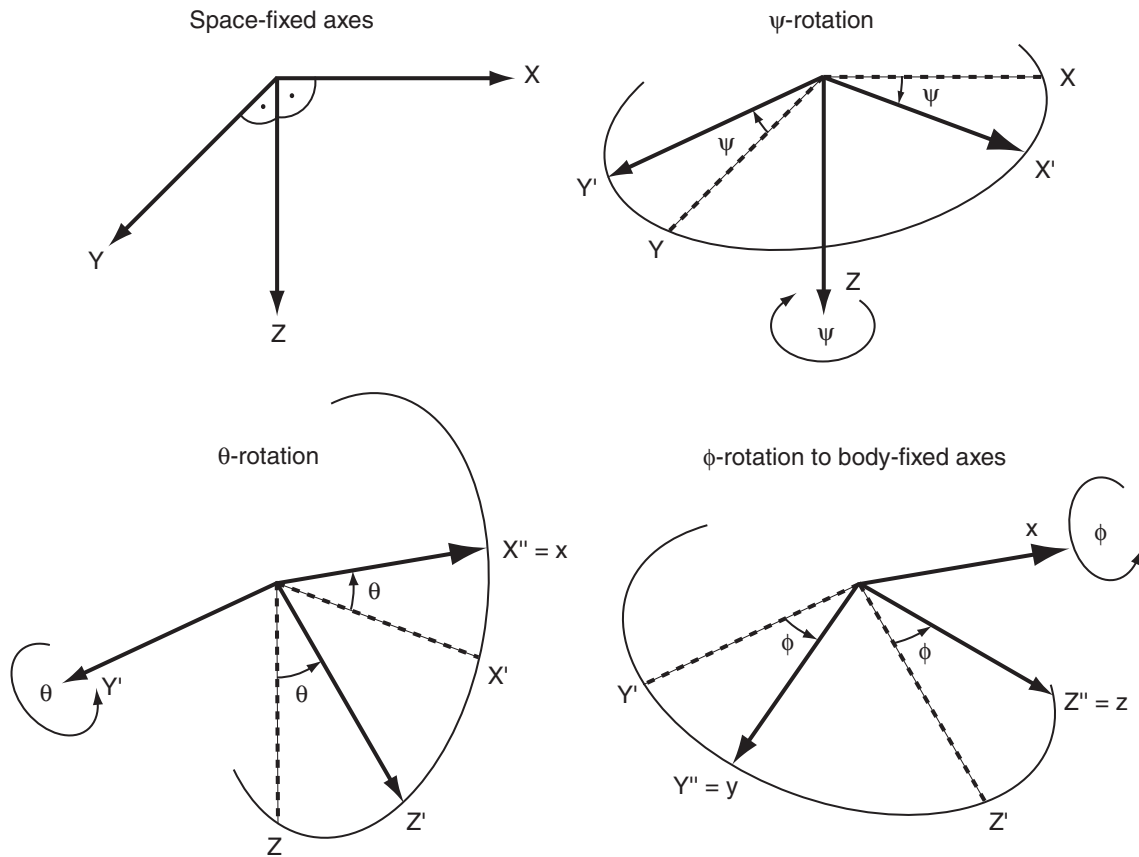


Figure 2.1: Sequence of rotation.

θ -rotation, and moreover it is the new x axis attached to BS). Note that \mathbf{X} , \mathbf{Y} and \mathbf{Z} are the space-fixed axes, and \mathbf{x} , \mathbf{y} and \mathbf{z} are the body-fixed axes. It should be also noticed that the procedure generates three axes intermediate to the space- and body-axes, which are denoted with single primes and not necessarily being orthogonal.

The following equations describe the intermediate axes as defined above in vector form:

$$\mathbf{X}' = \frac{\mathbf{x} - (\mathbf{x} \cdot \mathbf{Z}) \mathbf{Z}}{|\mathbf{x} - (\mathbf{x} \cdot \mathbf{Z}) \mathbf{Z}|}, \quad (2.35)$$

$$\mathbf{Y}' = \mathbf{Z} \times \mathbf{X}', \quad (2.36)$$

The three Eulerian angles ψ , θ and φ can be obtained:

$$\psi = \arcsin [(\mathbf{X} \times \mathbf{X}') \cdot \mathbf{Z}], \quad (2.37)$$

$$\theta = \arcsin [(\mathbf{X}' \times \mathbf{x}) \cdot \mathbf{Y}'], \quad (2.38)$$

$$\varphi = \arcsin \left[\left(\mathbf{Y}' \times \mathbf{y} \right) \cdot \mathbf{x} \right] . \quad (2.39)$$

Here, the Eulerian angles ψ , θ and φ are defined as *yaw*, *pitch* or *trim* and *roll* or *heel* angles respectively.

The transformation matrix \mathbf{T}_T from BS to GS can now be expressed in terms of the Eulerian angles φ , θ and ψ by pursuing the reverse sequence of the rotation:

$$\begin{aligned} \mathbf{T}_T &= \begin{pmatrix} \cos \psi & -\sin \psi & 0 \\ \sin \psi & \cos \psi & 0 \\ 0 & 0 & 1 \end{pmatrix} \cdot \begin{pmatrix} \cos \theta & 0 & \sin \theta \\ 0 & 1 & 0 \\ -\sin \theta & 0 & \cos \theta \end{pmatrix} \cdot \begin{pmatrix} 1 & 0 & 0 \\ 0 & \cos \varphi & -\sin \varphi \\ 0 & \sin \varphi & \cos \varphi \end{pmatrix} \\ &= \begin{pmatrix} \cos \theta \cos \psi & \sin \varphi \sin \theta \cos \psi - \cos \varphi \sin \psi & \cos \varphi \sin \theta \cos \psi + \sin \varphi \sin \psi \\ \cos \theta \sin \psi & \sin \varphi \sin \theta \sin \psi + \cos \varphi \cos \psi & \cos \varphi \sin \theta \sin \psi - \sin \varphi \cos \psi \\ -\sin \theta & \sin \varphi \cos \theta & \cos \varphi \cos \theta \end{pmatrix} . \end{aligned} \quad (2.40)$$

As shown in Fig. 2.1, the orientation of the body in space can be fully described by the Eulerian angles φ , θ and ψ about the axes \mathbf{x} , \mathbf{Y}' and \mathbf{Z} , respectively. As the rate of change of the body's orientation is its angular velocity, it follows that the angular velocity $\boldsymbol{\omega}_{C^g}$ has scalar components of $\dot{\varphi}$, $\dot{\theta}$ and $\dot{\psi}$ along the aforementioned axes in the following form:

$$\begin{aligned} \begin{pmatrix} \omega_{C^g,1} \\ \omega_{C^g,2} \\ \omega_{C^g,3} \end{pmatrix} &= \begin{pmatrix} 0 \\ 0 \\ \dot{\psi} \end{pmatrix} + \begin{pmatrix} \cos \psi & -\sin \psi & 0 \\ \sin \psi & \cos \psi & 0 \\ 0 & 0 & 1 \end{pmatrix} \cdot \begin{pmatrix} 0 \\ \dot{\theta} \\ 0 \end{pmatrix} \\ &+ \begin{pmatrix} \cos \psi & -\sin \psi & 0 \\ \sin \psi & \cos \psi & 0 \\ 0 & 0 & 1 \end{pmatrix} \cdot \begin{pmatrix} \cos \theta & 0 & \sin \theta \\ 0 & 1 & 0 \\ -\sin \theta & 0 & \cos \theta \end{pmatrix} \cdot \begin{pmatrix} \dot{\varphi} \\ 0 \\ 0 \end{pmatrix} \\ &= \begin{pmatrix} \cos \psi \cos \theta & -\sin \psi & 0 \\ \sin \psi \cos \theta & \cos \psi & 0 \\ -\sin \theta & 0 & 1 \end{pmatrix} \cdot \begin{pmatrix} \dot{\varphi} \\ \dot{\theta} \\ \dot{\psi} \end{pmatrix} \end{aligned} \quad (2.41)$$

Constrained motion

It is sometimes desirable that kinematical constraints can be considered for the simulation of body motion. Either they can be some *imaginary* constraints to simplify the computational model and reduce the computational effort or they are *physical* constraints as often used in the model tests to concentrate on some degrees of freedom of the model and restrict others.

The analytical expression of the constraint equations for a rigid body can be generally formulated as:

$$\phi_k(\mathbf{d}, t) = 0 \quad k = 1, 2, \dots, p, \quad p < 6, \quad (2.42)$$

here t is time and \mathbf{d} denotes the dependent coordinates, i.e.:

$$\mathbf{d} = \begin{pmatrix} r_x \\ r_y \\ r_z \\ \varphi \\ \theta \\ \psi \end{pmatrix}, \quad (2.43)$$

p is the total number of the constraints. The degrees of freedom of the rigid body therefore reduces to

$$f = 6 - p. \quad (2.44)$$

The number of degrees of freedom f indicates the minimum number of variables which would have described the motion of the rigid body completely and therefore are called independent variables. It is possible to formulate the equations of motion under constraints with both dependent or independent coordinates, García De Jalón and Bayo [27]. In general, the method of the Lagrange multipliers using dependent coordinates offers a simple concept and permits the calculation of forces associated with the constraints (which depends on the Lagrange multipliers) with a minimum additional effort. However, as the numerical integration proceeds, this method may suffer a violation of constraint conditions progressively leading to unacceptable results in all but short simulations (constraint stabilization is usually required for long simulations). In contrast, in the formulation of independent coordinates the instability problem in the integration of constraint equations using Ordinary Differential Equation (ODE) solvers disappears. Another important advantage of using independent coordinates is a reduction in the number of equations to be integrated. Only $f = 6 - p$ equations are obtained using the independent coordinates instead of $6 + p$ equations if dependent coordinates and the method of the Lagrange multipliers are used (at least p equations in case that projection matrix is employed). Therefore the independent coordinates have been selected here; the method used here is based on the Jacobian matrix, as explained below.

If f independent coordinates can be pointed out first, one can actually rearrange the above constraint equation, Eq. (2.42), to define the body position (dependent coordinates) \mathbf{r}_C^g and \mathbf{T}_T^g as a function of independent coordinates and time:

$$\mathbf{r}_C^g = \mathbf{r}(\mathbf{q}, t), \quad \mathbf{T}_T^g = \mathbf{T}_T(\mathbf{q}, t), \quad (2.45)$$

where \mathbf{q} denotes the selected independent coordinates (there might be more than one possibility):

$$\mathbf{q} = \begin{pmatrix} q_1 \\ q_2 \\ \dots \\ q_f \end{pmatrix}. \quad (2.46)$$

Differentiating the above equations, one obtains

$$\mathbf{v}_C^g = \frac{\partial \mathbf{r}}{\partial \mathbf{q}} \cdot \dot{\mathbf{q}} + \frac{\partial \mathbf{r}}{\partial t} = \mathbf{J}_T \cdot \dot{\mathbf{q}} + \mathbf{v}' \quad (2.47)$$

and

$$\boldsymbol{\omega}_C^g = \frac{\partial \mathbf{s}}{\partial \mathbf{q}} \cdot \dot{\mathbf{q}} + \frac{\partial \mathbf{s}}{\partial t} = \mathbf{J}_R \cdot \dot{\mathbf{q}} + \boldsymbol{\omega}' \quad (2.48)$$

Here, the $3 \times f$ Jacobian matrix for translation motion is

$$\mathbf{J}_T = \frac{\partial \mathbf{r}}{\partial \mathbf{q}} = \begin{pmatrix} \frac{\partial r_x}{\partial q_1} & \frac{\partial r_x}{\partial q_2} & \cdots & \frac{\partial r_x}{\partial q_f} \\ \frac{\partial r_y}{\partial q_1} & \frac{\partial r_y}{\partial q_2} & \cdots & \frac{\partial r_y}{\partial q_f} \\ \frac{\partial r_z}{\partial q_1} & \frac{\partial r_z}{\partial q_2} & \cdots & \frac{\partial r_z}{\partial q_f} \end{pmatrix} \quad (2.49)$$

and the $3 \times f$ Jacobian matrix for rotation motion is

$$\mathbf{J}_R = \frac{\partial \mathbf{s}}{\partial \mathbf{q}} = \begin{pmatrix} \frac{\partial s_x}{\partial q_1} & \frac{\partial s_x}{\partial q_2} & \cdots & \frac{\partial s_x}{\partial q_f} \\ \frac{\partial s_y}{\partial q_1} & \frac{\partial s_y}{\partial q_2} & \cdots & \frac{\partial s_y}{\partial q_f} \\ \frac{\partial s_z}{\partial q_1} & \frac{\partial s_z}{\partial q_2} & \cdots & \frac{\partial s_z}{\partial q_f} \end{pmatrix} \quad (2.50)$$

$\partial \mathbf{s} = [\partial s_x, \partial s_y, \partial s_z]^T$ is an instant vector about which the rigid body rotates. Its components can be obtained from the following tensor:

$$\partial \mathbf{T}_T \cdot \mathbf{T}_T^T = \begin{pmatrix} 0 & -\partial s_z & \partial s_y \\ \partial s_z & 0 & -\partial s_x \\ -\partial s_y & \partial s_x & 0 \end{pmatrix} \quad (2.51)$$

The elements in the matrix \mathbf{J}_R , Eq. (2.50), can be calculated as shown in the following. Take the first column as an example:

$$\frac{\partial \mathbf{T}_T}{\partial q_1} \cdot \mathbf{T}_T^T = \begin{pmatrix} 0 & -\frac{\partial s_z}{\partial q_1} & \frac{\partial s_y}{\partial q_1} \\ \frac{\partial s_z}{\partial q_1} & 0 & -\frac{\partial s_x}{\partial q_1} \\ -\frac{\partial s_y}{\partial q_1} & \frac{\partial s_x}{\partial q_1} & 0 \end{pmatrix} \quad (2.52)$$

Further differentiating the velocities, Eqs. (2.47) and (2.48), the accelerations of the rigid body are obtained:

$$\dot{\mathbf{v}}_C^g = \mathbf{J}_T \cdot \ddot{\mathbf{q}} + \mathbf{L}_T \cdot \dot{\mathbf{q}} + \dot{\mathbf{v}}' \quad (2.53)$$

and

$$\dot{\boldsymbol{\omega}}_C^g = \mathbf{J}_R \cdot \ddot{\mathbf{q}} + \mathbf{L}_R \cdot \dot{\mathbf{q}} + \dot{\boldsymbol{\omega}}' . \quad (2.54)$$

Here

$$\mathbf{L}_T = \frac{\partial (\mathbf{J}_T \cdot \dot{\mathbf{q}})}{\partial \mathbf{q}} + 2 \frac{\partial \dot{\mathbf{v}}'}{\partial \mathbf{q}} \quad (2.55)$$

and

$$\mathbf{L}_R = \frac{\partial (\mathbf{J}_R \cdot \dot{\mathbf{q}})}{\partial \mathbf{q}} + \frac{\partial \dot{\boldsymbol{\omega}}'}{\partial \mathbf{q}} + \frac{\partial \mathbf{J}_R}{\partial t} , \quad (2.56)$$

with

$$\dot{\mathbf{v}}' = \frac{\partial^2 \mathbf{r}}{\partial t^2}, \quad \dot{\boldsymbol{\omega}}' = \frac{\partial^2 \mathbf{s}}{\partial t^2} . \quad (2.57)$$

Substituting Eqs. (2.48), (2.53) and (2.54) into Eqs. (2.32) and (2.33), the governing equation under constraint conditions reads:

$$\overline{\mathbf{M}} \cdot \ddot{\mathbf{q}} + \overline{\mathbf{N}} = \mathbf{F}^g , \quad (2.58)$$

where

$$\overline{\mathbf{M}} = \begin{pmatrix} m\mathbf{J}_T \\ \mathbf{M}_C^g \cdot \mathbf{J}_R \end{pmatrix} , \quad (2.59)$$

$$\overline{\mathbf{N}} = \begin{pmatrix} m\mathbf{L}_T \cdot \dot{\mathbf{q}} + m\dot{\mathbf{v}}' \\ \mathbf{M}_C^g \cdot (\mathbf{L}_R \cdot \dot{\mathbf{q}}) + \mathbf{M}_C^g \cdot \dot{\boldsymbol{\omega}}' + (\mathbf{J}_R \cdot \dot{\mathbf{q}} + \dot{\boldsymbol{\omega}}') \times \mathbf{M}_C^g \cdot (\mathbf{J}_R \cdot \dot{\mathbf{q}} + \dot{\boldsymbol{\omega}}') \end{pmatrix} , \quad (2.60)$$

$$\mathbf{F}^g = \begin{pmatrix} \mathbf{f}^g \\ \mathbf{m}_C^g \end{pmatrix} . \quad (2.61)$$

Here \mathbf{F}^g can be divided into two parts:

$$\mathbf{F}^g = \mathbf{F}^{i,g} + \mathbf{F}^{q,g} . \quad (2.62)$$

$\mathbf{F}^{i,g}$ denotes the impressed forces (or moments) acting on the body, which can be obtained either from the fluid flow (see section 2.2.3) or any external sources and $\mathbf{F}^{q,g}$ denotes the forces (or moments) which maintain the given constraints.

The forces (or moments) $\mathbf{F}^{q,g}$, usually called *forces of reaction*, remain yet unknown at this point. To eliminate $\mathbf{F}^{q,g}$, D'Alembert's Principle can be applied:

$$\sum_k \delta \mathbf{r}_k^T \mathbf{F}_k^e = 0 . \quad (2.63)$$

Note that the superscript g has been omitted here since the principle is generally valid for all coordinates. In Eq. (2.63), $\delta \mathbf{r}$ denotes the virtual displacements which are assumed to be reversible and the index k denotes the body in a multi-body system, which will be omitted since only one single body is considered here. \mathbf{F}_k^e are the so-called *effective forces* (see Lanczos [47]), which result if the forces of inertia \mathbf{I}_k are added to the impressed forces \mathbf{F}_k^i which act on a point P_k . The effective forces can be expressed as

$$\mathbf{F}^e = \mathbf{F}^i + \mathbf{I} = \mathbf{F}^i - m\mathbf{A} , \quad (2.64)$$

where \mathbf{A} denotes the acceleration of the body. From the second Newton Law,

$$m\mathbf{A} = \mathbf{F} . \quad (2.65)$$

Substituting Eqs. (2.64) and (2.65) into Eq. (2.63), one obtains

$$\sum \delta \mathbf{r}^T \cdot (\mathbf{F}^i - m\mathbf{A}) = \sum \delta \mathbf{r}^T \cdot (\mathbf{F}^i - \mathbf{F}) . \quad (2.66)$$

With the help of Eq. (2.62)

$$\sum \delta \mathbf{r}^T \cdot (\mathbf{F}^i - \mathbf{F}) = \sum \delta \mathbf{r}^T \cdot (-\mathbf{F}^q) = 0 . \quad (2.67)$$

$\delta \mathbf{r}$ must be consistent with the given kinematical constraints:

$$\delta \mathbf{r} = \mathbf{J} \cdot \delta \mathbf{q} , \quad (2.68)$$

with

$$\mathbf{J} = \begin{pmatrix} \mathbf{J}_T \\ \mathbf{J}_R \end{pmatrix} , \quad (2.69)$$

where \mathbf{J}_T and \mathbf{J}_R are given in Eqs. (2.49) and (2.50) respectively. Substituting Eq. (2.68) into Eq. (2.67), it can be obtained

$$\delta \mathbf{q}^T \cdot (\mathbf{J}^T \cdot \mathbf{F}^q) = 0 . \quad (2.70)$$

So

$$\mathbf{J}^T \cdot \mathbf{F}^q = 0 . \quad (2.71)$$

Substituting Eq. (2.62) into (2.58), then multiplying the matrix \mathbf{J}^T to both sides of Eq. (2.58), the unknown term $\mathbf{F}^{q,g}$ is eliminated with the help of Eq. (2.71). The resultant equation reads

$$(\mathbf{J}^T \cdot \overline{\mathbf{M}}) \cdot \ddot{\mathbf{q}} + \mathbf{J}^T \cdot \overline{\mathbf{N}} = \mathbf{J}^T \cdot \mathbf{F}^{i,g} . \quad (2.72)$$

The above equation has $f = 6 - p$ variables and can be solved similarly as Eqs. (2.32) and (2.33). If one is interested in obtaining the reaction forces, they can be obtained after the equations of body motion are solved (Eqs. (2.62) and (2.58)):

$$\mathbf{F}^{q,g} = \overline{\mathbf{M}} \cdot \ddot{\mathbf{q}} + \overline{\mathbf{N}} - \mathbf{F}^{i,g} . \quad (2.73)$$

An example in ship hydrodynamic applications

An often encountered case in ship hydrodynamic applications is taken here as an example to demonstrate how the constraint conditions can be constructed. The ship is supposed to advance with constant velocity \overline{V} and constant course angle $\overline{\psi}$. That is to say, four degrees of freedom, namely sway, heave, roll and pitch motion are free and therefore can be selected as independent variables. So the independent coordinates \mathbf{q} can be expressed correspondingly

$$\mathbf{q} = \begin{pmatrix} y \\ z \\ \varphi \\ \theta \end{pmatrix}, \quad f = 4 . \quad (2.74)$$

The ship position \mathbf{r}_C and orientation \mathbf{T}_T , see Eqs. (2.45) and (2.40), can be expressed by the independent coordinates and time:

$$\mathbf{r}_C = \begin{pmatrix} r_x \\ r_y \\ r_z \end{pmatrix} = \begin{pmatrix} -y \sin \overline{\psi} + \overline{V} t \cos \overline{\psi} \\ y \cos \overline{\psi} + \overline{V} t \sin \overline{\psi} \\ z \end{pmatrix}, \quad (2.75)$$

$$\mathbf{T}_T = \begin{pmatrix} \cos \theta \cos \overline{\psi} & \sin \varphi \sin \theta \cos \overline{\psi} - \cos \varphi \sin \overline{\psi} & \cos \varphi \sin \theta \cos \overline{\psi} + \sin \varphi \sin \overline{\psi} \\ \cos \theta \sin \overline{\psi} & \sin \varphi \sin \theta \sin \overline{\psi} + \cos \varphi \cos \overline{\psi} & \cos \varphi \sin \theta \sin \overline{\psi} - \sin \varphi \cos \overline{\psi} \\ -\sin \theta & \sin \varphi \cos \theta & \cos \varphi \cos \theta \end{pmatrix} \quad (2.76)$$

The Jacobian matrices for translation and rotation motions are obtained following Eqs. (2.49) and (2.50) respectively:

$$\mathbf{J}_T = \begin{pmatrix} -\sin \bar{\psi} & 0 & 0 & 0 \\ \cos \bar{\psi} & 0 & 0 & 0 \\ 0 & 1 & 0 & 0 \end{pmatrix}, \quad (2.77)$$

$$\mathbf{J}_R = \begin{pmatrix} 0 & 0 & \cos \bar{\psi} \cos \theta & -\sin \bar{\psi} \\ 0 & 0 & \sin \bar{\psi} \cos \theta & \cos \bar{\psi} \\ 0 & 0 & -\sin \theta & 0 \end{pmatrix}. \quad (2.78)$$

Other matrices and vectors are calculated according to Eqs. (2.55), (2.56), (2.47), (2.48) and (2.57):

$$\mathbf{L}_T = 0, \quad (2.79)$$

$$\mathbf{L}_R = \begin{pmatrix} 0 & 0 & 0 & -\dot{\phi} \cos \bar{\psi} \sin \theta \\ 0 & 0 & 0 & -\dot{\phi} \sin \bar{\psi} \sin \theta \\ 0 & 0 & 0 & -\dot{\phi} \cos \theta \end{pmatrix}, \quad (2.80)$$

$$\mathbf{v}' = \begin{pmatrix} \bar{V} \cos \bar{\psi} \\ \bar{V} \sin \bar{\psi} \\ 0 \end{pmatrix}, \quad \boldsymbol{\omega}' = 0, \quad (2.81)$$

$$\dot{\mathbf{v}}' = 0, \quad \dot{\boldsymbol{\omega}}' = 0. \quad (2.82)$$

2.2.3 Coupling of Fluid Flow and Rigid Body Motion

For computing the interaction between fluid flow and rigid body motion, the equations of the rigid body motion have to be coupled with the flow solver. All variables describing the fluid flow and boundary conditions have to be revised or updated according to the transient rigid body motion. At the same time, the motion of the rigid body is strongly influenced by the forces acting on the body surface from the fluid flow around the body.

Since the RANS equations describing the fluid flow around the body are expressed in terms of the GS, it is then convenient to compute the body motion also in the GS (or IS). Such that the surface forces acting on the body surface from the fluid flow can be integrated directly from the fluid solver and the body velocity acting on the body can also be directly fed back to the fluid as part of moving non-slip wall boundary conditions.

Computation of impressed forces

The impressed forces acting on the body consist of field forces, surface forces and external forces. The surface forces can be integrated from the pressure and shear forces acting on the body surface and the field forces are usually regarded as gravity force. The resultant force $\mathbf{f}^{i,g}$ can be computed by the following expression:

$$\mathbf{f}^{i,g} = \int_S (\mathbf{T} - pl) \cdot \mathbf{n} dS + m\mathbf{g} + \mathbf{f}_e^g . \quad (2.83)$$

Here \mathbf{T} stands for the viscous stress tensor whose components are τ_{ij} introduced in Eq. (2.4), l is the unit tensor, \mathbf{g} is the gravity acceleration vector and \mathbf{f}_e^g denotes any explicit external forces acting on the rigid body.

Field forces do not contribute to the moment around the center of mass, but the moments due to surface forces (pressure and shear forces) need to be integrated:

$$\mathbf{m}_C^{i,g} = \int_S (\mathbf{r} - \mathbf{r}_C) \times (\mathbf{T} - pl) \cdot \mathbf{n} dS + \mathbf{m}_{C,e}^g . \quad (2.84)$$

Here the vector \mathbf{r} represents the position of a certain point on the body surface and \mathbf{r}_C the position of the mass center of the body with respect to GS, see Fig. 2.2. The vector $\mathbf{m}_{C,e}^g$ includes all explicit external moments applied to the rigid body.

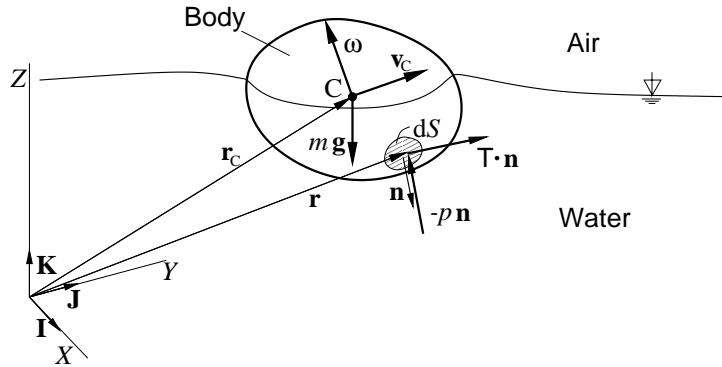


Figure 2.2: Motion of the floating body due to the forces acting on the body

Moving no-slip walls

The surface of the rigid body is usually considered as non-slip wall. The velocities at such a moving wall should therefore be specified and updated at each time instant. The velocities at the body surface \mathbf{v}_b can be computed once the position and the velocity of the rigid body are known (see Fig. 2.2):

$$\mathbf{v}_b = \mathbf{v}_C + \boldsymbol{\omega} \times (\mathbf{r} - \mathbf{r}_C) . \quad (2.85)$$

2.3 Numerical Implementation

2.3.1 Fluid Flow

Since all the governing equations of fluid flow have the form of Eq. (2.1), this equation will be taken as an example to show how the mathematical model is transformed into a system of algebraic equations. Three choices are made first:

- Vectors and tensors will be expressed in their Cartesian components, which leads to a form of all equations strongly conservative and less sensitive to grid smoothness.
- Control volumes will be organized in an unstructured manner and can have arbitrary shape, which offers the great flexibility to adapt the grid to complex 3D geometry.
- The computational node lies in the center of each CV and collocated variable arrangement is used. Such an arrangement requires least memory to store geometry data and makes it easier to implement boundary conditions and local grid refinement.

The spatial domain has to be subdivided into a finite number of CVs, which can in principle be of any shape. For practical purposes CVs are usually defined by a finite number of vertices, which are connected by straight lines or edges. Closed polygons of edges define cell faces, which may not be planar since the vertices may not all lie in one plane. The CV is thus enclosed by a certain number of cell faces. The Eq. (2.1) can be expressed for each CV as

$$\underbrace{\frac{d}{dt} \int_V \rho \phi dV}_{\text{unsteady term}} + \underbrace{\sum_{j=1}^m \int_{S_j} \rho \phi (\mathbf{v} - \mathbf{v}_b) \cdot \mathbf{n} dS}_{\text{convective term}} = \underbrace{\sum_{j=1}^m \int_{S_j} \Gamma_\phi \nabla \phi \cdot \mathbf{n} dS}_{\text{diffusive term}} + \underbrace{\sum_{j=1}^m \int_{S_j} \mathbf{q}_{\phi,S} \cdot \mathbf{n} dS + \int_V q_{\phi,V} dV}_{\text{source term}} \quad (2.86)$$

where j is the index of the CV face with m being the total number of the cell faces.

As indicated, Eq. (2.86) has four distinct parts: unsteady term, convective term, diffusive term and source term. These terms have to be evaluated by different approximations, which will be briefly given below, for more details see Demirdžić et al. [21] and Ferziger and Perić [25].

Discretization of the unsteady term

Only implicit methods are considered to discretize the unsteady term, in which the solution at a new time level n depends on the unknown variable values also at the new time level n and therefore cannot be computed without iteration and solution of large algebraic equation systems. The reason is that explicit methods, which compute the new solution solely from the information on past data and are therefore much simpler, suffer from severe constraints on the allowed time-step size for stability reasons. The maximum allowed time

step by explicit schemes is proportional to the square of the spatial mesh size; this makes explicit schemes especially inefficient when the grid is locally very fine (e.g. near walls).

For most cases in this work, the second order Implicit Three Time Levels (ITTL) scheme is selected to approximate the unsteady term in Eq. (2.86), the expression for constant time step is given below:

$$\frac{d}{dt} \int_V \rho \phi dV \approx \frac{3(\rho \phi V)^n - 4(\rho \phi V)^{n-1} + (\rho \phi V)^{n-2}}{2\Delta t}, \quad (2.87)$$

where ϕ stands for the dependent variables (c, u_i, k, ϵ) and n for the time level. Since ϕ is required at three time levels, the solutions of ϕ at two previous time levels have to be stored, and to start the computation two time levels scheme, e.g. the implicit Euler (IE) scheme, has to be used:

$$\frac{d}{dt} \int_V \rho \phi dV \approx \frac{(\rho \phi V)^n - (\rho \phi V)^{n-1}}{\Delta t_n}. \quad (2.88)$$

To assess the influence of the time integration scheme on the results, the IE scheme is tested in some analyses. All other terms, see Eq. (2.86), are evaluated at the new time step n in implicit methods as indicated above.

Discretization of the convective term

The convective term is nonlinear and needs to be linearized, the Picard iteration approach is adopted here:

$$\int_{S_j} \rho \phi (\mathbf{v} - \mathbf{v}_b) \cdot \mathbf{n} dS_j \approx \phi_j^* \cdot \dot{m}_j, \quad (2.89)$$

here ϕ_j^* stands for the averaged value of the convected variable ϕ at the cell-face j (normally the value at the cell-face center is used as approximation) and \dot{m}_j denotes the mass flux through this cell face:

$$\dot{m}_j = \int_{S_j} \rho (\mathbf{v} - \mathbf{v}_b) \cdot \mathbf{n} dS_j, \quad (2.90)$$

Applying SCL (see Eq. (2.5)), \dot{m}_j can be expressed as:

$$\dot{m}_j \approx \rho_j (\mathbf{v}_j^* \cdot \mathbf{n}_j S_j - \dot{V}_j), \quad (2.91)$$

where \mathbf{n}_j and S_j are the normal vector and the area of the cell-surface j and \dot{V}_j is the rate of change of the CV volume due to the motion of the cell-surface j . The calculation of \dot{V}_j should be consistent with the discretization scheme of the unsteady term. If the ITTL scheme is used,

$$\begin{aligned}
\Sigma \dot{V}_j &= \frac{d}{dt} \int_V dV \approx \frac{3V^n - 4V^{n-1} + V^{n-2}}{2\Delta t} \\
&= \frac{3(V^n - V^{n-1}) - (V^{n-1} - V^{n-2})}{2\Delta t} \\
&= \frac{3\delta V^n - \delta V^{n-1}}{2\Delta t}, \tag{2.92}
\end{aligned}$$

where δV^n and δV^{n-1} are the changes of the CV volume between the time level n and $(n-1)$ and between $(n-1)$ and $(n-2)$ respectively. The change of the CV volume is the sum of the swept volume of all CV surfaces, i.e. $\delta V^n = \Sigma \delta V_j^n$ and $\delta V^{n-1} = \Sigma \delta V_j^{n-1}$. Then

$$\dot{V}_j \approx \frac{3\delta V_j^n - \delta V_j^{n-1}}{2\Delta t}, \tag{2.93}$$

where δV_j^n and δV_j^{n-1} denotes the swept volume by the CV surface S_j between the time level n and $(n-1)$ and between $(n-1)$ and $(n-2)$ respectively.

If the IE scheme is used, similar derivation is valid. i.e.

$$\dot{V}_j \approx \frac{\delta V_j^n}{\Delta t}. \tag{2.94}$$

The evaluation of ϕ_j^* and \mathbf{v}_j^* for the cell-face S_j has a strong influence on both the accuracy and stability of the numerical method. The interpolation operation for \mathbf{v}_j^* needs some special attention to ensure the strong coupling of velocity and pressure, which will be introduced later. The calculation of ϕ_j^* follows common interpolation practices for convective terms, which are briefly introduced here:

- First-order Upwind Differencing (UD) scheme, which relies on the donor-acceptor concept and can be expressed as

$$\phi_j^{UD} = \begin{cases} \phi_P, & \text{when the flow is from } P \text{ to } P_j \\ \phi_{P_j}, & \text{when the flow is from } P_j \text{ to } P \end{cases}, \tag{2.95}$$

where P and P_j denote the CV center P and its neighbor CV center P_j , which share the cell-face j . In this work, the UD scheme has always been used for the discretization of the turbulence quantities.

- Second-order Central Differencing (CD) scheme, which is basically a linear interpolation scheme. Based on the simplest second-order linear approximation

$$\phi(\mathbf{r}) = \phi_P + (\nabla \phi)_P \cdot (\mathbf{r} - \mathbf{r}_P), \tag{2.96}$$

the cell-face value can be calculated:

$$\phi_j^{CD} = \frac{1}{2} (\phi_P + \phi_{P_j}) + \frac{1}{2} \left((\nabla\phi)_P \cdot (\mathbf{r}_j - \mathbf{r}_P) + (\nabla\phi)_{P_j} \cdot (\mathbf{r}_j - \mathbf{r}_{P_j}) \right), \quad (2.97)$$

where \mathbf{r}_P , \mathbf{r}_{P_j} and \mathbf{r}_j are the vectors pointing to the CV center P , P_j and their common face j .

Using Gauss theorem,

$$\int_V \nabla\phi dV = \int_S \phi \mathbf{n} dS, \quad (2.98)$$

the gradients at the CV center, i.e. $(\nabla\phi)_P$, can be approximated:

$$\begin{aligned} (\nabla\phi)_P &\approx \frac{\int_S \phi \mathbf{n} dS}{V} \\ &\approx \frac{1}{V} \sum_{j=1}^m \phi_j S_j \mathbf{n}_j. \end{aligned} \quad (2.99)$$

- Blend of UD and CD schemes, which is intended to avoid both the extensive numerical diffusion of the UD scheme and the unbounded solution and unphysical wiggles of the CD scheme, and therefore is a compromise between accuracy and stability. By introducing the blending factor β_ϕ ($0 \leq \beta_\phi \leq 1$),

$$\phi_j^o = \phi_j^{UD} + \beta_\phi (\phi_j^{CD} - \phi_j^{UD}). \quad (2.100)$$

- High-Resolution Interface Capturing (HRIC) scheme, specially designed for the scalar variable $\phi = c$ in free-surface flows. Effort is focused on both keeping the interface sharp and avoiding non-physical oscillations. It belongs to the family of blending of UD and CD schemes but with a varying blending factor, more details see Appendix B.
- Deferred correction approach, adopted whenever possible to improve the stability and efficiency of the numerical method. Only first-order approximations and the nearest neighbors contribute to the coefficient matrix and the correction terms involving higher-order schemes or too many neighbors are calculated explicitly from the previous iteration and added to the source terms.

Discretization of the diffusive term

The diffusive term can be discretized using midpoint rule approximation for the surface integral:

$$\begin{aligned} \int_{S_j} \Gamma \nabla\phi \cdot \mathbf{n} dS_j &\approx \Gamma_{\phi_j} S_j (\nabla\phi_j^*) \cdot \mathbf{n}_j \\ &\approx \Gamma_{\phi_j} S_j \left\{ \left(\frac{\partial\phi}{\partial\xi} \right)_j + \left[\overline{\left(\frac{\partial\phi}{\partial n} \right)_j} - \overline{\left(\frac{\partial\phi}{\partial\xi} \right)_j} \right]^{\text{old}} \right\}, \end{aligned} \quad (2.101)$$

where Γ_{ϕ_j} stands for the value of diffusivity at the cell-face center, calculated using the CD scheme, Eq. (2.97), ξ denotes the local coordinate connecting the CV centers on either side of the surface j . The first term in the brackets is an implicit part of flux approximation, being expressed as:

$$\left(\frac{\partial\phi}{\partial\xi}\right)_j = \frac{\phi_{P_j} - \phi_P}{L_{P,P_j}}, \quad (2.102)$$

where $L_{P,P_j} = |\mathbf{r}_{P_j} - \mathbf{r}_P|$ is the distance between points P_j and P . The second term denoted with 'old' is the deferred correction and calculated using interpolated cell center gradients from the previous iteration. The cell center gradients can be obtained using Gauss theorem, see Eq. (2.99). The deferred correction term takes account of the non-orthogonality of the grid, it becomes zero when ξ coincides with n (i.e. $\frac{\xi}{|\xi|} = \mathbf{n}$).

Discretization of source terms

The source terms are integrated using the midpoint rule:

$$\sum_{j=1}^m \int_{S_j} \mathbf{q}_{\phi,S} \cdot \mathbf{n} \, dS \approx \sum_{j=1}^m \mathbf{q}_{\phi,S_j} \cdot \mathbf{n}_j S_j \quad (2.103)$$

and

$$\int_V q_{\phi,V} \, dV \approx q_{\phi,V,P} V_P. \quad (2.104)$$

The source term is usually treated explicitly, except that a positive contribution to the coefficient matrix can be obtained in the final algebraic equations by treating them implicitly.

Treatment of pressure

As already mentioned in section 2.2.1, special attention has to be paid when the Navier-Stokes equations are dealt with. In the momentum equation the pressure featuring in the source term is mostly unknown, while at the same time no explicit variable for the pressure can be found in the continuity equation. This naturally rises the question how the indirect information contained in the continuity equation can be converted into a direct algorithm for calculation of the pressure.

If the momentum equations are discretized and the pressure gradient term is not included in the source terms but explicitly arranged, these may be written as (here only one velocity component u_i is taken as example):

$$A_P^{u_i} u_{i,P}^{m*} + \sum_j A_j^{u_i} u_{i,P_j}^{m*} = Q_{u_i}^{m*} - V_P \cdot \left(\frac{\partial p^{m-1}}{\partial x_i} \right)_P, \quad (2.105)$$

where P is the index of an arbitrary CV center and the index j denotes the neighbor CVs P_j that appear in the discretized momentum equation; m is the outer iteration counter, thus u_i^{m*} represents the current estimate of the solution u_i at the m th iteration. The source term Q contains all of the source terms except the pressure term, which is given explicitly and written in the integral form. The terms on the right hand side are evaluated using the variables at the preceding outer iteration $m - 1$.

The velocity at node P can therefore be expressed as:

$$\begin{aligned} u_{i,P}^{m*} &= \frac{Q_{u_i}^{m*} - \sum_j A_j^{u_i} u_{i,P_j}^{m*}}{A_P^{u_i}} - \frac{V_P}{A_P^{u_i}} \left(\frac{\partial p^{m-1}}{\partial x_i} \right)_P \\ &= \bar{u}_{i,P}^{m*} - \frac{V_P}{A_P^{u_i}} \left(\frac{\partial p^{m-1}}{\partial x_i} \right)_P. \end{aligned} \quad (2.106)$$

As only the gradient of pressure appears in the above equation, which is normally calculated using a second-order Central Differencing Scheme (CDS), a checkerboard pressure field might be produced with the discretized momentum equation being satisfied. A similar danger is encountered by discretizing the continuity equation since a zigzag velocity field would satisfy the equation although it is fully unrealistic. To couple the pressure field properly with the velocity field and to avoid the aforementioned situations, the SIMPLE¹-type algorithm, see Patankar and Spalding [66], has been adopted here.

In this algorithm, a pressure-correction is used instead of the actual pressure. The velocities computed from the linearized momentum equations $u_{i,P}^{m*}$ and the pressure p_P^{m-1} are taken as provisional values to which a small correction must be added:

$$u_{i,P}^m = u_{i,P}^{m*} + u'_{i,P} \quad \text{and} \quad p_P^m = p_P^{m-1} + p'_P. \quad (2.107)$$

Writing a similar equation as Eq. (2.106) for $u_{i,P}^m$ and p_P^m and subtracting (2.106) from this equation, one can get

$$u'_{i,P} = \bar{u}'_{i,P} - \frac{V_P}{A_P^{u_i}} \left(\frac{\partial p'}{\partial x_i} \right)_P, \quad (2.108)$$

where $\bar{u}'_{i,P}$ is defined:

$$\bar{u}'_{i,P} = - \frac{\sum_j A_j^{u_i} u'_{i,j}}{A_P^{u_i}}. \quad (2.109)$$

Since the velocity correction $\bar{u}'_{i,P}$ is related to velocity corrections at the neighbor CVs and unknown at this point, it is neglected here. So Eq. (2.108) becomes:

$$u'_{i,P} = - \frac{V_P}{A_P^{u_i}} \left(\frac{\partial p'}{\partial x_i} \right)_P. \quad (2.110)$$

¹Semi-Implicit Pressure-Linked Equations

To evaluate the continuity equations, the cell face velocities are however needed. They are calculated by interpolating neighbor CV values and subtracting a correction term which should detect oscillations and help to smooth them out (Rhie and Chow [71]):

$$u_{i,j}^{m*} = \overline{u_{i,j}} - \frac{\overline{V_P}}{A_P^{u_i}} \left[\left(\frac{\partial p}{\partial x_i} \right)_j - \overline{\left(\frac{\partial p}{\partial x_i} \right)_j} \right], \quad (2.111)$$

where an overbar denotes interpolation and $\overline{v_{i,j}}$ follows the common interpolation practice in calculating the cell-face values, see Eq. (2.97). The second term is a third-order pressure diffusion term, acting as a correction of the interpolated velocity. The correction term vanishes if the pressure variation is smooth.

The continuity equation is necessarily satisfied by velocities resulted from the momentum equation under an assumed pressure field, so their sum results in a mass source (see Eq. (2.91)):

$$\sum_j \dot{m}_j = \sum_j \left(\rho_j \mathbf{v}_j^{m*} \cdot \mathbf{n}_j S_j - \dot{V}_j \right) = \Delta \dot{m}, \quad (2.112)$$

which must be corrected to be zero. The corrections of the cell face velocities are also proportional to the pressure correction gradient (c.f. Eqs. (2.110) and (2.111)):

$$u'_{i,j} = -\frac{\overline{V_P}}{A_P^{u_i}} \left(\frac{\partial p'}{\partial x_i} \right)_j. \quad (2.113)$$

To make the continuity equation be satisfied, the velocity correction has to compensate the mass source of Eq. (2.112):

$$\sum_j \left(\rho \mathbf{v}'_j \cdot \mathbf{n}_j S_j \right) = -\Delta \dot{m}. \quad (2.114)$$

By substituting Eq. (2.113) into Eq. (2.114), one can obtain

$$-\sum_j \left\{ \rho \sum_i \left[\frac{\overline{V_P}}{A_P^{u_i}} \left(\frac{\partial p'}{\partial x_i} \right)_j n_{i,j} \right] S_j \right\} = -\Delta \dot{m}. \quad (2.115)$$

Once the pressure correction p'_P is obtained, the velocity and pressure can be corrected:

$$u_{i,P} = u_{i,P}^{m*} - \frac{V_P}{A_P^{u_i}} \left(\frac{\partial p'}{\partial x_i} \right)_P, \quad (2.116)$$

The pressure correction p'_P computed above tends to overestimate its magnitude due to the neglected term above (Eq. (2.109)) and therefore needs to be under-relaxed by a factor β_p (typically 0.2 to 0.3) to avoid slow convergence or divergence of the solution procedure:

$$p_P = p_P^{m-1} + \beta_p p_P' . \quad (2.117)$$

Resulting algebraic equations

The integrals in Eq. (2.86) have now been evaluated by using appropriate quadratures and assumptions about the spatial and temporal variation of the variables. After assembling all the terms, there results an algebraic equation for each CV of the form

$$A_P \phi_P + \sum_j A_j \phi_{P_j} = Q_P , \quad (2.118)$$

where P denotes the cell center and P_j is the center of the j neighbor CV. The coefficient A_j contains contributions from surface integrals over faces common to the cell around node P and the corresponding neighbor P_j ; A_P contains in addition contributions from the unsteady term and possibly from source terms (volume integrals). Q_P contains all terms which are treated as known (source terms, parts of surface integrals treated explicitly as deferred corrections, and a part of the unsteady term).

For the solution domain as a whole, the algebraic equation system can be written as

$$\mathbf{A} \cdot \boldsymbol{\phi} = \mathbf{Q} , \quad (2.119)$$

where \mathbf{A} is a square $M \times M$ coefficient matrix, $\boldsymbol{\phi}$ is the vector of unknowns, \mathbf{Q} is the vector of right-hand sides, and M is the number of CVs. The matrix \mathbf{A} is sparse, having in each row only a small number of non-zero elements (usually equal to the number of CVs which have faces common to the cell centered around node P). The non-zero elements may be distributed in a regular, diagonal pattern, or be completely irregular, depending on the type of grid used.

To solve the system of linearized algebraic equations, iterative methods are adopted. The iterative solvers are especially attractive since the linearized system of algebraic equations is only an approximation of the original system of nonlinear equations, and a sufficiently improved solution can sometimes be achieved in just a few iterations. For equations with a symmetric coefficient matrix (e.g. pressure-correction equation), the ICCG (Incomplete Cholesky Conjugate Gradient) method is used. While the CGSTAB (CG Stabilized) method is adopted for equations with an asymmetric coefficient matrix (e.g. velocity component equations), see Van den Vorst [86].

The algorithm of fluid flow

Equations of the form of Eqs. (2.118) and (2.119) are obtained for each variable (velocity components, pressure-correction, energy etc.). As stated above, the solution of each linearized algebraic equation system is sought by iterative methods (inner iterations). The underlying nonlinear equations are re-evaluated and newly linearized in the so-called outer

iterations. The equation systems are still coupled after linearization. Direct solving the coupled system requires excessive storage and sometimes computational time, therefore it is rarely done; instead, the segregated algorithm has been adopted here:

- 1) Provide the initial values for the variables at the time t_0 in the whole domain of fluid flow.
- 2) Advance the time by Δt and, if the grid moves due to the prescribed motion of the boundary (e.g. at a flapping wave maker or the surface of a moving body), determine the current location of CV vertices and calculate the current estimate of volumes δV_j swept by each CV face.
- 3) Assemble and solve the linearized algebraic equations for the velocity components in turn, employing the currently available other variables (e.g. pressure and the other two velocity components).
- 4) Assemble and solve the algebraic equations for the pressure correction and correct mass fluxes, velocity components, and pressure.
- 5) Assemble and solve the algebraic equations for volume fraction c and use the calculated values to update the properties of the effective fluid, such as density and viscosity.
- 6) Assemble and solve the algebraic equations for turbulent kinetic energy k and its dissipation rate ϵ and obtain turbulent diffusion coefficients.
- 7) Return to Step 3 (one outer iteration is concluded here.) and repeat until the sum of the absolute residuals (R_ϕ) for all equations has fallen by a prescribed number of orders of magnitude p .

$$R_\phi = \frac{\sum_i^N |A_P \phi_P + \sum_j A_j \phi_{P_j} - Q_P|}{\sum_i^N |A_P \phi_P|} < p, \quad (2.120)$$

where p has typically the value of 10^{-3} , which is normally sufficiently small for unsteady flow computation. To obtain a steady flow solution, it is often set one or two orders of magnitude lower to eliminate the iteration errors.

- 8) Return to step 2 and repeat until the prescribed number of time steps is completed.

2.3.2 Rigid Body Dynamics

As explained, the forces and moments acting on the free floating body are obtained from the flow around the body; at the same time, the fluid flow is influenced by the motion of the body. Therefore, the problem has to be solved in a coupled manner, considering the interaction of body and flow. Since the fluid flow has to be solved in an iterative manner due to its nonlinearity, the determination of the body motion can also be implemented in a similar way to take advantage of the iterative feature of the fluid solver. Here, a second order predictor-corrector method is used for predicting the body motion.

Translation motion

The Eq. (2.32) can be written in the following form with respect to the GS (the label g is omitted from now):

$$\frac{d\mathbf{v}_C}{dt} = \frac{\mathbf{f}}{m}. \quad (2.121)$$

After integrating the forces around the body surfaces, the velocity at the new time step $n + 1$ is predicted using the velocity at the previous time step n (explicit Euler method) first, then corrected for later iterations by applying the trapezoidal rule to compute the derivative (i indicates the i -th iteration):

$$\begin{aligned} \mathbf{v}_{C,n+1}^{i+1} &= \mathbf{v}_{C,n} + \frac{\mathbf{f}_n + \mathbf{f}_{n+1}^{i+1}}{2m} \Delta t \\ &= \underbrace{\mathbf{v}_{C,n} + \frac{\mathbf{f}_n}{m} \Delta t}_{\text{predictor}} + \underbrace{\frac{\mathbf{f}_{n+1}^{i+1} - \mathbf{f}_n}{2m} \Delta t}_{\text{corrector}}. \end{aligned} \quad (2.122)$$

When the velocities of the body have been obtained, the position of the body can be also determined in a similar way:

$$\begin{aligned} \mathbf{r}_{C,n+1}^{i+1} &= \mathbf{r}_{C,n} + \left(\mathbf{v}_n + \mathbf{v}_{n+1}^{i+1} \right) \frac{\Delta t}{2} \\ &= \underbrace{\mathbf{r}_{C,n} + \mathbf{v}_n \Delta t}_{\text{predictor}} + \underbrace{\frac{\mathbf{v}_{n+1}^{i+1} - \mathbf{v}_n}{2} \Delta t}_{\text{corrector}}. \end{aligned} \quad (2.123)$$

The incremental displacement of the rigid body can be computed:

$$\Delta \mathbf{r}_{C,n+1}^{i+1} = \mathbf{r}_{C,n+1}^{i+1} - \mathbf{r}_{C,n+1}^i \quad (2.124)$$

Rotation motion

A similar method has been applied to Eq. (2.33) to compute the angular velocities of the body and the orientation of the body. The discretized form of Eq. (2.33) reads

$$\begin{aligned} &M_{C,n+1}^i \cdot \boldsymbol{\omega}_{C,n+1}^{i+1} \\ &= M_{C,n} \cdot \boldsymbol{\omega}_{C,n} + \left(\mathbf{m}_{C,n} + \mathbf{m}_{C,n+1}^{i+1} \right) \frac{\Delta t}{2} \\ &\quad - \left(\boldsymbol{\omega}_{C,n} \times M_{C,n} \cdot \boldsymbol{\omega}_{C,n} + \boldsymbol{\omega}_{C,n+1}^i \times M_{C,n+1}^i \cdot \boldsymbol{\omega}_{C,n+1}^i \right) \frac{\Delta t}{2} \end{aligned}$$

$$\begin{aligned}
&= \underbrace{M_{C,n} \cdot \boldsymbol{\omega}_{C,n} + (\mathbf{m}_{C,n} - \boldsymbol{\omega}_{C,n} \times M_{C,n} \cdot \boldsymbol{\omega}_{C,n}) \Delta t}_{\text{predictor}} \\
&\quad + \underbrace{\frac{\mathbf{m}_{C,n+1}^{i+1} - \mathbf{m}_{C,n}}{2} \Delta t - (\boldsymbol{\omega}_{C,n+1}^i \times M_{C,n+1}^i \cdot \boldsymbol{\omega}_{C,n+1}^i - \boldsymbol{\omega}_{C,n} \times M_{C,n} \cdot \boldsymbol{\omega}_{C,n}) \frac{\Delta t}{2}}_{\text{corrector}} .
\end{aligned} \tag{2.125}$$

$M_{C,n+1}^i$ is computed as follows, see Eq. (2.34):

$$M_{C,n+1}^i = T_{T,n+1}^i \cdot M_C \cdot (T_{T,n+1}^i)^{-1} . \tag{2.126}$$

The orientation of the body is determined by the tensor T_T , whose columns are the unit vectors \mathbf{x} , \mathbf{y} and \mathbf{z} attached to the BS as stated in section 2.2.2. The easiest approach to obtain the new orientation of the unit vector \mathbf{x}_{n+1}^i is

$$\mathbf{x}_{n+1}^i = \mathbf{x}_n + \frac{\Delta t}{2} (\boldsymbol{\omega}_{C,n} + \boldsymbol{\omega}_{C,n+1}^i) \times \mathbf{x}_n , \tag{2.127}$$

\mathbf{y}_{n+1}^i and \mathbf{z}_{n+1}^i being similarly computed. This approach, however, can not guarantee the magnitude of these vectors being always unity during the integration process, neither them being orthogonal to each other. Therefore, another approach is employed here to compute $T_{T,n+1}^i$ at the new time step (i indicates the i -th iteration):

$$T_{T,n+1}^i = T_t^i \cdot T_{T,n} , \tag{2.128}$$

where T_t^i is a rotation operator, by which the body can be rotated about an axis in space by a certain angle. The rotation of the body is executed about the axis \mathbf{u} (defined below as a unit vector in the direction of the vector $\boldsymbol{\omega}_C^o$) through the mass center of the body. Suppose the rotational angle about \mathbf{u} is ϕ^o (see below), this rotation operator T_t^i is expressed by (for more detail, see Appendix C):

$$\begin{aligned}
&T_t^i = \\
&\left(\begin{array}{ccc}
u_x^2 (1 - \cos \phi^o) + \cos \phi^o & u_x u_y (1 - \cos \phi^o) - u_z \sin \phi^o & u_x u_z (1 - \cos \phi^o) + u_y \sin \phi^o \\
u_x u_y (1 - \cos \phi^o) + u_z \sin \phi^o & u_y^2 (1 - \cos \phi^o) + \cos \phi^o & u_y u_z (1 - \cos \phi^o) - u_x \sin \phi^o \\
u_x u_z (1 - \cos \phi^o) - u_y \sin \phi^o & u_y u_z (1 - \cos \phi^o) + u_x \sin \phi^o & u_z^2 (1 - \cos \phi^o) + \cos \phi^o
\end{array} \right) ,
\end{aligned} \tag{2.129}$$

in which

$$\mathbf{u} = \frac{\boldsymbol{\omega}_C^o}{|\boldsymbol{\omega}_C^o|} = (u_x, u_y, u_z) , \quad \phi^o = |\boldsymbol{\omega}_C^o| \cdot \Delta t , \tag{2.130}$$

$$\boldsymbol{\omega}_C^o = \frac{\boldsymbol{\omega}_{C,n} + \boldsymbol{\omega}_{C,n+1}^i}{2} , \tag{2.131}$$

$$|\boldsymbol{\omega}_C^o| = \sqrt{(\boldsymbol{\omega}_{C,x}^o)^2 + (\boldsymbol{\omega}_{C,y}^o)^2 + (\boldsymbol{\omega}_{C,z}^o)^2}. \quad (2.132)$$

Here, Δt is the time step size in the computation.

This rotation operator such ensures the vectors \mathbf{x} , \mathbf{y} and \mathbf{z} attached to the BS being both unity and orthogonal as the simulation proceeds.

Once $\mathbb{T}_{T,n+1}$ is known, the Eulerian angles of the body can be computed either from Eq. (2.37)-(2.39) or Eq. (2.40). The incremental Eulerian angles between two successive time steps (or iterations) and related intermediate axes which serve for grid-moving at each instant can be computed if the space-fixed axes are replaced in Eqs. (2.35) and (2.36) by the body-fixed axes of the previous body position:

$$\mathbf{x}' = \frac{\mathbf{x}_{n+1}^{i+1} - (\mathbf{x}_{n+1}^{i+1} \cdot \mathbf{z}_{n+1}^i) \cdot \mathbf{z}_{n+1}^i}{|\mathbf{x}_{n+1}^{i+1} - (\mathbf{x}_{n+1}^{i+1} \cdot \mathbf{z}_{n+1}^i) \cdot \mathbf{z}_{n+1}^i|}, \quad (2.133)$$

$$\mathbf{y}' = \mathbf{z}_{n+1}^i \times \mathbf{x}', \quad (2.134)$$

The three incremental Eulerian angles $\delta\psi_{n+1}^{i+1}$, $\delta\theta_{n+1}^{i+1}$ and $\delta\varphi_{n+1}^{i+1}$ used for rotation of the computational grid are obtained as

$$\Delta\psi_{n+1}^{i+1} = \arcsin \left[(\mathbf{x}_{n+1}^i \times \mathbf{x}') \cdot \mathbf{z}_{n+1}^i \right], \quad (2.135)$$

$$\Delta\theta_{n+1}^{i+1} = \arcsin \left[(\mathbf{x}' \times \mathbf{x}_{n+1}^{i+1}) \cdot \mathbf{y}' \right], \quad (2.136)$$

$$\Delta\varphi_{n+1}^{i+1} = \arcsin \left[(\mathbf{y}' \times \mathbf{y}_{n+1}^{i+1}) \cdot \mathbf{x}_{n+1}^{i+1} \right]. \quad (2.137)$$

Constrained motion

As stated in section 2.2.2, Eq. (2.72) has to be applied instead of Eqs. (2.32) and (2.33) when the motion of the rigid body is under kinematical constraints. Equation (2.72) can be discretized in the following way:

$$\begin{aligned} \left(\mathbf{J}_{n+1}^{T,i} \cdot \overline{\mathbf{M}}_{n+1}^i \right) \cdot \dot{\mathbf{q}}_{n+1}^{i+1} &= \left(\mathbf{J}_n^T \cdot \overline{\mathbf{M}}_n \right) \cdot \dot{\mathbf{q}}_n + \frac{\Delta t}{2} \left(\mathbf{J}_n^T \cdot \mathbf{F}_n + \mathbf{J}_{n+1}^{T,i} \cdot \mathbf{F}_{n+1}^{i+1} \right) \\ &- \frac{\Delta t}{2} \left(\mathbf{J}_n^T \cdot \overline{\mathbf{N}}_n + \mathbf{J}_{n+1}^{T,i} \cdot \overline{\mathbf{N}}_{n+1}^i \right) \\ &= \underbrace{\left(\mathbf{J}_n^T \cdot \overline{\mathbf{M}}_n \right) \cdot \dot{\mathbf{q}}_n + \left(\mathbf{J}_n^T \cdot \mathbf{F}_n - \mathbf{J}_n^T \cdot \overline{\mathbf{N}}_n \right) \Delta t}_{\text{predictor}} \end{aligned}$$

$$+ \underbrace{\frac{\left(\mathbf{J}_{n+1}^{\text{T},i} \cdot \mathbf{F}_{n+1}^{i+1} \right) - \mathbf{J}_n^{\text{T}} \cdot \mathbf{F}_n - \left(\mathbf{J}_{n+1}^{\text{T},i} \cdot \mathbf{F}_{n+1}^{i+1} - \mathbf{J}_n^{\text{T}} \cdot \bar{\mathbf{N}}_n \right)}{2}}_{\text{corrector}} \Delta t . \quad (2.138)$$

Once the independent variables $\dot{\mathbf{q}}$ are obtained, the dependent variables \mathbf{v}_C and $\boldsymbol{\omega}_C$ can be computed from Eqs. (2.47) and (2.48), then the position and orientation of the rigid body can be easily obtained in the same way as in the case of free motion, already given above.

The algorithm of body motion

The algorithm to compute the body motion with or without constraints is summarized below:

- 1) Integrate the pressure and shear forces over body surfaces following Eqs. (2.83) and (2.84) and add field forces and the external forces;
- 2) Go to step 3^a in case of constraint motion; otherwise go to step 3^b;
- 3^a) Determine the matrices \mathbf{J}_{n+1}^i , $\bar{\mathbf{N}}_{n+1}^i$ and $\bar{\mathbf{M}}_{n+1}^i$ following Eqs. (2.69), (2.60) and (2.59); assemble and solve the discretized Eq. (2.138); $\mathbf{v}_{C,n+1}^{i+1}$ and $\boldsymbol{\omega}_{C,n+1}^{i+1}$ can be obtained from Eqs. (2.47) and (2.48);
- 3^b) Determine the matrices \mathbf{T}_t^i , $\mathbf{T}_{T,n+1}^i$ and $\mathbf{M}_{C,n+1}^i$ following Eqs. (2.129), (2.128) and (2.126); assemble and solve the discretized Eqs. (2.122) and (2.125) to obtain $\mathbf{v}_{C,n+1}^{i+1}$ and $\boldsymbol{\omega}_{C,n+1}^{i+1}$;
- 4) Compute the position $\mathbf{r}_{C,n+1}^{i+1}$ and the orientation $\mathbf{T}_{T,n+1}^{i+1}$ of the body by Eqs. (2.123) and (2.128);
- 5) Obtain the incremental Eulerian angles $\delta\psi_{n+1}^{i+1}$, $\delta\theta_{n+1}^{i+1}$ and $\delta\varphi_{n+1}^{i+1}$ by Eqs. (2.135)-(2.137); the global Eulerian angles ψ , θ and φ can be either calculated from Eqs. (2.37)-(2.39) or Eq. (2.40);
- 6) Monitor the residual of body velocities:

$$R_{\mathbf{v}}^i = \frac{\|\mathbf{v}_{C,n+1}^{i+1} - \mathbf{v}_{C,n+1}^i\|}{\|\mathbf{v}_{C,n+1}^i\|} < p_{\mathbf{v}} . \quad (2.139)$$

$$R_{\boldsymbol{\omega}}^i = \frac{\|\boldsymbol{\omega}_{C,n+1}^{i+1} - \boldsymbol{\omega}_{C,n+1}^i\|}{\|\boldsymbol{\omega}_{C,n+1}^i\|} < p_{\boldsymbol{\omega}} , \quad (2.140)$$

where $p_{\mathbf{v}}$ and $p_{\boldsymbol{\omega}}$ are both set to the value of 10^{-3} .

2.3.3 Coupling of Fluid Flow and Rigid Body Motion

For computing the interaction between fluid flow and rigid body motion, equations of the rigid body motion are included into the flow solver package COMET via its user coding interface. The variables describing the fluid flow and body motion have to be updated whenever necessary. As mentioned in section 2.2.3, the flow-induced body motion is influenced by the pressure and shear forces exerted from the fluid flow and simultaneously the fluid flow is effected by the body motion due to the changes of its boundary conditions. Therefore a method which can accurately predict the coupled solution of fluid flow and the floating-body motion is required. As already stated in section 2.3.1, the second order ITTL scheme for the time integration, a segregated algorithm and an iterative solver have been adopted to compute the flow motion. The predictor-corrector scheme of the same order for integration of the body motion (see section 2.3.2) can easily coupled with the fluid solver. The information like hydrodynamic forces integrated along the body surfaces and the resulting body velocities (and displacements) can be updated and exchanged between fluid flow solver and body motion program module at each outer iteration of the fluid solver. The process continues until the residuals of all equations are satisfied for the current time step. Usually it takes about 10-15 iterations for each time step.

The coupling algorithm of fluid flow and body motion

Combining the algorithms of fluid flow (section 2.3.1) and body motion (section 2.3.2), the coupled procedure of flow and body motion is given in Fig. 2.3.

In Fig. 2.3, the absolute residuals for forces ($R_{\mathbf{f}}$) and moments ($R_{\mathbf{m}}$) acting on the body are computed as

$$R_{\mathbf{f}}^i = \frac{\|\mathbf{f}_{n+1}^{i+1} - \mathbf{f}_{n+1}^i\|}{\|\mathbf{f}_{n+1}^i\|} < p_{\mathbf{f}} \quad (2.141)$$

and

$$R_{\mathbf{m}}^i = \frac{\|\mathbf{m}_{C,n+1}^{i+1} - \mathbf{m}_{C,n+1}^i\|}{\|\mathbf{m}_{C,n+1}^i\|} < p_{\mathbf{m}} , \quad (2.142)$$

where $p_{\mathbf{f}}$ and $p_{\mathbf{m}}$ are both given the value of 0.5 in this work. These criteria avoid the body motion module being called if the forces vary largely.

Under-relaxation and added mass

Under-relaxation factors ($0 \leq \beta \leq 1$) are employed for both fluid flow and body motion to enhance the stability of the coupling procedure.

In the flow solver, the under-relaxation is done (except for the pressure-correction equa-

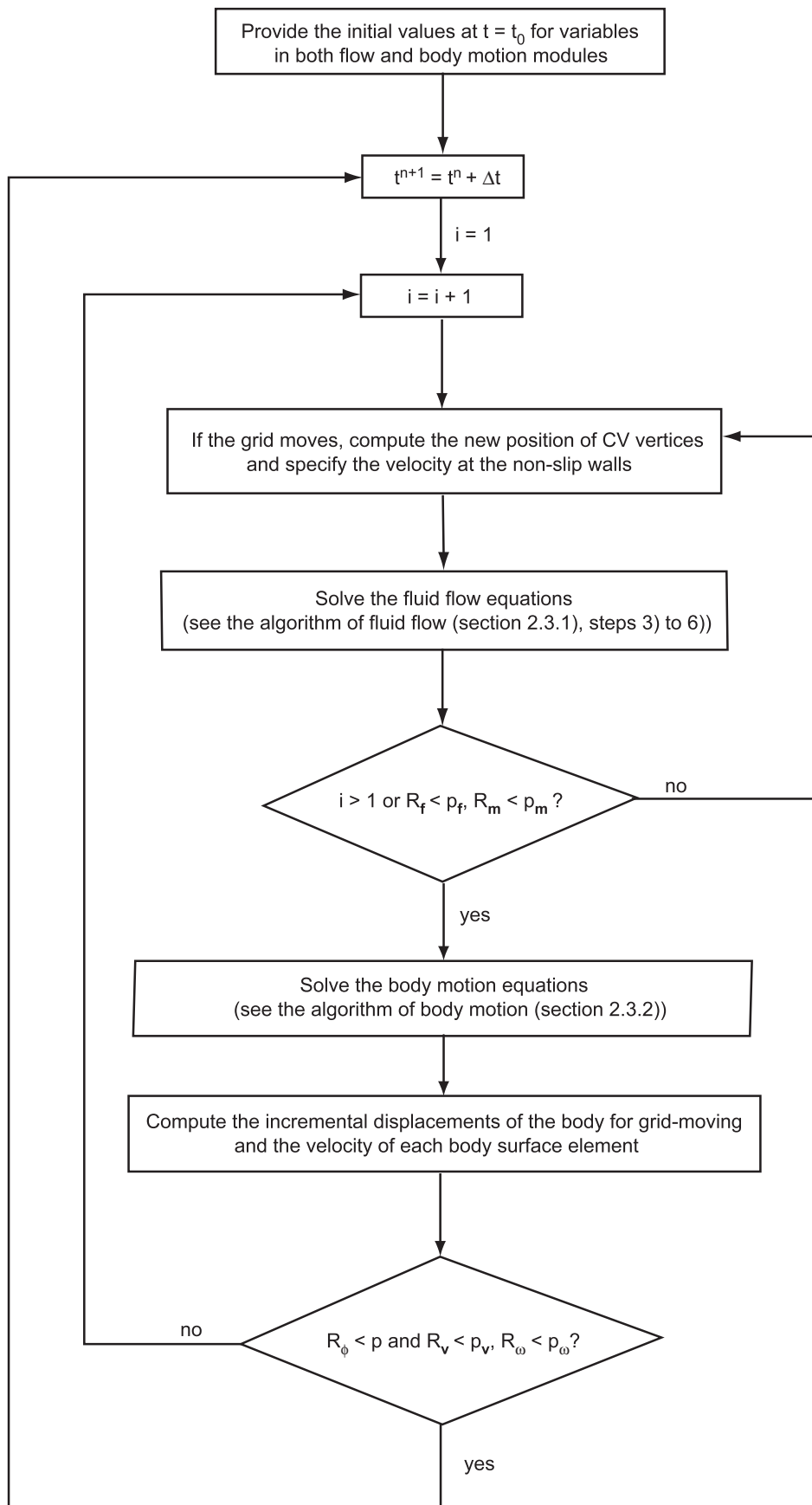


Figure 2.3: The coupled algorithm for flow and body motion.

tion) by replacing the \mathbf{A} and \mathbf{Q} in Eq. (2.119) by

$$\mathbf{A} \Rightarrow \mathbf{A} + \frac{1 - \beta}{\beta} \mathbf{D} \quad (2.143)$$

and

$$\mathbf{Q} \Rightarrow \mathbf{Q} + \frac{1 - \beta}{\beta} \mathbf{D} \cdot \phi^{k-1}, \quad (2.144)$$

where β is an under-relaxation factor for the transport of momentum, mass, turbulence quantities or species, whose value employed in this work is given in Table 2.3. \mathbf{D} is a diagonal matrix consisting of the diagonal elements of the matrix \mathbf{A} , and ϕ^{k-1} is the dependent vector from previous iteration/time step. As can be seen, the under-relaxation enhances the diagonal dominance of the linearized equations, which improves the convergence rate of most iterative linear equation solvers.

For the body motion, under-relaxation acts actually like a varying hydrodynamic mass term, as will be proven below.

If the implicit second order integration (predictor-correct) scheme is used, it is found to be neutrally stable irrespective of time step size. So the under-relaxation is not *a must* but rather used to improve the convergence rate of the iterations aiming at a robust and economic solution procedure. Söding [79] argued that an *added mass* term should be considered in the integration of the body motion to increase the stability or convergence rate of the solution procedure. Several methods are proposed to estimate the *added mass* matrix, [79]. However, all of them are yet rather computationally expensive if the added mass matrix is solved for each iteration (it is also possible to do this less often). Since it is found that an appropriate under-relaxation corresponds directly to an *added mass* term in the equation of body motion, only the latter varies automatically in time, under-relaxation is used in this work for simplicity.

To find out how the under-relaxation is related to the *added mass* term, the problem is simplified and investigated first for a system of one degree of freedom. The extension to other degrees of freedom is obvious. Involving the under-relaxation factor β , the discretized equation for the velocity at the new time step (see Eq. (2.122)) is replaced by

$$v_{C,n+1}^{i+1} = \beta \left[v_{C,n} + \left(\frac{f_n + f_{n+1}^{i+1}}{m} \right) \left(\frac{\Delta t}{2} \right) \right] + (1 - \beta) v_{C,n+1}^i \quad (2.145)$$

$$= v_{C,n} + \frac{\beta \Delta t}{2m} (f_n + f_{n+1}^{i+1}) + (1 - \beta) (v_{C,n+1}^i - v_{C,n}). \quad (2.146)$$

We now add the *added mass* term $a \geq 0$ to the discretized equation of motion. The motion equation, Eq. (2.121), becomes

$$(m + a) \frac{dv_C}{dt} = f + a \frac{dv_C}{dt}. \quad (2.147)$$

Following the implicit integration scheme, it can be obtained

Table 2.3: Selected values of under-relaxation factors for the flow solver

$\beta_{\mathbf{v}}$	β_m	β_k	β_ϵ	β_c
0.7	0.3	0.7	0.7	0.9

Table 2.4: Proposed values of under-relaxation factors for the body motion

β_u	β_v	β_w	β_φ	β_θ	β_ψ
0.80	0.60	0.60	0.95	0.85	0.85

$$v_{C,n+1}^{i+1} = v_{C,n} + \frac{\Delta t}{m+a} \left(\frac{f_n + f_{n+1}^{i+1}}{2} + a \frac{v_{C,n+1}^i - v_{C,n}}{\Delta t} \right) \quad (2.148)$$

$$= v_{C,n} + \frac{\Delta t}{2(m+a)} (f_n + f_{n+1}^{i+1}) + \frac{a}{m+a} (v_{C,n+1}^i - v_{C,n}) . \quad (2.149)$$

By comparing Eqs. (2.146) and (2.149), the following relations result:

$$\frac{\beta \Delta t}{2m} = \frac{\Delta t}{2(m+a)} \quad \text{or} \quad 1 - \beta = \frac{a}{m+a} \quad \Rightarrow \quad \beta = \frac{m}{m+a} . \quad (2.150)$$

Thus, the under-relaxation factor β can be proposed for each degree of freedom of body motion with the help of an approximated *added mass* a (see Newman [59]). The values of the under-relaxation factors proposed in this work are listed in Table 2.4. Constant under-relaxation factor has been used for simplicity. In the case of heavy bodies with moderate motion, the solution is not sensitive to slightly different choices of under-relaxation factors. As can be observed from Eq. (2.150), a larger rate of the *added mass* relative to the mass of the body be expected, a smaller under-relaxation factor be required, as it is the case when light bodies like water airplanes are subject to high acceleration in a fluid of substantial density like water.

2.4 Initial and Boundary Conditions

2.4.1 Initial Conditions

For time-dependent problems, initial values should be correctly specified for all variables, including components of velocity vector \mathbf{v} , pressure p , volume of fraction c , turbulent kinetic energy k and its dissipation rate ϵ in the fluid flow module. If the initial values are known, they can be directly given; otherwise they should be approximated as closely as possible to

reality. For steady problems with a single final solution, the initial values specified do not effect the final solution, however, a good approximation of these values can help to achieve a fast convergence of the solution.

In the seakeeping applications of this work, the relative velocity of the fluid to the advancing ship has been directly initialized in the whole fluid domain (both water and air) under the assumption that no current or wind is expected and the fluid is at rest at the beginning. The undisturbed water surface is specified at the beginning of computation. Since the turbulent kinetic energy and its dissipation rate is mostly unknown, it is assumed that the turbulence intensity is about 1% and the turbulence viscosity μ_t is of the same order as the molecular viscosity μ , which are related to k and ϵ by

$$k = \frac{3}{2}V^2 I^2 \quad \epsilon = \frac{k^{\frac{3}{2}}}{L}, \quad (2.151)$$

where V is the initial velocity field and L is the turbulence length scale (Eq. (2.18)).

For parameter or grid studies, the initial values of the dependent variables can be best guessed from a converged solution of a similar problem or the same problem using other grids or methods. One of the examples is the steady flow computation around a hydrofoil for different angles of attack. Once the solution is obtained for one angle of attack (e.g. $\alpha = 0^\circ$), one can proceed the computation from the previous one taking its converged solution as the initial condition for another angle of attack by only changing the boundary condition. This operation, used in section 5.2.3, has been observed to speed-up the convergence of the solution by a factor of two to four. Another example is the convergence study on systematically refined grids. Solutions from the coarser grid can be used as initial condition to accelerate the convergence of the solution on the finer grid (the principle in the multi-grid method). Moreover, analytical solutions or solutions obtained from other codes (e.g. codes based on the potential flow theory or boundary layer analysis) can also be used as initial guess for a similarly bounded flow to obtain a fast convergence of the RANSE computation.

In the body motion module, initial values are specified for the position and the velocity of the body, together with the body's mass (normally unchanged throughout the computation) and its moments of inertia for the initial position. All values are given with respect to the GS in this work.

2.4.2 Boundary Conditions

The solution domain is discretized by a finite number of CVs expanding to both water and air and bounded by a number of boundaries. The outer boundary of the solution domain is in all cases a rectangular box; the inner solution domain boundary consists of body surfaces such as the ship hull and its appendages. These boundaries can be largely divided into two groups:

- *Natural* boundaries, consisting of impermeable walls which may be stationary or moving (e.g. a flapping wave-maker or surfaces of moving-bodies, such as the ship and its appendages).

- *Artificial* boundaries, which do not exist physically, but are rather imagined in the flow field to reduce the size of the solution domain. The so-called inlet, outlet, pressure boundaries and the symmetry plane belong to the group of the *artificial* boundaries. These boundaries (except the symmetry plane) are normally located at a distance away from the region of interest to minimize their bounding effects.

Both *Natural* and *Artificial* boundaries have to be used in the applications of this work. The guidelines of these boundary conditions and their arrangements are briefly introduced below:

- *Inlet* boundary:
The components of the velocity vectors, k and ϵ are specified. The inflow velocities can be positive or negative, constant (e.g. the constant speed of ship) or varied (e.g. for wave generation) according to given velocity profiles.

In the ship seakeeping applications, the relative velocity of the water particle at the free stream to the mass center of the ship is specified for both water and air at the inlet assuming that no wind or current exists. It is also assumed that the turbulence intensity at the free stream is about 1% and the turbulence viscosity μ_t is of the same order as the molecular viscosity μ .

The inlet boundaries are always located in front of the body and sometimes at the sides of the body if the transverse velocity of the body is not zero (e.g. ship in drift motion) or oblique waves are generated. The special topic about wave generation by inlet boundary condition will be introduced in details in section 3.3.1.

- *Outlet* boundary:
The outlet boundary condition can be specified at the portion of the computational domain where the flow is fully-developed (or far away from the regions of interest) and leaves the domain. A flow rate can be directly prescribed if it is known; otherwise a zero gradient of all variables in the flow direction is assumed.
- *Pressure* boundary:
The pressure distribution is given and the velocity at the boundary is obtained with the Neumann boundary condition by zero-gradient. Other variables (e.g. c , k and ϵ etc.) are either specified if they are known at the inflow or extrapolated from the interior using zero-gradient assumption if they are unknown.

The pressure boundary is normally used in combination with inlet-like conditions at the boundaries where the flow leaves the computational domain for the applications in this work. The static air pressure is adopted for the top boundary of the solution domain, which normally lies in the air throughout the computation and is of little practical interest. The hydrostatic pressure according to the undisturbed free-surface level is set at the boundary behind the ship which extends to both air and water. In case of ship maneuvering applications, such pressure boundary is also adopted at the rear parts of the side boundaries, where the fluid is flowing in or out at different time instants with unknown velocities due to the influence of ship-induced waves. Waves produced by the ship have been first damped by a numerical beach (a gradually coarsened grid) of $2 - 5 L$ behind and beside the ship before they reach the pressure boundary to reduce

the error made by the hydrostatic pressure assumption. If a damping zone is not sufficient to eliminate all waves (especially in case of incoming waves), a dynamic pressure boundary is specified to take into account the pressure variation due to the waves:

$$p(\mathbf{r}_B, t) = p(\mathbf{r}_{P_0}, t - \delta t) , \quad (2.152)$$

where P_0 is the center of the control volume next to the boundary and δt can be computed:

$$\delta t = \frac{k_{\text{in}}(\mathbf{r}_B - \mathbf{r}_{P_0}) \cdot \mathbf{i}}{\omega_{\text{in}}} , \quad (2.153)$$

here k_{in} and ω_{in} are the wave number and the circular frequency of the incoming waves.

- *Symmetry plane:*

The normal velocity is set to zero and the tangential velocity together with all other scalar variables has zero gradient in the normal direction. The symmetry condition is applied at the longitudinal plane of the ship when both geometry and motion of the ship can be supposed to be symmetric as in the case of a ship advancing in head waves (section 4.3). The symmetry plane is also used to restrict the third dimension if only effects in two-dimensions are of interest (Chapter 3).

- *Wall:*

This boundary is the only natural one. No fluid can flow through it and the velocity of the wall is specified. The wall function concept in conjunction with the standard k - ϵ (for some tests the RNG k - ϵ) turbulence model is adopted to model the near-wall effects, see Wilcox [90]. At such a so-called non-slip wall, the shear stress is calculated and the tangential velocity is zero. In contrast, a so-called slip wall condition ignores the shear stress and lets the fluid slip along the wall.

Since the viscous effects play an important role for the motion of a maneuvering ship, the no-slip wall condition is applied at the ship hull and its appendages. The velocities of wall boundaries are specified according to the ship motion (see section 2.2.3). The slip wall condition is used when the shear stress on the wall is of less importance or interest (e.g. at the bottom of the tank or at the flapping wave-maker etc.).

2.5 Numerical Grids

To obtain the solution of the discretized equations for fluid flow, the computational domain is divided into a number of control volumes (CVs). The CVs should provide an adequate resolution of the whole geometry. The art how these CVs are distributed in the computational domain plays a vital role as far as both accuracy and efficiency are concerned. The guidelines used to generate the control volume grid are given below:

- Avoid highly skewed cells.

The angle between the line connecting the centers of the neighboring CVs and the vector normal to the common surface of the neighboring CVs should be optimized in

such a way that the angle approaches to zero degree. Angles which are larger than 50 degrees should be avoided because they often show a deterioration in the results or lead to numerical instabilities, especially in the case of transient simulation.

- Be as orthogonal as possible to the boundaries of the computational domain (e.g. the wall, or the inlet and pressure boundaries).
The angle between the line connecting the centers of the CV and the boundary surface element and the vector normal to the boundary surface should be ideally zero degree. This requirement is stronger than the requirement for the angles in the flow field far away from the domain boundaries (the above criterion).
- Avoid too high aspect ratios.
The aspect ratio (the ratio of the edges of the CV) should be ensured to be typically not larger than 20. This restriction can be relaxed near walls.
- Avoid too large mesh stretching or expansion ratios.
The expansion ratio (rate of change of cell size for adjacent cells) should be kept moderate (less than 2) to benefit from the cancellation of the leading term in the truncation error when spacing of the points is uniform. The change in mesh spacing should be continuous and mesh size discontinuities be avoided, particularly in regions of high gradients.
- Avoid too large warp angles.
The warp angles specify the extent to which the vertices making up a cell face are non-coplanar, which are measured by the angles between surface normals of triangular surfaces making up the cell surface. The warp angle should be zero degree as optimum and not larger than 50 degrees.
- Locally refine the grids in the critical regions.
The regions with high flow gradients, high shear or significant changes in geometry should be refined in accordance with the turbulence wall modeling. In the case of wall function assumption in conjunction with the $k - \epsilon$ turbulence model, the meshing should be arranged so that the value of Y^+ at all mesh points adjacent to the wall is greater than 30 (the form usually assumed for the wall functions is not valid much below than this value, at least not be less than 11) and does not exceed 100. Furthermore, the locations of refinement interfaces should be away from large flow variations.
- Avoid too large density differences of the cells at both sides of the sliding interfaces.
The length of the cells should be similar at both sides of the sliding interfaces to satisfy the aforementioned criteria. The sliding interfaces should also be away from large flow variations.

Three different types of grids have been used in this work. In the next section, these three types of grids will be discussed: stepwise regular, surface-fitted and overlapping grids. Results obtained using these grids will be presented later in the following chapters. As mentioned before, moving-grids are adopted here to realize the motion of the body; the applicability of grid-moving strategies is overviewed in section 2.5.2 and the grid-moving method mainly used in this work is explained in more details.

2.5.1 Types of Numerical Grids

The CVs making up the computational grids can have in principle arbitrary shapes, which gives great degree of freedom in the choice of the type of the grid. Each grid type has certainly advantages and disadvantages, therefore choice of the grid type is not a trivial issue. The grid is furthermore subject to the constraints imposed by the discretization method. In case of complex geometry, the constraints are often not fulfilled and compromises have to be made. Three types of numerical grids are tested and applied in this work, whose properties are discussed below.

Stepwise regular grids

The stepwise regular grid, illustrated in Fig. 2.4, is the simplest approach to generate a grid; in case of solution domains with inclined or curved boundaries, the boundaries have to be approximated by staircase-like steps, as shown in Fig. 2.4. The steps at the boundaries introduce errors in the solution, so that the grid should be locally refined near the inclined or curved boundaries to minimize such errors.

The stepwise regular grid of Fig. 2.4 has been applied in the water-entry/exit case of a horizontal circular cylinder (section 3.2). The computational result is compared with both experiment and results using other types of grids (e.g. surface-fitted grid as will be introduced next). The results using stepwise regular grid show good agreement with the experiments as both the free surface deformation and the cylinder motion are concerned; the surface-fitted grid (see Fig. 2.5) gives however not as good results in this case as the stepwise regular grid does. More discussions on this issue will be given in the section 3.2.

The stepwise regular grids are however seldom used in ship hydrodynamics mainly due to the aforementioned errors at the boundaries, which could be large and difficult to control in complex geometry. Further limitations on the solution procedure imposed by stepwise regular grid are: Special attention has to be paid to treatment of the boundary conditions at the stepwise walls and the solution algorithm has to allow for local grid refinement near the wall.

Surface-fitted grids

Surface-fitted grids are the most popular type of grids applied in complex geometry (e.g. ship hydrodynamics) since the grid lines are following the boundaries and such the boundary conditions are more easily implemented than at the stepwise approximation of curved boundaries. This type of grids is generally rather flexible; they can be structured, block-structured or unstructured. Furthermore, such grids can be adapted to any geometry or the streamlines of the flow. The spacing near the wall or other regions with strong variable variation can be made much smaller to reduce the discretization errors.

Surface-fitted grids are mostly used in the applications of this work. One simple example is shown in Fig. 2.5, corresponding to the water-entry case of the horizontal circular cylinder as mentioned above. More complicated grids for ships and its appendages will be individually introduced in the corresponding chapters.

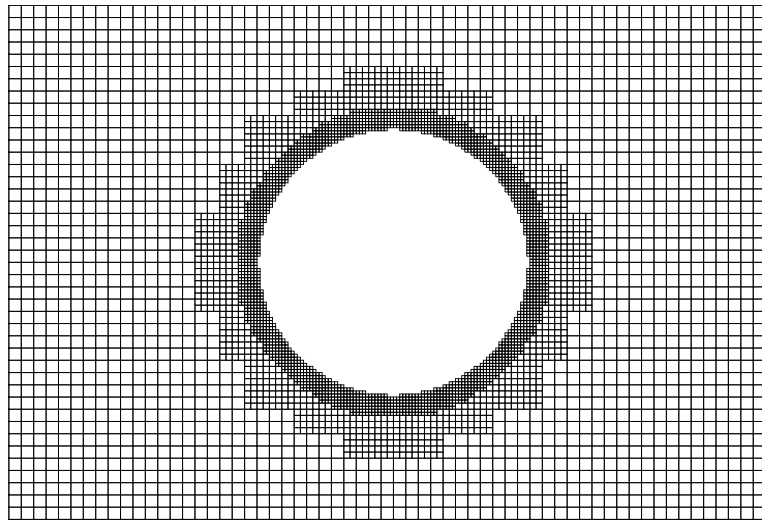


Figure 2.4: An example of a stepwise regular grid of a 2D circular cylinder

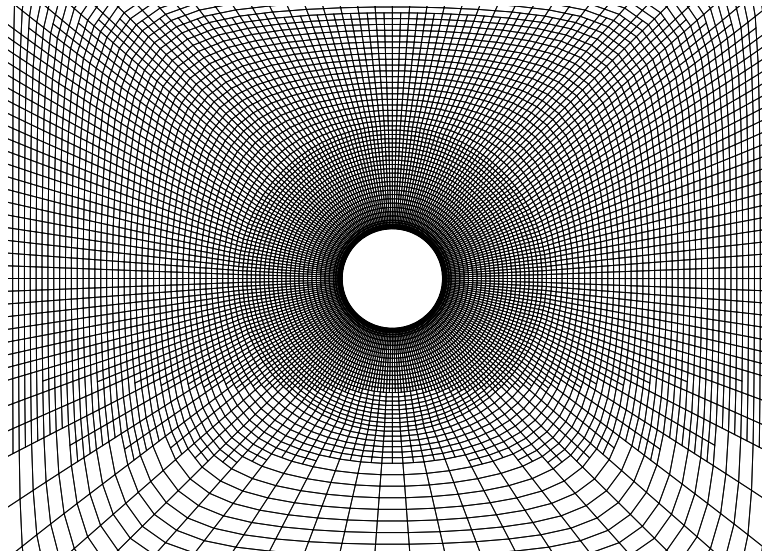


Figure 2.5: An example of a surface-fitted grid of a 2D circular cylinder

Overlapping grids

This kind of grids is also called *Chimera grids*, since it is more a combination of different grids. With surface-fitted grids used in the foreground near the body (region of most interest), Cartesian grids or grids of other type are used in the background of the solution domain, partially overlapping with the foreground grids.

The advantages of this kind of grids are obvious. Grids for different components of the solution domain can be separately generated without the constraints from each other, which makes the grid generation much simpler especially when the geometry is getting complicated and multi-components are involved. Furthermore, the foreground grids can be moved relative to the background grids or each other without additional difficulty, which offers the method great potential in tackling problems involving one or more moving bodies. However, prices have to be paid in winning these advantages as it is always the case. The programming and

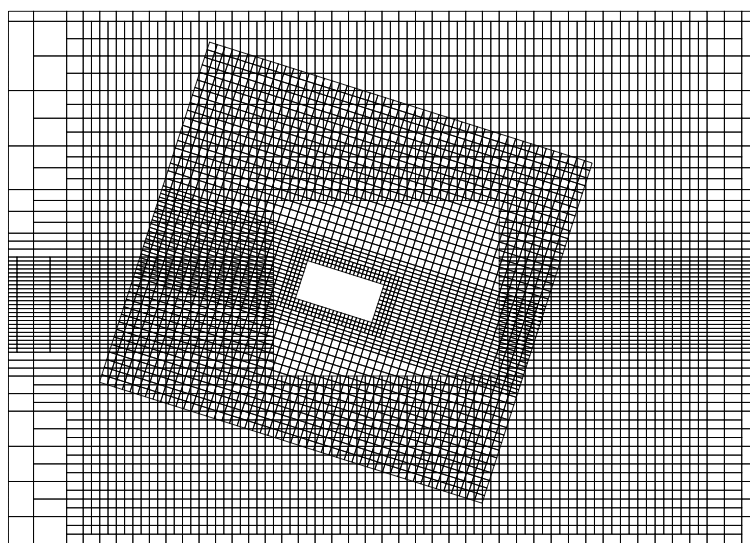


Figure 2.6: An example of an overlapping grid of a rectangular cylinder

coupling of the grids could be complicated and additional storage and computational effort are normally required. The solution procedure is usually sequential and applied on one grid after another. The interpolation process performed between the grids at the overlapping parts may introduce additional errors and cause convergence problems if the solution exhibits high gradients across the interfaces. Furthermore, it is not easy to ensure a unique solution on the overlapping region and the overall mass and momentum conservation.

One example of such grid is shown in Fig. 2.6, which has been employed in section 3.5.2. The computational results are compared later with the results using a single block of grid with similar grid topology showing promising agreement.

2.5.2 Grid-Moving Strategies

The numerical grid has to be moved in order to remain adapted to the varying geometry induced by moving bodies/walls.

There are several possibilities for moving-grid strategies:

- 1) Moving the entire grid with the body without deformation:
In the applications with free surface/waves considered, special care has to be taken at outer boundaries, since the free-surface location changes there due to the grid motion. This strategy is only applicable when a single body in an infinite domain is considered. This approach has been used by Azcueta [5]. In this work, it is used in the case of water-entry/exit of a horizontal circular cylinder in section 3.2.
- 2) Moving a part of the grid around the body with it (part A in Fig. 2.7 (a)), keeping the distant part fixed (part B in Fig. 2.7 (a)), and deforming or remeshing the grid (part C in Fig. 2.7 (a)) between the two regions A and B, while keeping its topology the same:
In this case the outer boundary of the solution domain is not affected by the body

motion, which makes the implementation of boundary conditions easier (e.g. at a wave-maker, inlet boundary, outlet boundary etc.). However, the grid in the remeshed region may deform too much and attain unacceptable properties (skewness, non-orthogonality etc.), therefore great care is needed during the moving-grid process. This approach is mainly used in this work.

3) Sliding interface:

Different blocks of grids can slide along each other. The cells lying at one side of the sliding interface are treated as neighbors of the corresponding cells at the other side of the sliding interface. For the cases where large rotation motion is expected, sliding interfaces are used such as in the modeling of a rotating rudder.

4) Using overlapping grids as shown in the previous section:

A surface-fitted grid is used in the neighborhood of the body and moving with it without deformation, see Fig. 2.6. The rest of the solution domain is covered by a fixed Cartesian grid (parts of it may move if the outer boundaries move, e.g. at a wave-maker wall) and the two grids overlap in the vicinity of the body. The body can then move without restriction, and one can also consider several bodies moving relative to each other. This approach offers the greatest flexibility but it requires more computational effort and the coupling of the solutions in the overlapping regions and maintaining the conservativeness are non-trivial issues especially when arbitrary unstructured grids are used. This approach has been used by Klemt [43]. In this work, the approach of overlapping grid is used for one case of the floating body motion in extreme wave packages in section 3.5.2 for comparison of different moving-grid strategies.

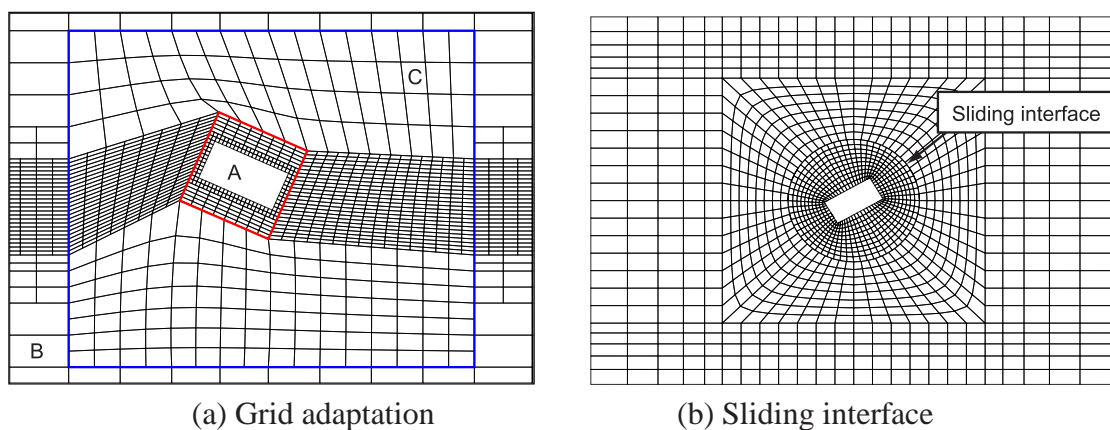


Figure 2.7: Examples of moving-grids

These four moving-grid strategies can be adopted either alone or combined. In particular, the first, second and third approach are used simultaneously in sections 6.3.2 and 6.4.2 to simulate the behavior of a maneuvering ship where the rudder is contained in a block of cells surrounded by sliding interfaces whereas the ship motion is realized by the first (for surge, sway and yaw motions) and second (for heave, roll, pitch motions) approach. Alternatively to moving grids, in some cases the body motion can be considered by introducing additional relative velocities and field forces on a fixed grid. In this work, it

is used in the case of water-entry/exit of a horizontal circular cylinder in section 3.2 as one example.

Technique for remeshing

The second moving-grid strategy is mainly used for grid-moving in this work. It is suitable since this method can allow up to 30° rotation (e.g. roll or pitch) motion and sufficient translation (e.g. heave) motion and the ship motion in moderate waves or during its maneuvering operation is not expected to be larger than these values. Figure 2.7 (a) shows a two-dimensional example of this moving-grid method for the application of a free-floating rectangular cylinder subject to wave packages (see section 3.5). As can be seen, the fine grids around the body and the free surface regions keep their fineness throughout the computation. So the advantage of this approach is that the grid retains good quality near the body and in the regions of the whole domain where the free surface lies; highly deformed cells are usually at some distance away from it. However, the grid smoothing (or remeshing) is a non-trivial issue in this approach. An appropriate estimation of the maximum grid motion should be made at the beginning of the grid generation to avoid too large distortion or deformation of grid cells at the block interfaces leading to larger errors or convergence problems. For example, if the body moves over large distance or rotates by more than 30° , some CVs may be so deformed that the numerical method would no longer converge. For this case, other grid managements such as sliding interface (which has been applied in the rotation of the rudder) may be used as shown in Fig. 2.7 (b).

The smoothing or remeshing algorithms for the deformed blocks of the grids (part C in Fig. 2.7 (a)) are implemented into the flow solver COMET via its user-coding interface together with the movement of the grid of part A in Fig. 2.7 (a). To resolve the high gradient of void fraction c in the free surface region, a layer of block-structured grids with fine resolution in the wave height direction is generated near the free surface and can be stretched, compressed or remeshed following the floating-body motion throughout the computation. The grids below or above the free surface region in part C can be much coarser and smoothed by an algebraic smoothing algorithm using the neighboring vertices:

$$\mathbf{r}_P = \frac{1}{N} \sum_{m=1}^N \mathbf{r}_m . \quad (2.154)$$

More examples illustrating the concept of moving grids are given throughout the following chapters.

Chapter 3

Interaction of Flow and Floating-Body

3.1 Introduction

This chapter presents a number of two-dimensional test cases of flow and floating-body interaction employing the method described in Chapter 2. The emphasis of this chapter is on verifying and validating the numerical method and demonstrating the robustness and reliability of this coupled approach. Though the main concern is not to study any specific problem in practice, it is however necessary to define the test cases properly and make them as close as possible to the practice. In ship hydrodynamics, predicting the dynamic response of floating-bodies is of great importance in a wide range of fields: slamming, launching, added resistance, roll damping by stabilizer (bilge keels), behavior of one ship or interaction of two adjacent ships in waves, ship maneuvering etc. Test cases in this chapter are so chosen that they are not only relevant to these practical applications, but also suitable to validate the code by available experimental data or analytical solutions. These 2D test cases serve also as preliminary study for further complex 3D problems, which will be presented in the following chapters.

This chapter includes several sections:

Section 3.2 presents water-entry and water-exit of a horizontal circular cylinder. The trajectory of the cylinder, the impact load during its water-entry and the free-surface deformation in a sequence of time instants are compared with experiments showing very good agreement. Some numerical study on effects of grid resolution, time integration scheme, turbulence and moving-grid is further carried out for the case of water-entry problem.

To study the behavior of floating-bodies in waves, the accuracy of wave generation in the numerical tank undoubtedly plays an important role. Section 3.3 describes two methods for wave generation in a numerical tank:

- 1) Imposing the inlet velocity
- 2) Moving a non-slip wall

Not only small but also large amplitude waves are generated and the numerical results are

compared to the potential wave theory, showing favorable agreement. Numerical aspects minimizing the artificial damping of waves in space and time are discussed.

The floating-body motion in small regular waves is then computed for bodies of simple geometry in section 3.4. Constrained motion as well as free-floating motion of a rectangular cylinder is first computed and the corresponding experiments are conducted to validate the results. Then, a mid-ship section with or without bilge keels is investigated in waves, showing the roll-damping effects of the keels. As the last case in section 3.4, the interaction of two adjacent floating-bodies in waves is predicted, demonstrating the applicability of this approach to investigate multi-floating-body interaction problems.

Section 3.5 investigates extreme motion of a free-floating rectangular cylinder under large amplitude wave packages. Experiments are conducted in the wave tank at the Technical University of Berlin with a computer-controlled wave-maker. The comparison of the time histories of body motion as well as the water elevation at two probes gives very good agreement. As mentioned before, the overlapping grid method as an alternative to the moving-grid method is tested here and results of these two approaches are compared to each other.

3.2 Water-Entry and Water-Exit of a Horizontal Circular Cylinder

In ship and offshore structure design, the prediction of water impact loads is of great importance. The hydrodynamic impact (slamming) on ships can necessitate the reduction of ship speed, cause hull vibration and damage the ship structure. In offshore operations, special care has to be taken in designing cross members in the splash zone of the incident waves, which suffer from wave impact loading frequently when continually entering (exiting) the water.

Owing to the importance of the water impact problem in ocean engineering, it has attracted a large number of investigations. Most previous studies on the water impact problem are based on the potential-flow assumption. The most important pioneering works can be attributed to von Karman [87] and Wagner [88]. As an initial work, von Karman developed a formula to determine the maximum pressure acting on the floats of seaplanes during landing. Wagner treated general problems of impact and planing on the free surface and took into account the effect of water splash-up on the body during take-off and landing of such planes. Further solutions for the water-entry problem based on potential flow assumption can be found in Faltinsen et al. [24], Greenhow [29] and Zhao & Faltinsen [100]. The water-exit problem has been relatively less studied, related works can be found in Greenhow [29] and Telste [84]. Korobkin [46] gives a recent review on this topic.

In this section, classical problems of water-entry and water-exit of a horizontal circular cylinder are solved using the present method to examine whether the method is able to predict the trajectory of the cylinder and the water surface elevation during water-entry/exit. The computational results are compared to published experimental data, Greenhow and Lin [28]. Numerical aspects such as grid resolution, time integration schemes, turbulence and moving-grid effects are further discussed to estimate the numerical accuracy.

3.2.1 Water-Entry of a Horizontal Circular Cylinder

The neutrally-buoyant circular cylinder used in the experiment and the calculation has a radius of 5.5 cm. It is released from a certain position above the still water level so that the instant velocity at which the cylinder intersects the water surface is 4.0 m/s ($R_n = \frac{\rho V D}{\mu} = 4.36 \cdot 10^5$, $F_n = \frac{V}{\sqrt{gD}} = 3.85$). After the cylinder contacts the water surface, the velocity of the cylinder is decreased significantly due to the effects of hydrodynamic forces. Two jets are thrown up at each side of the cylinder and travel straight upward until they become unstable. Due to gravity effect, the water fronts collapse against each other to throw up another jet. The cylinder moves further down into the water until it reaches the bottom of the tank at $t = 0.50$ s and bounces up at the depth of 30 cm. A detailed sequence of photographs has been taken for the whole process, as shown in the right column in Fig. 3.1.

The numerical tank has been set up as a rectangle with 60 cm height and 60 cm width, see Fig. 3.2 for the whole domain of the numerical grid (12590 cells) employed here. The non-slip wall condition has been applied at the cylinder surface. Symmetry planes are located in the longitudinal direction since the problem is supposed to be two-dimensional. The hydrostatic pressure is applied at the left- and right-hand boundaries and the inlet condition is specified at the lower boundary assuming the fluid domain to be infinite. The upper boundary is high enough above the water level so that the static air pressure condition can be applied. A non-deforming grid is attached to the body and moving all the time with the body. The CD and IE schemes have been applied here for space and time approximations.

The bounce-up of the cylinder at the bottom of tank is approximated by reversing the velocity of the cylinder corresponding to a loss-free re-bounce. This simplification is too inaccurate to simulate the bounce-up process correctly, but is allowed here to avoid complexity since the water-entry process is of main interest and the free surface deformation should not be much affected by this simplification, as indicated by comparing the numerical results and experimental photos after $t = 0.50$ s in Fig. 3.1. The numerical grid used here is fully made of Cartesian cells with local cell-wise refinement in the vicinity of the cylinder as shown in Fig. 3.2. Other grid topologies like different types of surface-fitted grids, Fig. 2.5, have been studied. Surprisingly their results (especially the jet formation beside the cylinder) are less accurate than the one produced by the Cartesian grid. The origin of the problem could be attributed to the near-wall meshing. Inaccuracies were initiated during the formation of the water jets after the impact of the cylinder on the water surface.

The numerical results are shown together with the experimental photos in a series of time instants in Fig. 3.1. As can be seen, jet forming, traveling and collapsing are predicted by the numerical scheme successfully. Air flow has been computed in the present method; therefore air effects such as air-cushion effect and cavity formation have been automatically taken into account. Some air bubbles can be seen along the cylinder due to high-speed water-entry, and they travel up to the free surface due to the buoyancy effect. The free surface has been broken in a complex manner by the combination of forming/falling jets, uprising air bubbles and the cylinder motion itself. A great similarity can be observed between the numerical prediction and the experimental record.

Figure 3.3 shows the velocity vectors of the fluid around the circular cylinder together with the pressure field at four selected time instants (cf. Fig. 3.1). One can see, the flow has been significantly accelerated by the cylinder and in reaction the cylinder suffers a high im-

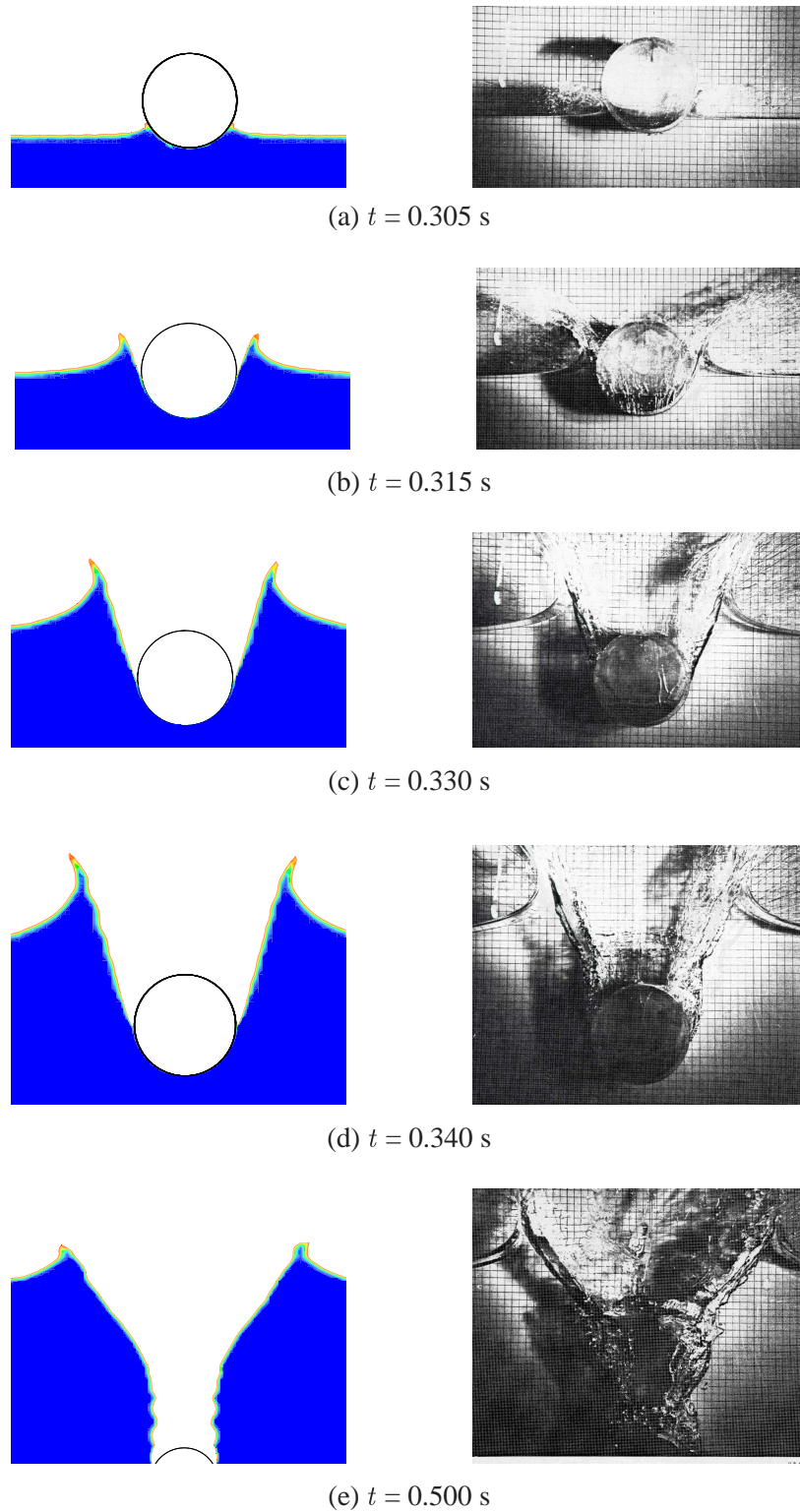


Figure 3.1: Free surface deformation of a neutrally-buoyant cylinder water-entry: simulation (left) and experiment (right).

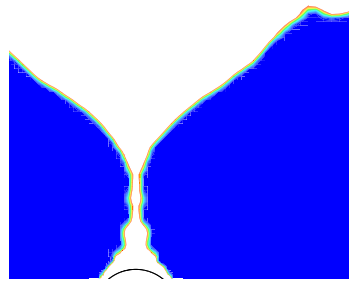
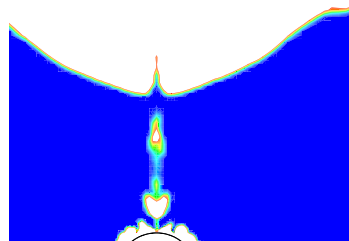
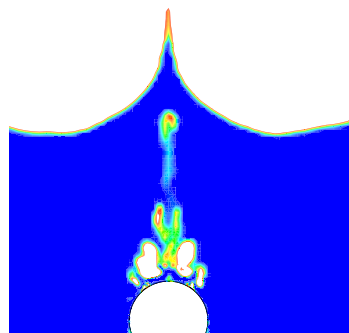
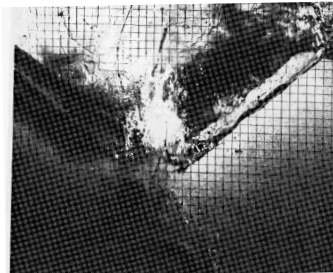
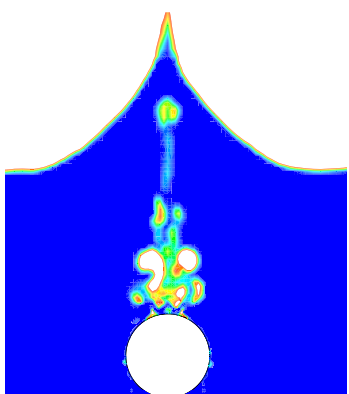
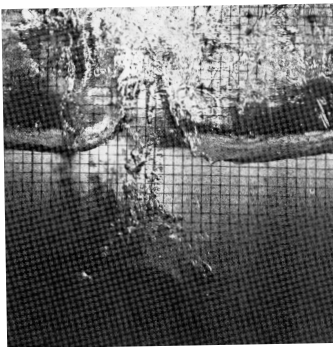
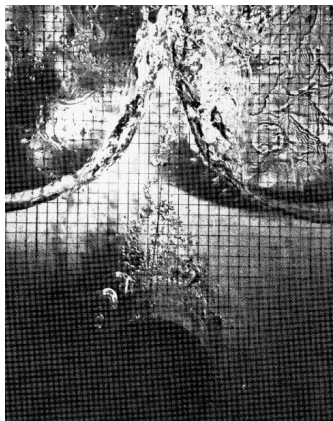
(f) $t = 0.560$ s(g) $t = 0.600$ s(h) $t = 0.690$ s(i) $t = 0.750$ s

Figure 3.1 (continued): Free surface deformation of a neutrally-buoyant cylinder water-entry: simulation (left) and experiment (right).

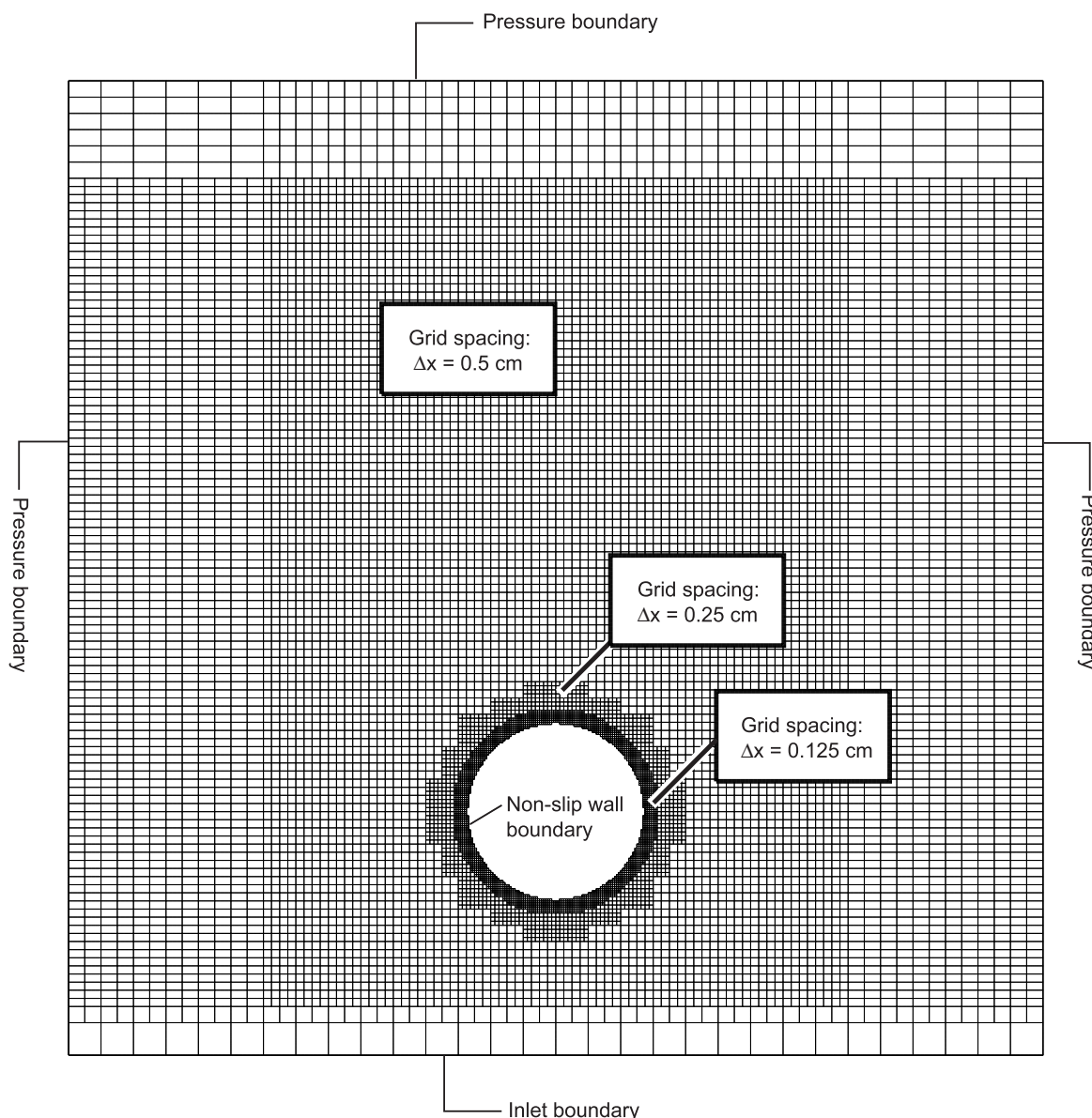


Figure 3.2: Numerical grid for the circular cylinder water-entry case.

impact load from the fluid and its vertical velocity decreases significantly at the moment when it enters the water. The impact load and vertical motion of the cylinder are computed by the code including the hydrodynamic, air and gravity effects. Figure 3.4 shows the time history of vertical motion and impact load of the cylinder. The vertical position y is measured from the initial still water line to the lowest point of the cylinder, which applies throughout this section. The instantaneous vertical positions of the cylinder are compared with experimental data with reasonably good agreement (The lower of the two deviating experimental points has also been doubted by the experimenters, see Greenhow and Lin [28]).

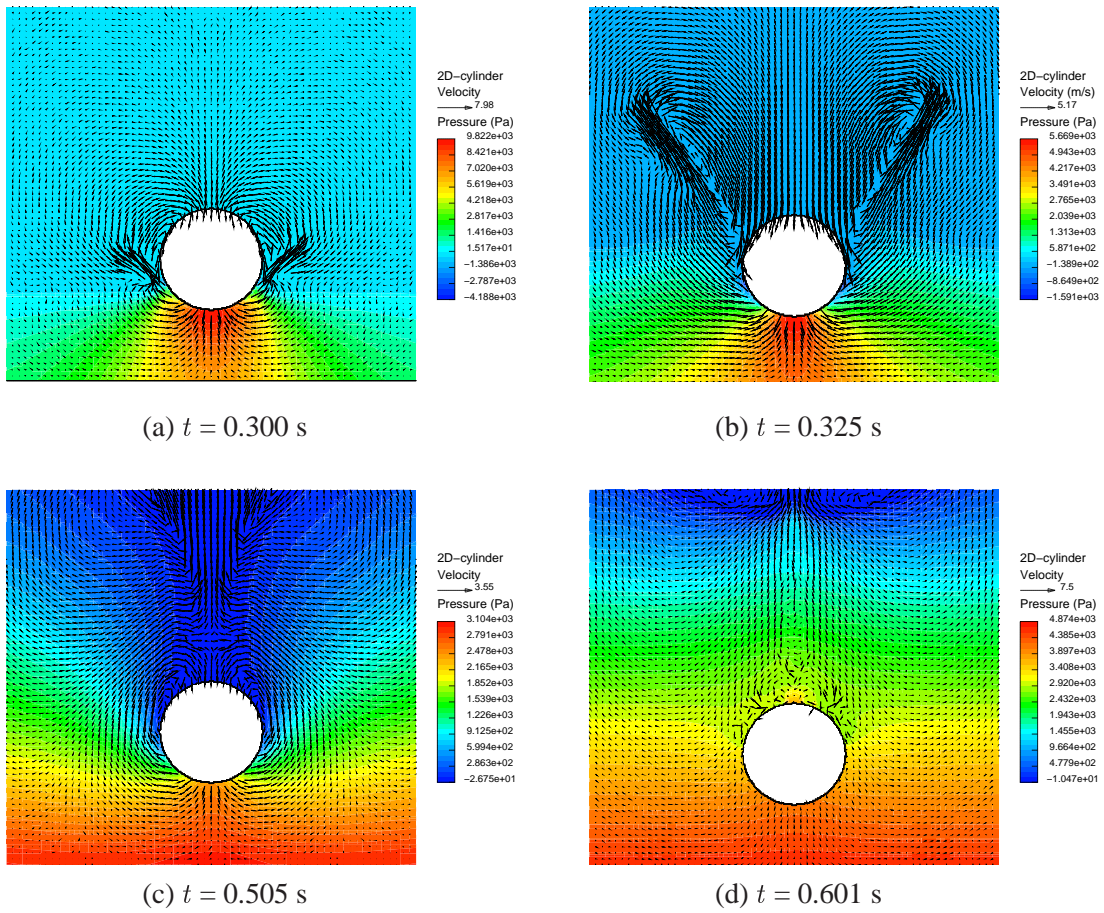


Figure 3.3: Velocity vectors and pressure fields of the fluid during the cylinder water-entry.

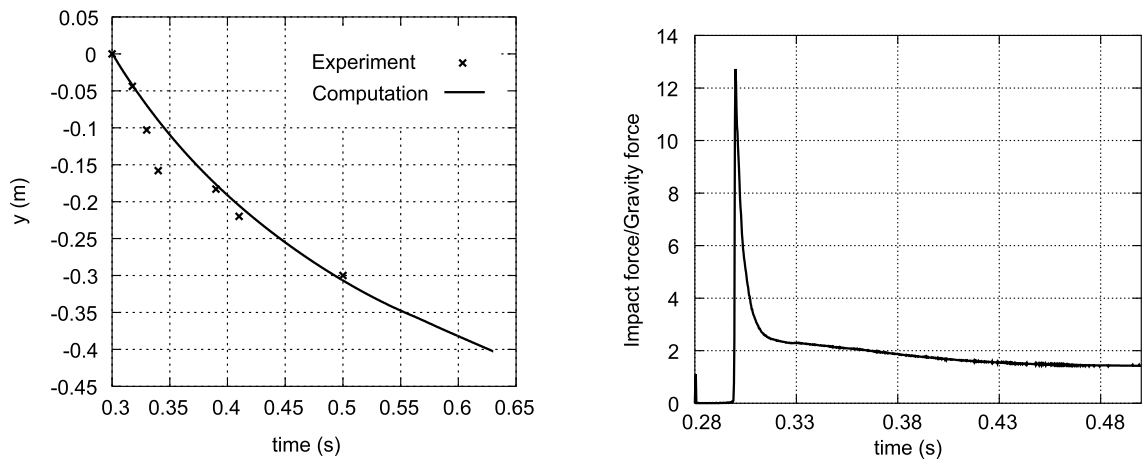


Figure 3.4: Time history of the vertical motion (left) and the impact force (right) during the cylinder water-entry.

3.2.2 Water-Exit of a Horizontal Circular Cylinder

The same cylinder has been taken again in the experiment of water-exit. It is pulled out of the water with a constant speed of 0.87 m/s ($R_n = 9.50 \cdot 10^4$, $F_n = 0.838$) in both experiment and calculation. The same Cartesian grid shown in Fig. 3.2 is used. Boundary conditions are applied analogously as in the water-entry case. The grid is not moved in this case; instead, the counter-speed of the water is specified at the inlet boundary. Results are compared to the experiments conducted by Greenhow and Lin [28].

The numerical simulation has successfully predicted the dominating phenomena during the cylinder water-exit: The water above the cylinder is lifted by the cylinder and thin layers are formed subsequently around the cylinder. With the cylinder further rising up, the water layers are drawn down to the water surface, which causes the rush-up and results in the breaking of the free surface. Figure 3.5 compares the results at six successive time instants between experiment and computation. As one can observe, favorable agreement has been obtained between simulation and experiment. The velocity vectors of the fluid around the cylinder together with the pressure field are shown in Fig. 3.6 at four instants of time. The pressure distributions along the cylinder circumference are given in Fig. 3.7 for the four corresponding time instants.

3.2.3 Study on Numerical Effects

A numerical method unavoidably introduces numerical errors, therefore it is necessary to monitor and estimate the errors caused by different numerical factors to ensure they are in the range of acceptance. This is important for the verification of the numerical method as well as the safety of practical design. In principle, one can estimate the numerical errors by systematically refining the grids and time steps (in case of transient problems) because if a numerical procedure is convergent and stable, the result is expected to converge towards a grid- and time-step-independent solution. Additionally, the effect of different time integration schemes is analyzed here. This study on numerical effects is performed for the water-entry case.

Grid resolution

To investigate the dependence of numerical error on the size of mesh, calculations have been carried out with systematically refined grids. The finer grid is generated by halving each single cell into 4 cells from the coarser grid. The time step size has also been halved since the problem is transient and the time is treated as the fourth dimension of the problem. In this way, three sets of grid are used for calculations intending to get the grid- and time-step-independent results. The coarse grid has about 1160 cells, while the medium grid has 4 times as many as the coarse grid and the fine grid is obtained by refining the medium grid only in the regions near the cylinder and the free surface, resulting in 12590 cells (this is allowable because the discretization errors are much lower in the regions far away from the body). The fine grid has been shown in Fig. 3.2. The time step size is set to $\Delta t = 0.001$ s, 0.0005 s, 0.00025 s accordingly. In a non-dimensional way, this corresponds to $\frac{\Delta t V}{D} = 0.072$, 0.036, 0.018. The results from the fine grid have already been presented in the previous section.

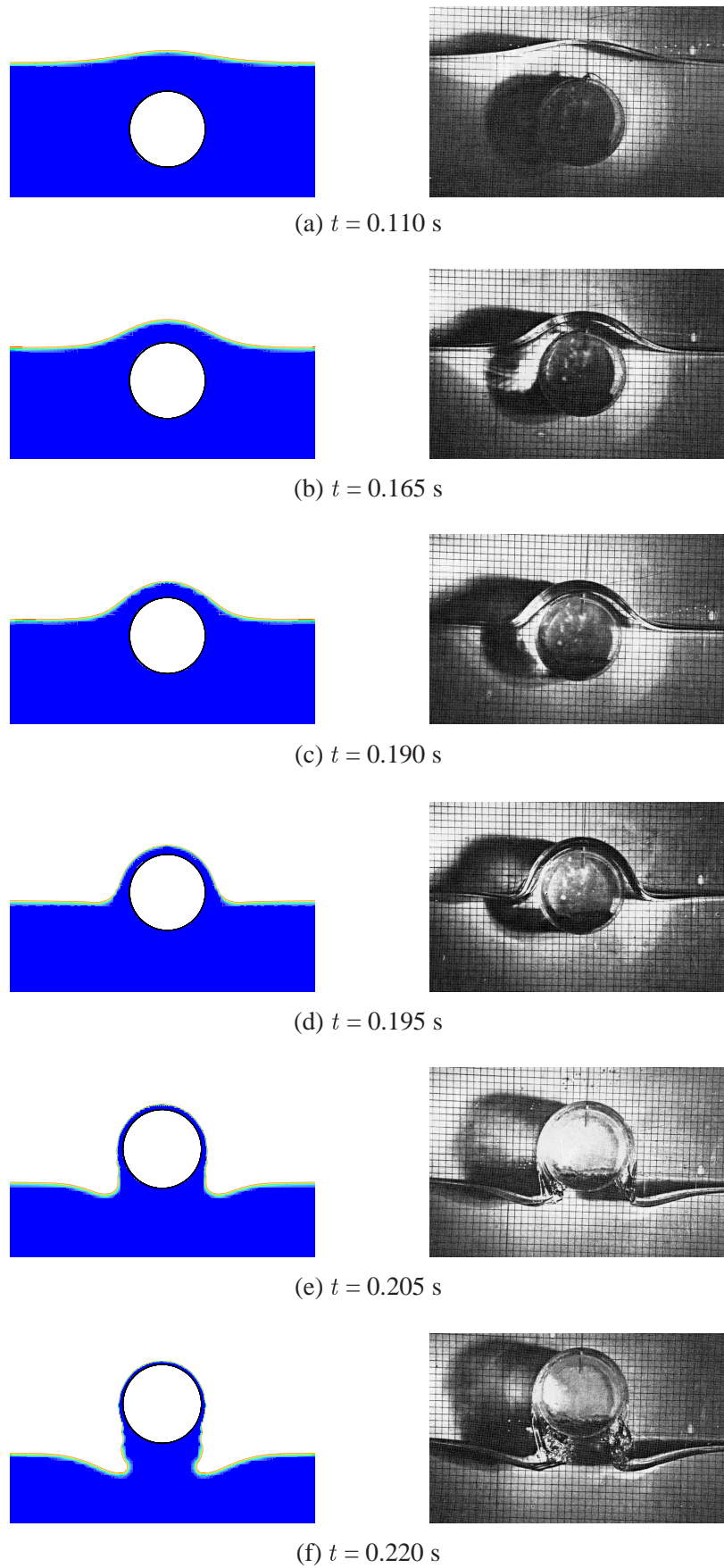


Figure 3.5: Free surface deformation of a constant-speed cylinder water-exit: simulation (left) and experiment (right).

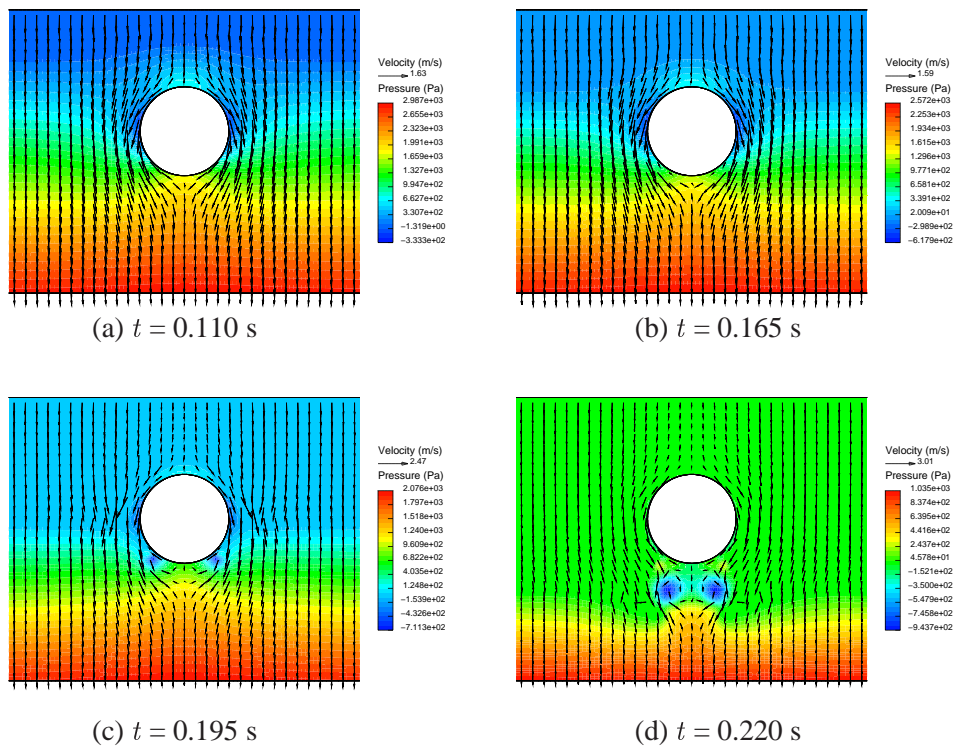


Figure 3.6: Velocity vectors and pressure fields during the cylinder water-exit.

Other numerical parameters are kept the same in order to exclude the influence of other factors.

Figure 3.8 compares the time histories of the cylinder trajectory and impact force using these three grids. As one can see, the coarse grid does not predict a satisfactory trajectory of the cylinder and the impact force oscillates strongly when the cylinder enters the water while the medium grid and the fine grid predict almost identical motion but a slightly different peak of the impact force. To capture the jet formation, it is shown in Fig. 3.9 that only the fine grid is able to predict precise shapes of the jets. So the fine grid seems to be necessary if the free surface deformation during the cylinder water-entry has to be predicted accurately. For further investigations, the fine grid has therefore been taken to limit the discretization error.

Time integration scheme

As mentioned in the previous section, the IE time integration scheme has been used so far. The second-order ITTL in time corresponding to the second-order CD scheme in space has also been tested here. Calculations are carried out with both time integration schemes keeping other configurations unchanged on the fine grid of Figure 3.2. Figure 3.10 shows the predicted vertical motion of the cylinder and the total impact force on the cylinder using these two time integration schemes. As can be seen, the vertical motion of the cylinder, identically predicted, is less sensitive to time integration scheme. However the impact force predicted by the second-order ITTL scheme is less smooth than the one from the IE scheme, indicating that the ITTL scheme is more prone to oscillations.

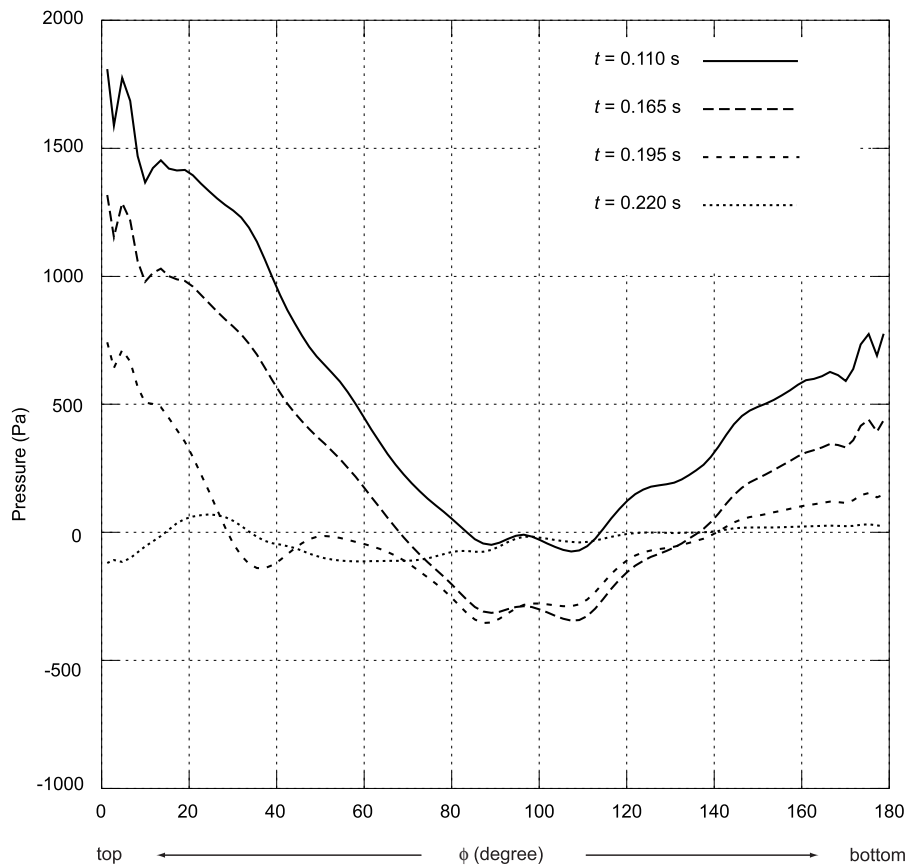


Figure 3.7: Pressure distribution along the cylinder circumference at different time instants (water-exit).

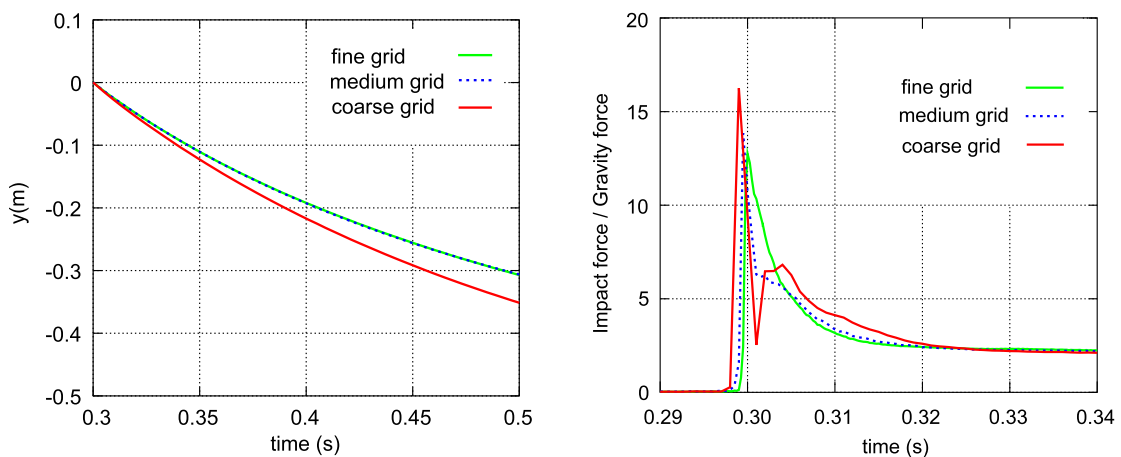


Figure 3.8: Computed time history of vertical motion (left) and impact force (right) using three grids (water-entry).

Turbulence effect

It is assumed that turbulence effect is not significant during the cylinder water-entry. Therefore laminar flow computations have been performed so far. To check whether the

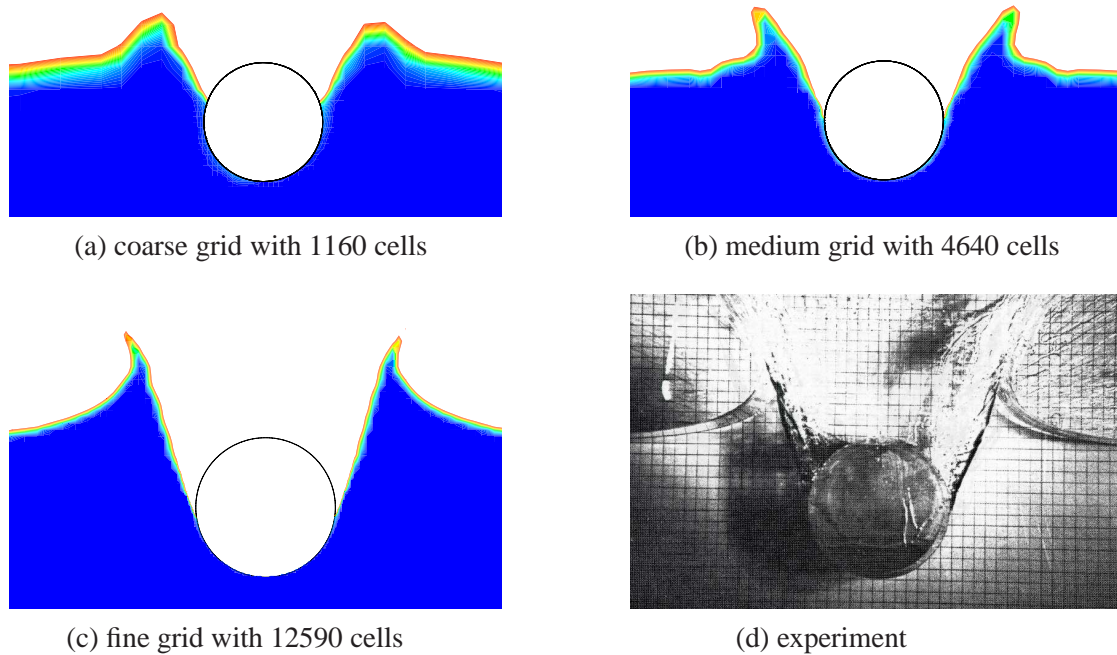


Figure 3.9: Free surface deformation at $t = 0.330$ s during cylinder water-entry.

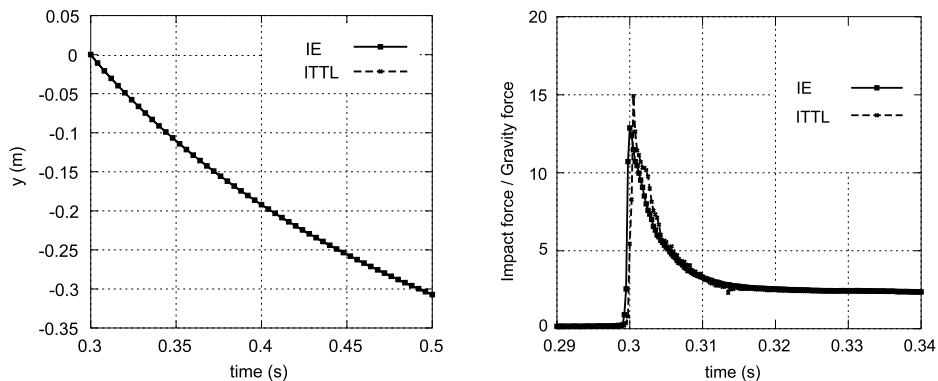


Figure 3.10: Computed vertical motion (left) and impact force (right) during cylinder water-entry using IE and ITTL time integration schemes.

assumption is valid, the RANS equations with the standard $k-\epsilon$ turbulence model have also been solved for this case. The fine grid and the ITTL time integration scheme have been chosen. The predicted motion and total impact force are given in Fig. 3.11. It can be seen that identical cylinder motions are obtained by the computations with and without turbulence modeled. The impact force predicted by RANSE has a slightly higher peak, but lower after the cylinder has entered the water. The second peak before 0.32 s is caused by a restart of the calculation. Figure 3.12 shows the pressure distribution on the cylinder at three selected instants of time, the same tendency can be observed as from the comparison of the total impact force in Fig. 3.11. The distribution of the magnitude of the shear stress along the cylinder wetted-surface at the corresponding time instants are shown in Fig. 3.13, which is much smaller in magnitude than the one of pressure (cf. Fig. 3.12).

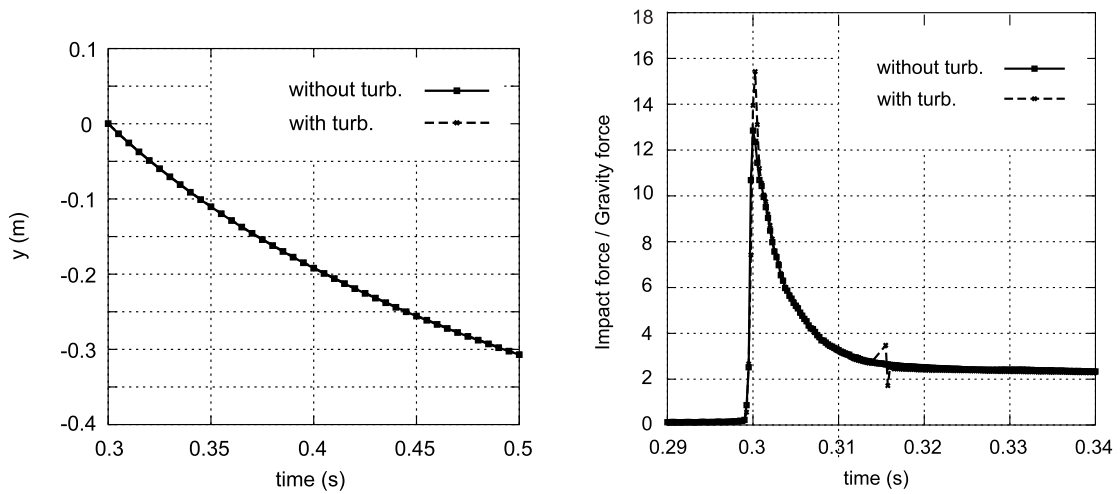


Figure 3.11: Computed vertical motion (left) and impact force (right) during cylinder water-entry with and without turbulence model.

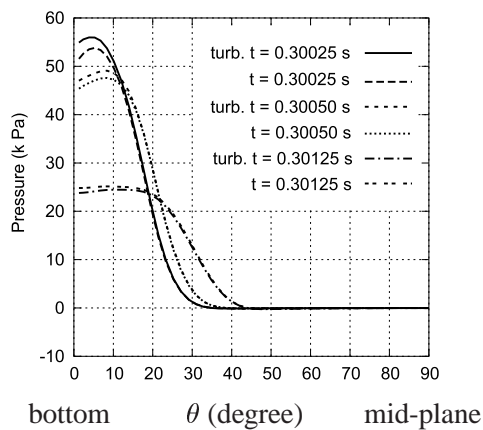


Figure 3.12: Pressure distribution on the cylinder surface.

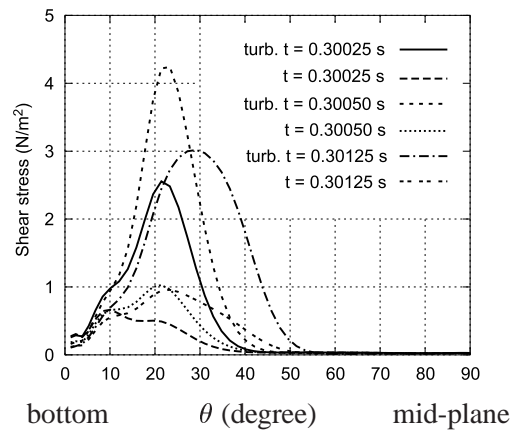


Figure 3.13: Shear stress distribution on the cylinder surface.

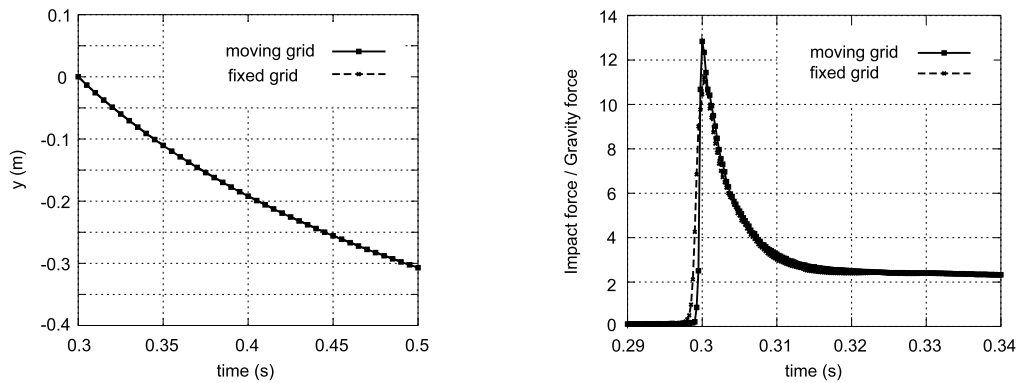


Figure 3.14: Computed vertical motion (left) and impact force (right) during cylinder water-entry using moving- and fixed-grid methods.

Alternative to moving-grid

As mentioned before, the results presented so far are obtained by employing the moving-grid technique. However the grid/body can also be kept fixed; instead, the fluid can be accelerated and the computation is performed in a body-fixed system. Such an analysis is carried out on the fine grid using the ITTL scheme. Theoretically these two alternatives should make no difference on the computational results, as can be seen in the predicted vertical motion of the cylinder in Fig. 3.14. However, certain error is introduced due to the different numerical interpretation. Single precision is used for coordinates of moving grids, whereas double precision is used for all other values. Since the impact force is a very sensitive variable, slightly different results are obtained for the predicted impact force, as shown in Fig. 3.14. It can be seen that the impact force calculated by using a moving grid has a higher peak value and a sharper increase over time than the one produced by using a fixed grid.

3.3 Wave Generation in Numerical Water Tank

Investigation of motions of a floating-body under the influence of waves is one of the main interests in this study. Since the accuracy of wave generation has a direct influence on an accurate prediction of the body motion in waves, waves are generated and analyzed first in the numerical tank.

Two methods are applied here for wave generation:

- Impose the velocities at inlet boundary.
Velocities can be specified according to the wave theory, see Newman [59].
- Simulate movements of a wave-maker as in experiments by a moving no-slip wall.
The velocity distribution at the moving boundary is specified according to the velocity of the wave-maker.

The first method is easier and more efficient from the numerical point of view, since the solution domain can be made smaller and the effort of grid-moving to simulate the flap motion of the wave-maker can be saved. The second method is more appropriate for the purpose of validation since the motion of the wave-maker can be exactly simulated as in the experiment. To investigate ship motions in waves, the first method is usually preferred since it is then straightforward to generate irregular ocean waves. However, special attention has to be paid when the first method is used because the velocity profile of water and air should match at the instant location of the free surface at the inlet boundary. This can cause numerical difficulties due to the opposite directions of the flow in water and air across the free surface (especially in large amplitude waves) and often an approximation is needed, as explained in the next section.

3.3.1 Wave Generation by Inlet Boundary Condition

For small amplitude waves, the velocities at the inlet boundaries can be derived from the linear wave theory. The velocity components (u, v) of water particles at inlet boundaries for regular plane progressive water waves are:

$$\begin{aligned} u_i &= \omega A e^{ky} \cos(kx_i - \omega t + \epsilon) , \\ v_i &= \omega A e^{ky} \sin(kx_i - \omega t + \epsilon) . \end{aligned} \quad (3.1)$$

The wave travels in positive x -direction, y points positive upwards with $y = 0$ at the undisturbed free surface. A is the wave amplitude, k the wave number, ω the circular frequency, and ϵ is an arbitrary phase angle which can be set equal to zero by a suitable choice of the origin $x = 0$. The corresponding water surface elevation is expressed as

$$\eta_i = A \cos(kx_i - \omega t + \epsilon) . \quad (3.2)$$

If air flow plays a minor role it might be ignored at most parts of the inlet boundaries except the region just above the free surface, where interpolation should be incorporated to avoid a large gradient of the imposed velocity across water and air. If the air flow is to be specified at the inflow, its velocity is given in a similar manner as for water. Figure 3.15 illustrates the velocity distribution of a plane progressive wave in water and air and the interpolation between water and air.

Small amplitude waves of an amplitude of 0.001 m and a wavelength of 0.196 m (corresponding to a circular frequency of 17.73 s^{-1} and a phase velocity of 0.553 m/s, see Newman [59]) have been generated first in the numerical tank. Figure 3.16 shows the computed instantaneous free surface location at one time instant and the comparison for one wavelength of wave profile between computation and the sinusoidal form (as in the linear theory) taking the highest elevation of the computation as amplitude. As can be seen, the sinusoidal wave profile agrees very well with the analytical solution according to the linear wave theory. The part of the numerical grid in the region of the free surface has 20 CVs per wavelength and 8 CVs in wave height to resolve the wave profile. The grid is gradually coarsened outside the free surface region. The time step is set to $\Delta t = 0.005 \text{ s}$, corresponding to 70 intervals per wave period. The CD and ITTL schemes have been adopted here for space and time approximations. The result is quite satisfactory since the decreasing rate between two successive wave heights due to numerical damping is about 2% which is almost negligible. Figure 3.17 compares the horizontal velocity component of the fluid particle directly beneath the wave crest and the vertical velocity component of the fluid particle at the free surface when $\eta = 0$ with the analytical solutions, again showing very good agreement. Only at the bottom of the tank the effect of the rather coarse grid outside the free surface region can be observed.

To generate large amplitude waves the equation (3.1) for the velocities at the inlet boundary are not any more exact; nevertheless a large wave amplitude is simply substituted into these formulae to specify the inlet boundary conditions. A typically nonlinear wave profile is generated automatically and compared with a second-order Stokes wave of the same total mean energy density, Newman [59], shown in Fig. 3.18. The agreement is satisfactory though not as good as for small amplitude waves due to the inaccurate boundary condition

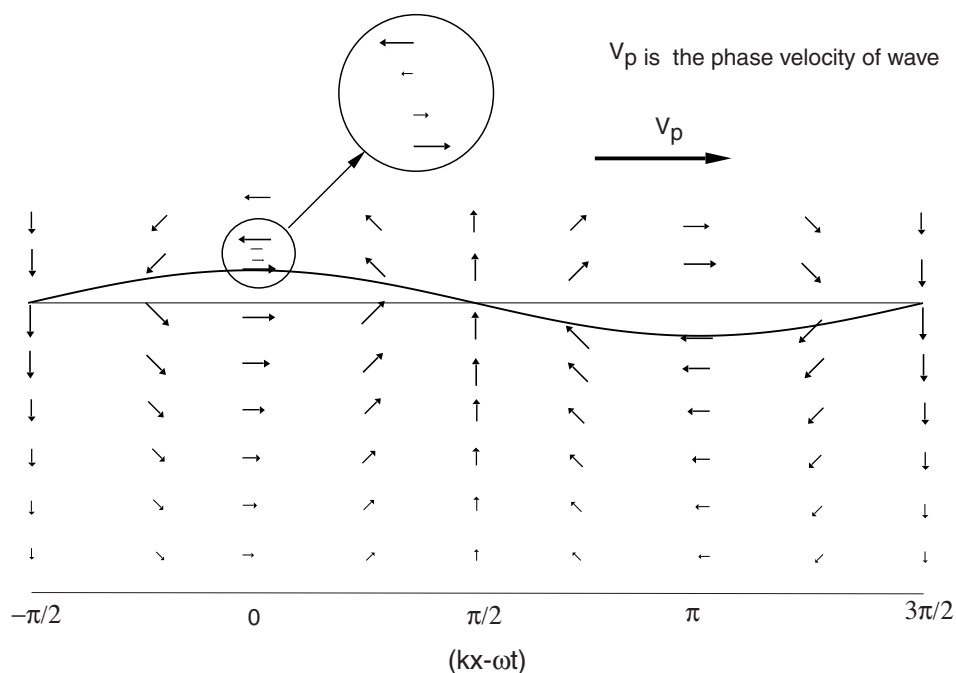


Figure 3.15: Velocity field of a plane progressive wave and interpolation between water and air.

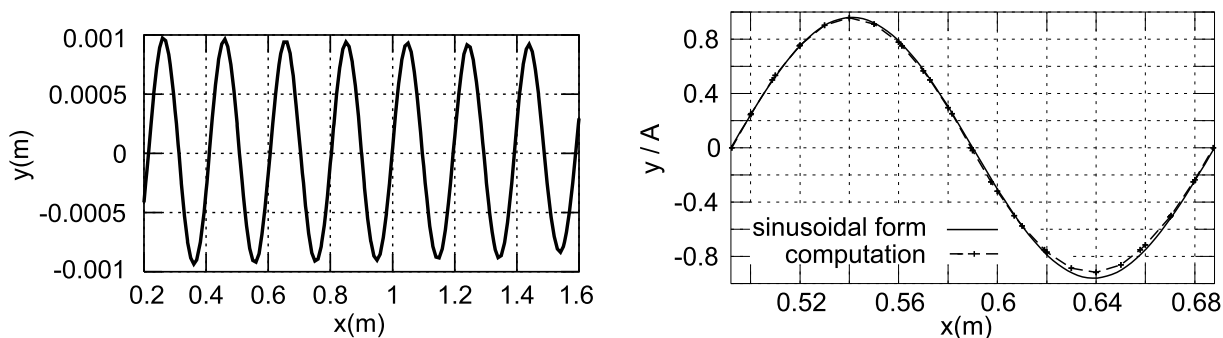


Figure 3.16: Computed instantaneous free surface (left) and wave profile comparison in one wavelength (right) for a small amplitude linear wave.

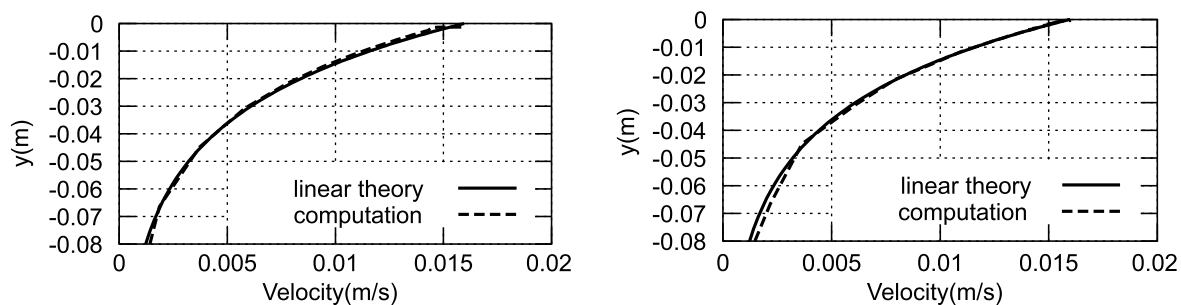


Figure 3.17: Horizontal velocity component of the fluid particle directly beneath the wave crest (left) and vertical velocity component of the fluid particle at the free surface when $\eta = 0$ (right).

in the computation and the ignored viscosity in the analytical solution. The computation predicts even narrower crests and wider troughs than the second order Stokes wave theory.

It has been shown that potential wave theory can be used in specifying the velocities at the inlet boundaries for wave generation in the numerical water tank with a satisfactory accuracy. However, attention has to be paid to the damping of wave amplitude in space and time during propagation of waves. The wave-damping can not be avoided though it can be decreased by carefully selecting the numerical parameters. In practice, one can try to estimate the wave-damping in advance and apply a higher amplitude at the inlet to generate a wave with expected amplitude around the position of the ship, but experience and care are needed since the damping factor is grid/case-dependent. Generally, the wave-damping factor can be influenced by the following numerical parameters:

- Grid resolution (the number of cells per wavelength and wave height)
- Time step size (the number of time steps per wave period)
- Time integration scheme (the first-order IE, second-order ITTL scheme etc.)
- Differencing scheme in space (UDS, CDS etc.)

A small amplitude wave ($A = 0.001$ m and $\lambda \approx 0.2$ m) has been generated here to show the effects of the grid resolution and the time integration schemes, see Fig. 3.19. The coarse grid used here has 10 cells per wavelength and 16 cells per wave height and the fine grid has doubled cells per wavelength. A numerical beach with gradually coarsen grids is connected to the tank for $x \geq 2$ m. The CDS is used as the differencing scheme in space and the time step size is kept the same for all cases.

It can be observed that both grid refinement in the direction of wave propagation and the time integration scheme have strong influence on the damping factor. The result from the second-order ITTL scheme and the fine grid seems to be rather satisfactory, but unacceptable results are produced by the coarse grid and the IE time integration scheme. The first-order IE scheme produces large numerical diffusion as expected, which is more serious if the grid is coarse.

The first-order IE scheme can basically not be applied to analyze problems requiring a time-accurate simulation (e.g. wave propagation) due to its first-order truncation error and requirement on too small a time step. It is strongly recommended for problems involving wave propagation that the second-order scheme (e.g. ITTL in time and CDS in space) should be employed and the numerical grid should be fine enough to capture the wave profile accurately (at least 20 cells per wavelength and 16 cells per wave height are needed according to the author's experience).

3.3.2 Wave Generation by a Flapping Wave-Maker

Experimental investigations of wave and floating-body interactions are usually conducted in a towing tank where waves are generated by one or more wave-makers. For the purpose

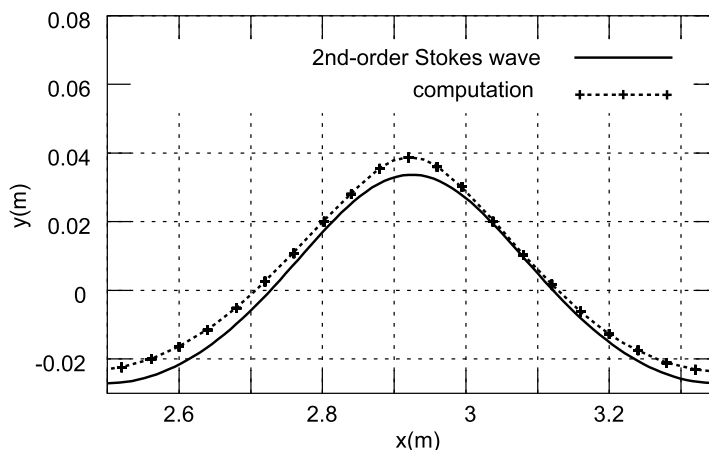


Figure 3.18: Wave profile for large nonlinear waves.

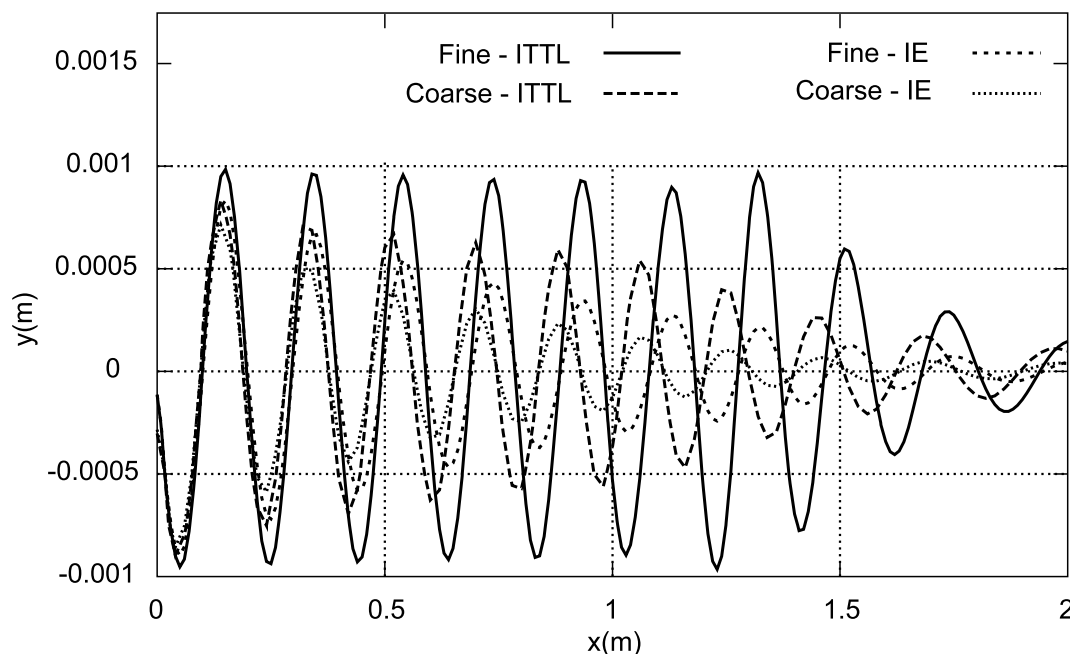


Figure 3.19: Comparison of wave profile on grid resolution and time integration scheme.

of validation of the numerical simulation by experiments, the flapping motion of the wave-maker is represented by moving boundaries in the present numerical tank.

As illustrated in Fig. 3.20, a moving no-slip wall boundary is imposed to move about its rotating axis at the left side of the solution domain. Regular waves have been tested first in the numerical tank. For convenience, the geometry of the wave-maker in the towing tank of the former Institut für Schiffbau (now TU Hamburg-Harburg) is taken as an example, which will be used again in the next section. It flaps sinusoidally from its original position with an amplitude of 0.018 m in horizontal direction (measured in still water plane) and a period of 0.7 s. The origin of the wave-maker is located at 0.8 m below the water level and the water depth of the tank is 1.0 m. The fine grid with 20 cells per wavelength and 16 cells per wave height is employed, together with the second order ITTL and CD schemes.

Figure 3.21 compares the computed wave profile (at $t = 8.0$ s) with the analytical solutions given by the linear wave theory and the second-order Stokes theory. The wavelength (also fluid velocity) is underestimated by the linear wave theory, which ignores all non-linear effects, but overestimated by the Stokes' solution due to its ignorance of the viscous effects. It is therefore reasonable that the numerical RANSE result just lies in between. Additionally, the horizontal velocity components of the fluid particle direct beneath the wave crest and the vertical velocity components of the fluid particle at the free surface when $\eta = 0$ are compared with the linear analytical solution in Fig. 3.22. The agreement is good except in the region near the bottom of the tank where the grid is coarse and the CDS tends to induce oscillations. Figure 3.23 shows the velocity field in the computational domain at a selected time instant where the solid line indicates the free surface position.

Also in this case, the IE scheme is tested here and its result is compared with the result from the ITTL scheme in Fig. 3.24. The first-order IE scheme tends to produce severe numerical damping and a phase shift as the wave propagates and therefore will not be used in later applications.

Since the agreement between computational and analytical solutions is rather satisfactory using both methods, experiments are conducted at our laboratory and at the Technical University of Berlin to investigate the interaction of flow and floating-body motion under different waves packages, where both small amplitude regular waves and large amplitude wave packages are generated. The computational results concerning both water elevation and body motion will be compared with the experiments in the following sections.

3.4 Motion of Simple Geometry Bodies in Regular Waves

Two-dimensional simple geometry floating-bodies are computed subject to small amplitude regular waves in this section, including a constrained or free-floating rectangular cylinder, a mid-ship section with or without bilge keels and two interacting floating-bodies. The predicted motions of both constrained and free-floating rectangular cylinder in small amplitude waves are examined by experiments conducted in the towing tank of the former Institut für Schiffbau, see section 3.4.1. The latter two test cases (sections 3.4.2 and 3.4.3) are carried out to show the further perspective of the coupled numerical method, e.g. in predicting roll-damping effects by keels and multi-body interaction in waves.

3.4.1 Constrained and Free-Floating Rectangular Cylinder in Waves

Constrained motion

An experiment is set up in the former Institut für Schiffbau to study the rotational motion of a cylinder about a longitudinal axis in regular waves. The model is made of wood and has a shape of a rectangular cylinder of 20 cm in length, 12 cm in width and 8 cm in height. The model is initially set up 3 cm immersed into the water and the rotating-axis is located at the vertical symmetry plane and 2.5 cm above the still water level, see Fig. 3.25. To minimize the 3D effects, the model is located with a small distance to the side wall of the towing tank

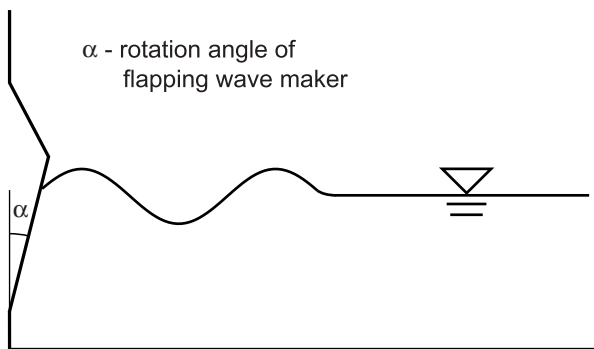


Figure 3.20: Wave generation by flapping wave-maker.

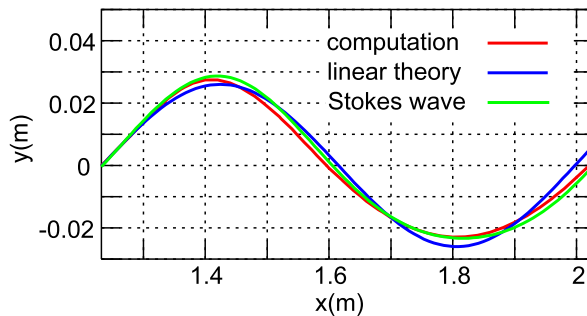


Figure 3.21: Comparison of wave profile for one wavelength.

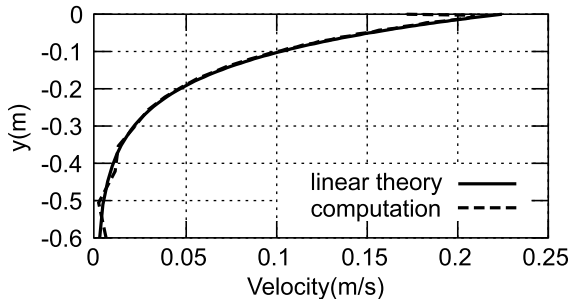
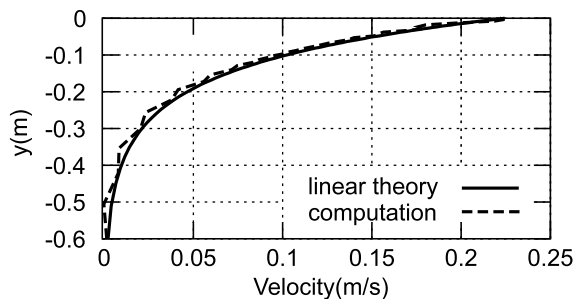


Figure 3.22: Horizontal velocity component of the fluid particle directly beneath the wave crest (left) and vertical component of the fluid particle at the free surface when $\eta = 0$ (right).

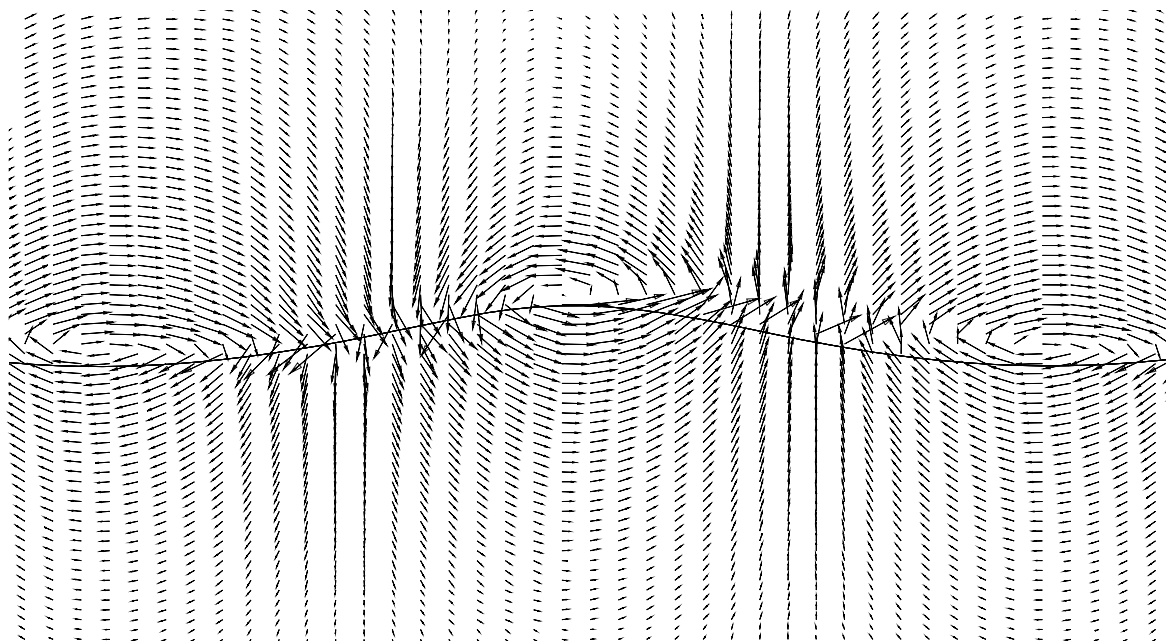


Figure 3.23: Computed velocity field for both water and air.

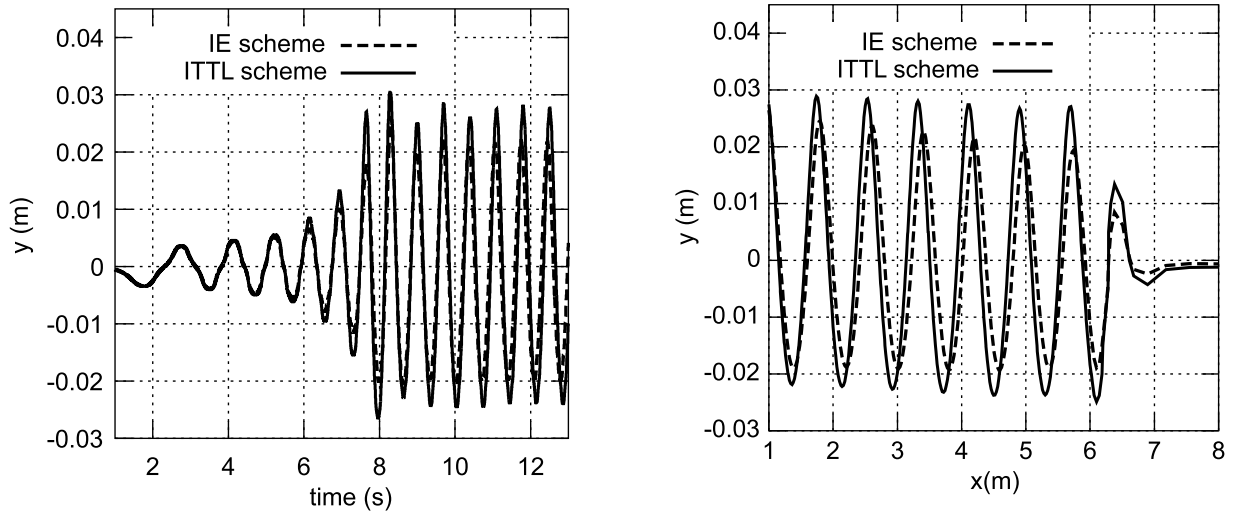


Figure 3.24: Computed water elevation against time (left) and wave profile at $t = 8.0$ s (right) using IE and ITTL time integration schemes.

(200 cm in width). An angle ruler is set at one end of the cylinder to record the rotation of the cylinder in reference to its vertical axis.

Waves are generated by simulating the flapping movements of the wave-maker in the towing tank, as described in section 3.3.2. The amplitude of the rotation angle of the wave-maker is 2.5° (the horizontal movement is about 35 mm at the still water level) and the period is 0.9 s. The cylinder is located at a distance of 2.4 m away from the flapping wave-maker. Sliding interfaces are employed to allow an arbitrary rotation of the cylinder. The CD and ITTL schemes have been adopted here for space and time approximations and the time step size is set to $\Delta t = 0.005$ s, which corresponds to $1/180$ of the wave period.

Figure 3.26 shows the body position and the free surface deformation at $t = 6.82$ s. The experimental photo at $t = 6.82$ s is shown in Fig. 3.27. As can be seen in Fig. 3.26, water is about to be splashed onto the top of body and waves break in the vicinity of the body resulting in small air bubbles enclosed in front of the body. These phenomena can also be observed in the experiment. Unfortunately, they could not be recorded by the camera (perpendicular to the angle ruler) due to the 3D effect at the end of the body, where the angle ruler was installed.

Figure 3.28 compares the angular displacement between experiment and computation. As can be seen, the phase of the motion in waves is predicted quite well. However relatively large differences appear in the amplitude of the angular displacement. A reduction of time step size results in an even larger deviation in the amplitude, shown in Fig. 3.29, indicating that the numerical error is unlikely to be responsible for these differences. The reasons are supposed to be the ignorance of the friction on the rotational axis and the three-dimensionality of the problem (the flow can not escape from the sides of the cylinder in the two-dimensional computation while it does escape in the three-dimensional experiment.). It is therefore reasonable that the predicted motion by computation is larger than the one in the experiment (note that the width of the tank is 2 m compared to 0.2 m of the cylinder length).

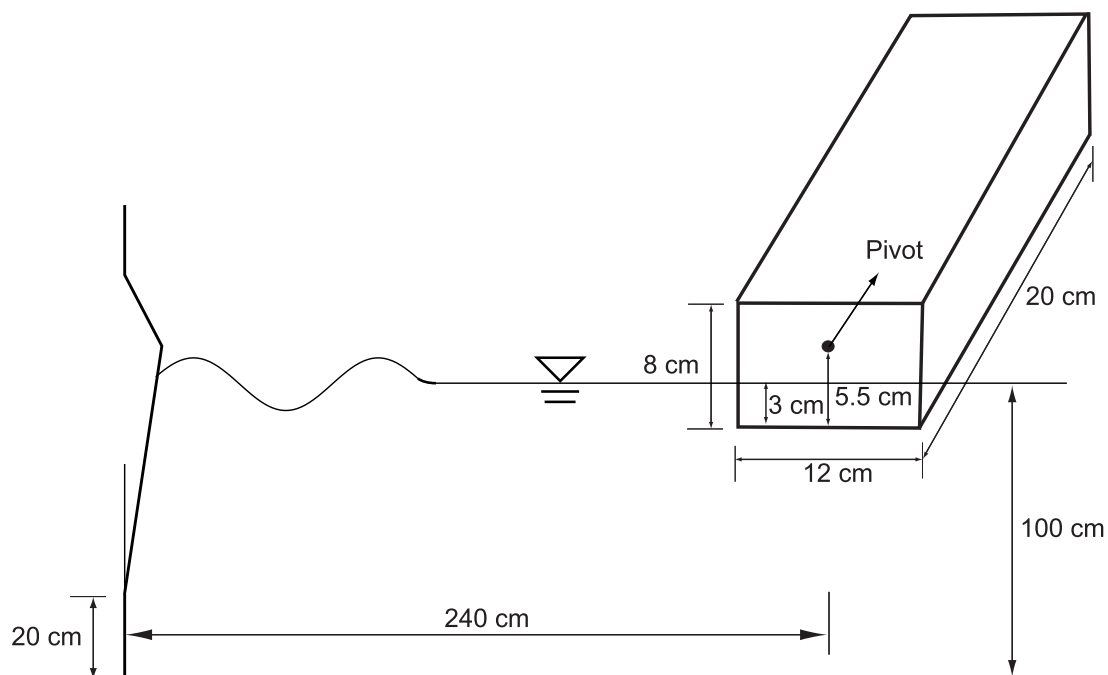


Figure 3.25: Set-up of the constrained motion experiment.

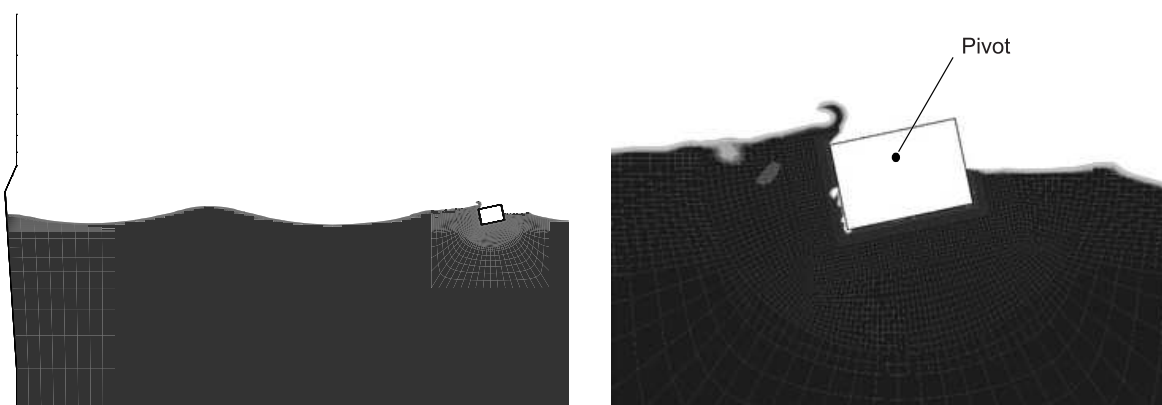


Figure 3.26: Free surface deformation at $t = 6.82$ s: far view (left) and near view (right).

Since the computational effort of three-dimensional computations is large, the next test case is set up to study a free-floating cylinder of larger aspect ratio (the ratio of length over width) in waves in expectation that the errors made by the 2D assumption can be reduced because the first source of error (the friction on the rotational axis) is automatically removed and the second source of error (the block effect on the flow in two-dimensions) become less significant due to the release of degrees of freedom (especially horizontal movement) and the larger aspect ratio of the body.

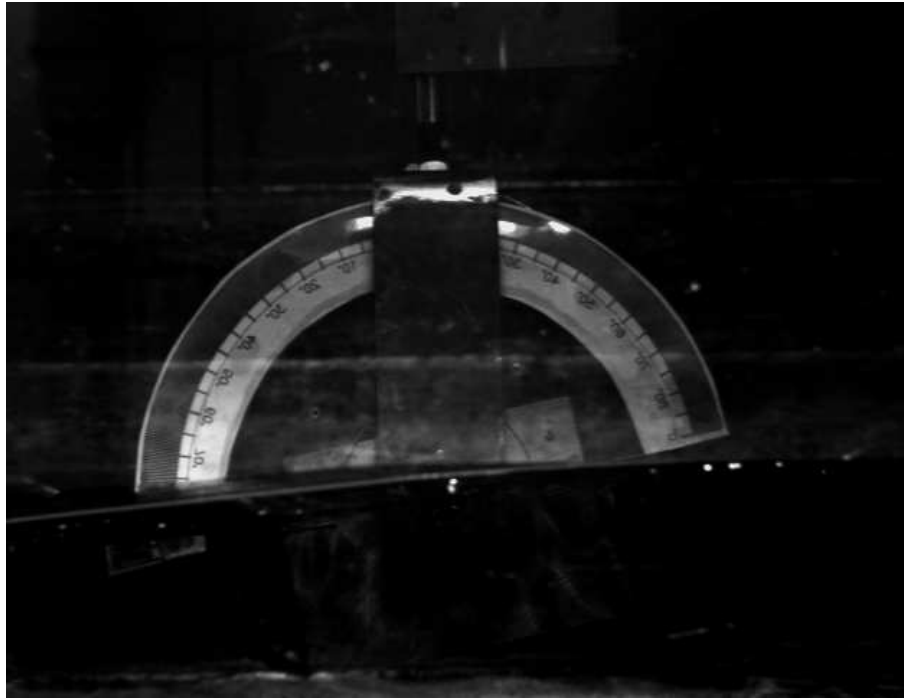


Figure 3.27: The experimental photo of the body in constrained motion at $t = 6.82$ s.

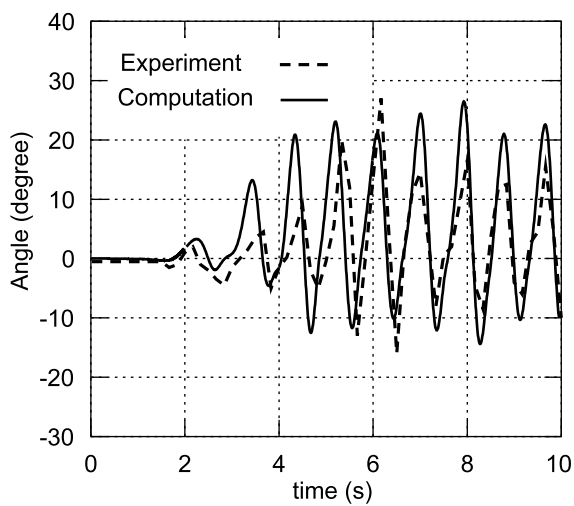


Figure 3.28: Comparison on the angular displacement of the body between computation and experiment (constrained motion).

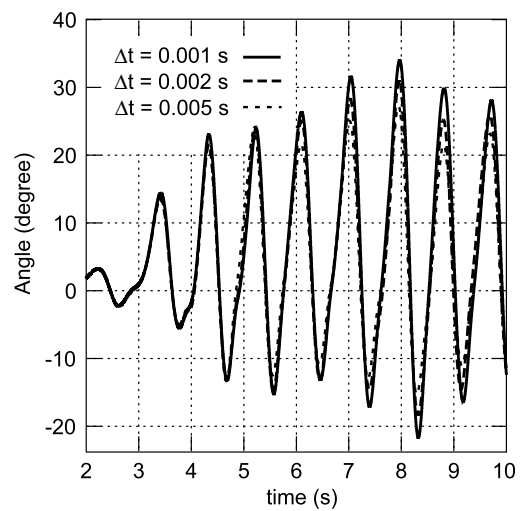


Figure 3.29: Computed angular displacement of the body using different time step sizes (constrained motion).

Free-floating motion

The experiment is again carried out in the same towing tank. The model is made of aluminum plates, which are formed into the shape of a rectangular cylinder with dimensions of 10 cm in width, 5 cm in height and 29 cm in length, as shown in Fig. 3.30. The averaged density based on the total weight over total volume is 680 kg/m^3 so that the model can float at the free surface in its stable equilibrium (positive GM, *Metacentric Height*) with 2/3 of the total volume submerged in the water. The model is initially located 2.5 m away from the flapping wave-maker with the longitudinal axis perpendicular to the direction of wave propagation. Regular waves are generated by the wave-maker with its flapping motion of an amplitude of 15 mm (at the still water level) and a period of 1.0 s.

The two-dimensional numerical water tank has been set up with 10 m in length and 2.2 m in height, in which water depth is 1.0 m and air height is 1.2 m. Fine grids are distributed near the body and in the region of free surface ($\Delta x = 1.5 \text{ cm}$ and $\Delta y = 0.5 \text{ cm}$) for the first 5 m of the tank. Successively coarsened grids as well as UDS are applied in the numerical beach ($x < 5 \text{ m}$) to damp the waves and avoid reflection. The time step size is set to $\Delta t = 0.005 \text{ s}$, corresponding to 1/200 of the wave period. The ITTL time integration scheme is applied for the computation.

An electric probe has been set up at a position 1.5 m away from the wave-maker in the experiment to record the water elevation as a function of time. A good agreement concerning both water elevation and the motion in time has been obtained between computation and measurement. Figure 3.31 compares the water elevation as a function of time at the probe position. The measured and computed horizontal, vertical and angular displacements of the body are compared in Fig. 3.32, Fig. 3.33 and Fig. 3.34 respectively.

The movement of the body is recorded by a digital video-camera saving 60 single frames per second. Each frame has the resolution of 320x240 pixel. The camera is set up so that 10 cm width of the body is represented by 80 pixel approximately. The body motion is then reconstructed from these frames and the assumed time spans between them. Uncertainty can appear here in the representation of the body motion, such as deviation of the time span from 1/60 second between two successive frames and the counting error of pixel. The agreement is however satisfactory except at the initial stage, where small disturbances may exist in the experiment. As can be seen, the horizontal and vertical motion are basically reproduced in the computation and the differences in the amplitude of the angular displacement become smaller as expected. It is noted that the computation generally overpredicts the body motion, especially the angular motion, which is attributed to neglecting 3D effects in the computation.

3.4.2 Mid-Ship Section with and without Bilge Keels in Waves

The amplitude of ships' roll motion in waves is of great concern in terms of ship safety. Often bilge keels are arranged to reduce the roll motion. In this section, a free-floating mid-ship section is investigated in waves with or without bilge keels to study the effects of the keels on roll-damping. The mid-ship section has the dimensions of 10 cm in width and 6 cm in height. The lower corners of the section are rounded with a radius of 2 cm. Two keels of 2 cm are added to the rounded-corners for the variation with keels inclined at 45° relative to the vertical axis of the section. The body has an average density of 665.4 kg/m^3 and is

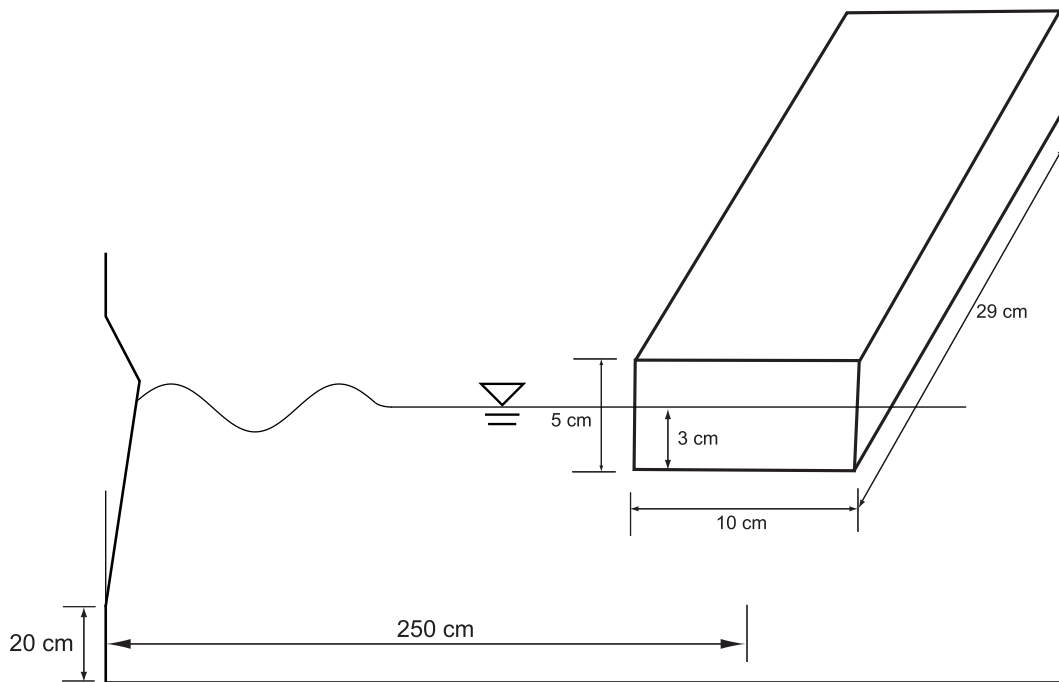


Figure 3.30: Set-up of the free-floating motion experiment.

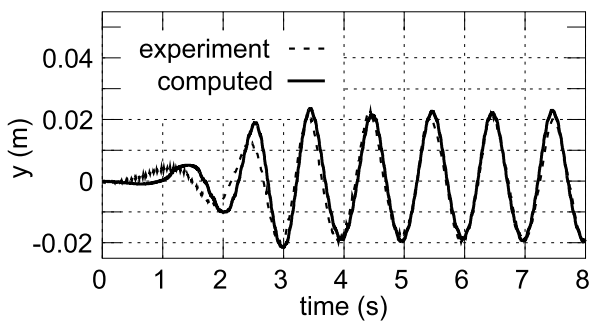


Figure 3.31: Time history of wave elevation at 1.5 m away from the wave-maker (free-floating motion).

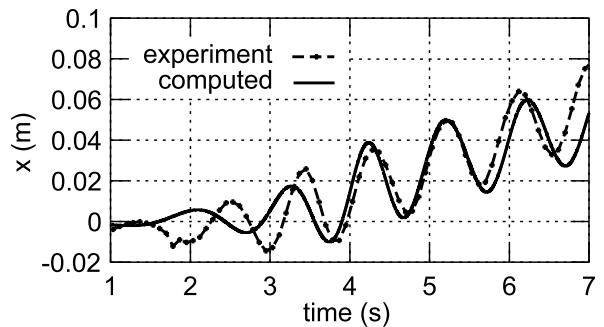


Figure 3.32: Time history of horizontal displacement of the body in waves (free-floating motion).

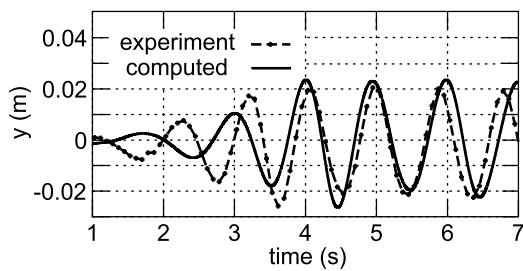


Figure 3.33: Time history of vertical displacement of the body in waves (free-floating motion).

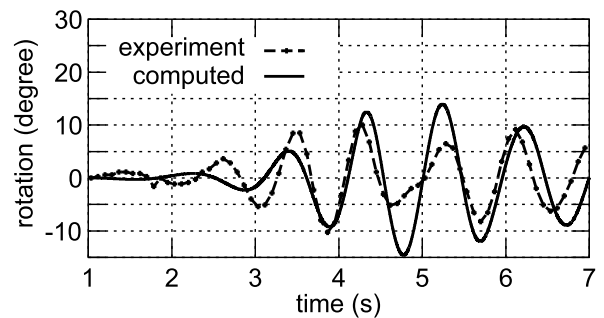


Figure 3.34: Time history of angular displacement of the body in waves (free-floating motion).

initially located at 2.4 m away from the wave-maker with no forward speed. Regular waves of 0.025 m amplitude and 0.7 s period are generated. Unfortunately no experimental data is available to validate the computational results for this test case.

Figure 3.35 shows the computed free surface deformation and the body position at $t = 6.0$ s for the cases without and with keels. It can be seen that the body without keels has experienced a large rotation (roll motion), while the body with keels has rolled only very slightly. The time histories of the horizontal, vertical and angular displacements for the section with and without keels are compared in Fig. 3.36, 3.37 and 3.38, respectively. As can be seen in Fig. 3.38, the amplitude of the roll motion for the section with keels is only 5° compared to the 25° for the section without keels, i.e. the rotation of the section with keels has been damped significantly by the keels. The velocity field around one keel is shown in Fig. 3.39 at $t = 8.0$ s. As can be observed, strong vortices have been produced due to the existence of keels, which are directly responsible for the roll-damping effect of the keel. From another point of view, the roll-damping effect of keels can also be interpreted as transferring the kinetic energy from the roll motion into the translation motion, as can be seen from Fig. 3.36, where the section with keels has drifted more than twice as much in the wave propagation direction as the one without keels.

3.4.3 Interaction of Two Floating-Bodies in Waves

Besides the behavior of a single body in waves, it is often of interest in practice that the interaction of two or more adjacent bodies in waves can be considered, e.g. a cargo ship and a barge during their loading or unloading processes. Therefore another test case is set up to study the free-floating motion of two adjacent bodies in regular waves. The generated wave has an amplitude of 0.025 m and a period of 0.7 s. The two bodies have the same rectangular cross sections of 10 cm in width and 6 cm in height and the density is half of the water density. The two bodies are initially located in still water with a distance of 25 cm from each other and are at rest at their equilibrium position, as shown in Fig. 3.40. Waves are generated and travel towards the two bodies. When the bodies are subjected to the incoming waves, they tend to move closer to each other, as shown in Fig. 3.41. This is also seen in the time histories of the computed horizontal distance between the two bodies, shown in Fig. 3.42. The horizontal, vertical and angular displacements of each body are given in Fig. 3.43, 3.44 and 3.45.

In this test case, the moving-grid method has been employed as shown in Fig. 3.46 for two selected time instants. The computation must be interrupted when the two bodies get too close to each other due to grid restriction; over-lapping grid would be a good alternative to study such collision problems.

3.5 Motion of a Rectangular Cylinder under Wave Packages

So far investigations have been restricted to the interaction between floating bodies and regular waves. To demonstrate the general applicability of the numerical method, studies on

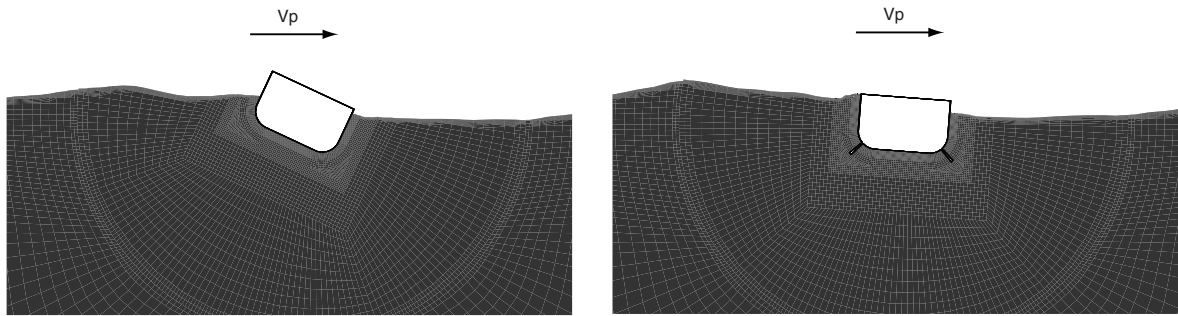


Figure 3.35: Free surface deformation and the position of the 2D mid-ship section at $t = 6.0$ s: without keels (left) and with keels (right).

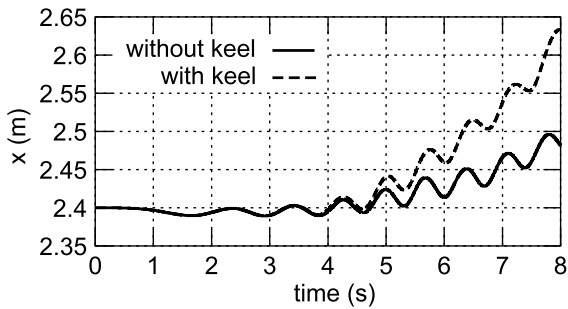


Figure 3.36: Horizontal displacement of the free-floating 2D mid-ship section with and without keels.

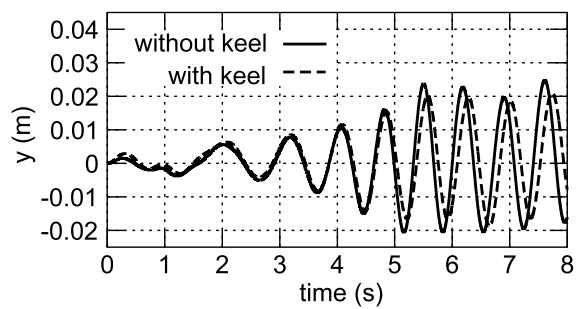


Figure 3.37: Vertical displacement of the free-floating 2D mid-ship section with and without keels.

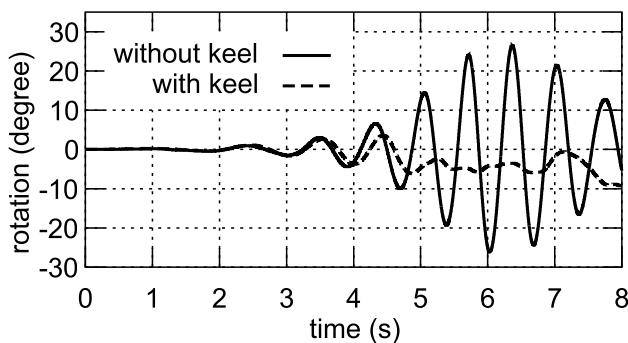


Figure 3.38: Comparison on the angular displacement of the free-floating 2D mid-ship section with and without keels.

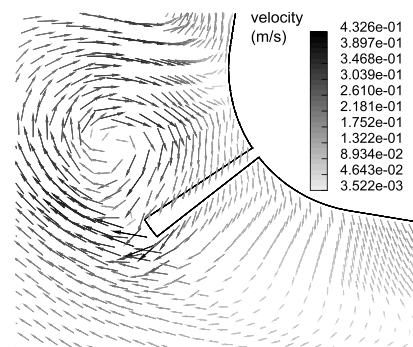


Figure 3.39: Velocity vector profile around one keel at $t = 8.0$ s.

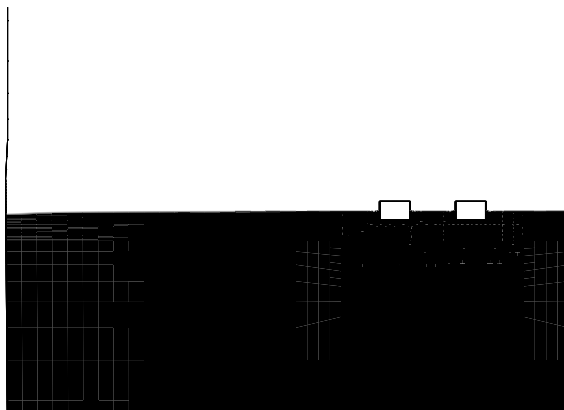


Figure 3.40: Initial state of free surface around two floating bodies.

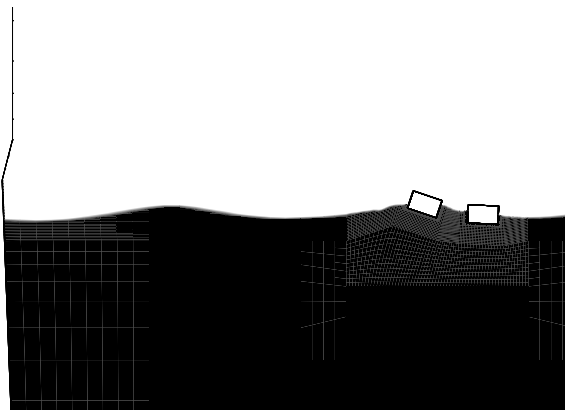


Figure 3.41: Free surface deformation around two floating bodies at $t = 3.8$ s.

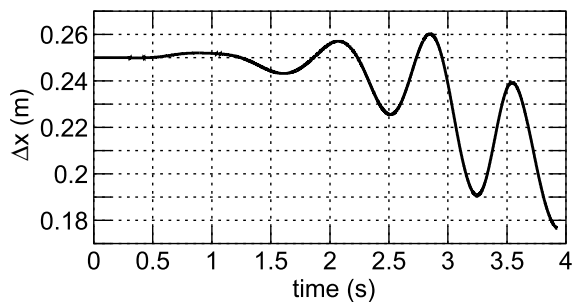


Figure 3.42: Time history of horizontal distance between two floating bodies.

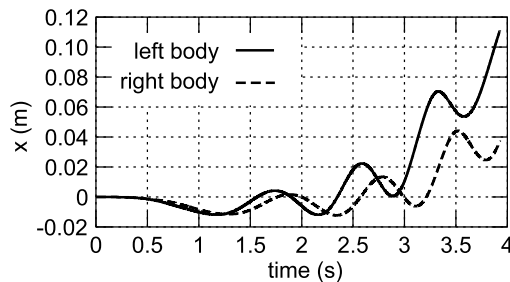


Figure 3.43: Time history of horizontal displacement of each floating body.

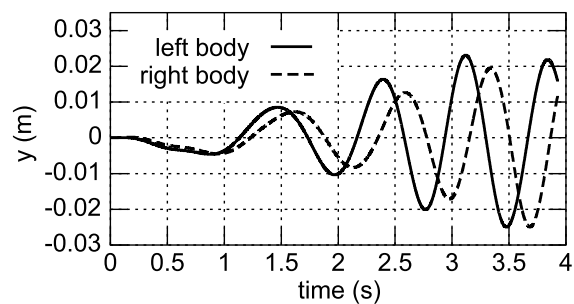


Figure 3.44: Time history of vertical displacement of each floating body.

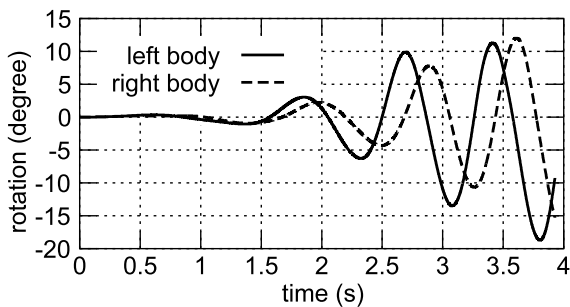


Figure 3.45: Time history of angular displacement of each floating body.

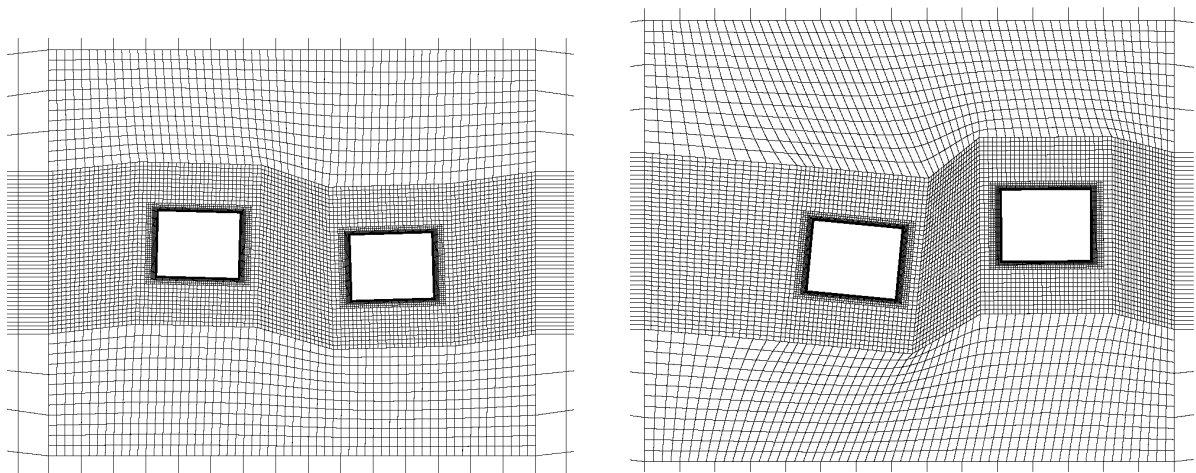


Figure 3.46: The grid around two floating bodies at two selected time instants.

the interaction between body and irregular waves are carried out in this section. The second order CD and the ITTL time integration scheme are applied for the computations if not mentioned specifically.

Experiments for validation purpose are conducted in a wave tank at the Technical University of Berlin, where the motion of the flapping wave-maker is controlled by a pre-defined computer-program so that in principle random wave packages can be generated, see Claus and Kühnlein [18]. The wave tank has the dimensions of 12.0 m in length, 0.3 m in width and 0.4 m in water depth. Both non-concentrating and concentrating wave packages are generated: The former travel in the wave tank with a constant wave profile and speed and the later concentrate at a predefined position to reach a maximum wave height by a combination of wave components of different speed and amplitude. Two probes at $x = 1.16$ m and $x = 2.66$ m (x is the distance from the wave-maker) are set up to measure the water elevation as a function of time. The same rectangular cylinder made of aluminum plates with 10 x 5 cm cross section and 29 cm length, see section 3.4.1, is positioned initially still at $x = 2.11$ m. A digital video-camera has been used to record the body motion in time domain. The water elevations are first measured without the disturbance of the body in the tank to examine whether the concentrating position coincides with the expected one. Furthermore they are used to validate the waves generated by simulating the flapping wave-maker in the numerical water tank so that the numerical errors produced in wave generation and in body motion prediction can be distinguished from each other.

3.5.1 Motion under Non-Concentrating Wave Packages

A two-dimensional numerical water tank has been set up with 8 m in length and 2 m in height, in which water depth is 0.4 m and air height is 1.6 m (the upper boundary is located high to minimize the air flow effect). Relatively fine grids are distributed in the region of free surface and the first 3 m of the tank. Successively coarsened grids as well as UDS are again applied in the air and in the numerical beach to damp the waves and avoid reflection.

To estimate the accuracy of the numerical results, three sets of grids have been generated. The finer grids are obtained by halving the coarser grid spacing in all directions of

space as well as in time so that the coarse grid has 1594 cells and the medium and fine grids have 6248 and 24992 cells, respectively. An example of the adapted grid around the body from the medium grid can be seen in Fig. 2.7. Cells in the free surface region have a spacing of $\Delta x = 1.5$ cm and $\Delta y = 0.5$ cm. The time step size is set to $\Delta t = 0.01$ s, 0.005 s and 0.0025 s for these three grids respectively. The moving-grid method, already described in section 2.5.2, is applied here to realize flapping motion of the wave-maker as well as the body motion.

Figure 3.47 shows the comparison of time histories of water elevation at two probes between measurement and results obtained from three grids. As can be seen, the coarse grid is insufficient to predict accurately free surface deformation, especially at the second probe where phase shifting appears. The phase has been well predicted by the medium and fine grids while the wave height has been over-predicted, which is quite surprising since the numerical diffusion tends to damp the wave height, as can be found in many publications. The numerical damping can also be seen here by comparing the results between medium and fine grids. It is assumed that the flapping wave-maker motion/amplitude was not exactly the same in the experiment and in the simulation; for the latter, the signal from the software, Clauss and Kühnlein [18], driving the wave-maker was used as the boundary condition, since the actual flap motion was not measured. This assumption is also valid for the next application, where wave height has again been over-predicted by the numerical prediction for a concentrating wave packages in the same water tank. Note that the results from the medium and fine grids almost coincide with each other, indicating that a further refinement would hardly produce any difference in the results and the medium grid with 6248 cells is sufficient for this application.

The computed body motions using three grids are compared with the measurement in Fig. 3.48. Again, the results from the coarse grid differ significantly from the ones from the medium and fine grids in both phase and amplitude and the latter two results are very close to each other. The over-predicted amplitude of motion is the consequence of the over-predicted wave height. In all three motions, a phase difference can be observed between computation and measurement, which however does not exist in the predicted water elevation. It indicates that the time span between two successive frames of the digital video-camera is not exactly equal to the assumed value of 1/60 second. Taking into account the uncertainty in the experiment, the numerical method has exhibited its ability in predicting both the wave profile and the body motion.

3.5.2 Extreme Motion under Concentrating Wave Packages

Large amplitude wave packages are now generated in the water tank (with or without body). The medium grid from the last section has been used here. Also the numerical parameters and schemes are applied here same as in the last section. As stated before, the flap motion is derived from a mathematical model to generate waves which concentrate and reach a large amplitude at a prescribed position ($x = 2.11$ m in this case), Clauss and Kühnlein [18].

Wave packages are generated in the numerical tank by simulating the flapping motion of the wave-maker in the experiment. Figure 3.49 gives the time function of the rotational angle of the wake-maker. The computed water elevations at the positions of two measuring probes

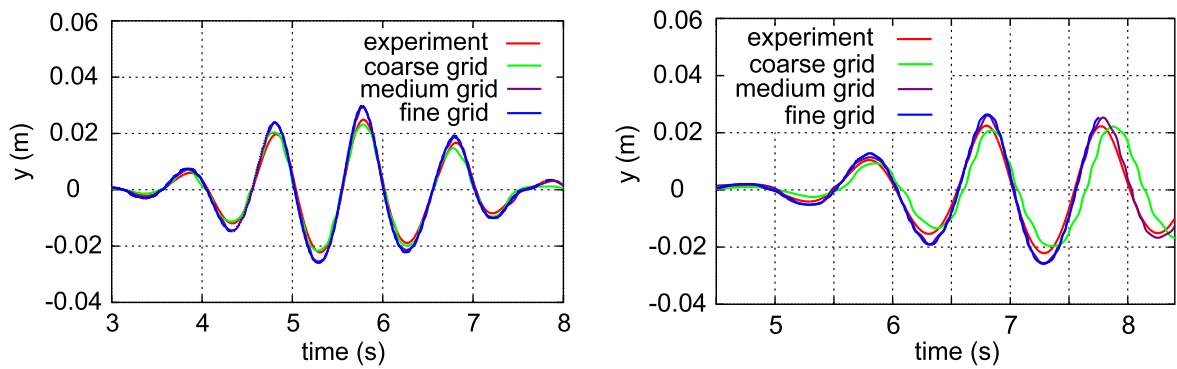


Figure 3.47: Time history of water elevation at two probes: $x = 1.16$ m (left) and $x = 2.66$ m (right).

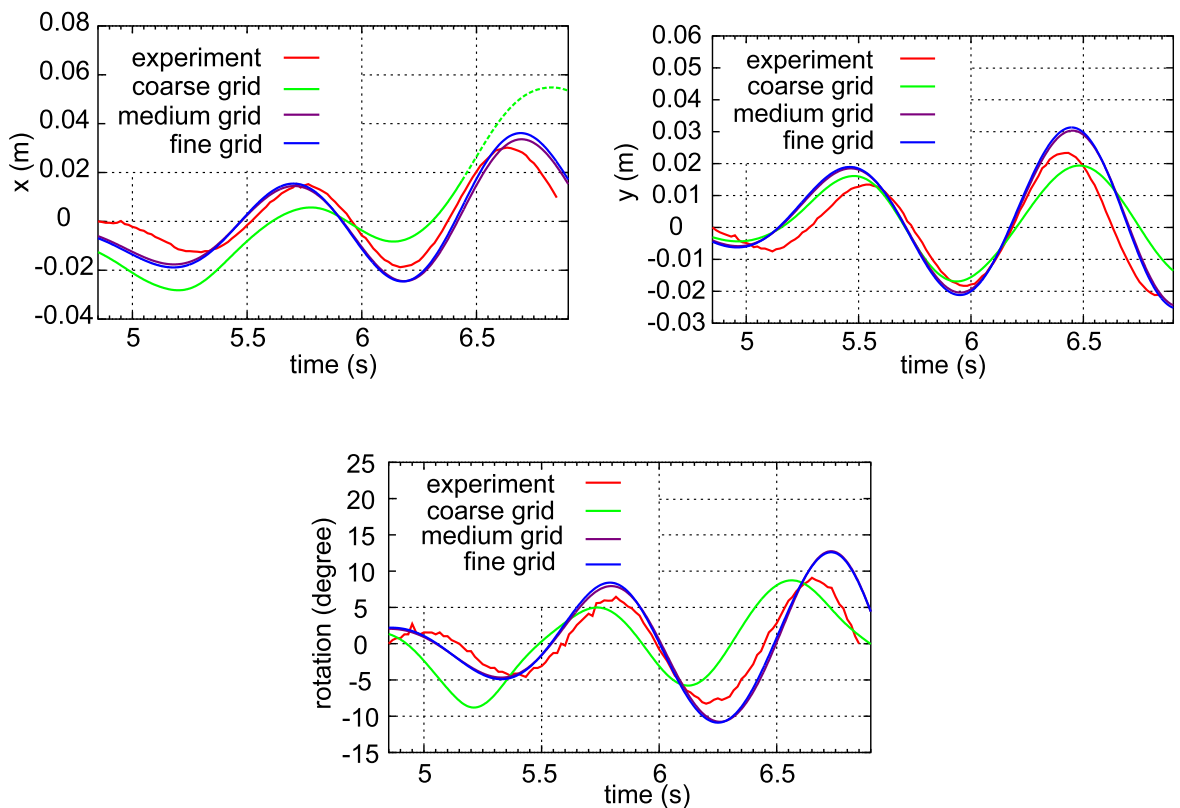


Figure 3.48: Comparison on body motion between experiment and computation: horizontal (left), vertical (right) and angular displacement (bottom).

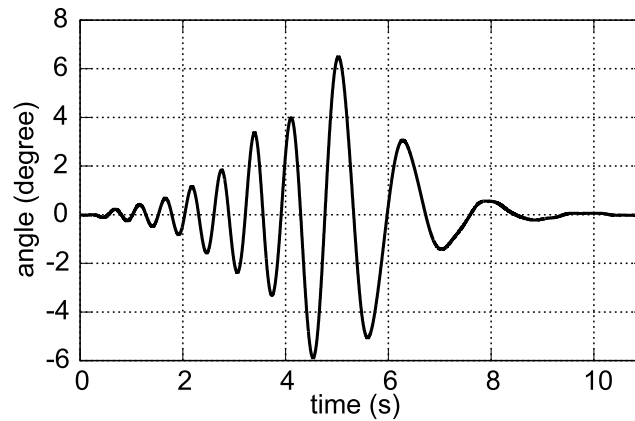


Figure 3.49: Time history of the angle of the wave-maker.

are compared with the experiment against time, see Fig. 3.50. A very good agreement is obtained concerning both the amplitude and the phase. The slight over-prediction of the wave amplitude reflects again the small difference of the boundary condition between computation and experiment, as explained before.

An overview of the water elevation, position of the floating body and the flapping wave-maker can be observed in Fig. 3.51 at four successive time instants. Time is set to zero when the wave-making flap starts. As can be seen, waves traveling with different speed are generated and become very steep (almost breaking) until the maximum amplitude is reached at the position where the body is. When the concentrated wave packages reach the body, the body is subjected to a large impact which results in extreme motion of the body. Also it is observed in both experiment and computation that water is splashed on top of the body and air bubbles are trapped in the water in front of the body.

The body motion under the load of wave packages is compared between computation and experiment in Fig. 3.52. The experimental data has been deduced from digital images as explained before. The uncertainty is around 5% in translation and 9% for rotation and the time span between images appears larger than assumed. The agreement between simulation and experiment is quite satisfactory for all three degrees of freedom, despite of the uncertainty in reconstructing the body motion from digital images. Note that the body is 5 cm high and the amplitude of its vertical motion is 4 cm. And the maximum rotations of about -25° and $+20^\circ$ are observed in both experiment and simulation. Figure 3.53 compares a close-up view on the extreme body position and the free surface deformation between computation and experiment at two time instants $t = 7.20$ s and 7.54 s. Additional information can be obtained from the computation, such as the velocity field in water and air as plotted in Fig. 3.53.

Using overlapping grid method

As already mentioned in section 2.5.1, the overlapping grid method has the advantage that it poses no restriction on any large motion of the body and therefore is attractive for studying the extreme motions. As an alternative, the overlapping grid method is examined here using the test case in this section and the result is compared to the one conducted by the moving-grid method in a single domain as presented above.

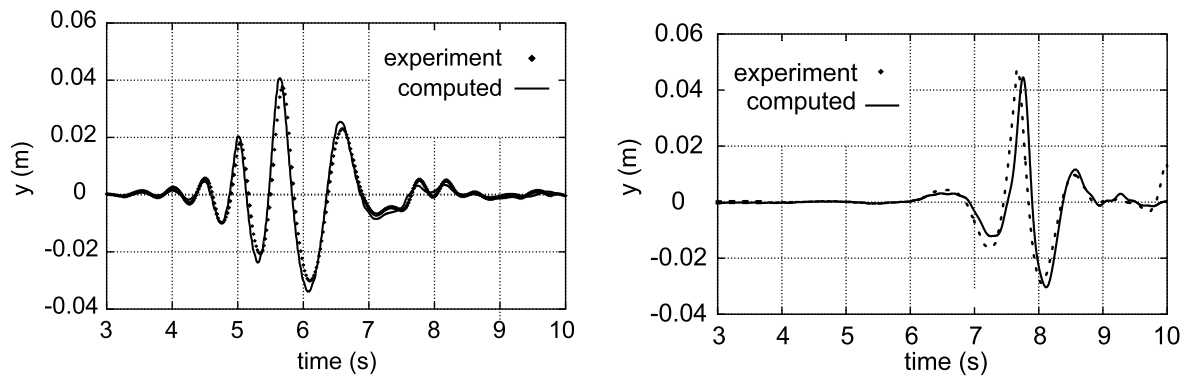


Figure 3.50: Time history of water elevation at two probes: $x = 1.65$ m (left) and $x = 2.66$ m (right)

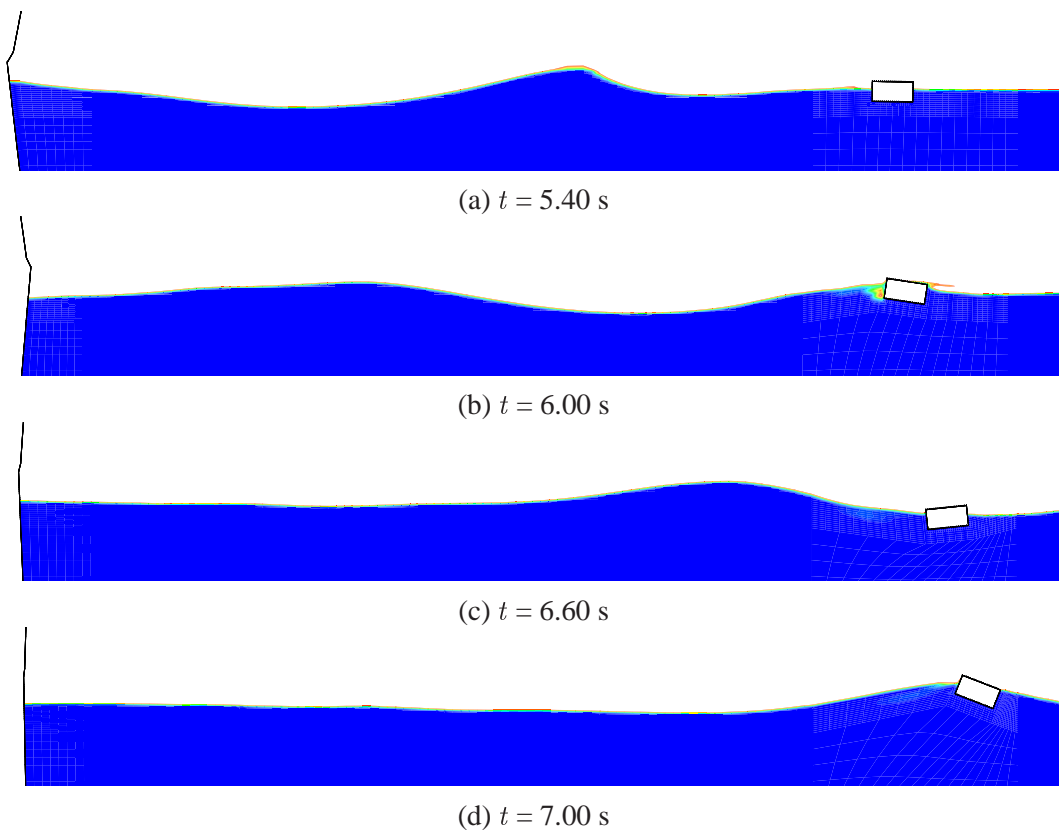


Figure 3.51: Free-surface deformation and position of the wave-maker and the floating body at four successive time instants.

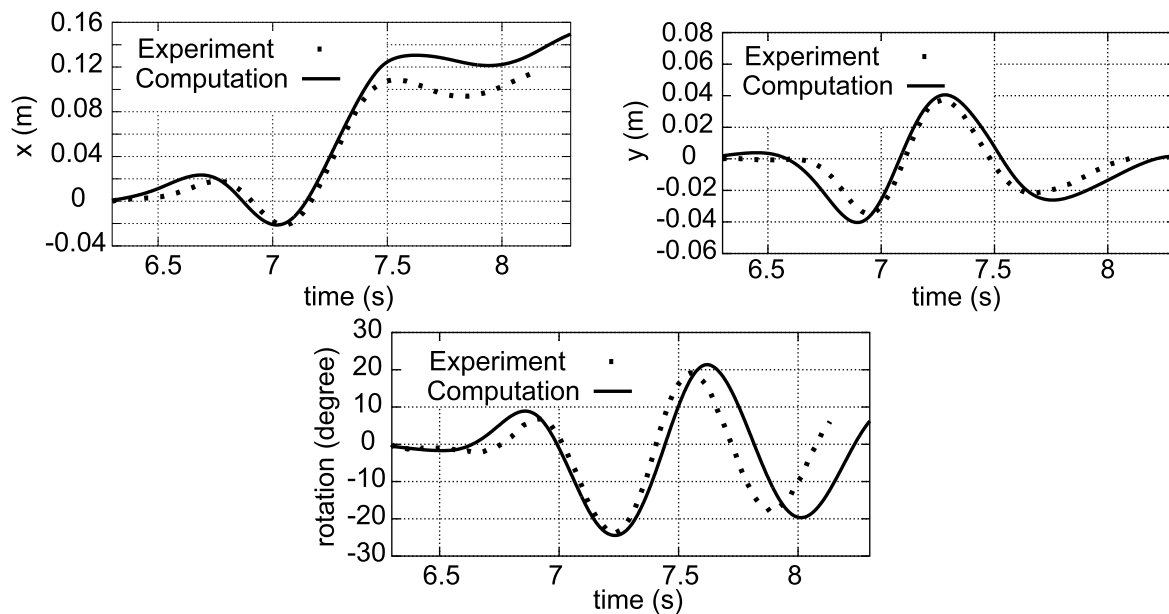


Figure 3.52: Comparison on body motion between experiment and computation: horizontal (left), vertical (right) and angular displacement (bottom).

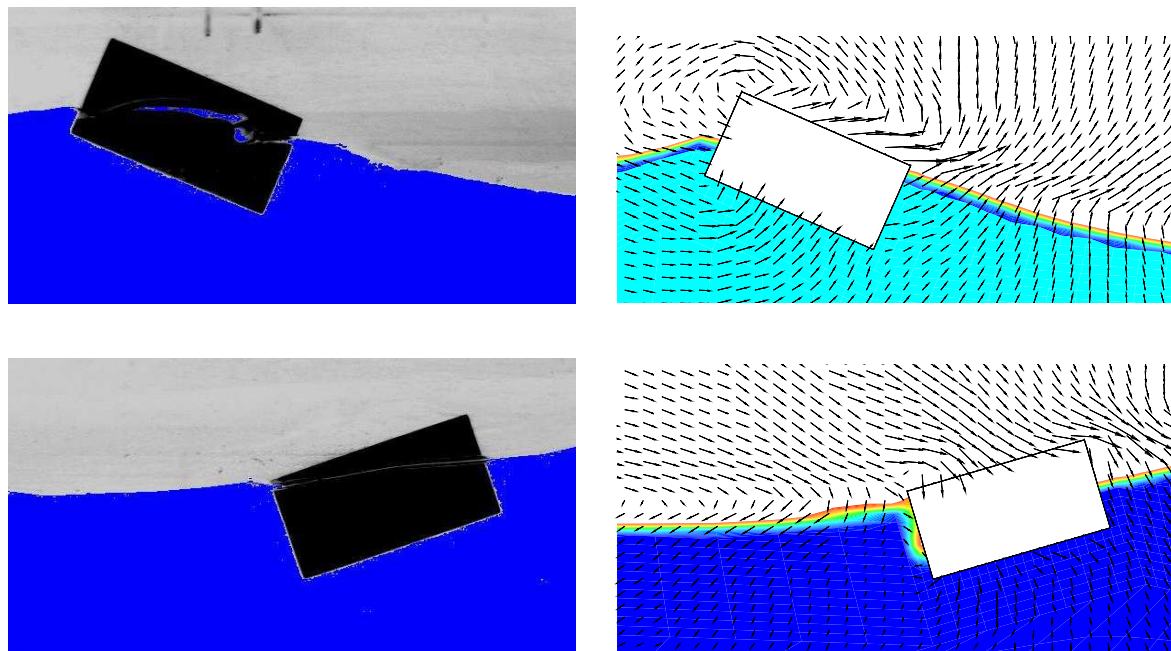


Figure 3.53: Free-surface shape and body position as observed in the experiment (left) and the computation (right) at $t = 7.2$ s (top) and $t = 7.54$ s (bottom).

The weak-coupling method has been used here which means the computational domain is separated into two parts: foreground and background domain, which are solved separately (two sets of systems of equations) and only connected by exchanging data through boundary conditions. The two separated domains are partially overlapped so that the values for the intermediate boundaries of the foreground domain can be interpolated from the solution of the background domain and vice versa. Linear interpolation has been used here. Figure 2.6 gives the example of such a grid used in this test case. Either inlet or pressure boundary condition is specified at these intermediate boundaries. In this case, a pressure condition has been specified at the upper boundary, inlet conditions have been specified at the other three boundaries. To enhance a unique solution in the overlapping region and satisfy the mass conservation, certain correction is necessary after the interpolation process. A detailed description of such overlapping-grid methods can be found in several publications, see Klemt [43] and Petersson [68] for recent works, and therefore will not be given here.

The computed body motion under the large amplitude wave package using overlapping grids is compared with the experiments as well as with the results using the moving-grid method in Fig. 3.54. The agreement is quite satisfactory in all three degrees of freedom. As can be seen, the difference between computations using these two methods is rather small indicating the error induced by the interpolation process and the intermediate boundaries is relatively small. Figures 3.55 and 3.56 show the free surface deformation, body position and pressure field together with the overlapped foreground and background grids. As can be seen, slight discontinuity of the free surface position can be found in the overlapping region, which is not surprising since the interpolation process only ensures the consistency of the solution at the intermediate boundary (if the interpolation error is negligible) but not necessarily in the whole overlapped region. Forming a consistent solution in the overlapped region is indeed difficult in this method. For a better consistency, a strong-coupling overlapping grid method should be used.

The computational time using the overlapping grid method has increased by a factor of 1.3 for this test case compared to the moving-grid method in a single domain, which is caused by not only the increased number of cells (cells doubled in the overlapping region) but also the searching algorithm and the interpolation process between the foreground and the background grids. This factor becomes larger for 3D applications since the searching algorithm and the interpolation process become much more computationally intensive. The computational time can also be increased dramatically when the computation is parallelized on computers with coarse granularity and a large amount of information concerning grid coordinates and variables between processors has to be exchanged at every outer-iteration/time step. For further 3D applications in this work, the moving-grid method is applied to avoid too large computational effort and to achieve a good balance between accuracy and efficiency.

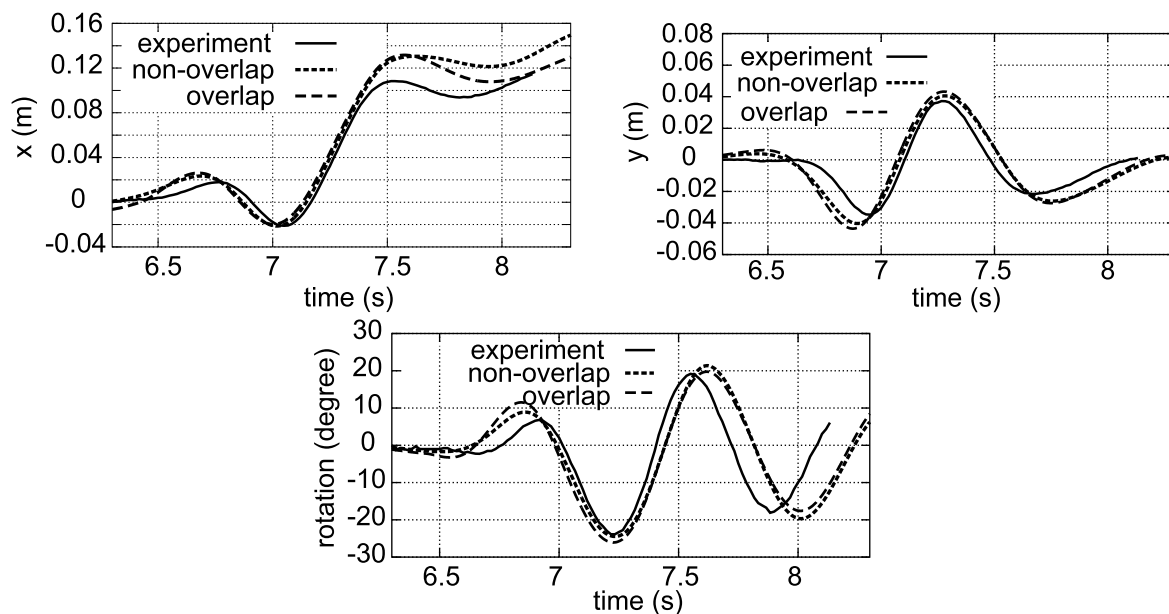


Figure 3.54: Comparison on body motion between experiment and computations using one-domain and overlapping grids: horizontal (left), vertical (right) and angular (bottom) displacement.

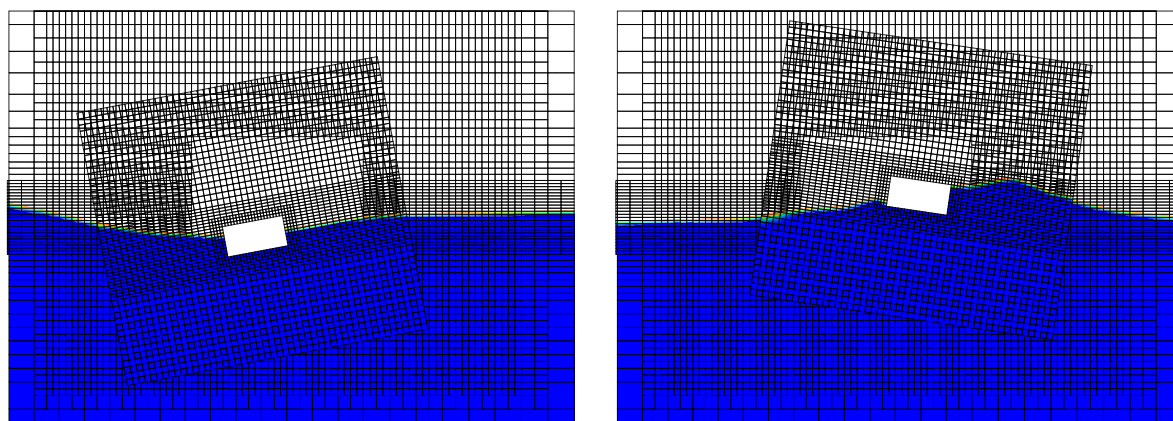


Figure 3.55: Free-surface deformation, body position and overlapping grids at $t = 6.8$ s (left) and at $t = 7.4$ s (right).

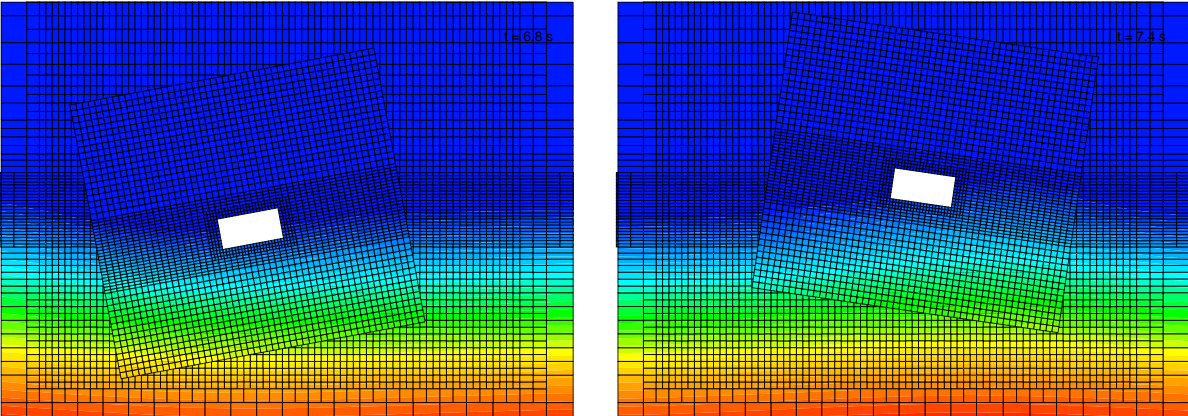


Figure 3.56: Pressure field and overlapping grids at $t = 6.8 \text{ s}$ (left) and at $t = 7.4 \text{ s}$ (right).

Chapter 4

Applications to Ship Motion in Waves

4.1 Introduction

In practice, ship motions in waves are either predicted using experiments or numerical methods based on the potential theory, which assumes an irrotational flow of ideal fluid. Motions and waves are mostly linearized (strip method or panel method), or potential flow computations with linearized boundary conditions are combined with non-linear simulations of motions. An overview of the variety of methods can be found in Bertram [11]. These methods are considered as fast and robust tools in the design stage because they allow a large number of variants to be analyzed for the purpose of optimization. They are applicable to the assessment of statistical quantities, which can be the only final result in a natural seaway due to its stochastic nature. The motion of a smooth body in waves can be computed using these methods with reasonably good accuracy (especially when empirical corrections are applied). However, they are not suitable for flows where viscous effects or breaking waves play an important role. Bilge keels, damping tanks, added resistance, maneuvering motions etc. can be dealt within the potential theory only with further empirical corrections, which not only decrease the accuracy of the prediction, but are also sometimes expensive because experimental data and many years of experience are required for such corrections. Strongly nonlinear effects like slamming or green water on deck can then only be dealt with by separate, more sophisticated methods, using results of potential flow calculations as boundary conditions. Computational methods predicting viscous free-surface flows can, however, deal with the aforementioned problems without difficulty, but the computing cost is much higher.

After the present method has been applied to a variety of two-dimensional test cases and validated by either analytical solutions or conducted experiments in the previous chapter, three-dimensional problems such as the dynamic response of an advancing ship in waves are studied in this chapter. The emphasis is on demonstrating the potential of the present numerical method in studying special problems in seakeeping applications to reduce the number of expensive model tests in a towing tank, leading to a more economical design phase. In addition, robustness, flexibility and accuracy of the coupled method are demonstrated here further for 3D problems to make the method straightforward for further complex simulations in ship maneuvering applications, which will be studied in the following chapters.

In this chapter, three application cases will be presented, which are of more relevance

in research than in practice. Nevertheless, they can be not only considered as demonstration cases for evaluating and validating the numerical approach as a practical tool in complex analyses, but are also easily extended to practical applications. These three cases simulate the dynamic response of a ship (without appendages) with constant speed in waves, where the moving-grid method is used to evaluate the varying ship position. A Wigley model is taken first due to its simple geometry. Motions of an advancing Wigley model in regular waves are presented in section 4.2. Section 4.2.1 studies heave and pitch motions for an advancing Wigley model subject to head waves. Roll motion is assumed to be negligible so that the symmetry condition can be applied to reduce the number of grid cells by half. Section 4.2.2 extends the test case to the motion of a Wigley model advancing with constant speed in oblique waves, where roll, pitch and heave motions are considered. The grid is mirrored about the symmetry plane so that twice the number of cells is required for this test case. Oblique waves with an angle of attack of 170° are generated by inlet conditions in front of and beside the ship. The influence of the differencing scheme in space is investigated for the case of a Wigley model in head waves in section 4.2.3. Then, the dynamic response of a RoRo vessel is simulated with forward speed in head waves in section 4.3. The predicted ship motions are compared with measurements from self-propelled model tests, showing good agreement.

4.2 Wigley Model in Waves

4.2.1 Wigley Model in Head Waves

The first coupled, three-dimensional simulation of fluid flow and flow-induced floating-body motion was performed for a Wigley model advancing with constant speed ($F_n = 0.3$, $R_n = 4.85 \cdot 10^6$ at model scale) in head waves. Only pitch and heave motions of the ship were considered. The Wigley model has the standard form: $L:B:D = 10:1:0.625$ and L is chosen as 3.0 m here. The center of mass and the rotation lever for pitch motion are set to $0.3125L$ above the keel and $0.25L$ respectively. The solution domain extended to $1.5L$ in front of and beside the ship and $2L$ behind the ship, in addition to a damping zone at the outlet boundary. The distance from the ship to the bottom of the tank was L . The grid had 44880 finite volume cells and most of the grid cells were located near the ship and the free surface, as can be observed in Fig. 4.1. The grid in the neighborhood of the ship was adapted to the ship motion at each time step while the grid far from the ship was kept fixed all the time. Regular waves were generated by specifying the inlet flow according to the Airy wave theory. The wavelength λ was chosen as $\lambda = L$, the wave height as $h = 0.065\lambda$.

The ship was kept fixed until the wave front approached the bow and then allowed to move with two degrees of freedom. Figure 4.2 shows the computed time histories of ship motions. The large motion at the beginning indicates that the initial position of the ship was not its equilibrium position. After a few periods, periodical motion occurs about its equilibrium position. Figure 4.3 shows wave contours together with the ship positions for four time instants. The wave system due to the ship motion has been strongly damped since the grid is gradually coarsened behind the ship; however, the interaction of the body and the incoming wave systems can be well observed.

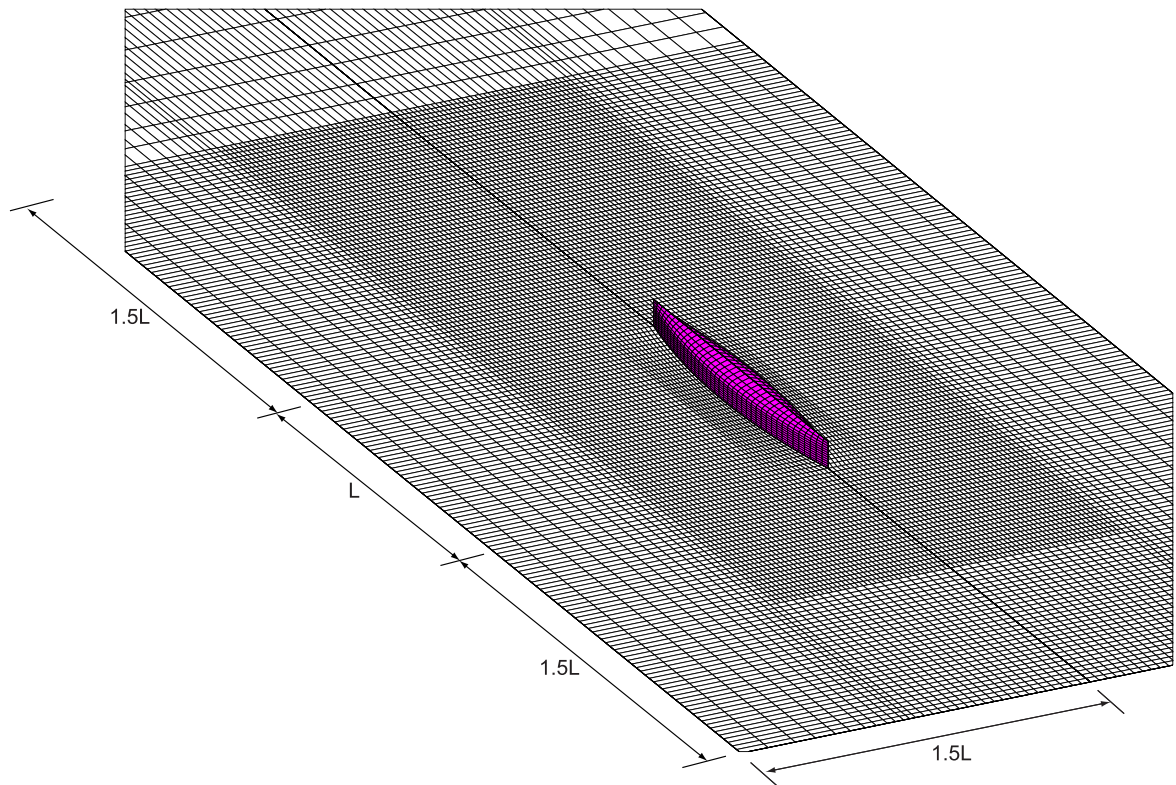


Figure 4.1: Computational grid at the free surface level around the Wigley model (mirrored about the longitudinal plane).

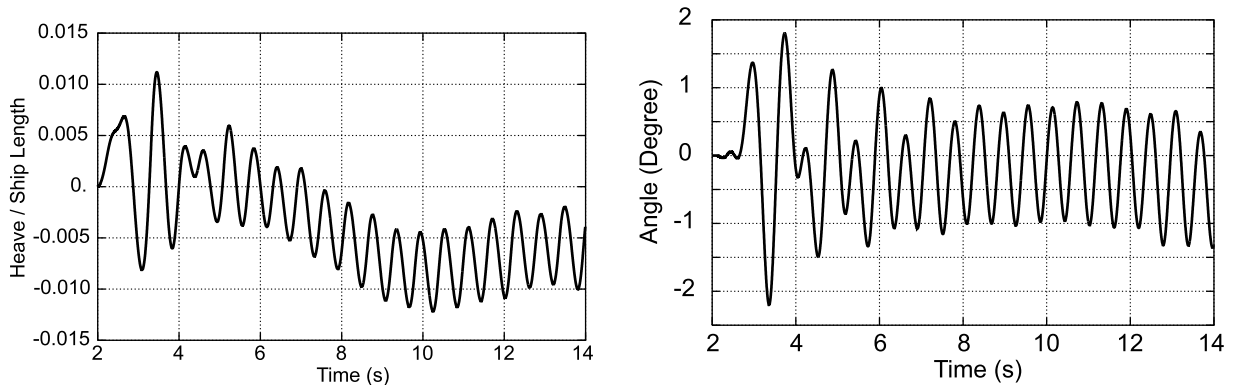


Figure 4.2: Computed time histories of heave (left) and pitch (right) motions of the Wigley model.

4.2.2 Wigley Model in Oblique Waves

Subsequently, the motion of a Wigley model advancing with constant speed ($F_n = 0.18$) in oblique waves was computed. The center of mass is kept the same as in the section 4.2.1 and the rotation levers for roll and pitch motions are set to $0.05L$ and $0.403L$ respectively. Waves were generated by specifying the velocities according to the Airy wave theory at the corresponding inlets (front and side boundaries of the solution domain), see Fig. 4.4. The angle between the direction of wave propagation and the direction of the ship velocity was 170° . The wavelength λ was chosen as $\lambda = L$, the wave height as $h = 0.01\lambda$. To obtain

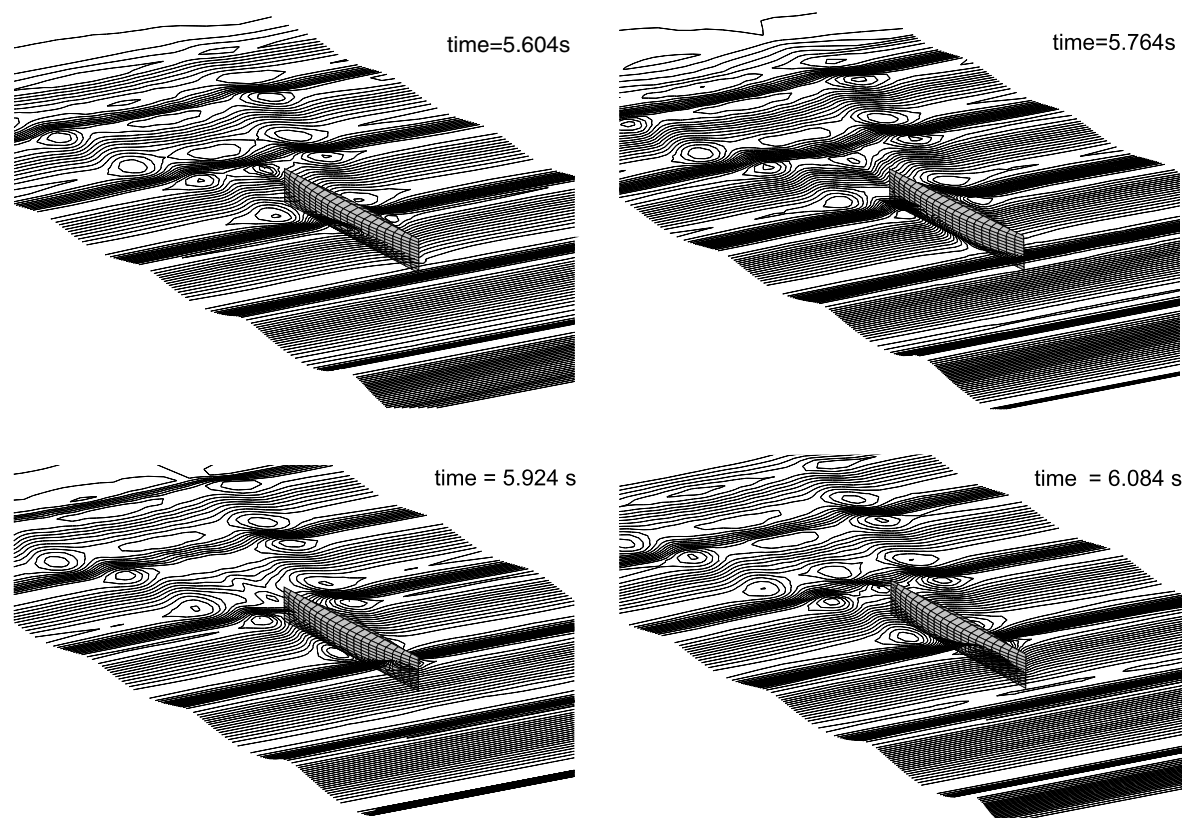


Figure 4.3: Computed wave patterns of the Wigley model in head waves at four selected time instants.

results without the influence of reflection of ship-induced waves at the boundaries for a longer period, the distance between the side boundaries and the ship is enlarged to $2L$. The computational grid had more than twice as many cells as in the former case, since here the asymmetric motion of the ship must be considered: the roll motion is free in addition to the heave and pitch motion. Surge, sway and yaw motions were suppressed, since neither rudder nor propeller was modeled in this case. Figure 4.4 shows the resultant interacting wave system of both the ship-induced and oblique wave systems. Figure 4.5 shows the resulting roll, heave and pitch motions, respectively. These three motions are coupled to each other and the time-averaged roll angle has a negative value under the impact of the oblique waves.

4.2.3 Effect of Differencing Scheme in Space

As mentioned before, differencing schemes in space have an effect on the damping of wave propagation in the numerical water tank. Their effects on both wave propagation and body motion are studied here for the case of a Wigley model advancing in head waves.

The first-order UD and the second-order CD schemes are selected here to show the effects more obviously. The predicted time histories of water elevation at $x = 2.2$ m are compared in Fig. 4.6. The strong damping on the wave amplitude can be observed as expected. The comparison of resulting heave and pitch motions of the Wigley model is given in Fig. 4.7. As can be seen, the UD scheme tends to dampen the ship motion substantially (almost

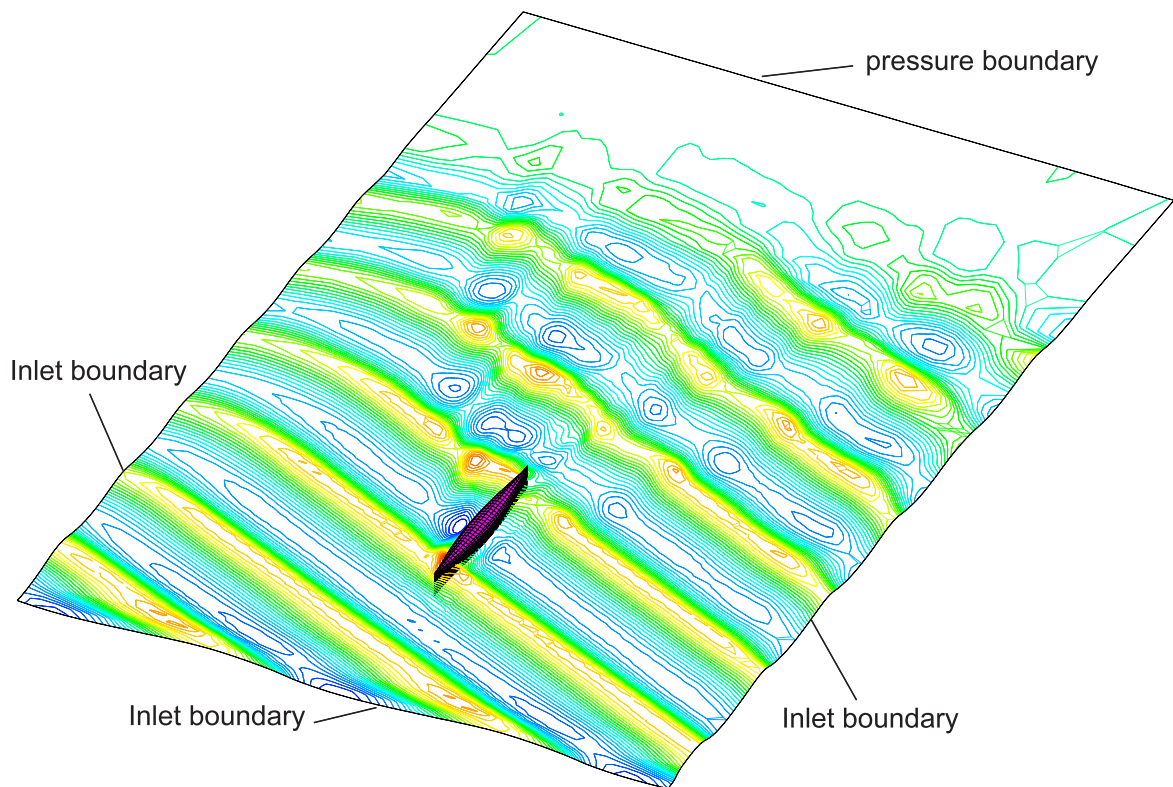


Figure 4.4: Computed wave pattern of the Wigley model in oblique waves (170°).

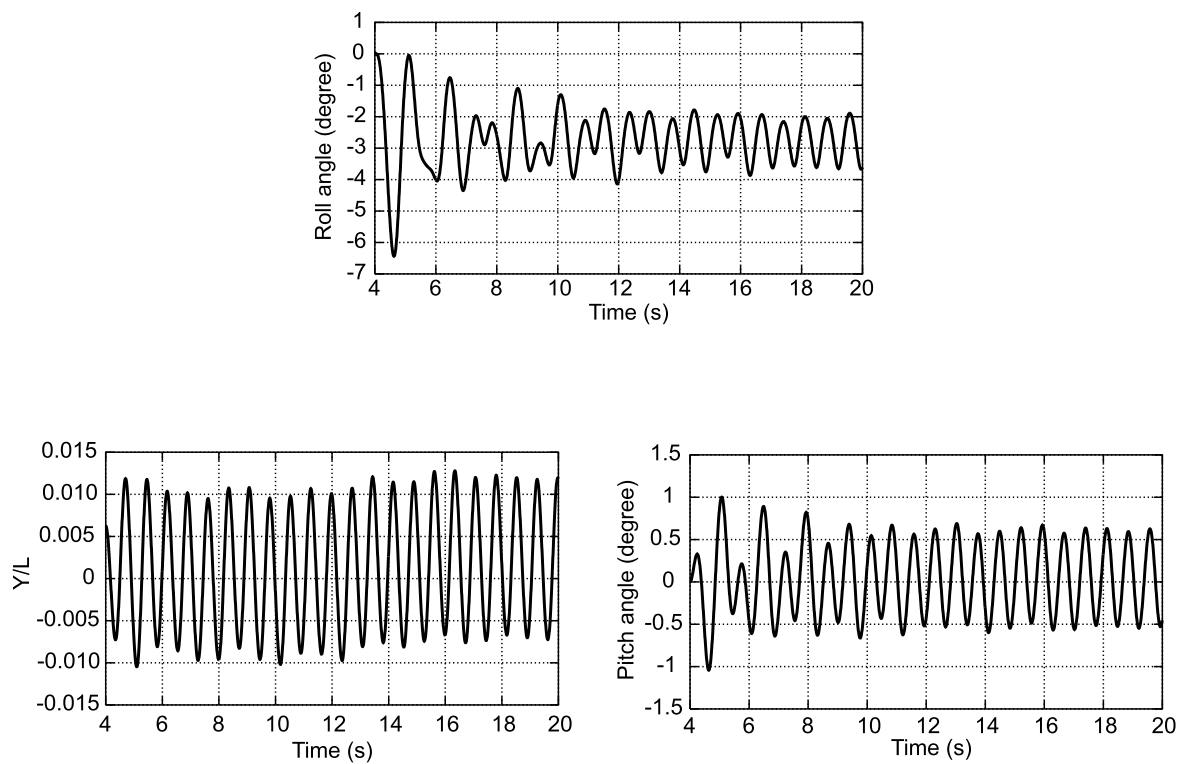


Figure 4.5: Computed time histories of roll (top), heave (left) and pitch (right) motions of the Wigley model in oblique waves (170°).

by half in heave motion) as consequence of wave damping.

The first-order UD scheme should basically not be used unless the spatial discretization is very fine. Normally such a fine grid is neither affordable nor necessary, especially when problems with complex geometry have to be dealt with. The second-order CD scheme allows lower grid resolution and offers higher accuracy but tends to oscillations. So it is often necessary to blend a portion of UD with CD scheme in practice. The optimum blending factor is case/grid-dependent and therefore difficult to find, but one should always use the highest value of CD scheme possible to achieve higher accuracy. The blending factor can be varied locally and higher values of CD scheme ($0.9 \leq \beta \leq 1.0$) can be used if the grid is smooth and well distributed. The issue of the effects of differencing schemes will be discussed again for rudder forces in section 5.2.3.

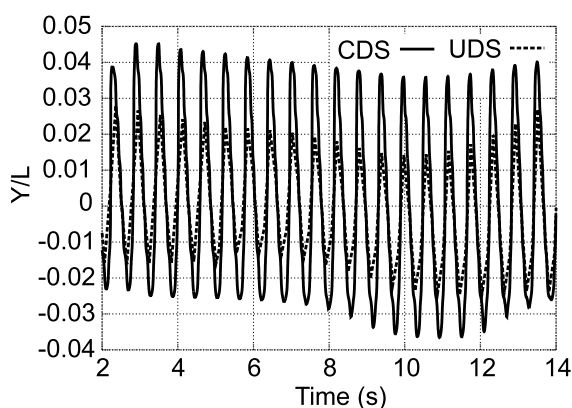


Figure 4.6: Computed time histories of water elevation using UD and CD schemes.

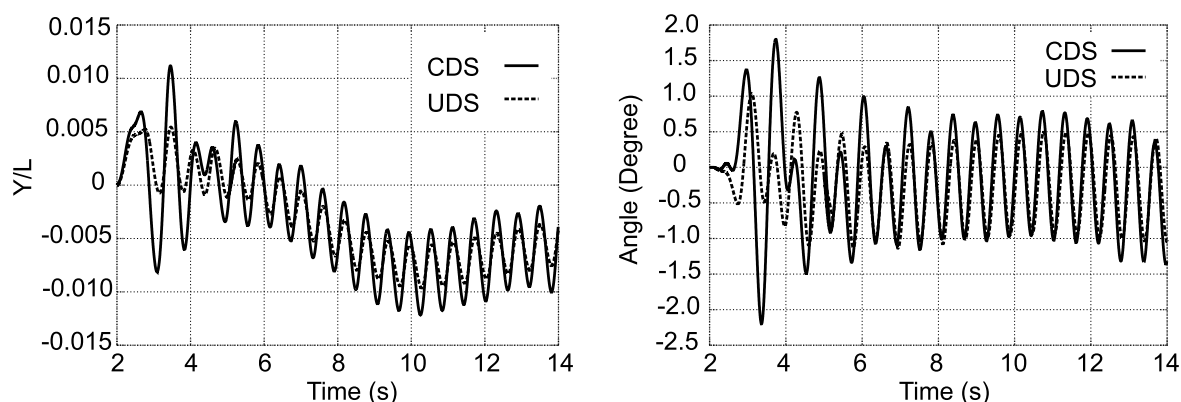


Figure 4.7: Computed time histories of heave (left) and pitch (right) motions of the Wigley ship using UD and CD schemes.

4.3 RoRo Ship Model in Head Waves

The RoRo vessel, designed by Flensburger Schiffbau-Gesellschaft (FSG), was taken as one of the test models in the experiments conducted at the Hamburg Ship Model Basin (HSVA). Parallel to the model tests, corresponding numerical simulations were carried out.

The dimensions of the RoRo ship model are given in Table 4.1. The lines plan for the RoRo ship is given in Appendix D. The ship model has the model scale of $1/34$. The GM of the ship model can be adjusted for different natural roll periods. The test case has been set up with the model running against incoming regular waves (180°) at $F_n = 0.22$. The regular waves generated by a flapping wave maker are of 0.15 m height and 4.0 m length, which is $0.7 L$. The model ship runs with its own propeller and a remotely controlled rudder to keep the designated course.

In the simulation, the constant speed of the ship is imposed, while heave and pitch motions are free. Roll motion has been disabled in the simulation since in this case the ship is running in head waves and the wave frequency is still far from the resonance frequency of the ship for roll motion. Therefore the roll motion is not expected to be significant, as proven in measurements. Regular waves are generated by an inlet boundary with velocities specified according to the Airy wave theory. Small errors could be introduced by the differences of boundary conditions between experiment and simulation. However, exact boundary conditions for such an experiment are always difficult to match and the selected approach lies within the uncertainties of the experiment.

The computation domain extends to $1.3L$ in front of the ship bounded by an inlet boundary with velocities specified, $1.5L$ behind the ship connecting to a $1.5L$ damping zone bounded by a hydrostatic pressure boundary, $1.5L$ at the side of the ship and $1.0L$ in water depth bounded by slip wall boundaries. Only half of the ship was modeled due to symmetry. The grid had 550,000 control volumes. A relatively fine grid and local refinement was used around the ship and the free surface region, see Fig. 4.8 for an overview of the grid at the free surface and the ship hull and Fig. 4.9 for a close view of stern and bow section of the grid. One quarter of all cells were in the vicinity of the ship to resolve the boundary layer and almost half of all cells were around the water surface region to improve the accuracy and sharpness of the free surface. The time step size is set to 0.01 s, corresponding to $1/160$ of the wave period ($T = 1.6$ s).

The ship runs with forward speed in head waves with free heave and pitch motions, as mentioned before. Fig. 4.10 compares time histories of computed heave and pitch motions of the ship with experimental data. The heave motion is non-dimensionalized by the ship length. The numerical results are compared with a corresponding period of time in the experiment. The agreement is quite satisfactory keeping in mind that boundary conditions for wave generation are not the same in the numerical tank and in the experiment.

The wetted-surface and the position of the ship are shown in a series of time instants in Fig. 4.11. The wave crest hits the ship bow at time 9.75 s and it travels along the ship until it reaches the mid-ship at 10.20 s, where the ship bow is approximately at the trough of the wave. The ship is under the condition of positive and negative bending at these situations. Therefore, these two critical time instants are taken for further discussion. Fig. 4.12 shows the wave patterns generated by the RoRo ship at these two time instants. The spread angle of

Table 4.1: Dimensions of the RoRo ship model

L_{pp}	B	T	∇	LCB
5.364 m	0.765 m	0.174 m	0.409 m ³	2.517 m
KM	GM	i_{xx}	i_{yy}	λ
0.393 m	0.0714 m	0.285 m	1.381 m	34

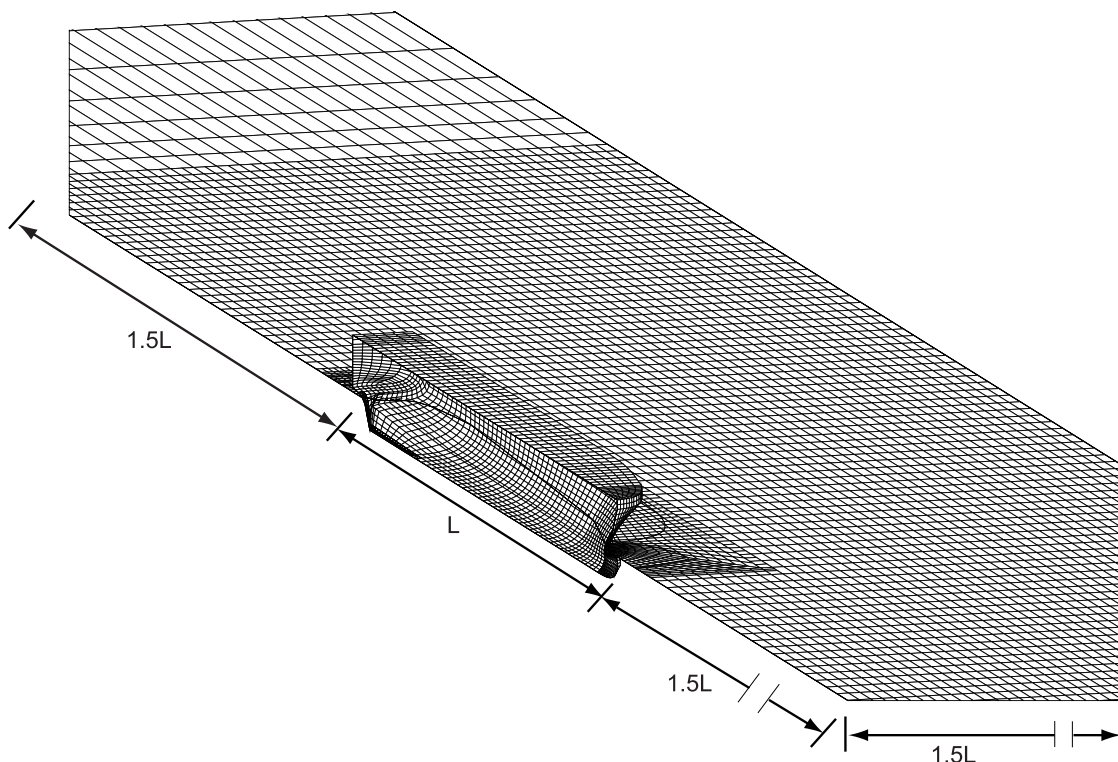


Figure 4.8: Computational grid at the free surface level around the RoRo ship.

the wave crests at the ship bow is about $2 \cdot 19.5^\circ$, which agrees with the analytical prediction of the steady wave system due to forward speed of the ship. This indicates that the computed wave system is actually a superposition of this steady wave system and the unsteady wave system due to incoming waves and resulting ship motion.

Figure 4.13 shows the dynamic pressure distribution on the ship hull at these two time steps and Fig. 4.14 the corresponding shear stress distributions. Higher pressure appears at the bow and the middle part of the ship at these two time instants, respectively. Relatively high pressure can be observed in the ship bow region at 9.75 s, which corresponds to the bow flare slamming and is critical when the wave height increases.

Velocity fields in the longitudinal symmetry plane of the ship are shown in Fig. 4.15. Higher velocity under the wave crest and lower velocity due to the wake of the ship can be recognized.

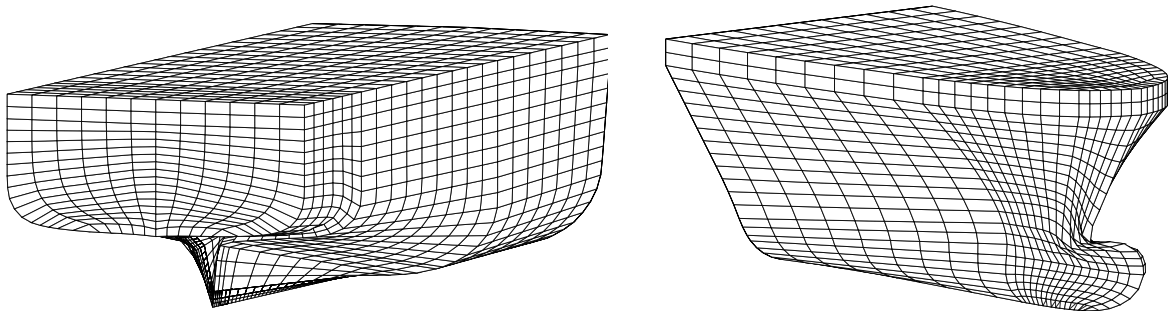


Figure 4.9: RoRo ship grid: viewed from stern (left) and bow (right).

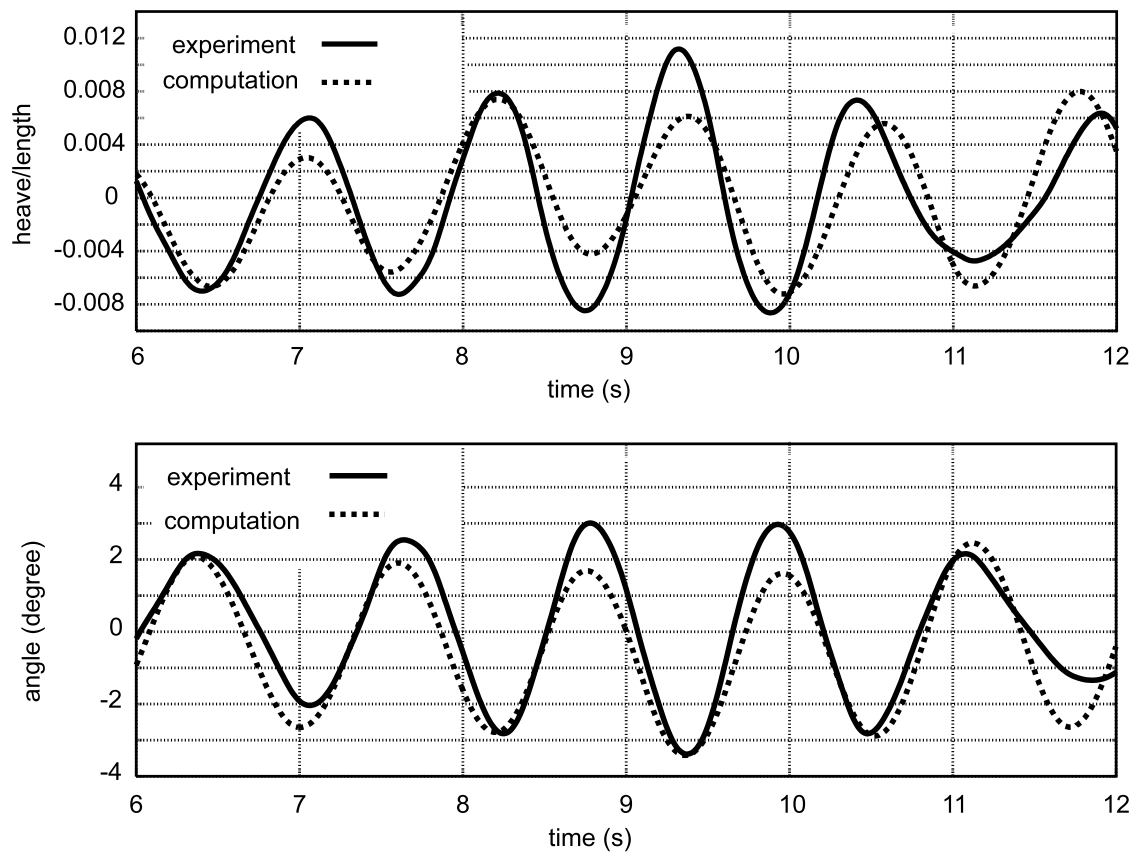


Figure 4.10: Time histories of heave (top) and pitch (bottom) motions of the RoRo ship.



(a) $t = 9.75$ s



(b) $t = 9.90$ s



(c) $t = 10.05$ s



(d) $t = 10.20$ s



(e) $t = 10.35$ s



(f) $t = 10.50$ s



(g) $t = 10.65$ s

Figure 4.11: Wetted-surface and the position of the RoRo ship within one wave period.

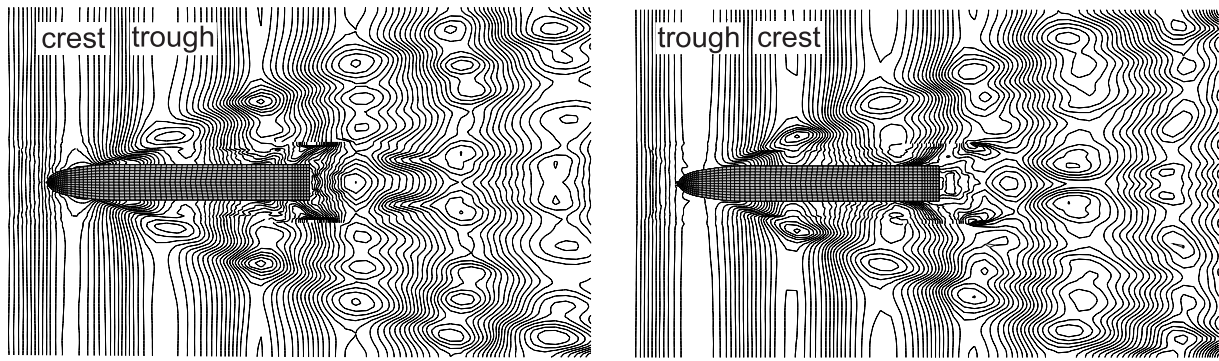


Figure 4.12: Computed wave patterns of the RoRo ship at $t = 9.75$ s (left) and $t = 10.20$ s (right).

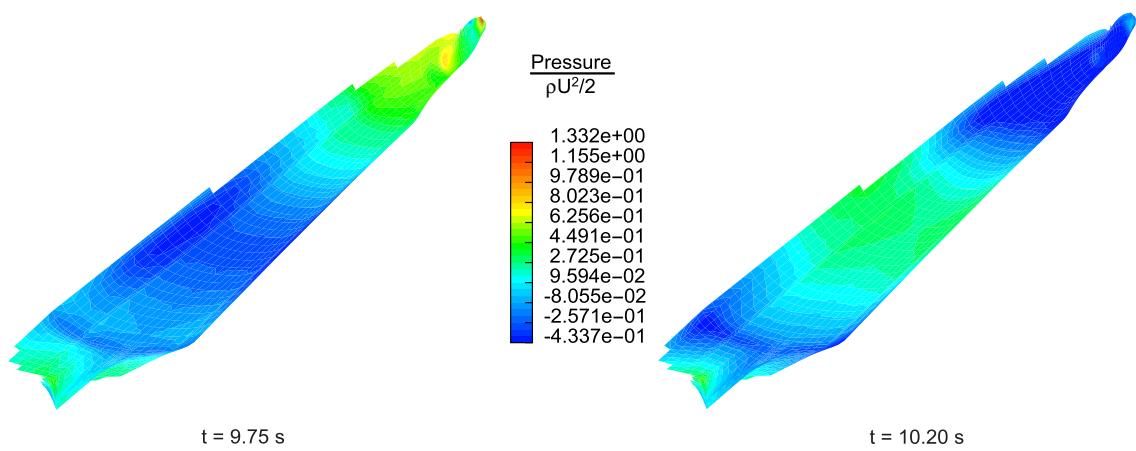


Figure 4.13: Dynamic pressure distribution on the RoRo ship surface at two time instants.

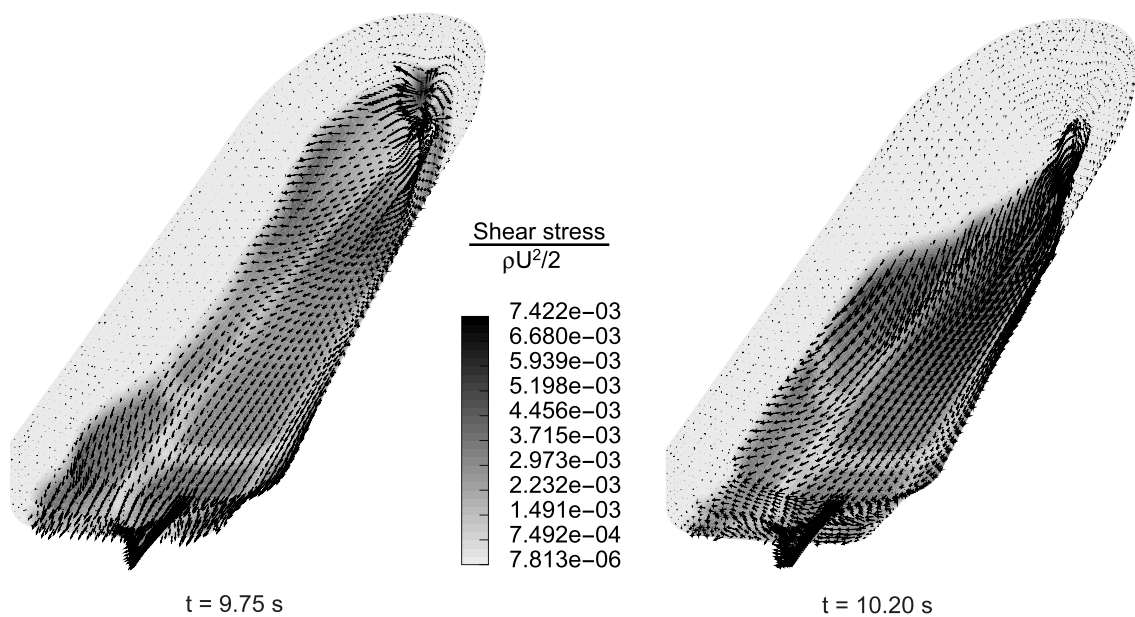


Figure 4.14: Wall shear stress magnitude on the RoRo ship surface at two time instants.

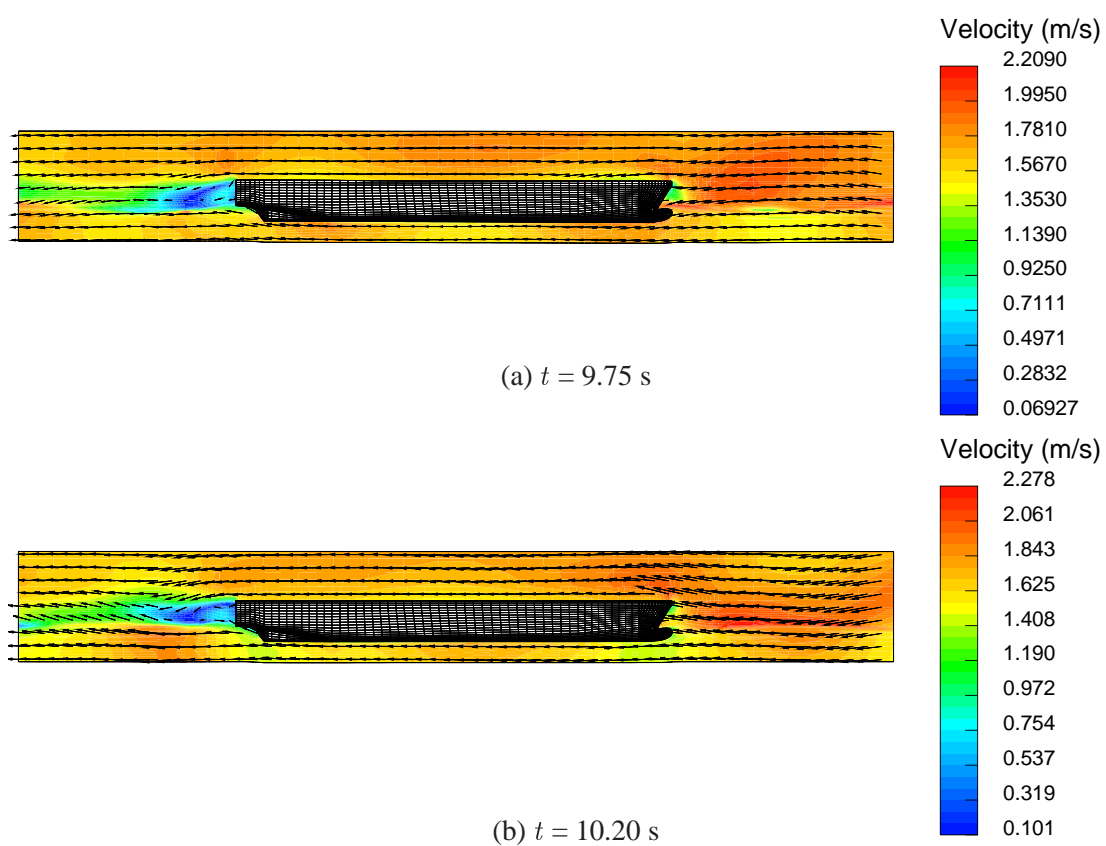


Figure 4.15: Velocity profile in the longitudinal symmetry plane of the RoRo ship.

Chapter 5

Modeling of Rudder, Propeller and their Interaction with Ship

5.1 Introduction

The importance of navigational safety of ships has become much higher nowadays; accordingly the maneuverability of a ship should comply with appropriate maneuverability standards. As recommended by IMO, an accurate estimation of a ship's maneuvering ability at the design stage is essential to meet these requirements.

At present, the property of a newly-designed ship is mainly predicted by three means:

- making use of data obtained from sea trials of similarly-shaped ships.
- performing model tests.
- simulating the maneuvering performance of ships by some mathematical/numerical models.

However, the first often lacks reliability and the second always consumes excessive time and costs. The accuracy of the third method entirely depends on the hydrodynamic coefficients, which are mostly obtained from potential flow solutions in practice. These methods concentrate themselves on ease of use and an appropriate approximation of magnitude of hydrodynamic forces rather than on the detailed structure of the flow field, they require several empirical parameters, such as determination of the point of flow separation or the location of the free vertex. Therefore, a tool that can resolve the details of the flow field and evaluate the forces and moments with a sufficient degree of accuracy is necessary for the further advancement of ship design technologies.

The described method, coupling the RANS equations with rigid body dynamics, can be an answer to this problem. Especially, the method has the advantage of requiring no linear approximations so that it is suitable for the analysis of viscous flow fields with strong nonlinearity, such as the flow field around a maneuvering ship. In Chapter 3, it has been demonstrated that the method is robust and accurate enough to predict the motion of a 2D

body during water-entry or subjected to small regular waves and large wave packages. Chapter 4 has further exhibited the accuracy and robustness of the method in 3D problems with complex hull forms in seakeeping applications. For simulating maneuvering motions of ships by the present method, three steps are necessary from a CFD point of view.

The first step is to model the flow about a rudder and a propeller individually, where the flow around a rudder is solved by CFD (section 5.2) and the propeller is modeled by a body force model at its position (section 5.3). Since the numerical parameters have an important influence on predicting the flow around a rudder and consequently on the computed rudder forces, a parametric study is first carried out for two-dimensional flows around a hydrofoil. Then the forces on a three-dimensional rudder are predicted for a rudder alone and a rudder with a rudder-fin under inflow conditions with different angles of attack.

The second step is the coupling of propeller and rudder (section 5.4) and also their interaction with a hull coupled by CFD but with no ship motion involved (section 5.5). A large increase in rudder forces (both lift and drag forces) can be observed from computations due to the location of the rudder in the slipstream of the propeller. The predicted rudder forces behind the propeller and ship hull are further compared with available experiments, showing satisfactory agreement.

The final step is to simulate the maneuvering motion of a ship with appendages, such as drift motion, turning circle maneuver and Zigzag maneuver. This is one of the main goals of the present study and will be focused on in the next chapter, which is then a straightforward application based on previous chapters.

5.2 Modeling of Rudder

5.2.1 General Description

Rudders are the most commonly used devices for ship maneuvering. They are normally placed at the stern of ships (favorably in the propeller slipstream) to deliver a transverse force and a steering moment about the gravity center of the ship during turning. Since only spade rudders are considered in this work, they will be introduced in the following. Their cross sections are profiles, which can generate a lift force under a certain angle of attack by re-directing the flow to follow the rudder surface. The drag and lift forces are defined as components of the total force acting on the rudder surface in the flow direction and perpendicular to it. The rudder forces are mainly influenced by the dynamic distribution of pressure on the rudder surface. Figure 5.1 shows definitions of the attack angle α , the lift force L , the drag force D , the stock moment Q_R and the main dimensions of the rudder.

The drag, lift forces and stock moment can be made non-dimensional by the product of the stagnation pressure q , the rudder area A_R and its mean chord length c :

$$C_D = \frac{D}{qA_R} = \frac{D}{(0.5\rho v^2)A_R}, \quad (5.1)$$

$$C_L = \frac{L}{qA_R} = \frac{L}{(0.5\rho v^2)A_R}, \quad (5.2)$$

$$C_{QR} = \frac{Q_R}{qA_{RC}} = \frac{L}{(0.5\rho v^2)A_{RC}}. \quad (5.3)$$

Here, ρ is the density of water, v is the main flow velocity. A_R is defined as

$$A_R = cb, \quad (5.4)$$

b is the height of the rudder, see Fig. 5.1. The aspect ratio of the rudder is defined as

$$\Lambda = \frac{b^2}{A_R}. \quad (5.5)$$

The drag coefficient C_D is decomposed in some cases into two components:

$$C_D = C_{Dp} + C_{Df}, \quad (5.6)$$

where C_{Dp} is the drag coefficient due to pressure and C_{Df} the one due to friction.

The Reynolds number R_n is defined as

$$R_n = \frac{\rho vc}{\mu}, \quad (5.7)$$

where μ is the dynamic viscosity of water.

One of the most widely used types of rudder profiles is the NACA-00 series, which has been investigated systematically in wind tunnel measurements, see Abott and von Doenhoff [1]. Numerical computations of such profiles in viscous flow have been carried out, see Chau [16] and El Moctar [22] and comparisons with experiments show that the lift force coefficients have been predicted very well up to the stall angle α_{stall} (the attack angle at which maximum lift force is produced). However, the predicted stall angle itself and the drag force coefficient are larger than the measured values. Other profile forms, such as HSVA MP series (MP stands for 'Mixed Profile') designed by Brix [14], have also been widely used. One such profile, the HSVA MP73 used for the rudder of the RoRo ship (section 4.3), will be investigated here.

The computational domain and numerical grid used for 2D computations of the rudder alone and for 3D computations of rudders with rudder fins and the ship will be introduced first. Then, numerical parameters are studied for the profile HSVA MP73-20 in 2D. Forces on the rudder with and without a fixed fin above are computed and compared with each other in 3D free stream flow. Rudder forces behind propeller and ship will be analyzed in section 5.5.

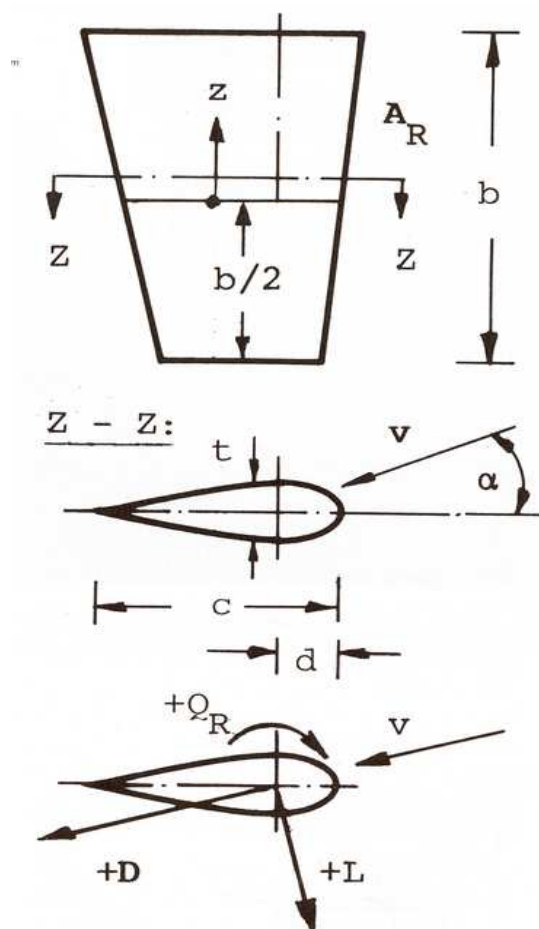


Figure 5.1: Main dimensions of the rudder (Brix [14]).

5.2.2 Computational Domain and Numerical Grid

The solution domain for 2D analyses is a rectangular block bounded by a non-slip wall representing the rudder surface as inner boundary and inflow, pressure or slip walls as outer boundaries. The rudder profile is put into a circular block bounded by a sliding interface, which enables an arbitrary rotation of the rudder. Since these analyses of rudder forces are performed as preparatory step for later ship maneuvering applications, the circular inner grid is embedded in an outer Cartesian block. The inlet and pressure boundaries are always perpendicular to the direction of flow and lie at a distance of $7c$ in front of and $13c$ behind the rudder, respectively, see Fig. 5.2. Slip wall boundaries are located $10c$ beside the profile and parallel to the flow direction. Chau [16] shows that the difference of the computed rudder lift force coefficients C_L is less than 1% between results obtained with outer boundaries located at $10c$ and $13.5c$ away from the profile. Therefore it is considered to be appropriate to have a distance of about $10c$ between profile and outer boundaries. The cells approaching outer boundaries are gradually enlarged as can be seen in Fig. 5.2. The coarse grid shown in Fig. 5.2 has 3000 cells. The grid is systematically refined in the vicinity of the profile resulting in a medium grid with 12000 cells and a fine grid with 39000 cells, see Fig. 5.3 for a close view of the fine grid around the rudder profile.

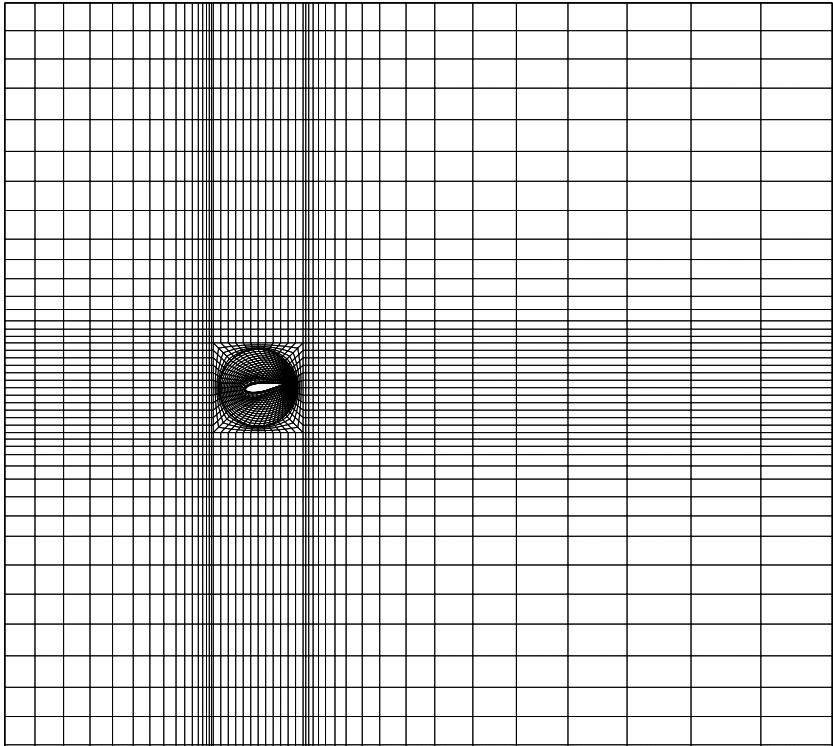


Figure 5.2: Computational domain of coarse grid in 2D.

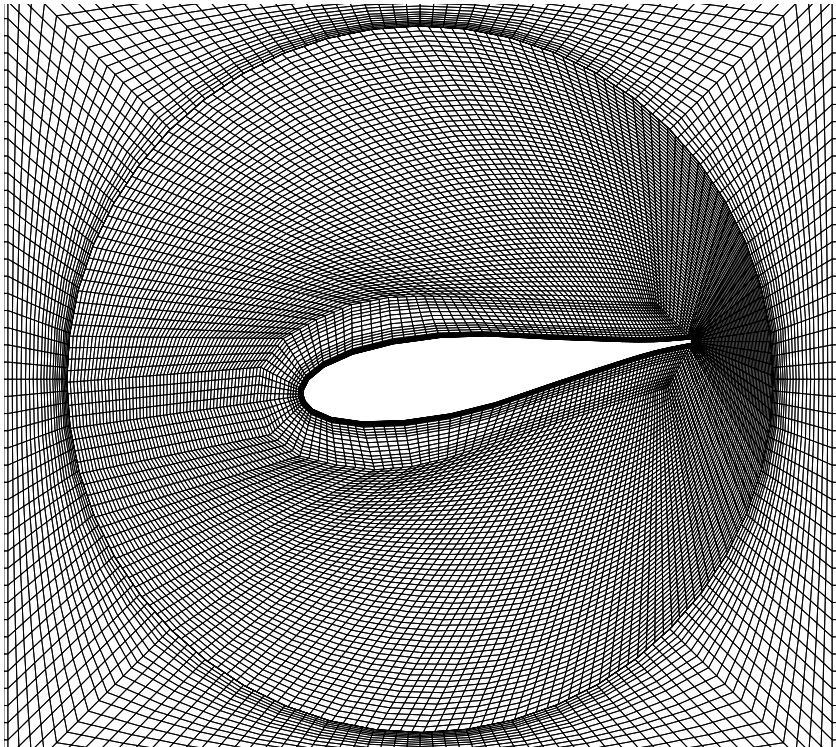


Figure 5.3: Fine grid in the vicinity of the rudder in 2D.

Three dimensional grids are generated by simple extension of the 2D grid, so that it has a similar structure with a rudder block surrounded by sliding interfaces. Care has to be taken at the top and bottom surfaces of the rudder, where the cross section of the rudder has to be closed with a grid of similar density. The sliding interfaces are used also here to allow the rotation of the rudder. They should be placed with some distance away from the surface of the rudder to avoid larger discretization errors near the top and bottom surfaces of the rudder (due to interpolation at the sliding interface). Thin grid layers are applied to the vicinity of top and bottom surfaces of the rudder to resolve the boundary layer. The total number of CVs used for 3D computation is 80,000 cells. The top and bottom outer boundaries are specified as slip walls. Figure 5.4 shows a frame of such a grid for the computation of the flow around a rudder alone.

More challenges in grid generation are met if a rotating rudder grid has to be fitted behind the ship and below a fixed rudder fin with only a narrow gap between rudder and fin (5 cm). First, a grid for a rudder and a rudder fin without the ship containing 110,000 cells has been generated, as shown in Fig. 5.5. The narrow gap is resolved by a number of thin layers of cells on each side attached to the top surface of the rudder and the bottom surface of the rudder fin. Then a sliding interface is used in between to connect the rotating rudder block and the fixed block containing the rudder fin. This technique seems to work well, although one can argue that the flow in the gap is rather slow and therefore can probably be neglected. El Moctar [22] has shown that the lift force acting on the rudder at the rudder angle of 5° without the gap is about 2% larger than the one in the case of a 5 cm gap between the rudder and the rudder fin while the influence of the gap on the drag force is much smaller.

Next, the blocks with rudder and rudder fin have to be arranged behind the ship. A RoRo ship with a double rudder system has been taken for this case. The Costa bulb of the rudder is neglected here to make the grid generation easier. Blocks with different cell density or topology are connected by unstructured block interfaces or sliding interfaces (if they move relatively to each other). The grid generated for such a complex system and a more detailed view of the ship stern together with rudders at 30° rotation angle are shown in Figs. 5.6. The discretization domain extends to $1.5L$ in front of and beside the ship and $3.0L$ behind the ship with an additional numerical beach. The top and bottom boundaries are $1.0L$ away from the ship, so the deep water condition is applied. The complete grid has about 1,050,000 cells, half of which are located near the ship hull and the rudder and a quarter of which are found in the region of the free surface.

As can be seen, the whole grid system turns out to be very complicated. That is also one of the reasons that most computations in practice are carried out for separated parts so far. This seems to ease the difficulties in grid generation, but the coupled effect has to be either ignored or approximated, which may deteriorate accuracy. It is well known that the rudder's behavior is completely different if it is placed in uniform stream or in the wake of a ship (and partially in the slipstream of the propeller). Thanks to techniques like sliding interfaces, unstructured blocks and cell-wise local refinements, it has become possible to compute the coupled complex system simultaneously.

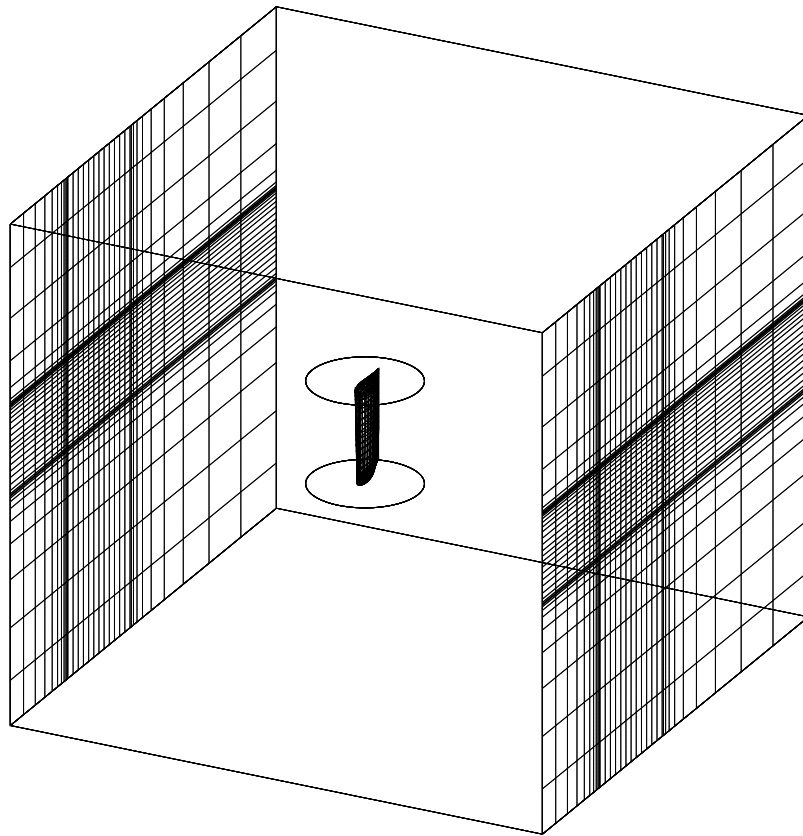


Figure 5.4: Computational domain for rudder without fin in 3D.

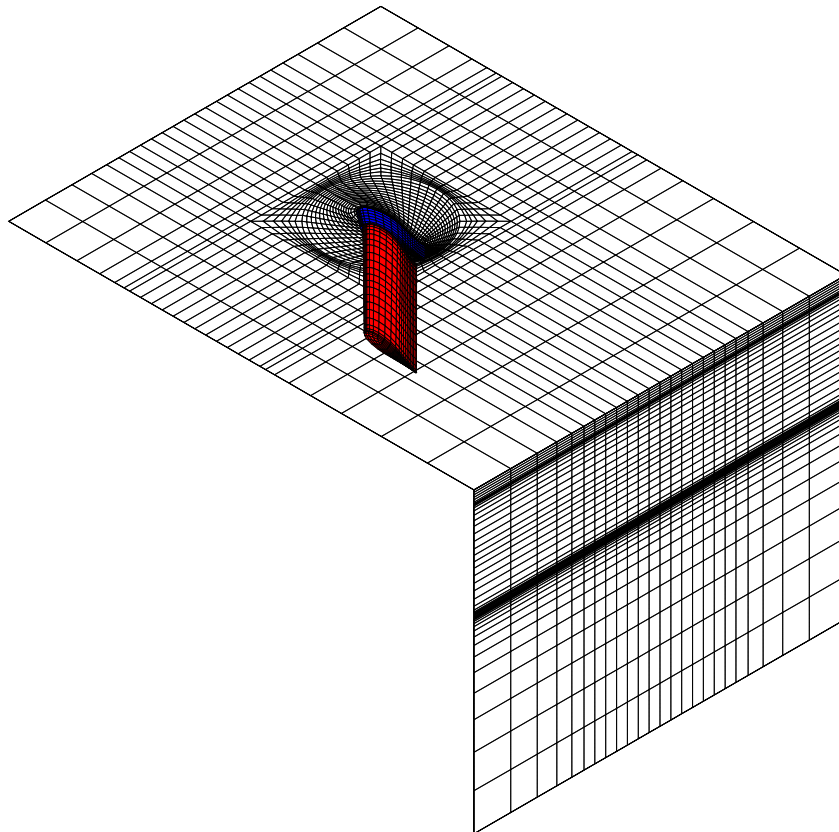


Figure 5.5: Grid for rudder with fin in 3D.

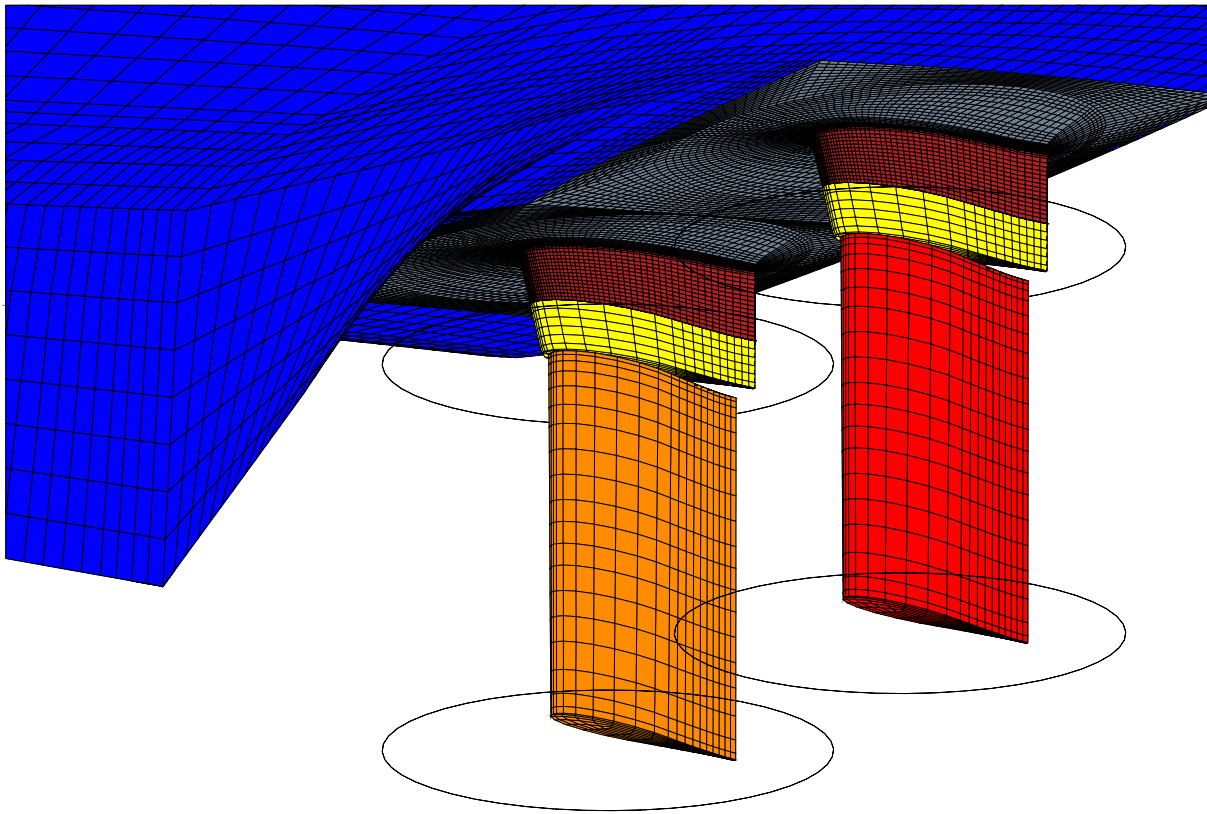


Figure 5.6: Grid for RoRo Ship with two rudders and fins.

5.2.3 Parameter Study of Rudder Forces in 2D

Error analysis and parameter study are first performed for the flow around the rudder profile HSVA MP73-20 in two dimensions. Both modeling errors due to employing different turbulence models and the discretization errors due to numerical grids and approximation schemes will be discussed in this section. Computations in real and model scales (different Reynolds number) will also be compared.

To study discretization error and modeling error, the iteration error should be kept at least an order of magnitude lower than the discretization error. To meet this criteria, the dimensionless residuals of all equations are reduced to 10^{-6} (10^{-5} in some cases), which is sufficient since the force coefficients do not change any more on the four most significant digits when the residual is below 10^{-5} (10^{-4} in some cases).

Turbulence models

The RNG $k-\epsilon$ turbulence model (mentioned before in section 2.2.1) is tested here and the results are compared to the standard $k-\epsilon$ model. The computations using these two turbulence models are carried out for the profile in a uniform flow at an angle of attack of $\alpha = 8^\circ$ and a Reynolds number of $R_n = 2.7 \cdot 10^6$. Different blending factors of CD scheme and UD scheme are varied for both models and computations on a coarse grid and a fine grid are carried out to study the tendency of the performance of turbulence models depending on approximation

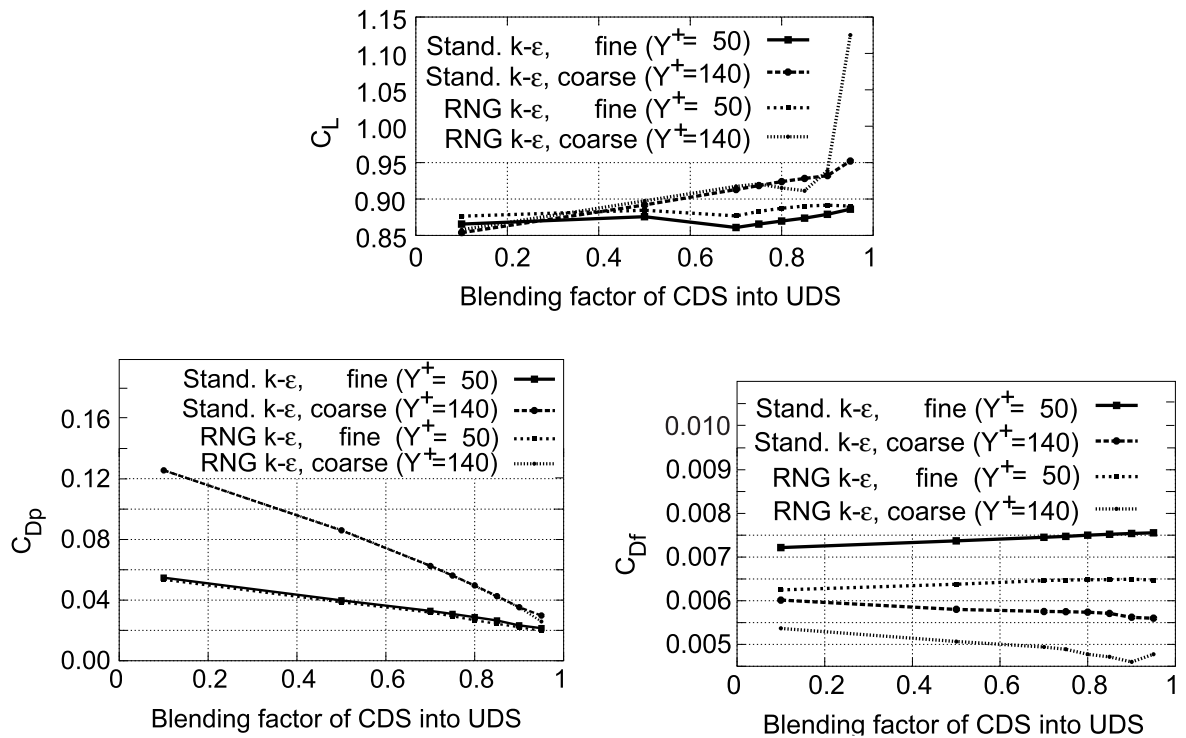


Figure 5.7: Dependency of computed lift and drag coefficients on blending of CD scheme and UD scheme for two turbulence models on coarse and fine 2D grids ($\alpha = 8^\circ$ and $R_n = 2.7 \cdot 10^6$).

schemes and the grid resolution.

The coarse and fine grids employed here have already been shown in Fig. 5.2 and 5.3. The non-dimensional Y^+ of the coarse grid is around 150. On the fine grid it has a value between 40 and 50. The computed force coefficients using these two models are compared in Fig. 5.7 as function of blending factors of CD scheme and UD scheme. As can be seen, both models behave similarly as the blending factor varies. The lift coefficient C_L increases slightly as the blending factor increases while the drag coefficient due to pressure C_{Dp} decreases linearly with a higher blending factor. As expected, the slope of the dependency of C_{Dp} on the blending factor is smaller when the grid becomes finer.

The RNG $k-\epsilon$ model seems to produce higher lift force than the standard $k-\epsilon$ model with fine grid, but seems to be more sensitive on the grid resolution and blending factors (Oscillations appear on coarse grid for the RNG model if the value of the blending factor is higher than 0.8). On both grids, the RNG $k-\epsilon$ model produces slightly smaller drag coefficients (concerning both C_{Dp} and C_{Df}) than the standard $k-\epsilon$ model, which agrees with the prediction of El Moctar [22]. This property of the RNG $k-\epsilon$ model is somehow favorable because the drag force coefficient is normally over-predicted by numerical computations, as shown by Chau [16] and El Moctar [22]. However, the difference of the total drag coefficient obtained by the standard and RNG $k-\epsilon$ model is less than 4% for coarse grid and 8% for fine grid in the computations presented here, while the difference of the total drag coefficient using either turbulence model to experimental values lies mostly in the range of 20% to 40% (a smaller value can be obtained for a certain attack angle as reported by El Moctar [22]).

The feature that the RNG k - ϵ turbulence model seems to be more prone to oscillations when a higher blending factor is used on a coarse grid (or larger Y^+) can also be seen in the convergence behavior of turbulence kinetic energy and mass in Figs. 5.8 and 5.9, respectively. The computations have been performed on three grids using a blending factor of 0.9. As can be observed, more iterations are needed using the RNG k - ϵ model and iterations stop to converge at some stage on coarse and medium grids. The residuals of turbulence equations using the standard k - ϵ model keep reducing on all three grids to a level below 10^{-6} . Since the standard k - ϵ model seems to be more diffusive and thus more robust and less sensitive to the fineness of grid (or Y^+) and values of blending factors than the RNG k - ϵ model and since the difference of the results using these two models is not large, the standard k - ϵ model is kept for further applications.

Differencing schemes in space

The blending factor of CD scheme and UD scheme has been discussed briefly above for the rudder lift and drag coefficients for an angle of attack of $\alpha = 8^\circ$. However, the approximation scheme for convective terms has not only great influence on the computed force coefficients but also on the stall angle and maximum lift coefficient of the rudder.

As stated before, a blending of CD scheme and UD scheme has been used for most computations. A lower blending factor means larger portion of UD scheme being used, which tends to smear the solution and has an effect of additional diffusion. This delays the flow separation and therefore results in a larger stall angle and a higher unrealistic maximum lift force coefficient as can be seen in Fig. 5.10. A higher blending factor indicates a higher order of the scheme (the error decreases more rapidly when the grid is refined), but often causes divergence problems. Therefore, the best strategy is to use the highest blending factor possible to make a compromise between stability and accuracy. Since the difference between the results using a blending factor of 0.90 and 0.95 is rather small, a blending factor of 0.9 is normally used here if it is not specifically stated in later applications.

Reynolds number

Model tests are usually performed in Froude similarity. The Reynolds number R_n is not obeyed in ship model tests. The numerical computations in this work are also mostly constructed in model scale for validation purposes though it is not necessary for the method itself. It is therefore useful to check what effect the Reynolds number has on the fundamental hydrodynamic characteristics of the rudder profile. Figure 5.11 shows the computed lift and total drag coefficients for different angles of attack α at two Reynolds numbers $R_n = 0.15 \cdot 10^6$ and $R_n = 2.7 \cdot 10^6$. The coarse grid has been employed here. Y^+ has values around 30 and 150 at these two corresponding Reynolds numbers, respectively. The smaller Reynolds number ($R_n = 0.15 \cdot 10^6$) corresponds roughly to a rudder in an uniform flow with a speed of ship in model tests without considering the wake and the slipstream of propeller. The numerical prediction coincides with the empirical conclusion from measurements (see Brix [14]) that smaller drag coefficients are obtained at larger Reynolds number for all attack angles. The stall angle α_{stall} as well as the maximum lift coefficient $C_{L\text{max}}$ of the profile becomes larger as the Reynolds number increases. As the later computations are mostly carried out in model scale, these effects should be taken into

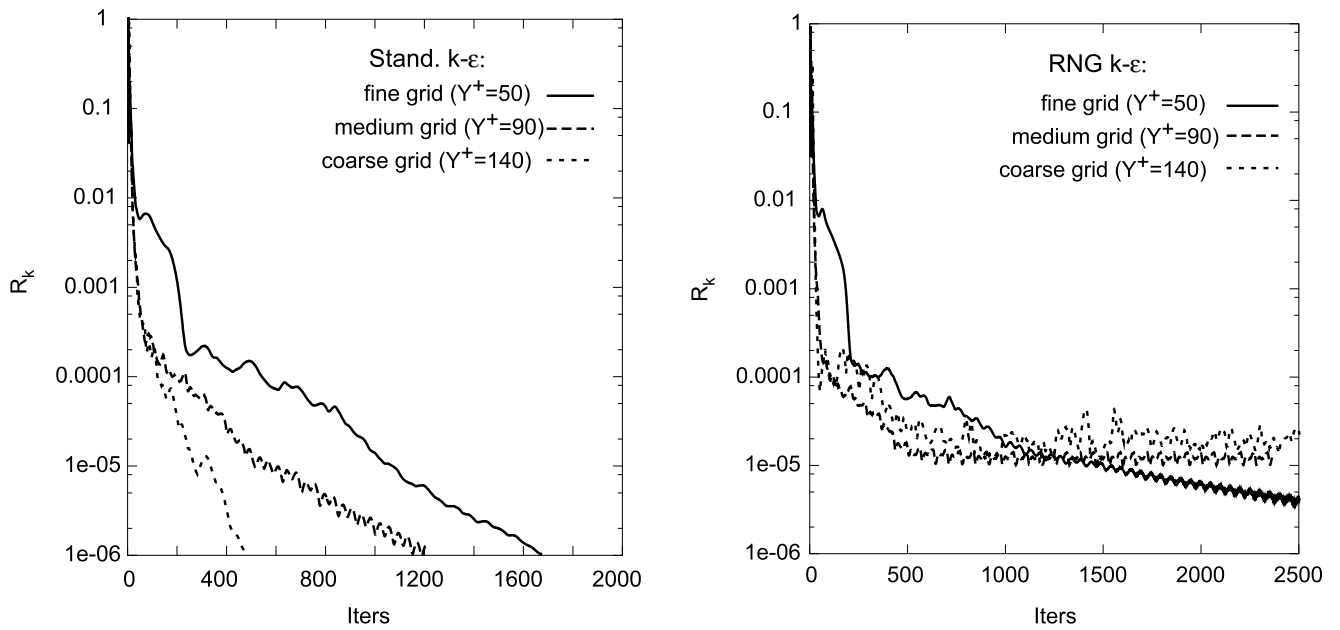


Figure 5.8: Comparison of normalized residuals of turbulence kinetic energy equations using two turbulence models on different grids (2D).

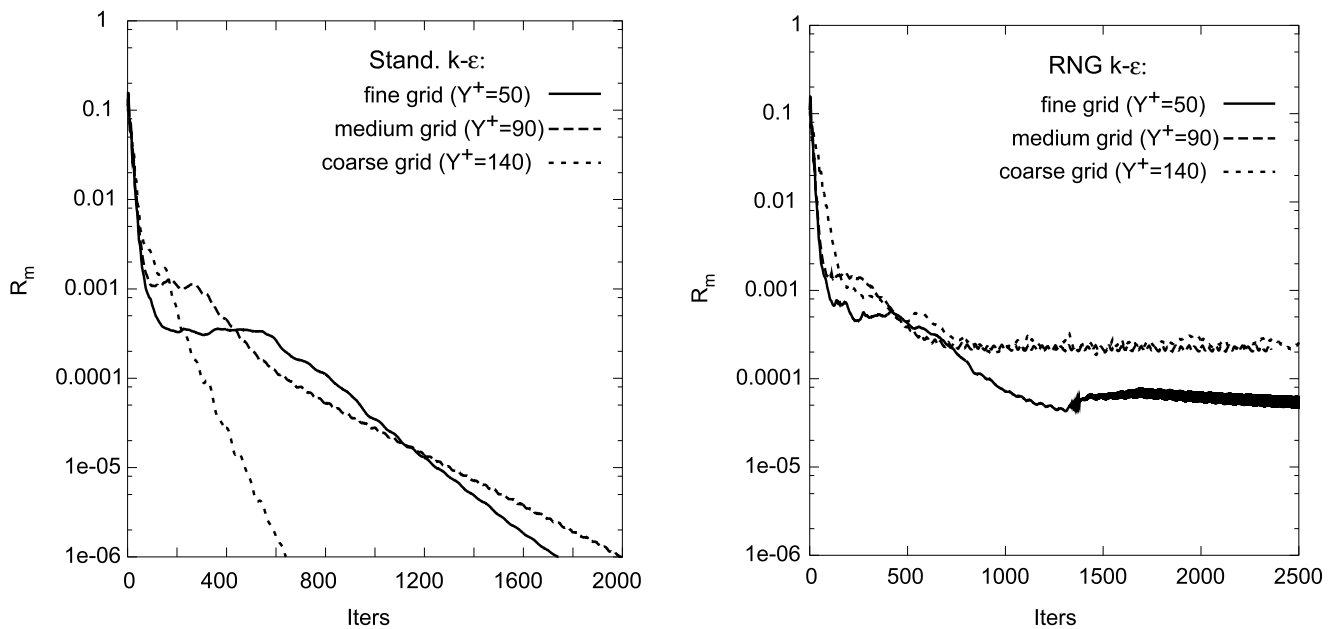


Figure 5.9: Comparison of normalized residuals of mass equations using two turbulence models on different grids (2D).

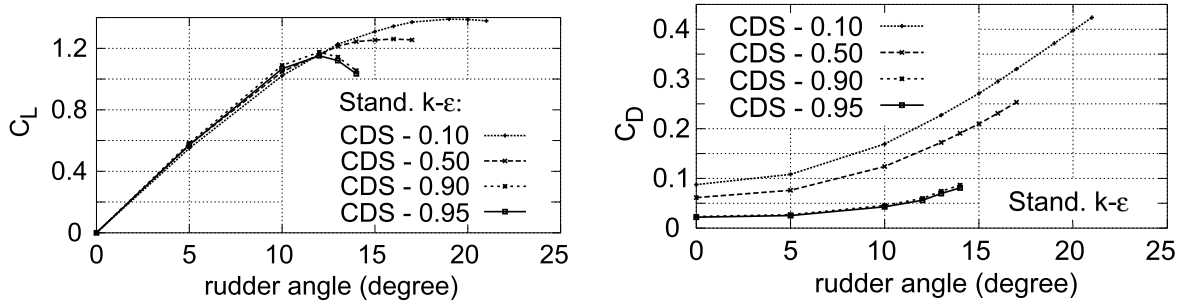


Figure 5.10: Dependency of force coefficients and stall angles on the discretization scheme (2D).

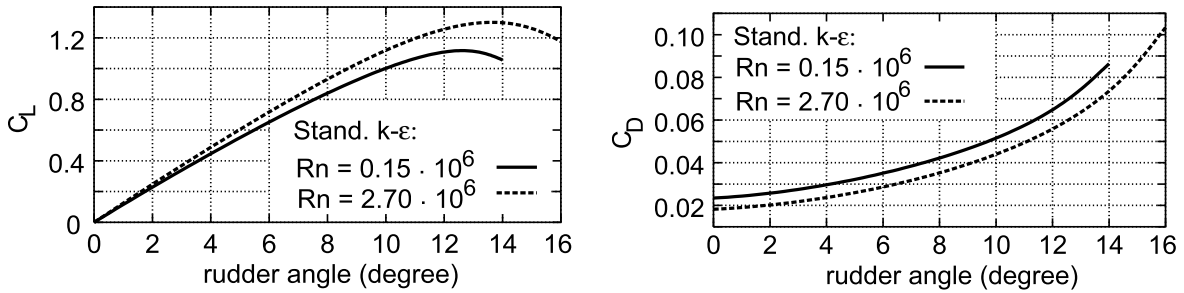


Figure 5.11: Rudder force coefficients of different Reynolds numbers (2D).

account in evaluating the numerical results.

Estimation of discretization error

The discretization error depends mainly on the numerical grid and approximation schemes used for different terms in the partial differential equations. It can be therefore best estimated by using systematically refined grids while keeping the schemes the same. Three grids (as used above) are generated by systematic refinement in the vicinity of the profile, where discretization error is expected to be large (larger than in the region far away from the profile). As already mentioned, the coarse and fine grid have 3000 and 39000 cells respectively and the medium grid has about 10500 grid cells. The non-dimensional wall distance Y^+ is kept at about 50 for all three grids in this case to minimize the effect of turbulence model (equalizing the modeling error due to turbulence models). The case is set up for the HSVA MP73-20 profile in a flow of an angle of attack of $\alpha = 8^\circ$ at $R_n = 2.7 \cdot 10^6$ using the standard $k-\epsilon$ model and a blending factor of 0.9. The Richardson extrapolation (Richardson [72]) is used here to estimate the discretization error and predict the grid-independent solution, for the predicted pressure drag coefficient C_{Dp} , Fig. 5.12.

5.2.4 Forces of Rudders without and with Fixed Fins in 3D

The RoRo ship has twin spade rudders mounted beside the skeg center of the ship, as shown in Fig. 5.6. The rudder head bearings are integrated into fixed fins in order to keep the bending moments on the bearings as small as possible. The dimensions of rudders and fixed fins of the RoRo ship are given in Table 5.1. The rudder thickness varies linearly along the

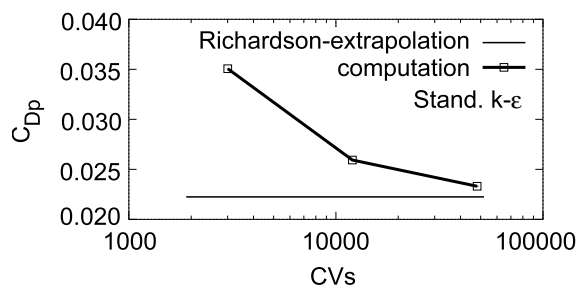


Figure 5.12: Richardson extrapolation of pressure drag using results from three grids (2D).

rudder height while the chord length of the rudder c has been kept the same. The ratio of rudder thickness over chord length t/c is 0.18 at the bottom of the rudder and 0.25 at the top of the rudder. Both the thickness and the chord length vary linearly for the fixed fin, as given in Table 5.1.

Three-dimensional computations are first carried out for the rudder alone in free stream at $R_n = 0.15 \cdot 10^6$. The grid with 80,000 cells is used as shown in Fig. 5.4 and the mean value of Y^+ is 50. The computed lift and drag force coefficients are shown in Fig. 5.13. The Figures 5.11 (left) and 5.13 (left) show the curves of lift force coefficient versus the rudder angle. As expected, the tangent of the curve, $dC_L/d\delta$, at $\delta = 0$ is much smaller in 3D than in 2D. For small rudder angles, the gradient $dC_L/d\delta$ is computed between 5.72 and 6.40 in 2D, close to the prediction of 2π according to potential theory [78]. In 3D flow, the computed gradient $dC_L/d\delta$ is reduced to 3.55. The stall angle $\alpha_{st,all}$ as well as the maximum lift force coefficient $C_{L,max}$ in 3D flow is, however, larger than in 2D flow.

It is known that the installation of fixed fins can not only reduce the bending moments but also improve the hydrodynamic characteristics of the rudder, given the gap between the rudder and the fixed fin is kept small. El Moctar [22] has investigated the influence of the width of the gap on the drag and lift force coefficients of the rudder. For a gap of 5 cm width, the reduction of C_L is found to be 2% at the angle of attack of $\alpha = 5^\circ$, compared to a gap of 0 cm width, and more than 6% reduction of C_L is predicted for a gap of 10 cm width. The reduction rate of C_L decreases as the angle of attack α is increased. C_D varies little if the thickness of the gap is increased from 0 cm to 5 cm; however, it becomes significantly larger if the width is increased to 10 cm. Therefore a width of 5 cm seems to be optimum to keep the drag/lift-ratio $\epsilon = C_D/C_L$ as small as possible, which is also used for the RoRo ship.

The hydrodynamic forces acting on the rudder and its fixed fin are computed here for a gap of width of 5 cm between them. The grid used has 110,000 cells as shown in Fig. 5.5. Figure 5.14 shows the computed force and moment coefficients at $R_n = 0.15 \cdot 10^6$ for both the rudder and the fixed fin. As the gap is relatively narrow, the fixed fin acts as prolongation of the rudder and prevents the flow from the pressure to the suction side of the rudder around the upper edge of the rudder. This has a similar effect as an increase of the rudder aspect ratio Λ and results in a larger lift force coefficient C_L and a smaller drag force coefficient C_D at a given rudder angle δ , as can be seen by comparing the rudder force coefficients in Fig. 5.13 and 5.14. The gradient $dC_L/d\delta$ is increased by approximately 10% at small rudder angles and the drag/lift-ratio is decreased by 31.8% at the rudder angle of $\delta = 10^\circ$ by installing the fixed fin above the rudder.

Table 5.1: Dimensions of rudder and fixed fin

	Rudder	Fixed fin
profile	HSVA MP 73	HSVA MP 73
profile thickness t	0.60 m - 0.83 m	0.83 m - 0.96 m
chord length c	3.333 m	3.333 m - 4.003 m
rudder height b	5.3 m	2.5 m

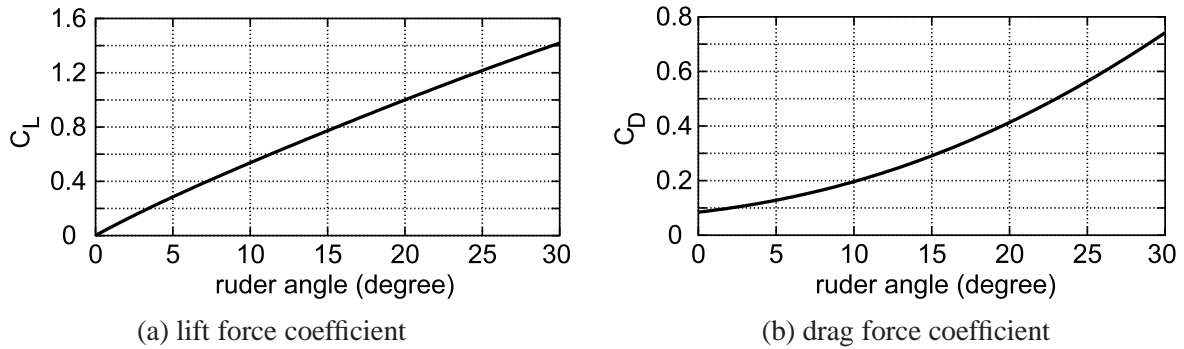


Figure 5.13: Computed force coefficients for rudder without rudder-fin (3D).

In Fig. 5.14, the induced forces on the fixed fin are also non-dimensionalized similarly as for the rudder (Eqs. (5.1) and (5.2)) and given for different rudder angles. Although the angle of attack for the fixed fin is 0° , the effective angle of attack α_{effect} is however non-zero due to the three-dimensional flow induced by the rudder below. The gradient $dC_L/d\delta$ for the fixed fin is more than half of the one for the rudder and keeps constant for small rudder angles. However, the increase of lift force coefficient C_L stops when the rudder angle δ becomes larger than 26° . The drag force coefficient for the rudder fin increases in a similar manner as for the rudder. The stock moment computed for the fixed fin is almost negligible, as can be observed in Fig. 5.14.

5.3 Modeling of Propeller

5.3.1 Body Force Model for Propeller

The propeller is modeled by the body-force distribution method in this work, as mentioned above. The effect of the propeller is accounted for by adding body-force terms $\mathbf{b} = \mathbf{b}(x, r, t)$ to the source terms of the momentum equations. Such a discrete force field (or actuator disk), approximating the forces exerted by the propeller on the fluid, is embedded into the flow field. The force vector \mathbf{b} is non-zero only when $x_p - \Delta x/2 < x < x_p + \Delta x/2$ and $r_h < r < r_p$, where x_p is the x -coordinate of the propeller, Δx is the appointed thickness of the propeller disk, r is the radial coordinate in the propeller plane, r_p and r_h are the radii of the propeller and the hub, respectively.

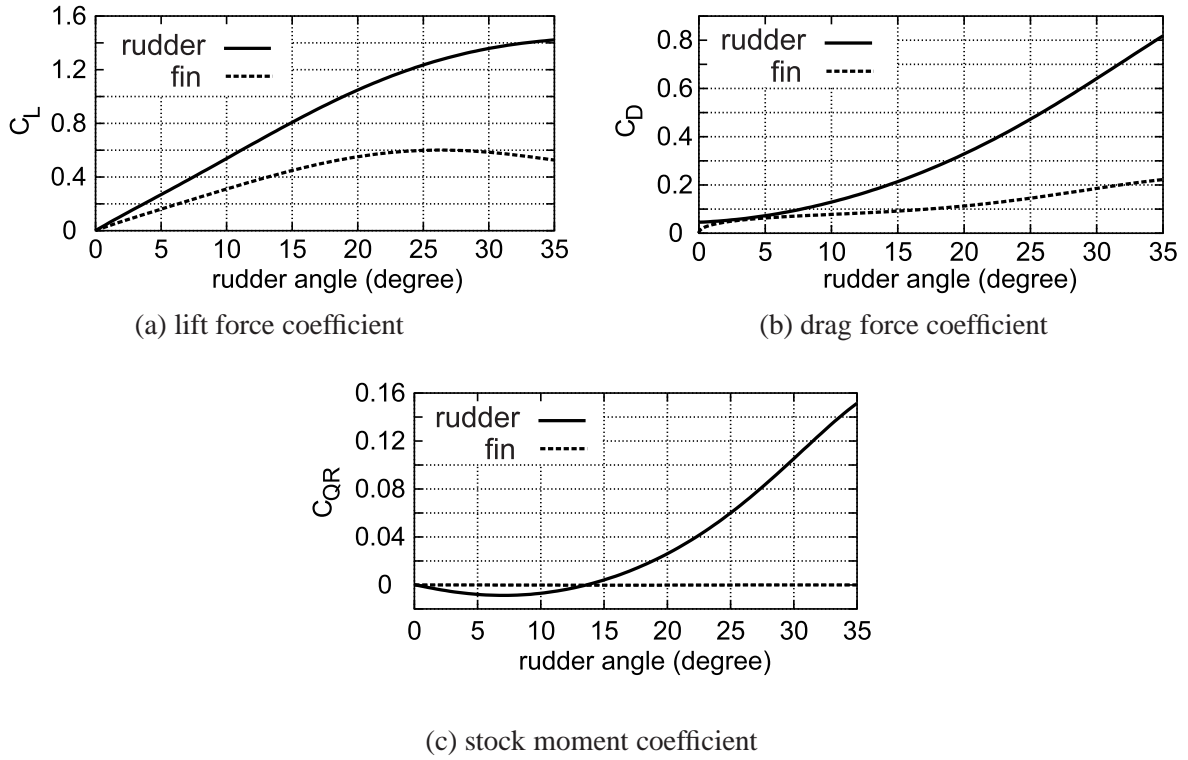


Figure 5.14: Computed force coefficients for rudder with rudder fin (3D).

The sum of the applied body forces in the x -axis is set equal to the propeller total thrust; the sum of the applied moments about the x -axis is set equal to the total torque of the propeller. The distributions of the body forces \mathbf{b} are assumed to be only a function of r and can be obtained analytically by assuming them being similar to the radial circulation distribution (see Stern et. al. [80]), which is proportional to r' , where

$$r' = \frac{r - r_h}{r_p - r_h} \sqrt{1 - \frac{r - r_h}{r_p - r_h}}. \quad (5.8)$$

The resulting distributions of axial and tangential forces are:

$$b_x(r') = c_x r' T_p, \quad (5.9)$$

$$b_\theta(r') = c_\theta r' Q_p. \quad (5.10)$$

T_p and Q_p are the total thrust and torque of the propeller. The constant coefficients c_x and c_θ can be obtained by making the sum of $b_x(r')$ and $b_\theta(r')r$ equal to T_p and Q_p :

$$c_x = \frac{T_p}{\sum_{N_{CV}} (r' T_p)} = \frac{1}{\sum_{N_{CV}} (r')}, \quad (5.11)$$

$$c_{\theta} = \frac{Q_p}{\sum_{N_{CV}} (r' Q_p) r} = \frac{1}{\sum_{N_{CV}} (r' r)}. \quad (5.12)$$

Here, N_{CV} represents the number of CVs, which lie in the propeller disk. These CVs are selected using the aforementioned criteria according to the propeller location (x_p) and dimensions (r_h and r_p). A graphic illustration of the body-force distribution model is given in Fig. 5.15.

If the inflow is oblique, the side force of the propeller is considered here as:

$$b_y = c_y Y_p, \quad (5.13)$$

where

$$c_y = \frac{1}{N_{CV}}, \quad (5.14)$$

and Y_p denotes the total side force of the propeller.

The total propeller forces (thrust, torque and side force) have to be given as input data for the body-force distribution method. If the propeller forces are known as a function of time, they can be applied directly. Otherwise, if the inflow velocities of the propeller are given, the trust and the torque can be obtained from the propulsion diagram for free stream and the side force can be estimated either from experiment or empirical formulae. However, in many cases neither the propeller forces nor the inflow velocities of the propeller are known. The inflow velocities of the propeller are normally difficult to estimate due to the complex inflow pattern of the propeller under the interaction of ship, propeller and rudder (the wake of the ship or the effect of the rudder in the propeller slipstream). To simulate the unsteady motion of ship maneuvers, propeller forces have to be calculated by methods which can take into account these unsteady interactions. Such a method is derived in the next section, where the propeller inflow velocities are obtained from the instant fluid flow through the propeller disk with the help of momentum theory.

Alternatively, if only the overall thrust is of interest such as in the case of a self-propelled ship moving straight ahead, an initial estimation of the thrust can be used and then corrected iteratively until the total thrust equals to the total resistance of the ship and a steady state is reached. In the following sections, two different methods for estimating the propeller forces are introduced for different applications presented later.

5.3.2 Determination of Propeller Forces from the Instant Fluid Flow

Since the propulsion diagrams of each propeller in free stream are normally available, the propeller forces can be obtained if the mean effective inflow velocities of the propeller are known. As already mentioned above, the inflow velocities of the propeller are not readily known (unless from measurements) if the propeller is placed in front of the rudder and both

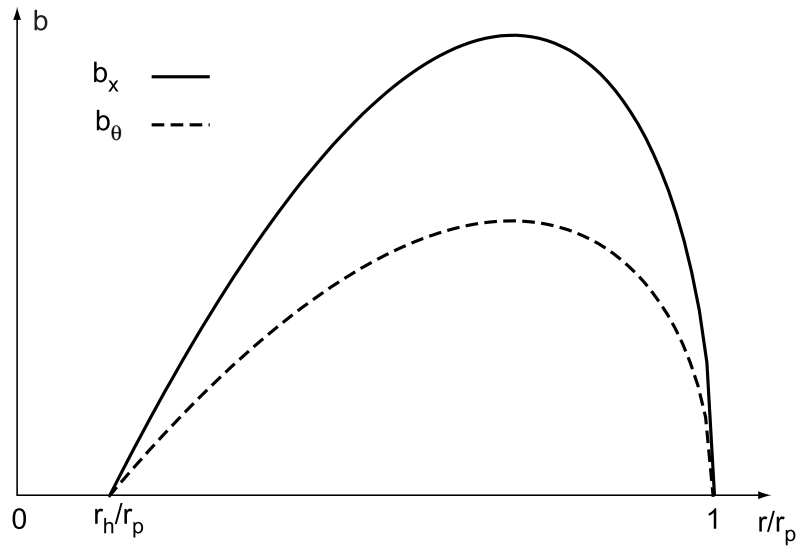


Figure 5.15: Body force distribution model for propeller.

of them are in the wake of the ship. A general method to obtain the instant inflow velocities is derived in this section with the help of the momentum theory. This method has been validated by evaluating the forces of a rudder which is placed in the propeller slipstream and the wake of a ship, see section 5.5.

The propeller thrust in free stream can be obtained using the propulsion diagram, where the forces are non-dimensionalized as

$$K_T = \frac{T_p}{\rho n^2 D^4}, \quad K_Q = \frac{Q_p}{\rho n^2 D^5}, \quad (5.15)$$

where ρ is the density of the fluid (water), n is the rate of rotation and $D = 2r_p$ is the diameter of the propeller. K_T and K_Q are called thrust and torque coefficients, which are the function of the advance coefficient J

$$J = \frac{v_A}{nD}, \quad (5.16)$$

where v_A is the advance (or axial) inflow velocity of the propeller. K_T and K_Q are approximated as linear functions of J :

$$K_T = c_{T1} - c_{T2}J, \quad K_Q = c_{Q1} - c_{Q2}J, \quad (5.17)$$

where c_{T1} , c_{T2} , c_{Q1} and c_{Q2} are coefficients taken to give a close fit to the propeller diagram. More coefficients can be added if necessary. Here, such a linear approximation of K_T and K_Q is sufficient since the real curves of K_T and K_Q in propeller diagrams are very close to straight lines.

The thrust T_p and torque Q_p can therefore be easily calculated if the axial inflow velocity of the propeller (J or v_A) is known. The propeller side force Y_p can be estimated (see El Moctar [23]) as

$$Y_p \approx 0.0032J\alpha^{0.95}, \quad (5.18)$$

where α is the angle of the inflow relative to the propeller x -axis and has the unit of *degree*.

Due to the aforementioned difficulties in estimating v_A or J , a method to obtain v_A directly from the flow field is derived and introduced here. As explained in Fig. 5.16, v_A and v_B are the flow velocities far in front of and behind the propeller, v_p is the flow velocity directly at the propeller disk. According to momentum theories originally from Rankine [70] and Froude [26], the relation between the velocities $v_p = \frac{1}{2}(v_A + v_B)$ can be derived by assuming:

1. A uniform acceleration applies to all fluid passing through the propeller.
2. Frictionless flow.
3. Infinite inflow of water to the propeller.

The volume of the fluid passing through the propeller disk per second is then

$$Q_p = v_p A_o, \quad (5.19)$$

where A_o is the area of the propeller disk $A_o = \pi D^2/4$. According to the conservation of the axial momentum of the fluid passing through the propeller disk, it can be obtained

$$T = \rho Q(v_B - v_A) = 2\rho v_p A_o (v_p - v_A). \quad (5.20)$$

From the Eqs. (5.15), (5.16) and (5.17), one gets

$$T = \rho n^2 D^4 (c_{T1} - c_{T2} \frac{v_A}{nD}). \quad (5.21)$$

By substituting Eq. (5.20) into (5.21), v_A is expressed as a function of v_p

$$v_A = \frac{2\rho v_p^2 A_o - c_{T1} \rho n^2 D^4}{2\rho v_p A_o - c_{T2} \rho n D^3}. \quad (5.22)$$

v_p can be obtained directly from the flow field by averaging the axial velocity v_x of N_{CV} CVs lying in the propeller disk ($x_p - \Delta x/2 < x < x_p + \Delta x/2$ and $r < r_p$):

$$v_p = \frac{1}{N_{CV}} \sum_{N_{CV}} v_x. \quad (5.23)$$

Once the advance velocity of the propeller v_A is estimated, the thrust T_p , the torque Q_p and the side force Y_p of the propeller can be easily obtained by Eqs. (5.15) to (5.18) if the revolution of the propeller is given (from measurements).

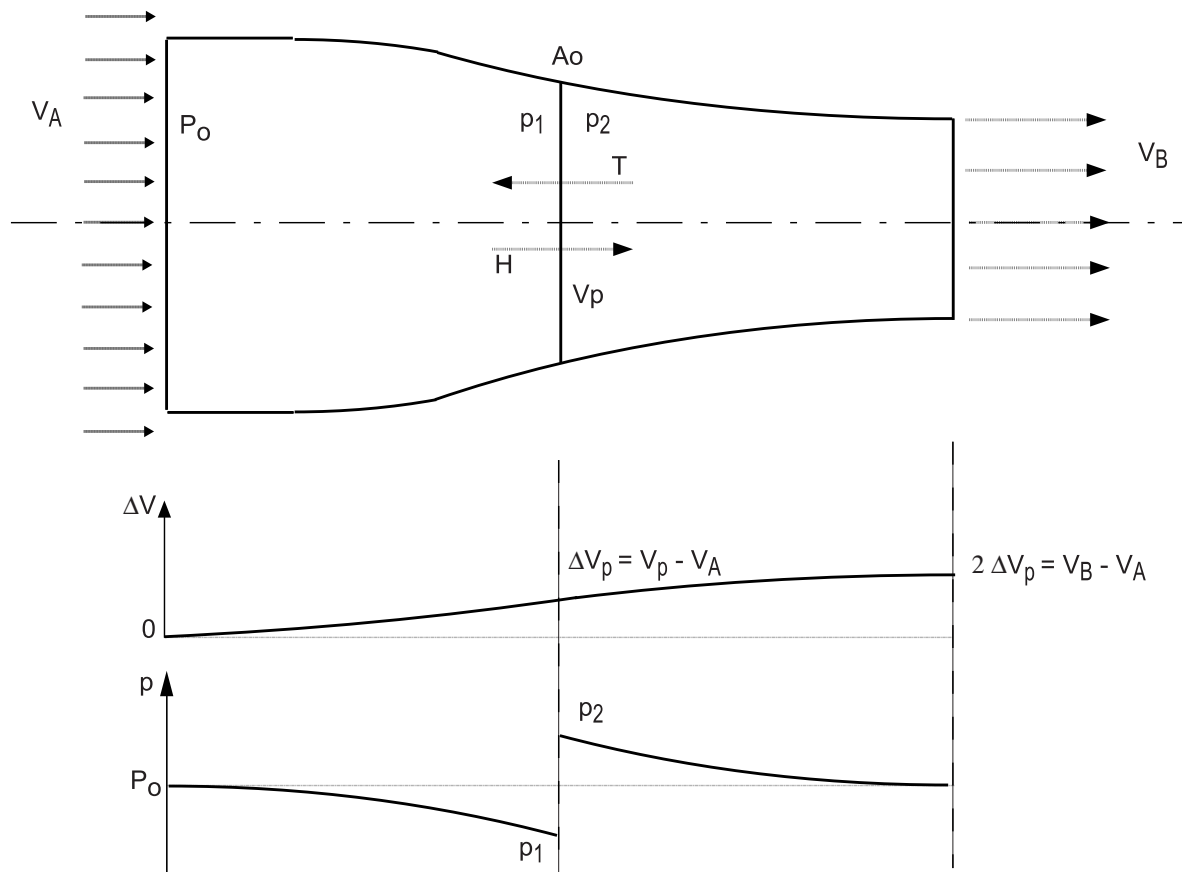


Figure 5.16: Flow through propeller disk.

This technique to predict the thrust T_p and the torque Q_p of the propeller is applied in section 5.4 and 5.5. The body-force module is integrated into the flow solver iteratively. Iterations continue until the steady state of the coupled system is reached, which means that both the propeller forces and the whole flow field (including flow velocities and the free surface etc.) do not vary any more and residuals satisfy the prescribed criteria. The final thrust predicted using this method has been proven to be very close to the computed drag on the ship (less than 5% variation), which is accurate enough to be applied here in approximating the thrust of a propeller during ship maneuvering motion.

5.3.3 Determination of Thrust by Numerical Self-Propulsion Test

For ship maneuvers with its own propulsion system and its own rudder, a steady state of the ship at a prescribed (design) speed in straight ahead motion is usually required before the maneuvering operation starts. In this section, a numerical method which is used to determine the necessary propeller thrust T_p for a ship to reach the steady state of the required velocity is introduced by keeping in mind that the numerical effort should be kept as low as possible.

The design speed of the ship is denoted as V_d , which is used as the inlet and initial velocity for the whole flow field (the relative flow motion to the ship). The computation is started with uniform flow field without propeller effect. The pseudo-time marching technique is applied here to speed up the development of a steady wave system. The total drag on the

ship R can be obtained by integrating forces on the ship surface. The residual of the total drag is computed as

$$R_R = \frac{\|R^{n+1} - R^n\|}{\|R^n\|} < p_R, \quad (5.24)$$

where p_R is given the value of 0.5 (a large tolerance is allowed here since the final solution is yet not reached). If the condition, Eq. (5.24), is fulfilled, the body equations are solved to account for the acceleration of the ship. If the ship is free to heave and pitch, the incremental displacement for grid-moving and the velocity of each body surface element are computed. Though the ship is not allowed to surge, V (*virtual speed*) is computed by considering the acceleration due to the resulting force $T - R$ if the ship had been set free.

Once V is updated, the effect of the propeller thrust T is added using the body-force distribution method (see section 5.3.1) by assuming

$$T = R \left(\frac{V_d}{V} \right)^{2 \sim 4}. \quad (5.25)$$

By considering the propeller action in the flow, the pressure decreases at the stern of the ship, which means that the total resistance R on the ship increases. Therefore V becomes smaller than V_d , which results in a higher propeller thrust T , see Eq. (5.25). A higher propeller thrust T increases the total resistance R again, but also V is increased at the next iteration/time step. Such, the computation converges to the state $V = V_d$ which indicates that $T = R$ is fulfilled, see Eq. (5.25). The residual of $T - R$ is computed as

$$R_{(T-R)} = \frac{\|T - R\|}{\|R\|} < p_{(T-R)}, \quad (5.26)$$

where $p_{(T-R)}$ is given the value of 0.01.

The coupled procedure is illustrated in Fig. 5.17. The order $2 \sim 4$ in Eq. (5.25) is selected according to experience. Other values can also be used, however the convergence rate will be influenced.

5.4 Interaction of Propeller and Rudder

Rudder forces have been computed in free stream in section 5.2. However, in practice rudders are often placed in the propeller slipstream behind the ship. Due to the actuating effect of the propeller, the inflow velocity for the rudder behind the propeller is much higher and both the magnitudes of inflow velocity and the angles of attack vary along the height of the rudder, which has a great influence on rudder forces. The wake of the ship has the opposite effect on the performance of the rudder. The integrated system considering rudder, propeller and ship will be discussed in the next section. In this section, the rudder and fixed fin of the rudder are placed in the slipstream of the propeller, which is subjected to free stream. A symmetry condition is applied on the top boundary above the rudder fin to approximate the effect of the

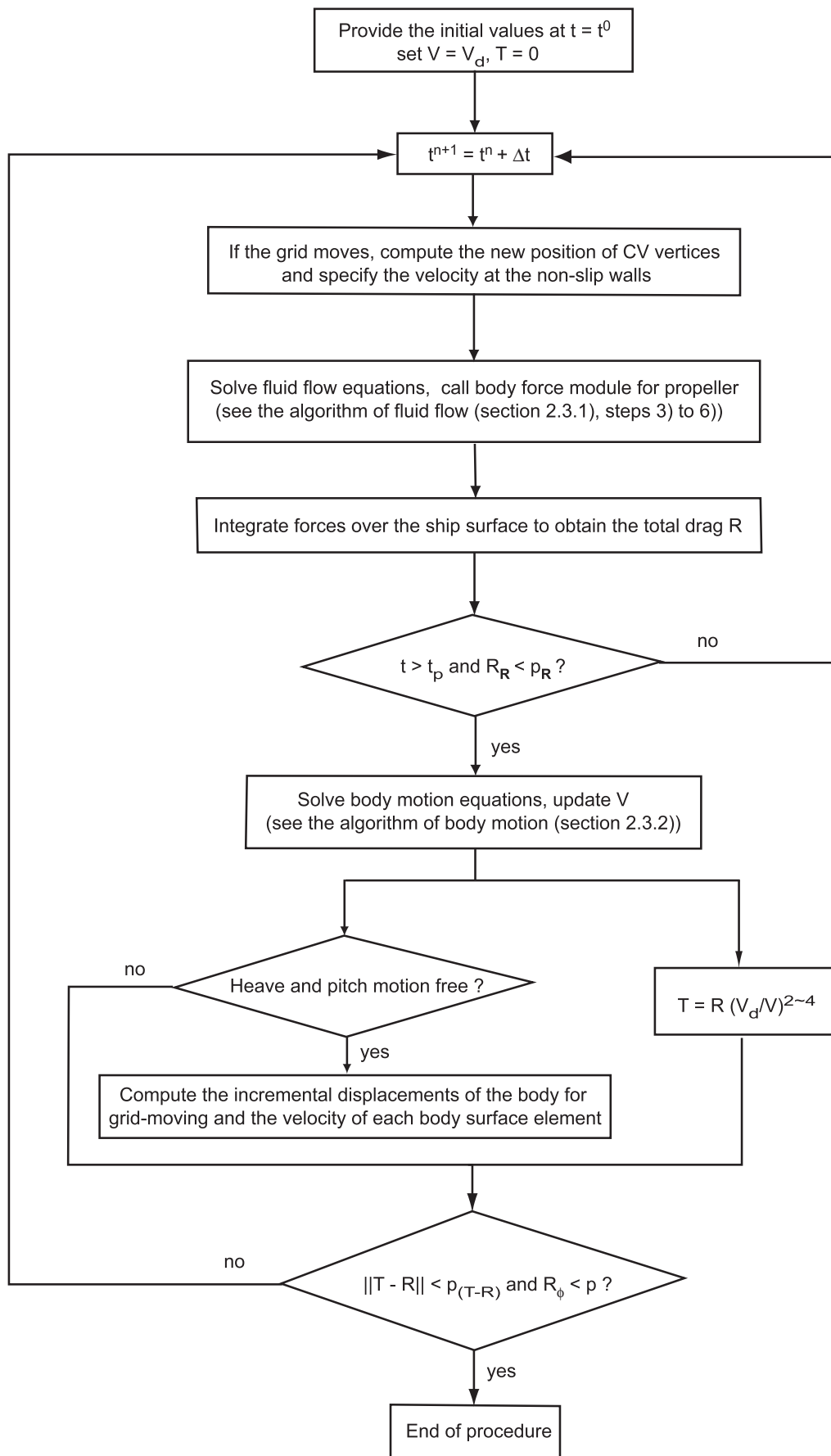


Figure 5.17: The coupled algorithm for self-propulsion test.

Table 5.2: Dimensions of the propeller.

D	D_h	P/D	A/A_o	x_p	z_p
5.000 m	1.471 m	1.168	0.513	3.00 m	2.805 m

Table 5.3: Coefficients from the propulsion diagram.

c_{T1}	c_{T2}	c_{Q1}	c_{Q2}
0.583	0.458	0.1145	0.0899

stern of the ship. The computed rudder forces considering propeller actions are compared with the free stream results from section 5.2.4.

The propeller model described in section 5.3.1 is employed to simulate the propeller effects. The thrust of the propeller is determined from the instant flow condition, using the method presented in section 5.3.2. The Propeller dimensions and its characteristics from open water tests are given in Tables 5.2 and 5.3. The dimensions of the rudder and the fixed fin are the same as in section 5.2.4, see Table 5.1. The distance and relative position of rudder and fixed fin to the propeller are illustrated in Fig. 5.18.

The same numerical grids and inflow conditions have been applied here as in section 5.2.4 and the resulting Y^+ is about 150 in average. The flow-determined propeller thrust loading coefficient C_{Th} is 1.94 in this case, which is defined as

$$C_{Th} = \frac{T}{0.5\rho V_A^2 A_o} . \quad (5.27)$$

The computed rudder forces in the propeller slipstream are higher than in free stream, as compared in Fig. 5.19. The transverse force increases by 50% at a rudder angle of $\delta = 10^\circ$ and 25% at $\delta = 30^\circ$ for the moderate propeller thrust loading coefficient $C_{Th} = 1.94$. The ratio will be higher for higher C_{Th} . The longitudinal force is almost double as the one in free stream for small and moderate rudder angles and the factor is less dramatic at higher rudder angles. The maximum transverse force of the rudder is reached at a larger rudder angle in propeller slipstream than in free stream, which is partially due to the higher degree of turbulence induced by the propeller and the different angles of attack for the upper and lower part of the rudder caused by the rotating flow field.

The axial velocity contours on the propeller plane ($0.30c$ in front of rudder) are shown in Fig. 5.20 at the rudder angle of $\delta = 10^\circ$. The corresponding velocity vectors on two planes $0.30c$ in front of and $0.30c$ behind the rudder are shown in Fig. 5.21 together with the dimensionless pressure distribution c_p ($c_p = \frac{p}{0.5\rho V^2}$) on the rudder surface. The asymmetrical axial velocity field on the propeller plane gives a reasonable impression: lower axial velocities in the region of the propeller hub where no body-force term is present; higher axial velocities at the suction side of the rudder. The rudder encounters varying angles of attack along its height due to the right-hand rotating propeller, as can be seen from the shifting of the maximum c_p

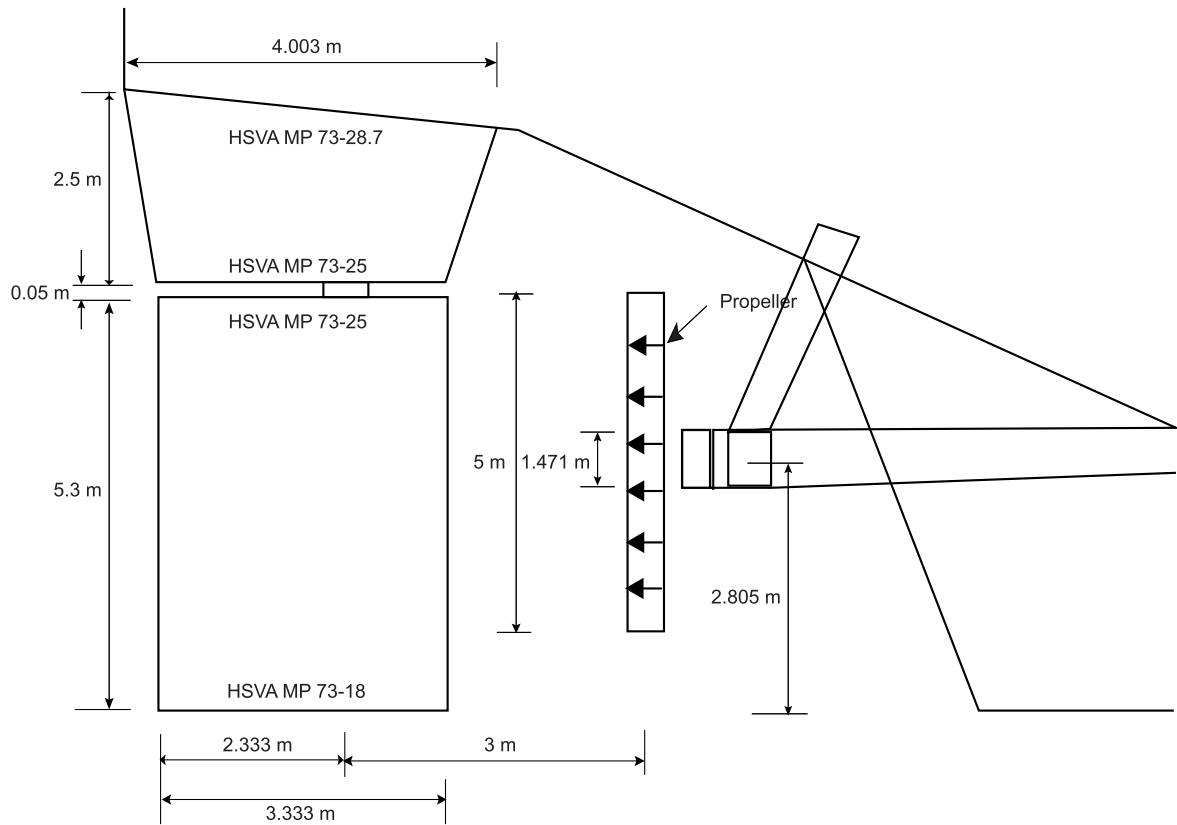


Figure 5.18: Rudder and propeller arrangement.

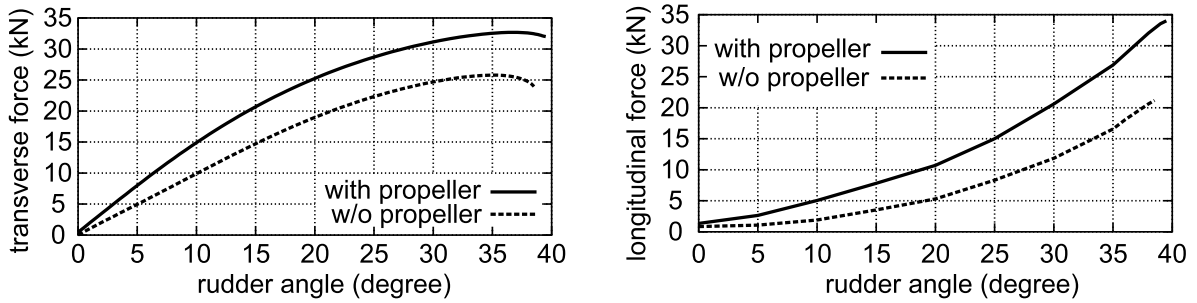


Figure 5.19: Rudder forces in propeller slipstream ($C_{Th} = 1.94$) and in free stream.

along the rudder height. Also strong vortices have been observed behind the upper and lower edge of the rudder, see Fig. 5.21 (b).

5.5 Computation of Rudder Forces behind Ship and Propeller

As already mentioned above, the rudder performance is strongly influenced by the presence of the ship and the propeller. In this section, the integrated system of propeller, rudder and ship will be investigated. The RoRo ship with twin propellers and twin spade rudders is considered here in a model scale of 1/34 and the results are compared with measurements of model tests. The model tests have been performed at HSVA at a constant ship speed ($F_n = 0.26$) and a constant propeller revolution of $n = 10.43 \text{ s}^{-1}$. Propellers rotate inwards against each other and simulated by the body-force distribution method described in section 5.3.1. The free surface is considered here to account for the effects of ship-induced waves and make the method straightforward for later applications to free-floating ship maneuvering by operating rudders.

The main dimensions of the RoRo ship are already given in Table 4.1. It has twin propellers and twin spade rudders, whose dimensions can be found in Tables 5.1 and 5.2. The multi-block grid has 1,050,000 cells and parts of the grid are shown in Fig. 5.6. The dimensionless Y^+ is about 100 on average.

Due to the presence of the free surface, the solution cannot be obtained by a steady-state solution method. Instead, the computations are performed in time domain using the pseudo-marching technique. That means the iterations do not have to be completely converged before the next time step begins. Therefore only one or a few iterations are performed per time step. As the residuals of flow variables and forces (concerning propeller, ship hull and rudder) decrease in time and fall below a prescribed criteria, the steady flow field (or wave system) has been finally obtained. Taking the advantage of the transient simulations and moving-grid techniques, the rudder can be rotated without the process being stopped, as in model tests. Therefore only a single computation is needed for computing the rudder forces at all rudder angles.

The computed rudder forces are given in Fig. 5.22 and compared with experimental results. The twin rudders are rotated from $\delta = -40^\circ$ to 40° by stepwise varying the rudder angle by $\Delta\delta = 8^\circ$ ($\delta = -40^\circ$ is not available in the experiments). As can be seen in Fig. 5.22, the agreement of the transverse force is quite good as far as moderate rudder angles (from $\delta = -24^\circ$ to $\delta = 24^\circ$) are concerned. The maximum transverse forces are under-predicted in the computation indicating that larger errors appear when the flow starts to separate. It is assumed that the modeling errors from the turbulence model and wall function become large in this case. The longitudinal forces have been over-predicted for all rudder angles as expected, which is partially due to the use of the turbulence model (standard $k-\epsilon$) and partially due to the propeller model (with the resistance effect of propeller hub neglected) as already explained before. In addition, the longitudinal force is more sensitive to discretization errors than the transverse force and the error would decrease if the grid spacing was further reduced, as grid-dependence tests in section 5.2.3 has shown. However, the basic rudder characteristic is predicted well by the computation.

Figures 5.23 and 5.24 show the non-dimensionalized axial velocity contours together with the tangential velocity vectors on the propeller plane $0.30c$ in front of the rudder at rudder angles of $\delta = 8^\circ$ and $\delta = 24^\circ$ respectively. Reversed flow can be found near the

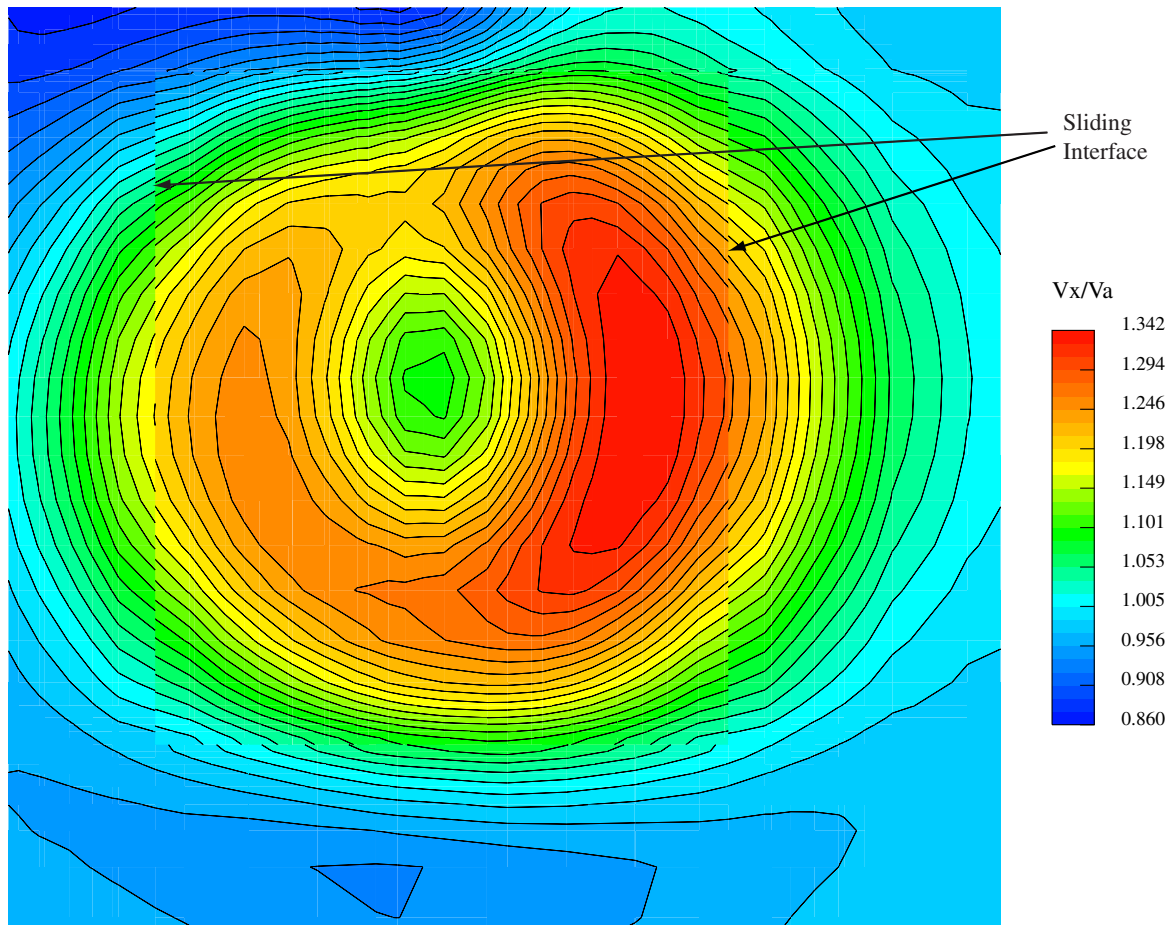


Figure 5.20: Axial velocity contour at the plane $0.30c$ in front of rudder ($\delta = 10^\circ$).

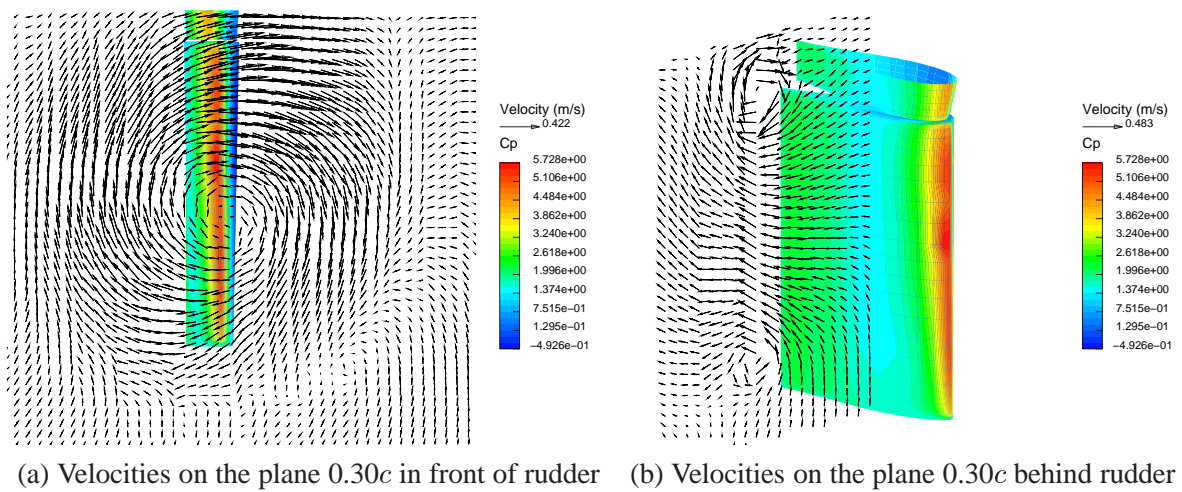


Figure 5.21: Pressure distribution on rudder and velocity vectors at two planes $0.30c$ in front of and behind the rudder ($\delta = 10^\circ$).

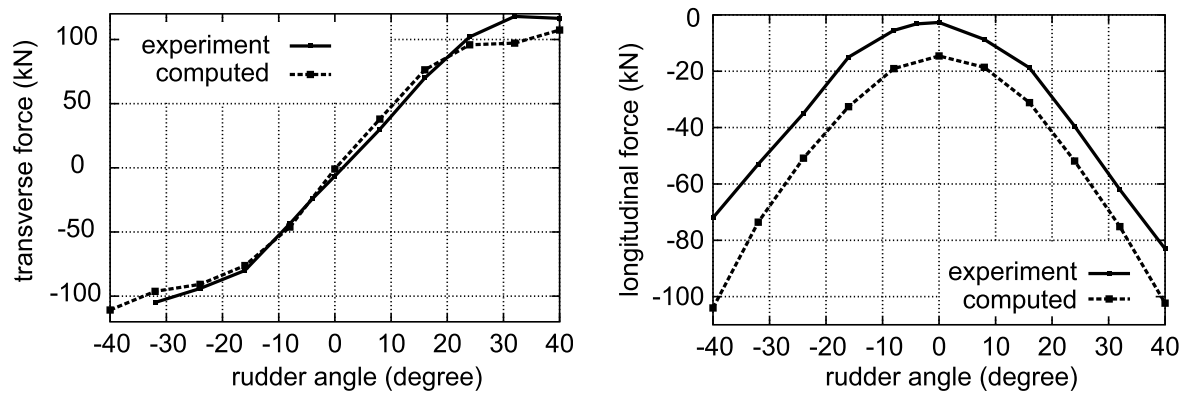


Figure 5.22: Comparison of rudder forces behind RoRo ship with experiment.

ship hull and a higher asymmetric flow field can be observed at $\delta = 24^\circ$. The corresponding velocity fields on the plane $0.10c$ behind the rudder are shown in Figs. 5.25 and 5.26. Thicker aft ship boundary layers can be observed and vortices are produced behind the lower edge of the rudder at $\delta = 24^\circ$.

Figure 5.27 shows the pressure distribution on the ship stern and rudder surfaces together with streaks of a few particles starting from the propeller plane giving an impression of the interaction of the coupled system. Finally, the computed ship-induced steady wave system is given in Fig. 5.28 at $\delta = 8^\circ$.

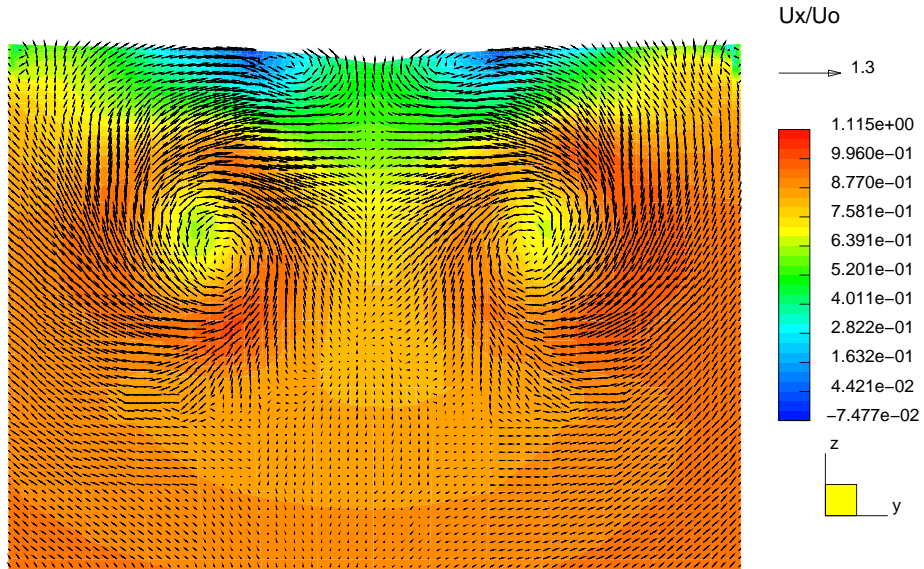


Figure 5.23: Axial velocity contours and tangential velocity vectors on the plane $0.3c$ in front of rudders ($\delta = 8^\circ$).

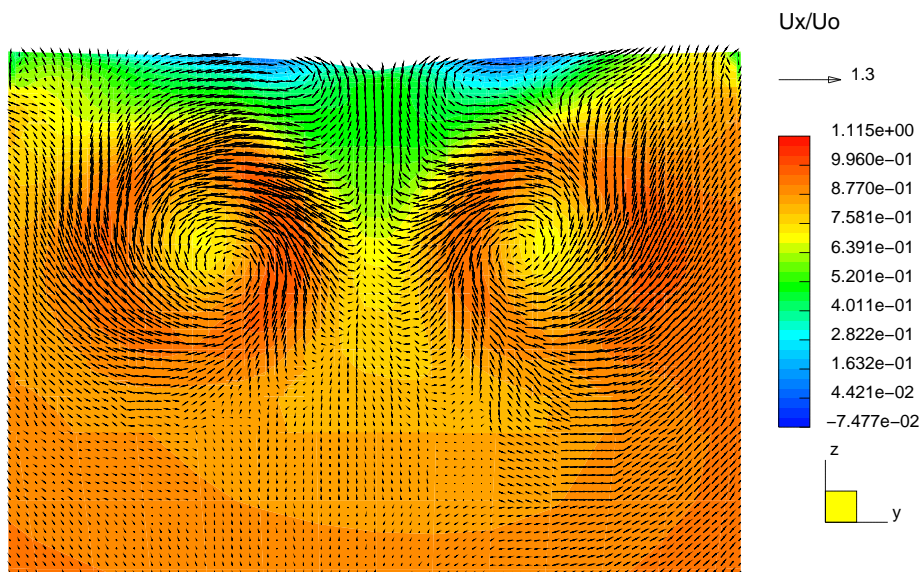


Figure 5.24: Axial velocity contours and tangential velocity vectors on the plane $0.3c$ in front of rudders ($\delta = 24^\circ$).

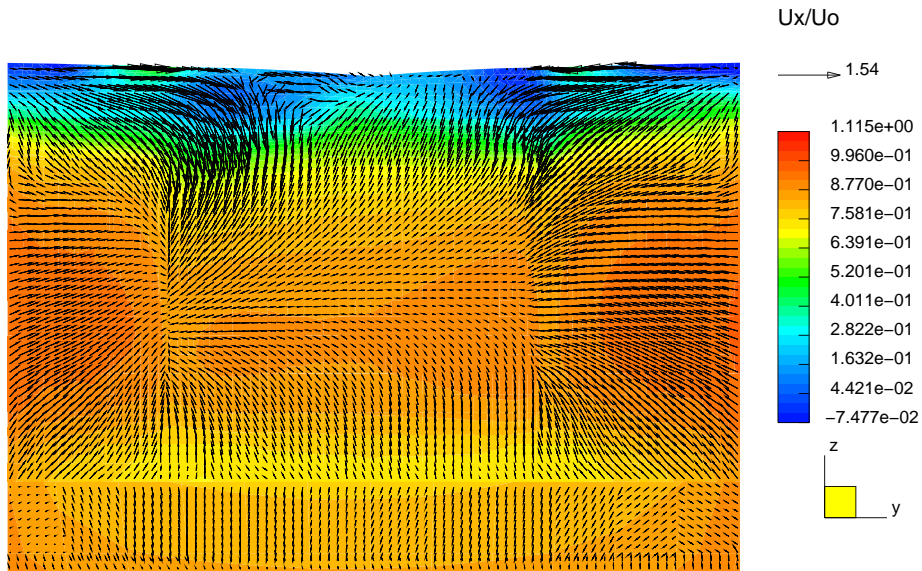


Figure 5.25: Axial velocity contours and tangential velocity vectors on the plane $0.1c$ behind rudders ($\delta = 8^\circ$).

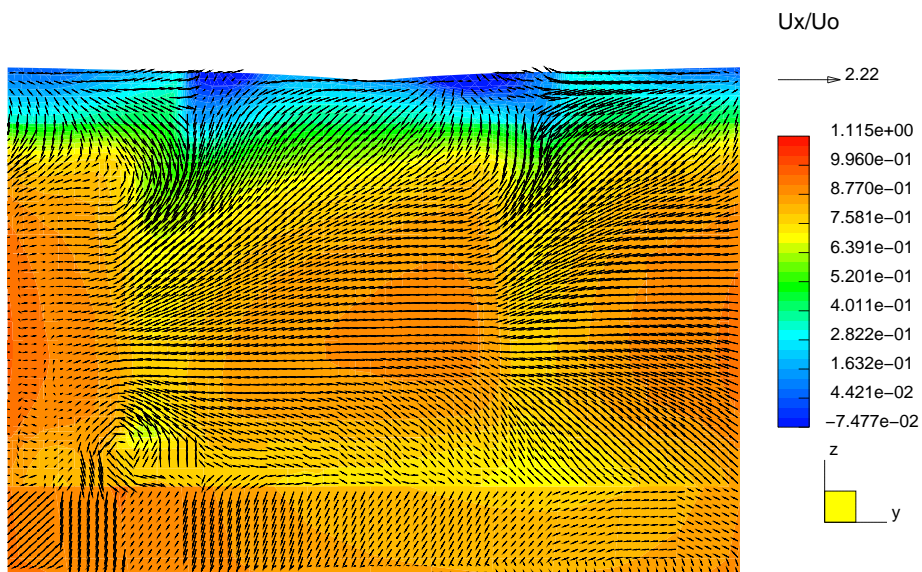


Figure 5.26: Axial velocity contours and tangential velocity vectors on the plane $0.1c$ behind rudders ($\delta = 24^\circ$).

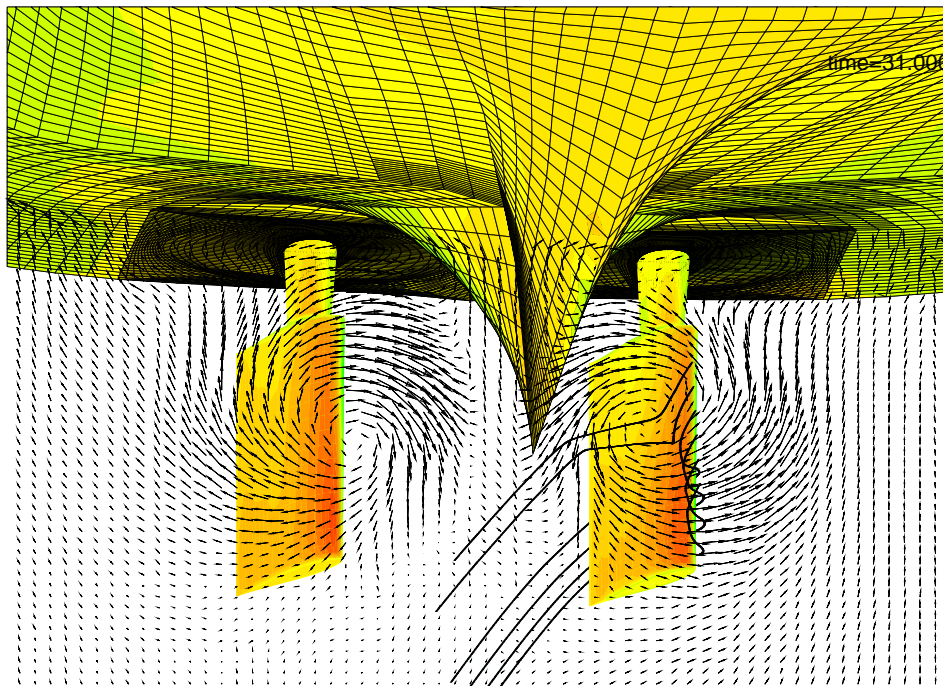


Figure 5.27: Pressure distribution on the ship stern and rudder surface, tangential velocity vectors on the propeller plane together with the paths of a few particles starting from the propeller plane ($\delta = 8^\circ$).

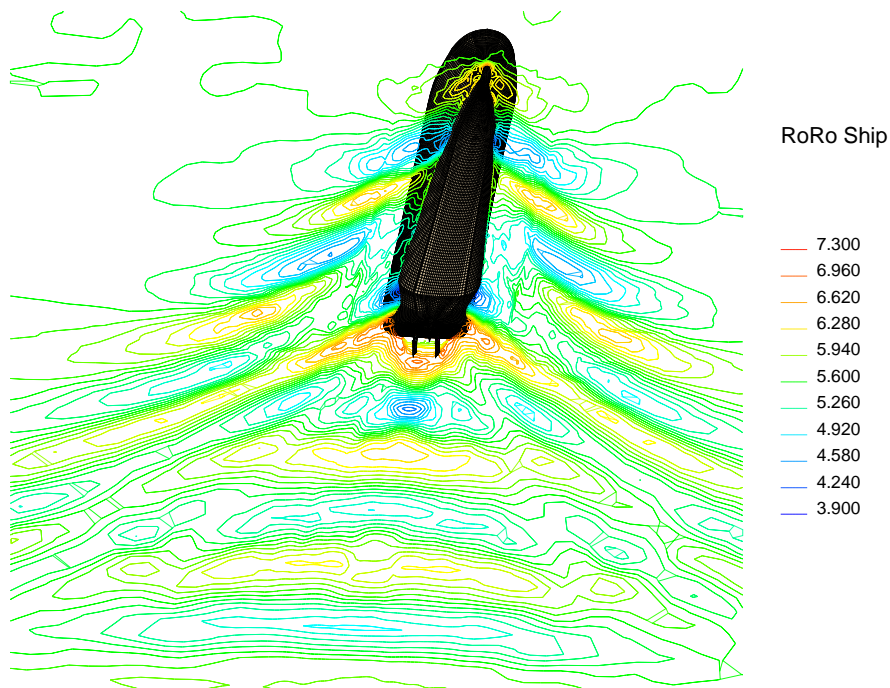


Figure 5.28: Ship-induced wave system at $\delta = 8^\circ$.

Chapter 6

Simulation of Ship Motion during Maneuvers

6.1 Introduction

In the previous chapter techniques for modeling individual maneuvering devices and their interaction with the hull have been presented. The emphasis of this chapter is on simulating the motion of a maneuvering ship with appendages in calm water or in waves using the present method.

Before motions of a ship during maneuvering are computed, the hydrodynamic forces and moments acting on the ship hull and the rudder surfaces during steady drift motion are examined. In section 6.2, steady drift motions of a container ship with appendages are computed, considering the free surface. The rudder is geometrically modeled with sliding interfaces around it to allow arbitrary rudder angles; the propeller is approximated by the body force model, as described in Chapter 5. The predicted forces and moments on the ship hull and rudder are compared with the measurements at a series of drift angles β .

Section 6.3 presents the turning circle maneuvers of two ship models. The Wigley hull, due to its simple geometry, is selected first to perform a captured turning circle maneuver to examine the suitability of the boundary conditions and moving-grid method. Roll, heave and pitch motions are free when the ship starts to turn while surge, sway and yaw motions are predefined since no rudder is modeled here. Next, the self-propelled container ship is considered during a turning circle maneuver in calm water with its own operating rudder.

Finally, Zigzag maneuvers are simulated for the Wigley hull and the container ship and the results are presented in section 6.4. First, a captured 25° Zigzag maneuver of the Wigley hull is simulated against incoming waves. Then, a $10^\circ/10^\circ$ Zigzag maneuver of the container ship with its own operating rudder is performed in calm water and in waves. The predicted track, motion and maneuvering characteristics of the ship are compared to available model test measurements.

6.2 Steady Drift Motion of a Container Ship Model

The container ship "CBOX", designed by FSG, has been taken as one of the test models in the ROLL-S project funded by the Germany Ministry of Education and Research (BMBF). The model tests with the CBOX ship have been carried out at model scale of 1/29 at the Hamburg Ship Model Basin (HSVA). The full-scale ship has the length of 145.75 m (L) between perpendiculars and the draught of 9.0 m. The dimensions of the CBOX ship model and its rudder are listed in Tables 6.1 and 6.2, respectively. The lines plan of the CBOX ship is given in Appendix E. The arrangement of rudder and propeller at the ship stern is illustrated in Fig. 6.1. Tables 6.3 and 6.4 give the dimensions and coefficients of the propeller. The captured ship model moves with constant forward speed ($F_n = 0.23$) and propeller revolution ($n = 12.3 \text{ s}^{-1}$) at several drift angles $\beta = -10^\circ, -5^\circ, -2.5^\circ, 2.5^\circ$ and 5° respectively. The rudder angle has been kept zero all the time. The side forces on the hull and the rudder have been measured for each drift angle.

The numerical computations are performed also at model scale for validation purposes. The computational domain extends to $1.5 L$ in front of the ship, $2.5 L$ beside the ship and $3 L$ behind the ship, connected to an additional region of gradually coarsened grid (numerical beach) to avoid reflected waves. The top and bottom boundaries are $1.0 L$ above and below the still water level to simulate a deep-water condition and minimize the air flow effect. The inlet boundary condition is applied at the boundaries in front of the ship and at the side where the flow enters the computational domain. The pressure boundary condition is specified at the boundaries behind the ship and at the side where the flow is supposed to leave the computational domain. The static air pressure boundary condition is given at the top boundary and the slip wall condition is specified at the bottom boundary. The computational grid consists of several blocks resulting in 1,200,000 cells. Figure 6.2 shows the grid around the ship hull, the rudder and the rudder fin, with the position of sliding interfaces indicated. The sliding interfaces are not activated in the analyses of this section ($\delta = 0^\circ$), but the same grid is used in sections 6.3 and 6.4 for the turning circle maneuver and the Zigzag maneuver with operating rudder.

The computation has been started at the drift angle $\beta = 0^\circ$ and a constant velocity corresponding to $F_n = 0.23$. The body forces simulating the effects of the propeller are added right after the start. The total thrust and torque of the propeller are determined by the instant inflow condition (section 5.3.2) and the distribution of the body forces follows the assumptions given by Stern et al. [80], as introduced in section 5.3.1. The fluid in front of and behind the propeller is accelerated by the imposed body forces and the iterations have to continue until a steady state of the fluid flow and the propeller forces is reached and residuals of both are below a prescribed value. Next, the boundary conditions are varied with different drift angles and the computations continue for each drift angle until flow field and forces on the hull and the rudder do not vary any more.

The side force, yaw and roll moments acting on the ship hull are made non-dimensional as follows:

$$Y' = \frac{Y}{0.5\rho V^2 L T}, \quad (6.1)$$

$$N' = \frac{N}{0.5\rho V^2 L^2 T}, \quad (6.2)$$

$$K' = \frac{K}{0.5\rho V^2 L^2 T}, \quad (6.3)$$

where ρ is the density of water, V is the ship speed, L is the ship length and T is the draft of the ship. The non-dimensional transverse force on the rudder is defined here in a similar way to the rudder lift force (Eq. (5.2)):

$$F'_y = \frac{F_y}{0.5\rho V^2 A_R}, \quad (6.4)$$

where A_R is the rudder area (see Eq. (5.4)).

The predicted forces (moments) on the ship hull and the rudder are compared between computation and experiment in Figs. 6.3 and 6.4. The agreement is rather satisfactory, especially for the forces on the ship hull. The larger differences of the rudder lift forces are assumed to be consequences of the simplified model of the propeller since the propeller slipstream has a strong influence on the rudder inflow and thus on rudder forces. The computed free surface deformation is shown in Fig. 6.5 for different drift angles $\beta = 0^\circ, 2.5^\circ, 5^\circ, 10^\circ$. As the drift angle increases, stronger asymmetry and increased/decreased wave amplitudes at the starboard/port sides can be observed.

The dynamic pressure distribution on the ship hull and the rudder surface and the shear stress distribution on the ship hull are shown in Fig. 6.6 for a drift angle of $\beta = 10^\circ$. As can be seen, the maximum pressure appears at the leading edge of the rudder due to the propeller slipstream. High pressure appears on the ship bow at starboard while the bow at portside is subjected to large shear stress. The corresponding axial velocity contour and tangential velocity vectors at the cross section $x = -0.45 L$ viewed from the stern are shown in Fig. 6.7. As can be seen, the flow becomes strongly asymmetric in this case and a small vortex is developed at the portside of the stern, as can also be seen in the kinetic energy distribution, Fig. 6.8, at this cross section.

The steady drift motion tests serves here as a preliminary step for further maneuvering simulations. The good agreement of forces acting on the ship hull and rudder has been obtained between experiment and simulation indicating that the applied numerical discretization (grid resolution and schemes) is sufficient in predicting the global forces on ship hull and rudder during maneuvering situations.

Table 6.1: Dimensions of the CBOX ship model

L_{pp}	B	T	∇	LCB
5.026 m	0.814 m	0.310 m	9.745 m ³	2.468 m
KM	GM	i_{xx}	i_{yy}	λ
0.348 m	0.059 m	0.255 m	1.060 m	29

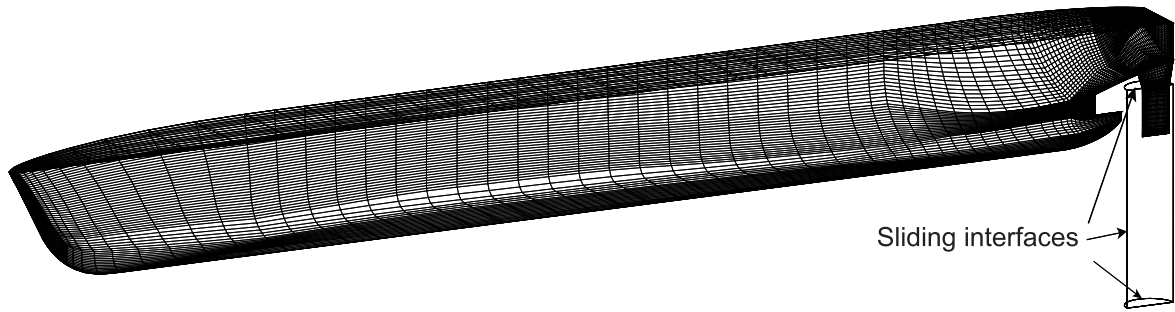


Figure 6.2: Numerical grid of the CBOX ship.

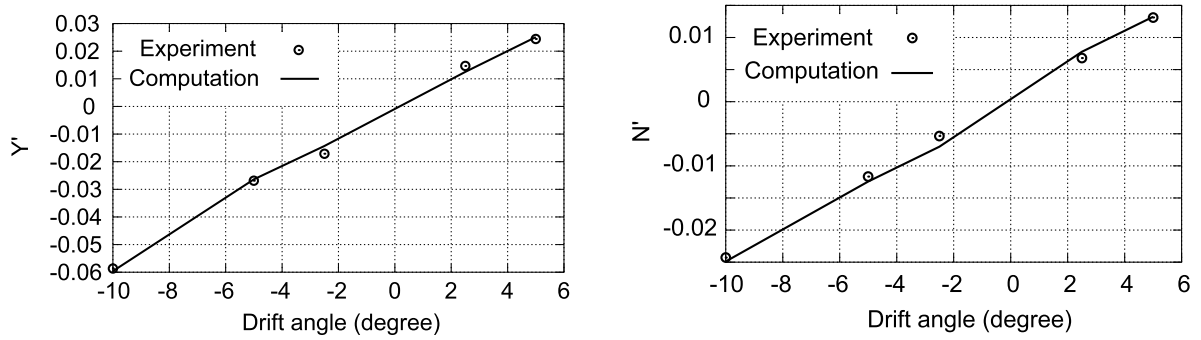


Figure 6.3: Comparison on the non-dimensional side force (left) and yaw moment (right) on ship hull as a function of drift angles.

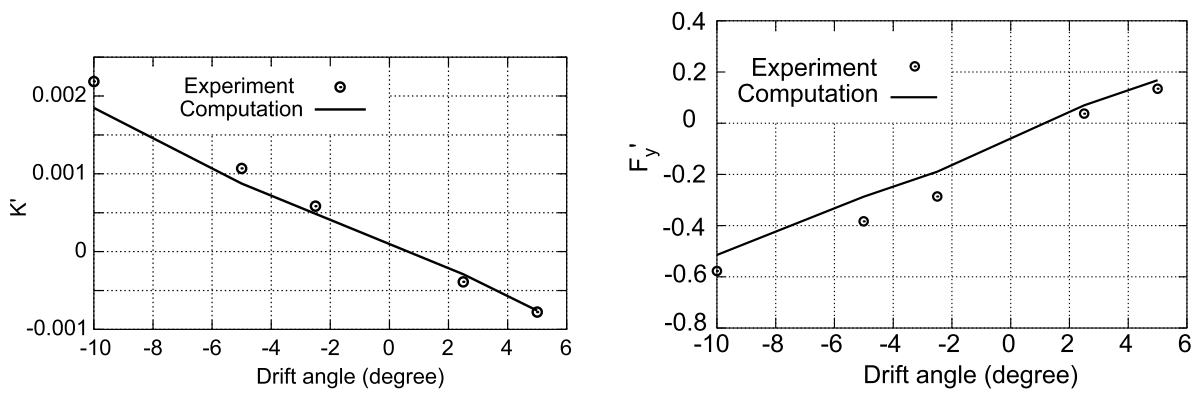


Figure 6.4: Comparison on the non-dimensional roll moment on the ship hull (left) and the non-dimensional transverse force on the rudder (right) as a function of drift angles.

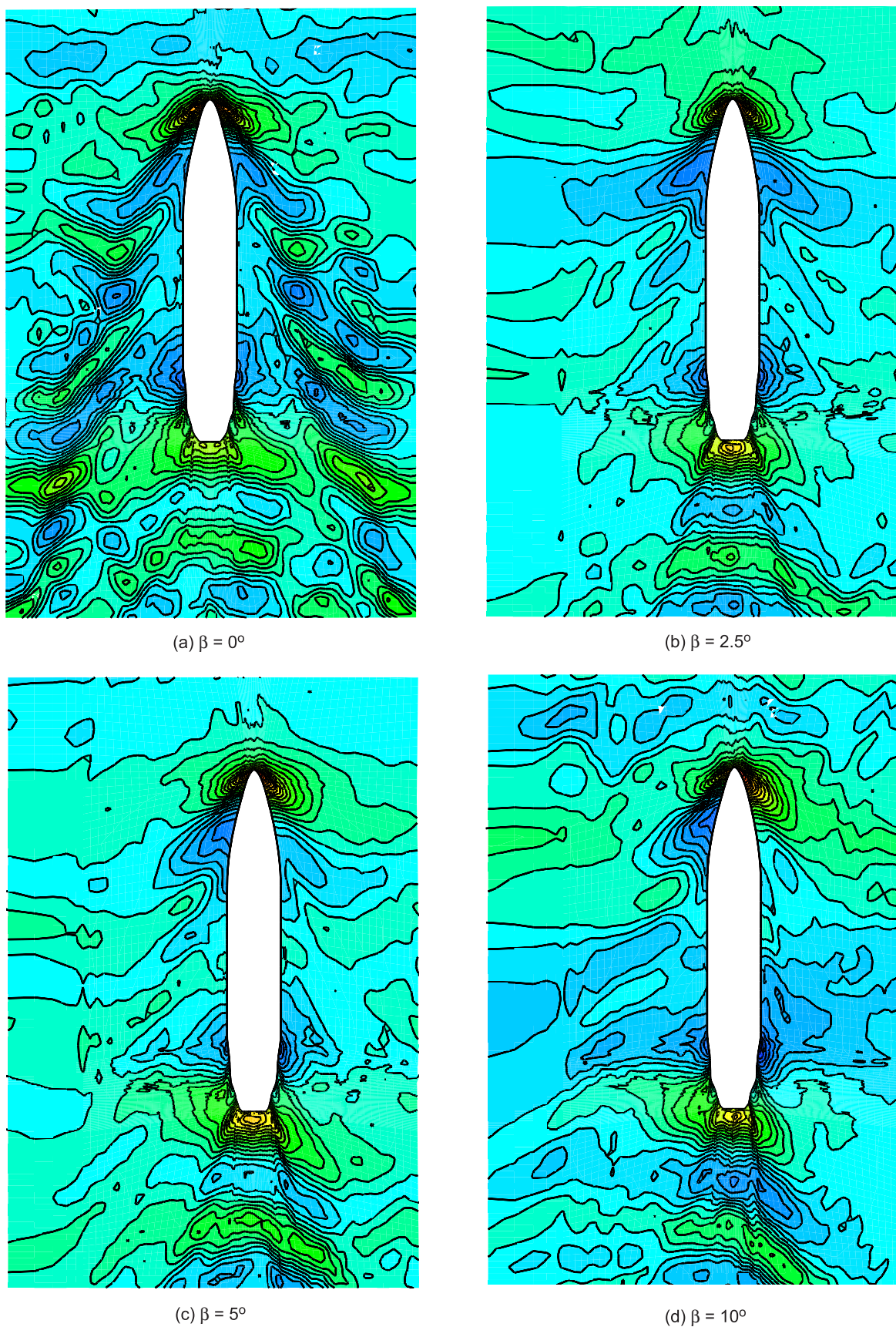


Figure 6.5: Free surface deformation of CBOX ship under different drift angles (delta of isolines $\Delta\zeta = 5.345 \cdot 10^{-3}$ m).

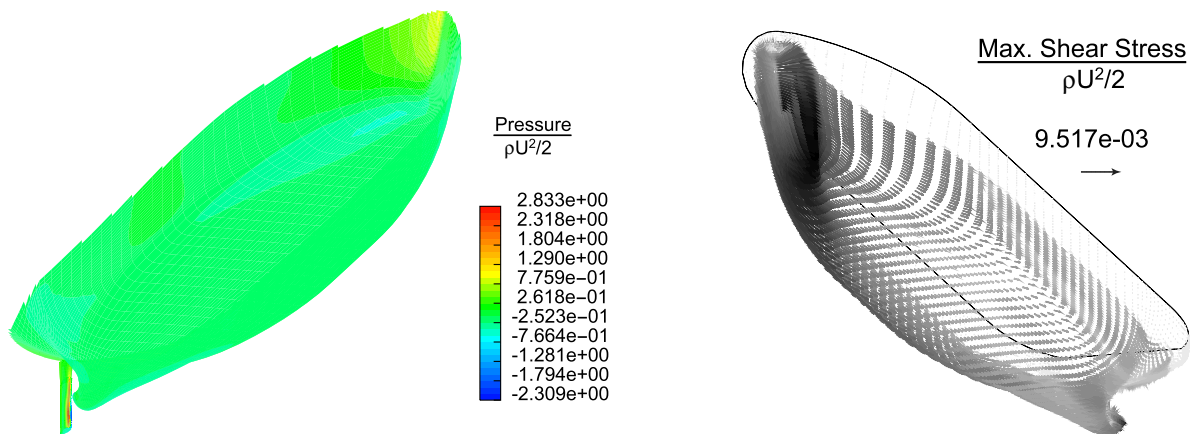


Figure 6.6: Dynamic pressure distribution (left) and shear stress (right) of CBOX ship ($\beta = 10^\circ$).

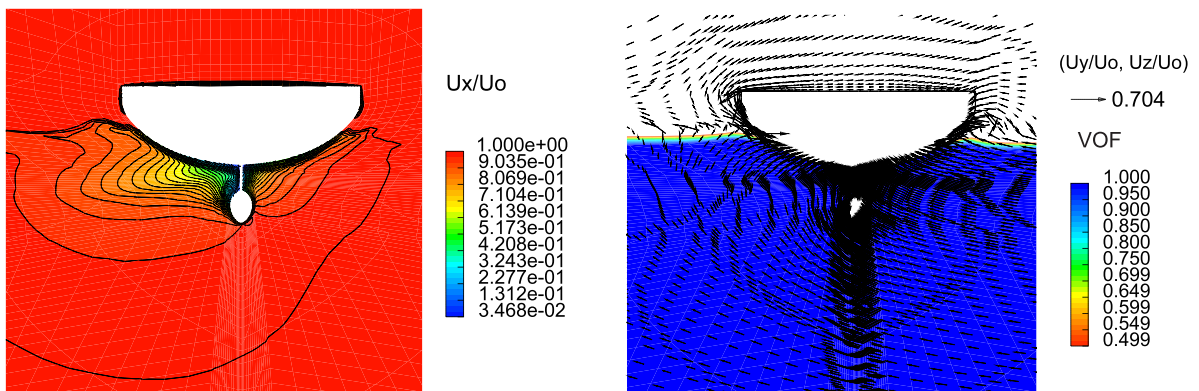


Figure 6.7: Velocity distribution at $x = -0.45 L$ ($\beta = 10^\circ$): axial velocity contours (left) and tangential velocity vectors together with free surface position (right), viewed from stern.

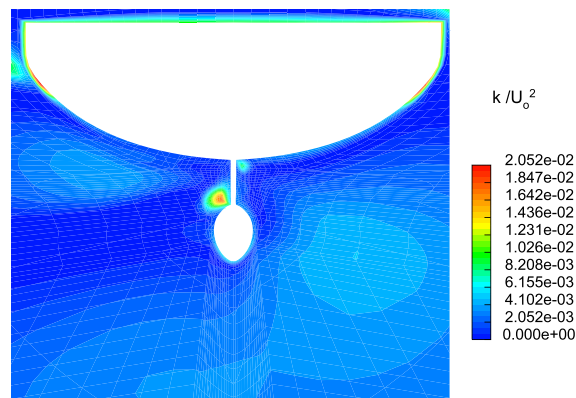


Figure 6.8: Turbulent kinetic energy distribution at $x = -0.45 L$ ($\beta = 10^\circ$), viewed from stern.

6.3 Turning Circle Maneuvers

6.3.1 Wigley Model

A semi-captured turning circle test of a Wigley model in calm water has been carried out in the numerical tank. The same numerical grid used in section 4.2.2 has been adopted here as shown in Fig. 6.9 together with the boundary conditions. Boundary conditions are somewhat special in this case. A combination of inlet and pressure boundary condition is applied to the side wall at the inner side of the turning circle as indicated in Fig. 6.9, since the fluid is flowing in and out simultaneously at this boundary. The inlet boundary condition is specified at the boundary in front of the ship. For the side wall at the outer side of the turning circle as well as the boundary behind the ship, the pressure boundary condition is employed.

Since no rudder is modeled here, the yaw motion and the track of the Wigley model are predefined, as given in Fig. 6.10. The turning circle maneuver is performed with a drift angle of $\beta = 0^\circ$. The speed of the ship corresponds to $F_n = 0.29$ and the non-dimensional yaw rate is set to be 0.4. The heave, pitch and roll motions are set free during the turning circle. The grid around the ship is adapted to the moderate heave, pitch and roll motions of the ship; for the large yaw motion and the motion due to ship's forward speed, the whole grid is moved with the ship.

The computation of the free surface for the turning circle maneuver of the Wigley ship gives quite reasonable wave patterns. Figure 6.11 shows the computed free surface deformation at different time instances when the heading of the model becomes 90° , 180° , 270° and 360° .

The computed roll, heave and pitch motions of the Wigley ship during the turning circle maneuver are shown in Fig. 6.12. All three motions oscillate and no steady state has been reached. The maximum roll angle appears at the end of the turning circle maneuver, where the model is forced to run straight forward again. The non-dimensional heave motion and the pitch motion are predicted negative in average over the period of turning circle maneuver.

6.3.2 Container Ship Model

A turning-circle maneuver has been performed for the container ship CBOX, see Appendix F for the definitions of the turning-circle maneuver test.

The computation has been started from a self-propelled ship in steady straight motion with a constant velocity corresponding to $F_n = 0.23$. Once the steady state is reached, the rudder is turned portside by a turning rate of $13.5^\circ/s$ until the maximum rudder angle ($\delta = 35^\circ$) is reached. This rudder angle is then kept until the ship has performed a turning-circle of 540° . To avoid complexity, the thrust of the propeller has been kept constant during the turning circle maneuver. The ship is expected to turn dramatically at the initial turning before the steady state of turning is reached. Free surface deformations can be seen from Fig. 6.13 during the turning circle maneuver at yaw angles $\psi = 0^\circ$, 30° , 60° and 90° , respectively. The block surrounding the rudder ($\delta = 35^\circ$) by sliding interfaces can also be seen from Fig. 6.13.

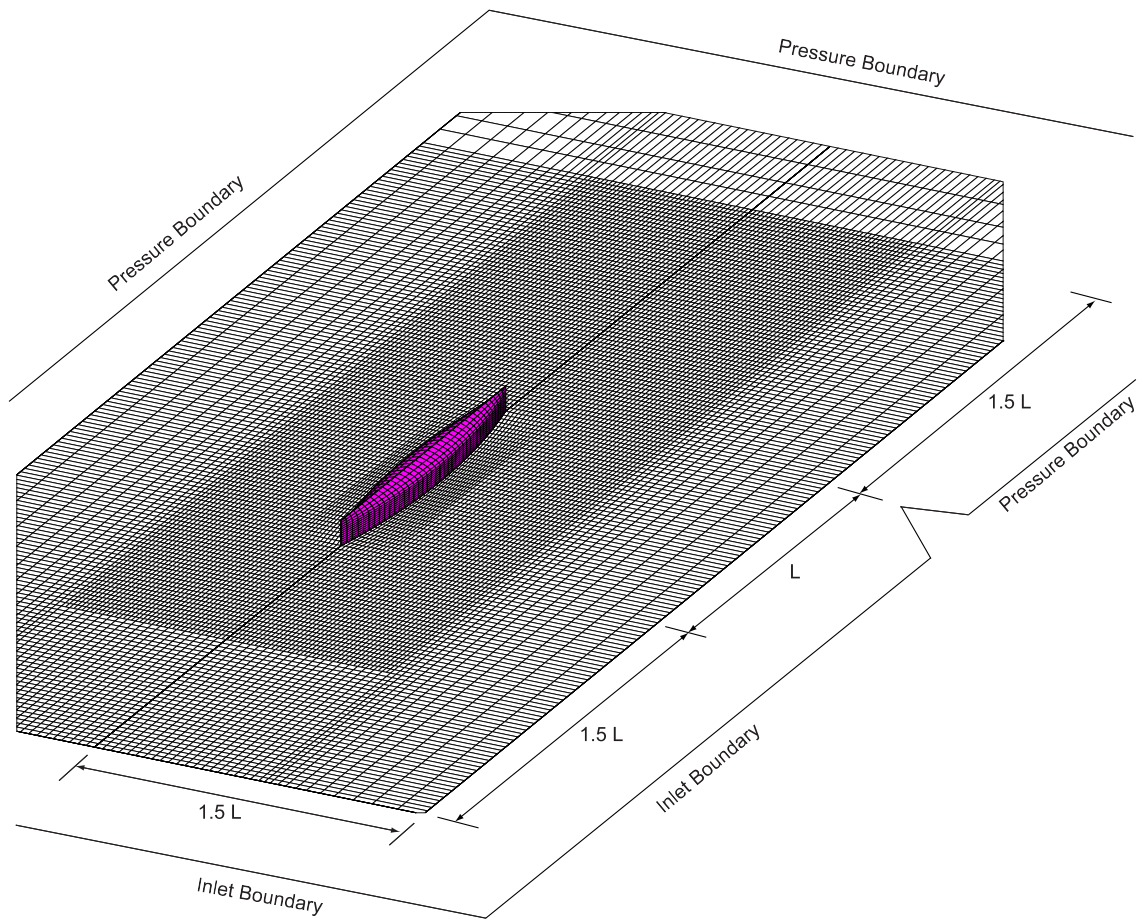


Figure 6.9: Numerical grid and boundary conditions for the turning circle maneuver of a Wigley model.

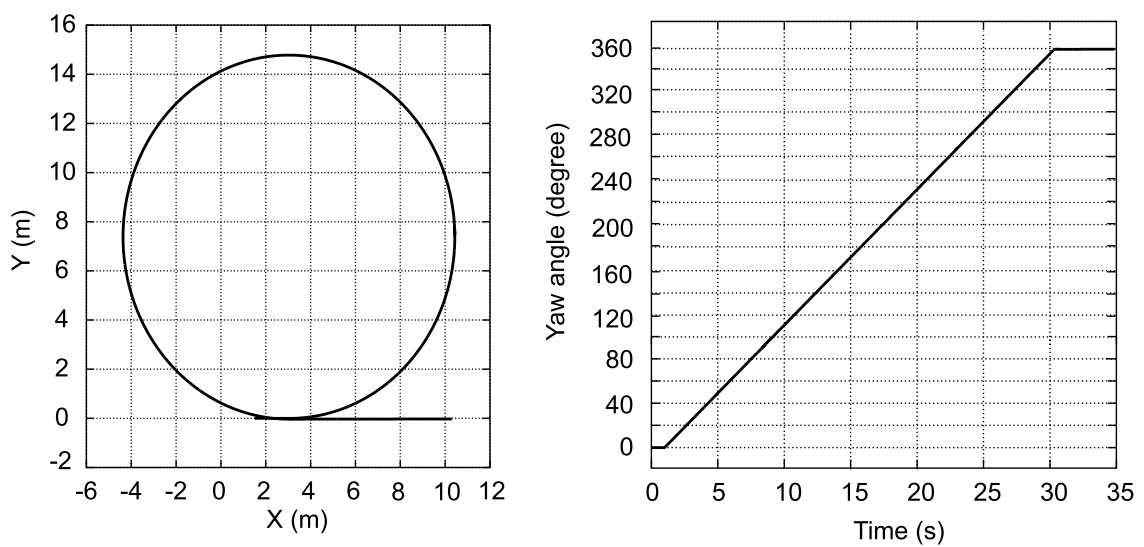


Figure 6.10: Predefined track (left) and heading (right) of the Wigley model during the turning circle maneuver.

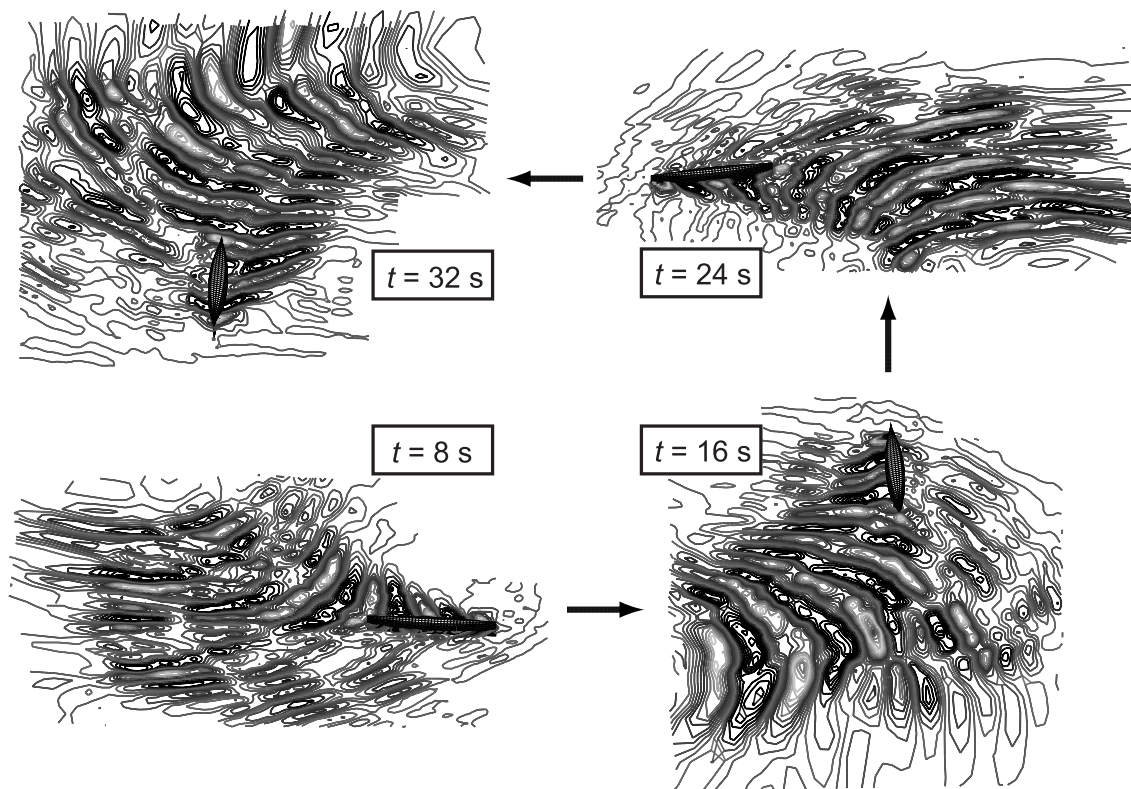


Figure 6.11: Free surface deformation during a turning circle maneuver of the Wigley model (Delta of isolines $\Delta\zeta = 0.004$ m).

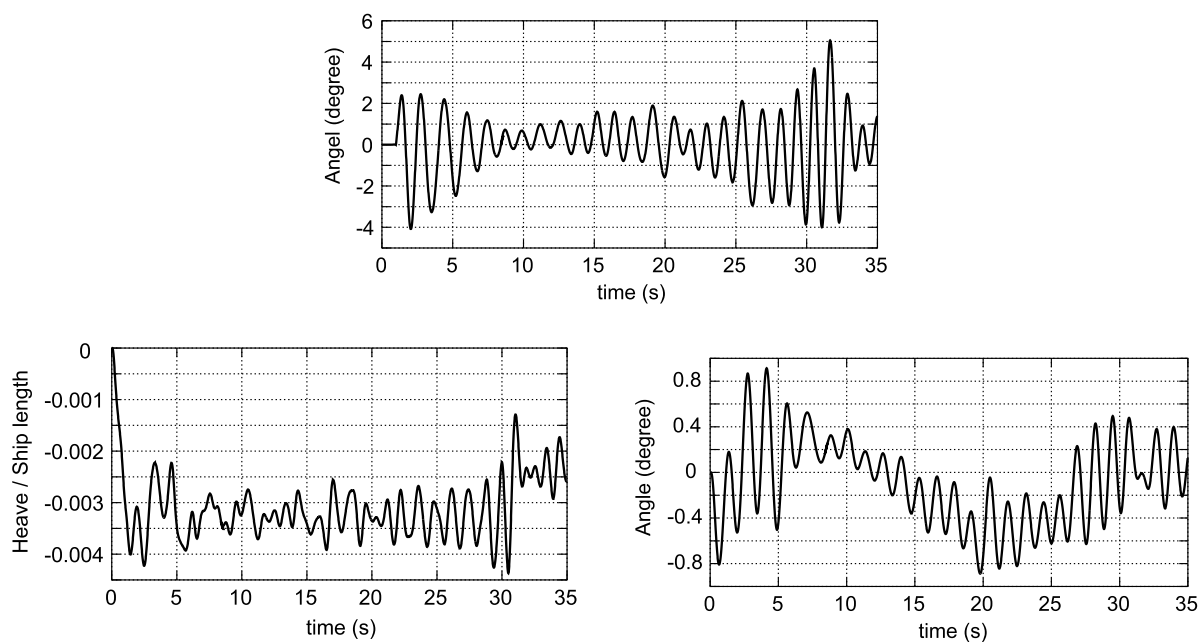


Figure 6.12: Roll (top), heave (left) and pitch (right) motion of the Wigley model during a turning circle maneuver.

Table 6.5: Computed characteristics of turning circle maneuver of the CBOX ship

	Froude Number	Tactical diameter	Max. Advance	Transfer (at 90°)	$\dot{\psi}'$	U/U_o
Computation (model scale)	0.23	2.70 L	3.50 L	1.37 L	0.3	0.48

The computed yaw rate and the horizontal velocity of the ship are given in Fig. 6.14 against time. The non-dimensional yaw rate $\dot{\psi}'$ approaches the value of 0.3 at the steady turning state. The speed of the ship has also been decreased dramatically at the beginning of the turning circle and then reached a steady state at half of the initial speed. The computed tactical diameter is about 2.70 L , which is in the range of typical values for a container ship. The computed characteristics of the turning circle maneuver are given in Table 6.5.

Figure 6.15 shows the dynamic pressure distribution on the ship hull and the rudder surface as viewed from portside and starboard. As can be seen, the dynamic pressure on the ship stern is positive at the starboard side and negative at the port side of the ship, respectively. The maximum pressure appears on the leading edge of the rudder (from starboard view). The axial velocity contour and tangential velocity vectors at the cross section $x = -0.45 L$ are shown in Fig. 6.16 together with distorted mesh and free surface position. As can be observed, the ship has slightly heeled toward starboard ($\phi = 2^\circ$), as expected.

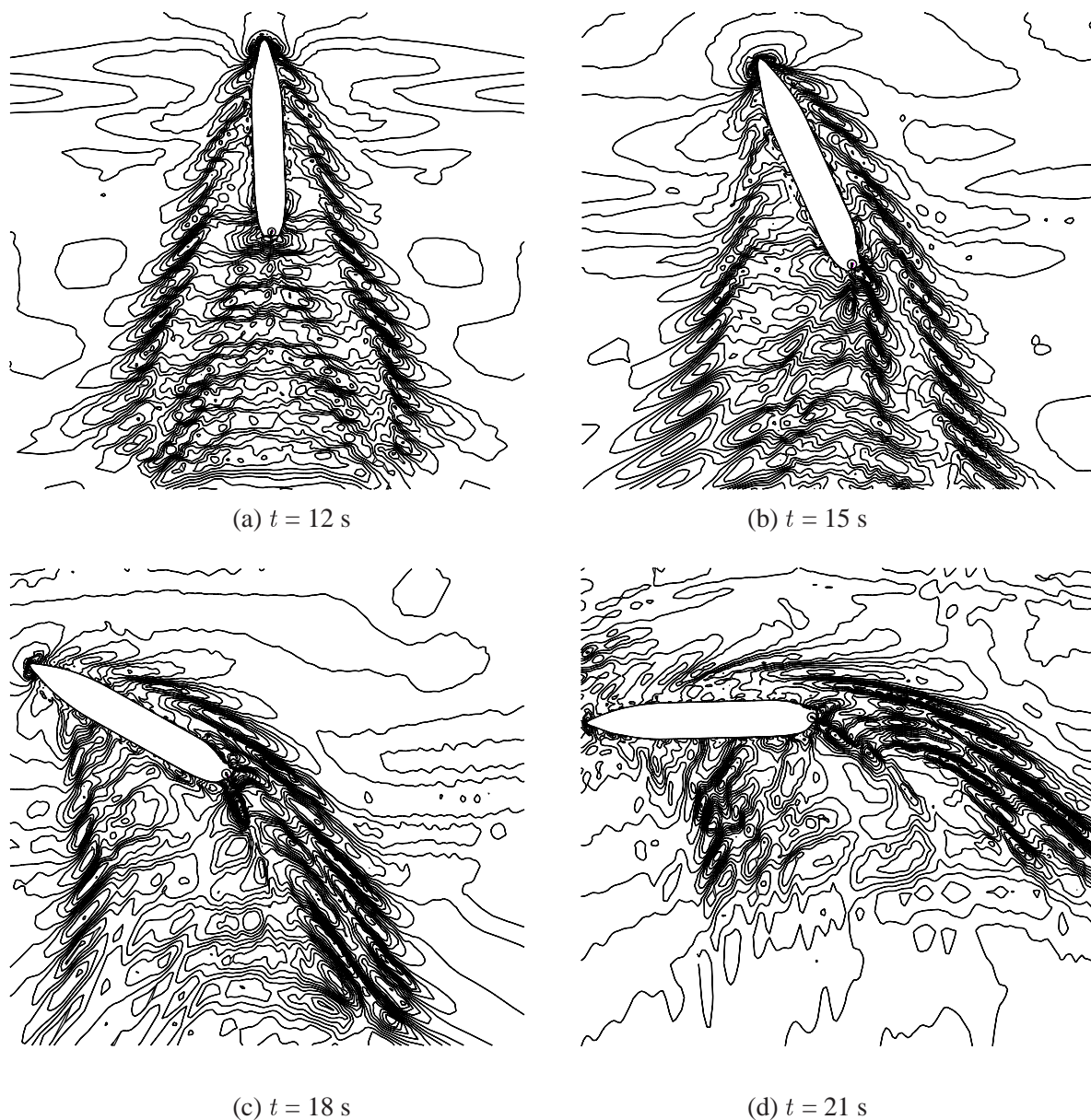


Figure 6.13: Free surface deformation during a turning circle maneuver of the CBOX ship ($\Delta\zeta = 5.414 \cdot 10^{-3}$ m).

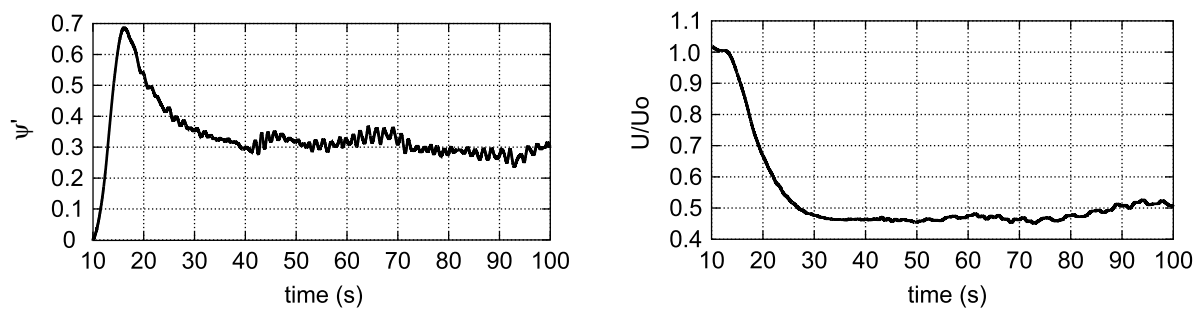


Figure 6.14: Yaw rate (left) and absolute velocity (right) for a turning circle maneuver of the CBOX ship.

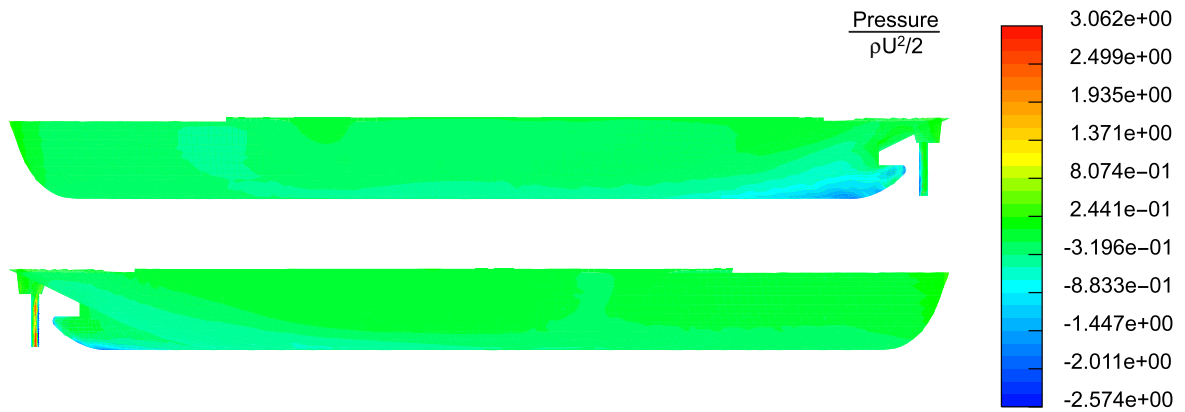


Figure 6.15: Dynamic pressure distribution on the ship hull and the rudder at port side (top) and starboard (bottom).

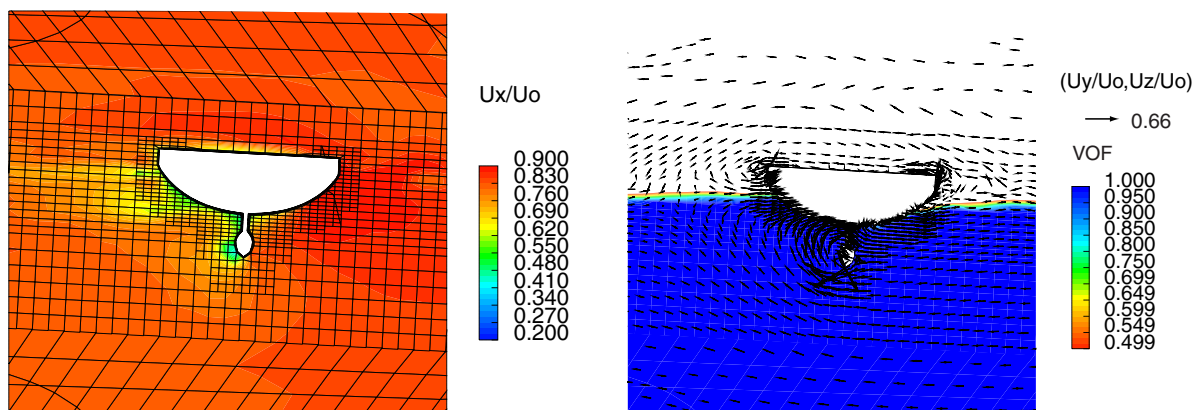


Figure 6.16: Axial velocity contours with distorted mesh (left) and tangential velocity vectors with free surface position (right) at the cross section $x = -0.45 L$ ($\phi = 2^\circ$), viewed from stern.

6.4 Zigzag Maneuvers

6.4.1 Zigzag Maneuver of a Wigley Model in Waves

Using the same grid system of the Wigley model as that employed in the simulations of ship motion in oblique waves (section 4.2.2) and the turning circle maneuver (section 6.3), a 25° captured Zigzag maneuver is performed in incoming head waves to test the applied boundary conditions and moving-grid strategies for Zigzag maneuvers. The model is forced to run at a constant forward speed ($F_n = 0.18$). Since no rudder exists here, prescribed transverse and yaw motion are applied, see Fig. 6.17.

The resulting wave pattern is given in Fig. 6.17 at a selected time instant $t = 7.0$ s, showing a reasonable coupled wave system.

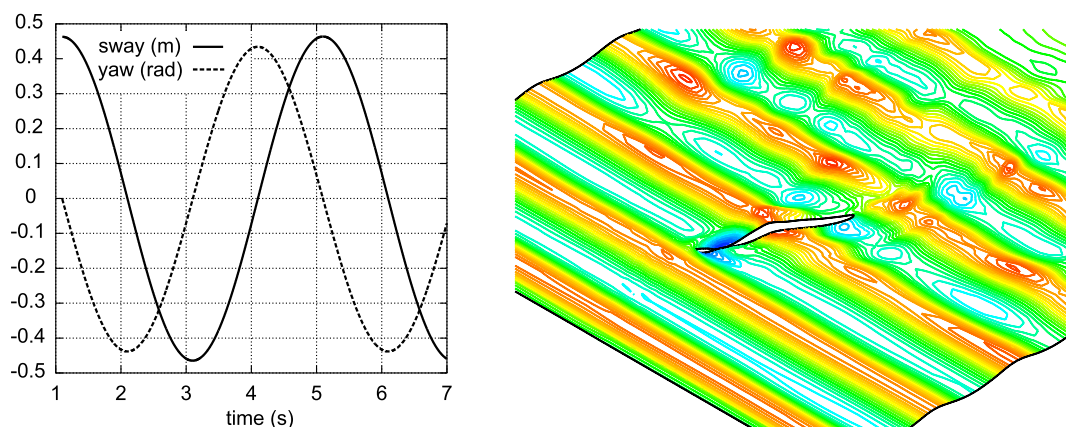


Figure 6.17: Sway and yaw motion (left) and computed wave pattern at $t = 7.0$ s (right) during a 25° Zigzag maneuver of the Wigley hull ($F_n = 0.18$).

6.4.2 Zigzag Maneuver of a Container Ship Model in Calm Water

Experiment

The Zigzag maneuvering tests were performed for the CBOX ship in the Hamburg Ship Model Basin (HSVA) at a model scale $\lambda = 1/29$. The typical procedure and definitions for conducting a Zigzag maneuver test are given in Appendix G.

The details of the ship and its appendages have already been given in Tables 6.1-6.4. The model is trimmed at the prescribed draft and the height of the center of mass is adjusted to fit the predefined GM.

In the Zigzag maneuvering test, the model is essentially free in all six degrees of freedom. It is maneuvered automatically by computer according to pre-programmed commands on propeller and rudder. The special tracking hardware consists of electro-mechanical tracking lag transducers in all six degrees of freedom and a model locking device. The six lag transducers can measure the motion of the ship model without introducing any force or moment on the model (almost frictionless). In the test the surge, sway, yaw and roll motions of

the ship are measured in time domain. The propeller forces and forces acting on the rudder are also recorded as well as the rudder angle. The revolution of the propeller is kept constant during the maneuver.

Different series of Zigzag maneuvers are performed for the CBOX ship model in combination with different rudder angles δ_R and the *switching angle* ψ_s for each predefined GM. The 'Zigzag Maneuver a°/b° ' denotes the rudder angle $\delta = a^\circ$ and the *switching angle* $\psi_s = b^\circ$.

From the series of measurements, the dependency of each acceleration component on the velocity components and rudder angles can be determined and such that the coefficients of the differential equations of maneuvering motion can be computed.

Computation

Using the same numerical grid of the CBOX ship as that used in the steady drift motion (section 6.2), a Zigzag maneuver $10^\circ/10^\circ$ in calm water is selected here for the numerical simulation with six degrees of freedom. The GM is predefined to be 0.059 m corresponding to the value in the model tests.

The steady-state ship motion in straight course ($F_n = 0.23$) is used as the initial state of the Zigzag maneuvering motion simulation. Firstly, the rudder starts moving to starboard side at a given constant turning rate ($\dot{\delta}_R = 13.5^\circ/s$) until its angle becomes 10° . The ship gradually starts yawing. As soon as the heading of the ship becomes 10° , the counter-steer is executed to set the rudder angle to 10° port side. After the overshoot of the heading, the ship turns towards the extension of the initial heading direction. The similar procedure is made when the heading becomes -10° and, consequently, the ship is maneuvered in a Zigzag curve.

Figure 6.18 shows the comparison of the time history of the simulated heading and rudder angle as well as the track of the ship with the experiment. As can be seen, the agreement is in general quite satisfactory, especially for the time until the first *overshoot angle* α_{o1} is reached. Although the first *overshoot angle* is a bit over-predicted in the simulation by 3.70%, the second *overshoot angle* α_{o2} is slightly under-predicted by about 1.78%. The *time to attain switching value of heading* τ_a and the first *time to check yaw* τ_{b1} (10°) are predicted rather accurately, namely with differences between measurement and computation ranging in 1.79% and 0.25%, respectively. The second *time to check yaw* τ_{b2} (-10°) is, however, predicted too short (by 19.1%), indicating that the maneuvering function of the rudder is stronger in the simulation than in the experiment. The cause might be partially from the simplified propeller model which produced larger thrust than the one in the experiment, as shown in Fig. 6.22 and will be discussed again later. In addition, the relatively low grid resolution might be another source of error (discretization error). The *reach time* τ_r is predicted shorter in the simulation than in the measurement (by 6.70%) again due to the stated reason, which results in the *maximum transverse* $y_{o\max}$ being predicted about 15.4% smaller than in the measurement, see Fig. 6.18. The dimensionless characteristics of the Zigzag maneuver are compared between measurements and computation in Table 6.6, showing promising agreement.

Figure 6.19 depicts the time histories of the drift angle and the yaw rate of the container ship during the Zigzag maneuver. The agreement is again quite good between measurement and computation, although the computed drift angles are a little larger than those of the

experiment. In particular, the maximum drift angle is predicted to occur earlier and being larger during the second *time to check yaw* suffering again from the larger propeller forces in this period. A similar tendency can be observed in the predicted time history of the yaw rate.

Despite the larger propeller forces in the simulation for the period of the second *time to check yaw* (Fig. 6.22), the ship has lower speed and smaller transverse in the simulation than in the model test (see Figs. 6.20 and 6.21) indicating that the ship is experiencing higher resistance due to a larger drift angle in the simulation than in the model test (see Fig. 6.19). The reason that the propeller forces are computed larger by the propeller model in the period of the second *time to check yaw* may lie in computing the thrust based on an ideal (homogeneous and frictionless) inflow field. In reality, the inflow of the propeller in this period is very complex and strongly inhomogeneous under unsteady angles of attack.

Although the simplified propeller model employed here introduces a certain degree of error, the overall agreement is reasonably good. Figures 6.23 and 6.24 compare the drag, lift forces and the stock moment of the rudder, showing good agreement. In particular, the magnitude of the rudder lift force has been well predicted during the first *time to check yaw*. Larger deviations of rudder forces in the period of the second *time to check yaw* can be again observed.

Figure 6.21 shows the time history of the roll motion. Until the final stage of the experiment ($t > 25$ s) the tendency of the roll motion is similar in experiment and computation. Since the roll motion is a very sensitive parameter in the Zigzag maneuver, no better agreement was expected. In the final phase, the larger deviation in the roll motion between experiment and computation is supposed to be a consequence of all deviations identified above.

The computed free surface deformations are shown in Fig. 6.25 at the headings $\psi = 10^\circ$ and $\psi = -10^\circ$, respectively. As can be seen, the wave pattern at $\psi = 10^\circ$ is somewhat similar to the one produced by steady drift motion although more asymmetry can be observed here keeping in mind that the drift angle is only about 3.5° at $\psi = 10^\circ$. However, the wave pattern at $\psi_s = -10^\circ$ has become much more complex at the beginning of the second *time to check yaw*. It seems to be the result of superposition and interaction of several wave systems due to dynamic yaw/drift motion of the ship. Although the wave pattern from the computation looks rather convincing, there is unfortunately no corresponding experimental pictures to be compared to.

The dynamic pressure distributions on the ship hull and the rudder surface of the CBOX ship are viewed from port and starboard sides in Figs. 6.26 and 6.27 at $\psi = 10^\circ$ and $\psi = -10^\circ$, respectively. The maximum pressure appearing at the leading edge of the rudder is much higher at $\psi = -10^\circ$ than at $\psi = 10^\circ$ due to higher propeller forces. As can be observed, the dynamic pressure at the stern is higher at $\psi = 10^\circ$ (in most areas positive) than the one at $\psi = -10^\circ$ (in most areas negative). As the distribution of the dynamic pressure on the bow is of similar magnitude for both yaw angles, the ship is experiencing higher resistance at $\psi = -10^\circ$ as stated above. The dynamic pressure at the stern is – as expected – higher at the starboard for $\psi = 10^\circ$ and at the port side for $\psi = -10^\circ$, respectively.

The axial velocity contours and tangential velocity vectors at the cross section $x = -0.45 L$ are shown in Figs. 6.28 and 6.29 together with the free surface position at

$\psi = 10^\circ$ and $\psi = -10^\circ$, respectively. As can be seen, the ship has slightly heeled about 0.5° starboard and 2.0° port side, respectively. As the initial ship speed has been taken to scale the axial velocity, a reduction of ship speed can be observed at $\psi = -10^\circ$.

The computations presented in sections 6.3 and 6.4 are one of the first maneuvering simulations by coupled solution of turbulent free surface flow and floating-body motion. As a first test of this kind of simulation, the method has shown its potential in reproducing the complex maneuvering behavior of a self-propelled and -steered ship in the *Virtual Towing Tank*. The method has demonstrated to be rather robust. The level of accuracy which can be achieved today is mainly restricted by grid resolution (computer resource), turbulence model and propeller model. From a practical point of view, this coupled technique will definitely replace more and more model tests in the future.

Table 6.6: Comparison of the characteristics of the $10^\circ/10^\circ$ Zigzag maneuver between model test and computation.

Non-dimensional Variables	Model Test ($F_n = 0.23$)	Computation ($F_n = 0.23$)	Error
α_{o1}	0.330	0.342	3.64%
α_{o2}	-0.590	-0.579	-1.86%
τ_a'	1.837	1.805	-1.74%
τ_{b1}'	2.553	2.546	-0.27%
τ_{b2}'	3.227	2.611	-19.1%
τ_r'	7.359	6.866	-6.70%
ψ'_{\min}	-0.396	-0.422	6.57%
y'_{\max}	1.940	1.642	-15.4%

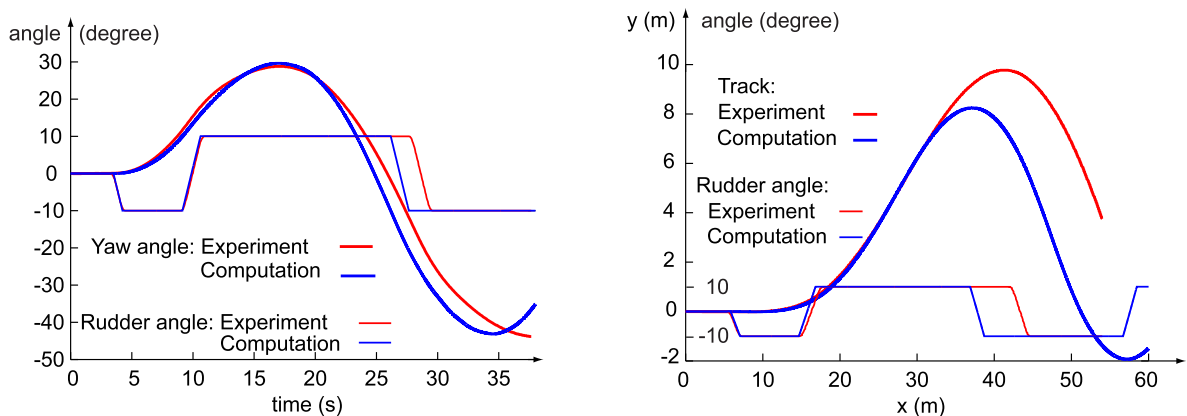


Figure 6.18: Time history of the heading (left) and the track (right) together with the rudder angle of the CBOX ship during the Zigzag maneuver.

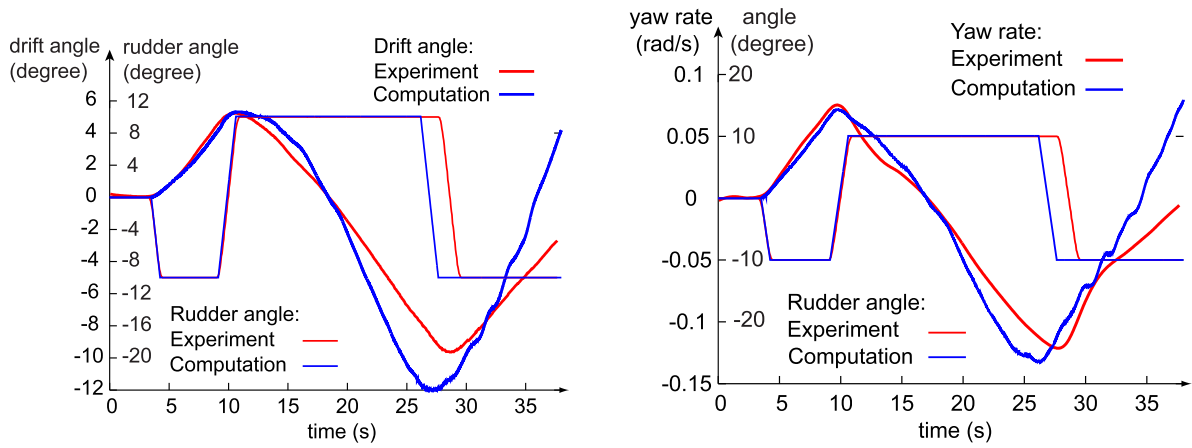


Figure 6.19: Time history of the drift angle (left) and the yaw rate (right) together with the rudder angle of the CBOX ship during the Zigzag maneuver.

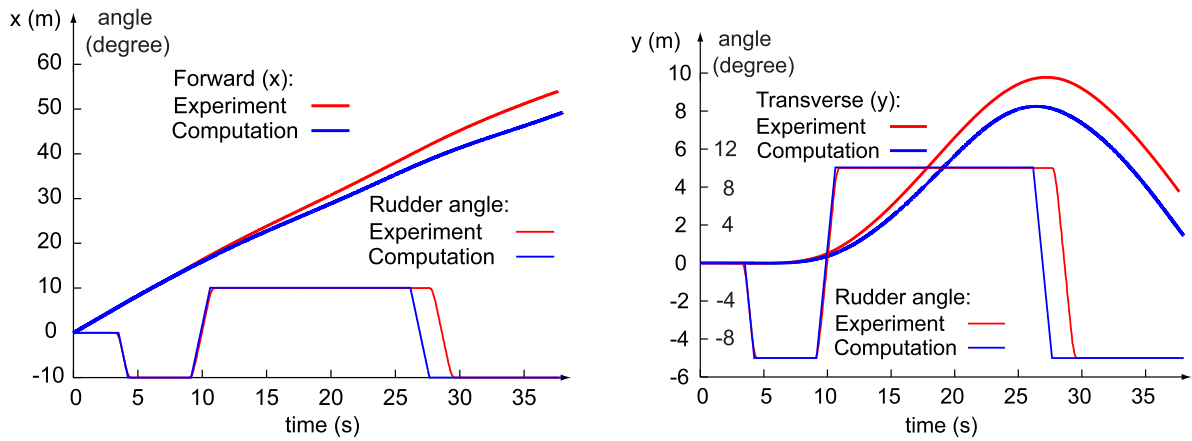


Figure 6.20: Time history of the forward (left) and the transverse (right) displacements together with the rudder angle of the CBOX ship during the Zigzag maneuver.

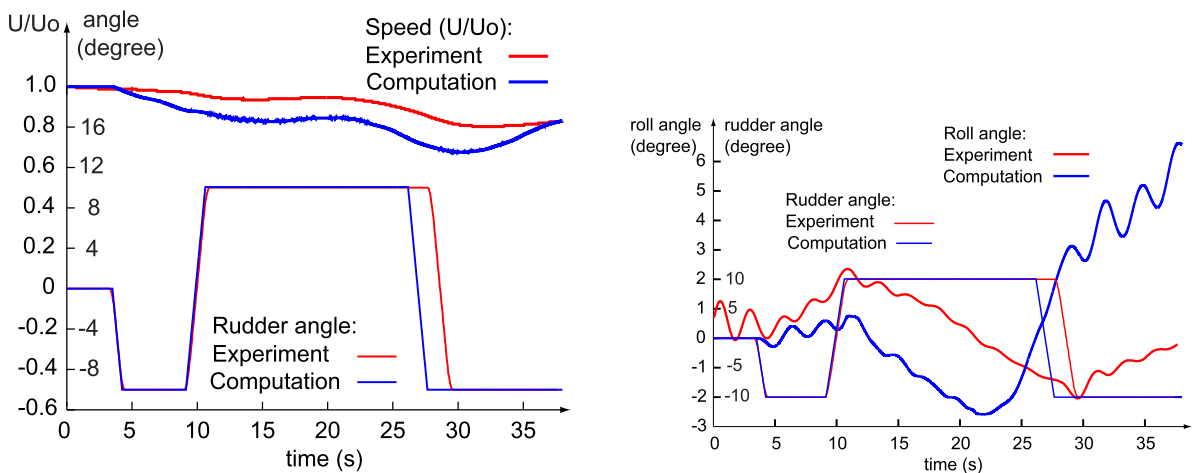


Figure 6.21: Time history of the non-dimensional ship speed (left) and the roll angle (right) together with the rudder angle of the CBOX ship during the Zigzag maneuver.

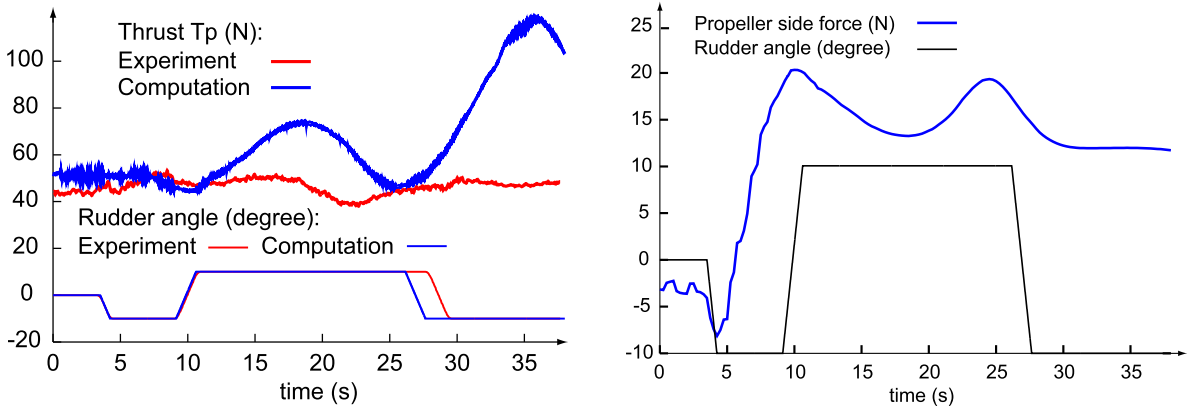


Figure 6.22: Time history of the propeller thrust (left) and the side force (right) together with the rudder angle of the CBOX ship during the Zigzag maneuver.

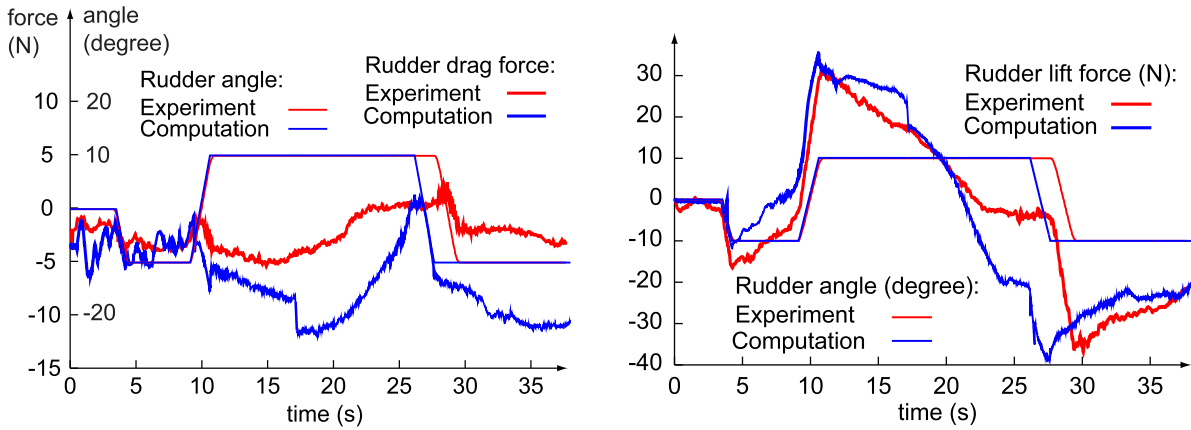


Figure 6.23: Time history of the drag (left) and the lift (right) forces on the rudder together with the rudder angle of the CBOX ship during the Zigzag maneuver.

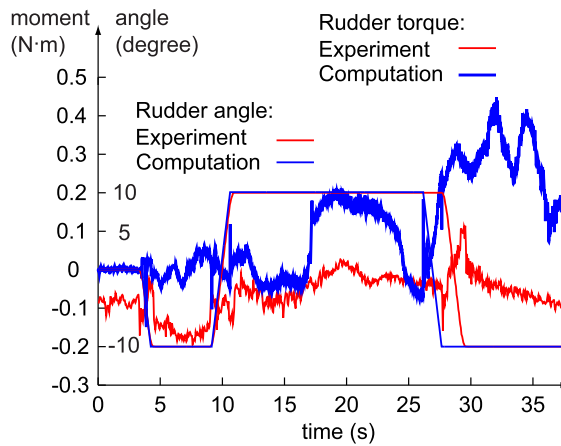


Figure 6.24: Time history of the torque on the rudder shaft together with the rudder angle of the CBOX ship during the Zigzag maneuver.

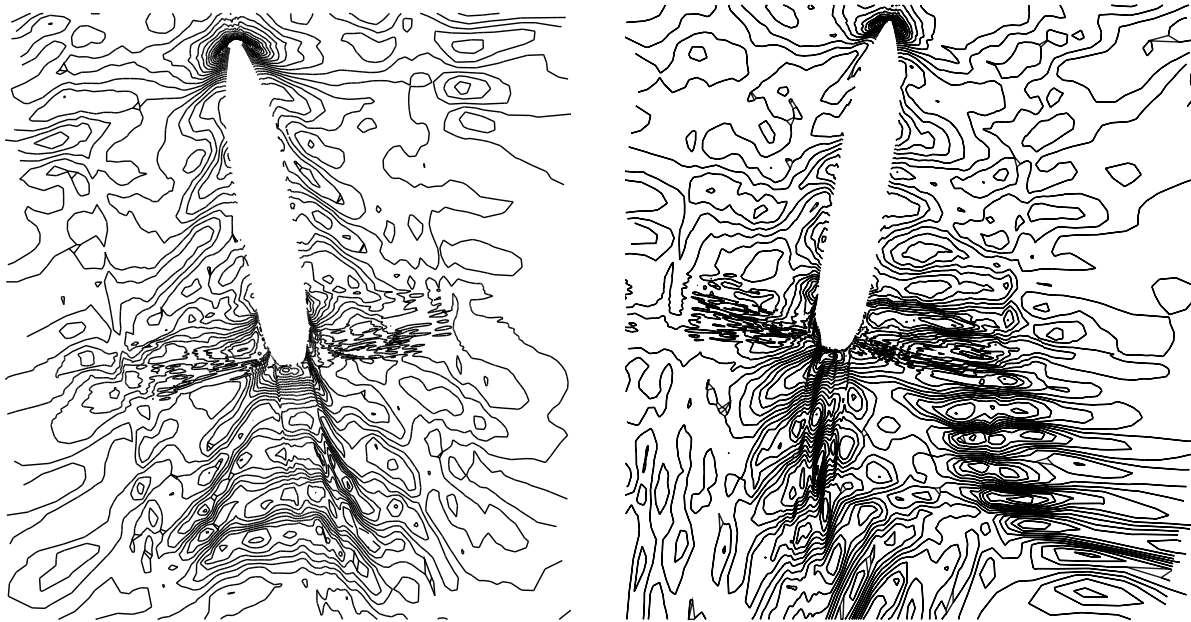


Figure 6.25: Computed free surface deformation of the CBOX ship at $\psi = 10^\circ$ (left) and $\psi = -10^\circ$ (right) during the Zigzag maneuver.



Figure 6.26: Dynamic pressure distribution on the ship hull and the rudder surface of the CBOX ship at $\psi = 10^\circ$ during the Zigzag maneuver, viewed from port side (top) and starboard (bottom).

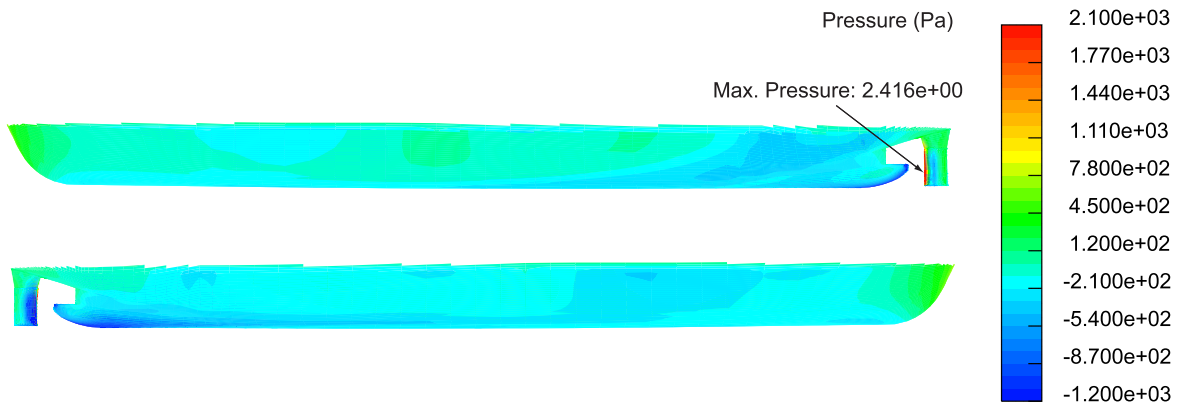


Figure 6.27: Dynamic pressure distribution on the ship hull and the rudder surface of the CBOX ship at $\psi = -10^\circ$ during the Zigzag maneuver, viewed from port side (top) and starboard (bottom).

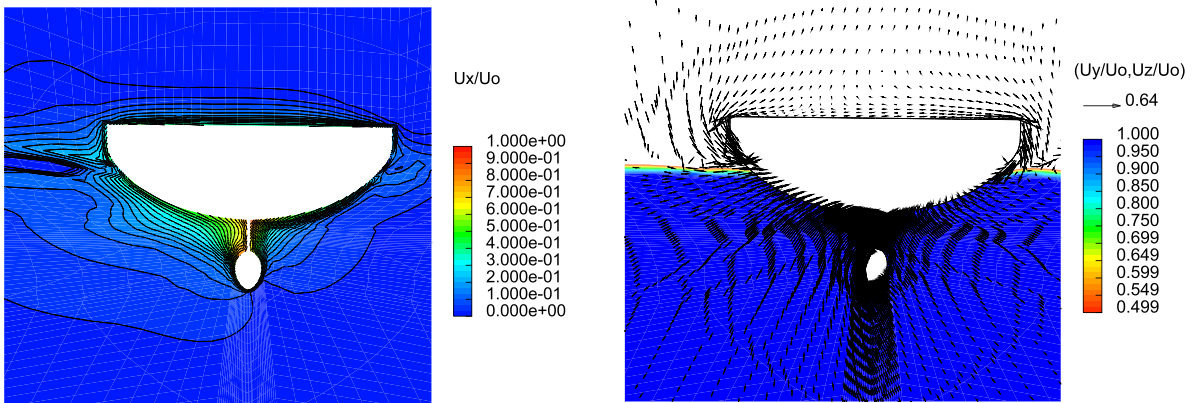


Figure 6.28: Velocity distribution at the cross section $x = -0.45L$ of the CBOX ship at $\psi = 10^\circ$ during the Zigzag maneuver: axial velocity contours (left) and tangential velocity vectors together with the free surface position (right), viewed from stern.

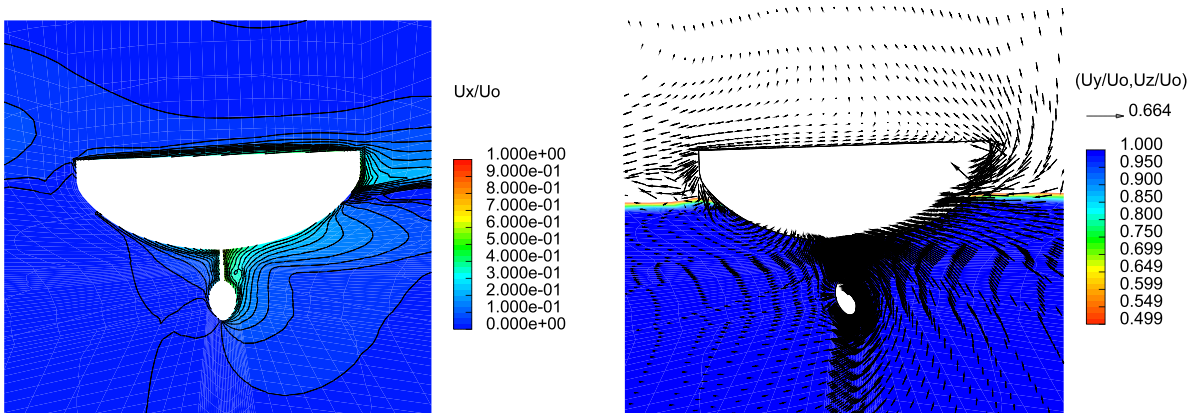


Figure 6.29: Velocity distribution at the cross section $x = -0.45L$ of the CBOX ship at $\psi = -10^\circ$ during the Zigzag maneuver: axial velocity contours (left) and tangential velocity vectors together with the free surface position (right), viewed from stern.

Chapter 7

Conclusion and Future Work

7.1 Conclusion

In the present work a coupled solution satisfying RANSE and 6-DOF rigid body motion equations is pursued to predict motions of floating-bodies in turbulent free surface flows. This approach has proved to be capable to reproduce the behavior of real ships in three-dimensional seakeeping and maneuvering applications, showing good agreement with experiments. The present work contributes to the long-term objective of ship hydrodynamics, namely the so-called *Virtual Towing Tank* agenda.

In the following, the conclusions drawn from the previous chapters are summarized, some numerical aspects are addressed, and the practical implications are highlighted:

- **Free surface modeling**

The VOF method applied in this work to predict the free surface deformation has the capacity to model breaking waves, spray, water jets as well as entrapped air bubbles in water, as can be observed from the water-entry and -exit test case of a horizontal circular cylinder in section 3.2. The formation and collapse of the water jets and entrapped air bubbles beside the cylinder in the water-entry case are reproduced with very good agreement with experimental photos. The accuracy of the free surface model is also examined by the water elevation comparison of generated waves with analytical solutions and experimental data for both small amplitude regular waves and large amplitude wave packages. The promising features and proven accuracy of the free surface model offer great flexibility of the method to be applied to ship motions in large waves, slamming, and sloshing as well as coupling of internal flow, external flow and ship motion.

- **Wave generation**

Different types of waves are generated in the present numerical wave tank with good accuracy achieved. Numerical parameters such as grid resolution, time step size, time integration scheme and differencing scheme in space have great influence on wave generation, especially when the wave-damping factor is concerned. The numerical grid should be fine enough – at least 20 cells per wavelength and 16 cells per wave height – to capture the wave profile accurately. The time step size, in principle, can

be determined by the local Courant number ($C_u = \frac{u\Delta t}{\Delta x} < 1.0$), but it must be small enough to get high enough a resolution per wave period (similar to the rule for grid resolution per wavelength and wave height). For the prediction of motion of a floating body in waves, the time step size is usually restricted by the magnitude of body/grid motion. First-order schemes should basically not be applied to analyze problems involving wave generation and propagation due to their first-order truncation error and requirement on too small a time step or grid size. Therefore, at least second-order schemes (e.g. ITTL in time and CD scheme in space) are recommended to avoid the numerical diffusion becoming higher than the physical diffusion.

Two methods – imposing inlet velocities and directly simulating a moving flap – are tested in this work for the generation of waves. The first method is more efficient from the CFD point of view due to a smaller solution domain and zero effort on grid-moving. The second method is more appropriate for the purpose of validation by exactly reproducing the motion of the wave-maker as in the experiment. However, to investigate ship seakeeping problems, the first method is preferred – with certain attention in numerical implementation – since it is then straightforward to generate irregular ocean waves. Waves produced by both methods are satisfactory.

- **Moving-grid method**

The computational effort on grid-moving is kept low if the number of grid points which are required to be moved during the computation is kept as small as possible and the moving-grid option can be regionally activated. Using the moving-grid strategy selected in this work, the distant part of the grid (far away from the body) is kept actually unchanged during the whole computation. Only the grid near the body is moved with the body and the grid in between is adapted to the body motion while keeping its topology the same. The determination on how large the size of moving-grid regions should be is indeed problem-dependent (body size, grid aspect ratio and amplitude of motion etc.). An ultimate criterion would be the quality of the adapted grid, in particular the orthogonality and spacing of grid lines and the resolution of grid points where variable gradients are high. As in the case of free surface modeling, regular hexahedral grids with two faces parallel to the free surface produce a minimum of error. The general guidelines on grid quality have been given in section 2.5, which will not be repeated here.

It has been found that the alternative of the overlapping grid method increases the computational time by a factor of 1.3 for a 2D test case due to the increased number of cells in the overlapping region and the cell-searching algorithm as well as the interpolation process between the foreground and the background grids. This factor tends to increase in 3D applications since the effort on cell-searching and interpolation would increase dramatically in 3D, especially when parallelization is necessary. Therefore, the selected moving-grid method is suitable and recommended to be used for similar problems as presented in this work in terms of both efficiency and accuracy. In case of large rotation, sliding interfaces are adopted as for the rotation of the geometrically modeled rudder. However, attention should be paid to the location of sliding interfaces, which should be put as far away as possible to the region of high variable gradients due to the errors introduced by the artificial interfaces.

- **Turbulence modeling**

The turbulent nature of the flow plays a crucial role in the determination of many relevant parameters in ship hydrodynamics, such as frictional drag, flow separation, thickness of boundary layer and spread of the wake. The turbulent states which can be encountered across the range of flows in ship hydrodynamics are rich and complex and therefore no single turbulence model is declared so far to be able to span all these states. It should be noticed that there is no universally valid general model of turbulence which is accurate for all classes of flows. The standard k - ϵ model with wall functions mainly used in this work has proven to be rather robust and little sensitive to the fineness of grid (e.g. Y^+) and orders of numerical schemes, compared to other alternative, e.g. the RNG k - ϵ model (section 5.2.3). This allows more cells to be concentrated in the region of the free surface or higher Reynolds number flows to be computed with an acceptable number of cells, which makes the standard k - ϵ model more attractive in practice. The results shown in this work using the wall function assumption in conjunction with the standard k - ϵ model are satisfactory provided that the value of Y^+ at all mesh points adjacent to the wall is greater than 30 (at least not less than 11) and does not exceed 100 or at least 10 grid points are located in the boundary layer. Attention, however, has to be paid on the major weaknesses of the standard k - ϵ model, such as over-prediction of turbulence effects in regions of flow impingement and re-attachment, under-prediction in regions of re-circulation, delay of flow separation from surfaces under the action of adverse pressure gradients and inaccuracy in laminar and transitional regions of flow. Nevertheless, the standard k - ϵ model with wall function remains the workhorse of practice-relevant computations and will continue to do so in the near future. Especially it is also a valid choice for full scale computations since the range of validity of wall functions increases as the Reynolds number rises.

- **Computational domain and boundary conditions**

As the solution domain cannot be infinite, it has to be enclosed by a number of boundaries. Both *natural* and *artificial* boundaries are employed in this work. The former are easier to set up since they exist physically while the latter are adopted in the flow field in order to reduce the size of the solution domain and therefore are normally located at a distance away from the region of interest to minimize their bounding effects. In principle, the *artificial* boundaries (like inlet, outlet and pressure boundaries except the symmetry plane) should be put as far as possible from the body/ship, but decisions have to be made by taking both economy and accuracy into account. In most ship sea-keeping and maneuvering applications of this work, the computational domains have shapes of rectangular boxes and extend to at least $1L$ in front of, above and below the ship, 4 - $5L$ behind the ship and 1 - $2L$ beside the ship, which has proven to be a good balance between economy and accuracy. If shallow water is applied, the boundary below the ship becomes a *natural* boundary so that the physical distance should be taken and a no-slip wall condition should be specified. Since the air flow is included in the present method, wind conditions for superstructures of ships or smoke from funnels can be computed by specifying appropriate inlet conditions. Gradually coarsened grids (by a factor of 1.2 ~ 1.4) serving as numerical beaches (extending from $1L$ to 4 - $5L$ behind the ship) are employed in connection with hydrostatic pressure boundaries, which has proven to be adequate to damp the waves and avoid their reflection

at the boundaries. In maneuvering applications, a combination of inlet and pressure boundary conditions is specified at the side boundaries where the fluid flows in and out simultaneously, which works well during the simulation of complex motions.

- **Applications to seakeeping**

In this work, the coupled solution of viscous fluid flow and body motion has been applied to simulate the motions of a RoRo ship in head waves. Encouraging agreement has been obtained between the experimental data and the computation. The effort required to perform such simulations is significantly smaller than that required for model tests. The simulation gives detailed insight into the flow field as well as pressure and shear stress distributions on the hull. The method accounts for nonlinearities of fluid flow and body motion and thus forms an ideal basis for ship form optimization.

- **Interaction of rudder, propeller and ship**

As a prerequisite to the simulation of maneuvering operations, the rudder forces behind ship and propeller have been analyzed and compared to experiments showing adequate agreement. Whereas ship and rudder are modeled geometrically to achieve high accuracy, the action of the propeller is idealized by a body force model. Two numerical procedures to determine the propeller thrust of a self-propelled ship have been introduced: One uses the propeller diagram and the instant flow field behind the ship; the other performs a numerical self-propulsion test. The former approach is applicable to any maneuvering simulation where the flow field and the thrust change.

- **Applications to ship maneuvering**

Several maneuvering simulations of practical importance have been performed for a commercial container vessel considering 6-DOF ship motion and free surface within a viscous flow computation. The numerical analysis of the forces on ship hull and rudder during steady drift motion shows favorable agreement with experimental data. The following analysis of a turning circle maneuver gives typical characteristics for such a container ship. The final comparison of numerical and model test results for a Zigzag maneuver of this ship demonstrates again the applicability of the computational method. These maneuvering simulations cover a long period of real time (A turning circle at model scale is typically performed in two minutes.) and thus require stable and reliable computational procedures. Such procedures have been demonstrated in this work, building the basis for further developments in the *Virtual Towing Tank*.

- **Further applicability of the present method**

The implemented method has been applied to investigate viscous roll damping problems of a 2D mid-ship section with and without keels. Viscous effects play an important role in roll motion and therefore should be included in predictions of roll motion. A study on interaction of two adjacent floating bodies in incoming waves further proves the robustness and the reliability of the method and demonstrates the possibility and potential of the method in further application areas such as multi-floating-body interaction in calm water and subjected to currents and waves. Analysis of complex operations is nowadays more and more asked for and has to be faced by the maritime industry. This includes loading operation between two vessels at sea and docking of barges in carrier ships as well as launching and recovering of life- and speed-boats.

In general, the present method has proven to be robust showing its capability to deal with complex applications. The computational effort will of course hinder the application of this approach to long-term studies of ship behavior in an irregular seaway. However, the author is convinced that more and more coupled RANSE and motion computations will be used to investigate a wide range of unsteady problems in maritime hydrodynamics.

7.2 Future Work

More exhaustive verification and validation in 3D ship hydrodynamics are certainly needed to further examine the accuracy of the present method. Especially, local flow patterns should be carefully looked at to ensure that the overall agreement is not only obtained because errors in different places/models cancel up. Sensitivity studies should be carried out on different grid densities, numerical schemes, sizes of computational domain, boundary conditions and turbulence models etc. to assess the uncertainty and the errors in the predicted results.

The efficiency of the coupled method can be improved – on the one hand – by the flow solver and – on the other hand – by the coupling technique. New generations of flow solvers should incorporate the capacity to accommodate and handle not only appropriately distributed, but also easy-to-generate grids for complex geometry. Grid generation is, unfortunately, still one of the challenging tasks. It is very time-consuming, especially if a high quality of grids is required. Development of multi-grid techniques would promote further improvement of efficiency and accuracy. Investigations on coupling methods could also accelerate the convergence rate of the coupled procedure, such as the criteria for activating or de-activating the body motion module and grid-moving subroutine, choices of (problem-dependent) under-relaxation factors or added-mass estimates, time integration schemes of body motion, influences of the time step size and use of varying time steps or different time steps for fluid flow and body motion.

After further validation of the method and further improvement of the efficiency of the coupled approach have been achieved, more sophisticated applications can be performed with the increased computer resources expected in the future:

- **Full scale computation**

Full scale resistance, propulsion, seakeeping and maneuvering simulations can be, in principle, performed by a single code with different boundary conditions and released DOFs of ship motion.

- **Including a geometrically modeled propeller**

A geometrically modeled 3D rotating propeller can be included to replace the simplified propeller body force model so that the unsteady behavior of propeller-rudder-hull interaction can be captured more accurately. Also, an appropriate simulation of the propulsion plant would enhance the prediction of propeller performance.

- **Ship maneuvers in restricted water**

Often ships have to operate in restricted waters like harbors or canals. The natural boundaries, e.g. canal walls, have to be modeled in these cases and there might be the presence of a third phase, e.g. sand or mud.

- **Simultaneous computation of internal and external flows**

Ships with filled ballast and/or cargo tanks and damaged ships in waves can be simulated with liquid flowing both inside and outside the ship. Also roll damping with the help of a stabilizing tank can be handled by the present method.

- **Simultaneous computation of water and air flow**

Aerodynamic and hydrodynamic effects on sailing yachts or ships with large super structures can be simultaneously considered by a single code in the present method. Also, unsteady wind conditions are possible to be simulated.

- **Fluid-structure interaction**

Further extension of the method would be the inclusion of the deformation of the structure – either elastic or plastic – to simulate slamming-induced deformations of ship structures, aircraft ditching on water or landing on a carrier.

- **More challenging multi-body interactions**

Overtaking maneuvers of ships in restricted water would be more challenging simulations, especially in terms of grid techniques. Furthermore, collisions of two ships would need to include further models to consider the nonlinear response of ship structures under large impact forces.

Although it is yet not foreseeable how fast the development of the method will be and how exactly the range of application will expand in the future, it is certain that a new era in ship hydrodynamics has begun. The ultimate goal is yet not the *Virtual Towing Tank*, but the *Virtual Reality*, which would help the captain on board to make precise decisions under any condition to ensure safety of people, cargo and ship.

Appendix A

Derivation of the Governing Equation of the Body Angular Motion in the Global Coordinate System

The computation of body motion is performed in the global coordinate system. The governing equation of angular motion of a rigid body in a body-fixed coordinate system (BS) is:

$$\frac{d(M_C \cdot \boldsymbol{\omega}_C)}{dt} = \mathbf{m}_C . \quad (\text{A.1})$$

In the above equations, M_C is the tensor of the moments of inertia of the body, $\boldsymbol{\omega}_C$ is the angular velocity vector of the body, and \mathbf{m}_C represents the moments of forces acting on the body with respect to its center of mass.

The body-fixed coordinate system is set to be originated at the center of gravity and maintaining a given orientation of the rigid body. Since M_C keeps constant with respect to the BS, Eq. (A.1) can be written in the following form:

$$M_C \cdot \dot{\boldsymbol{\omega}}_C + \boldsymbol{\omega}_C \times M_C \cdot \boldsymbol{\omega}_C = \mathbf{m}_C . \quad (\text{A.2})$$

In the following, the angular motion equation with respect to the global coordinate system (GS) will be derived. The superscript g indicates the variables expressed in terms of the GS.

Assuming T_T as the transform matrix from BS to the GS, one can easily get:

$$[\delta\boldsymbol{\phi}] = (T_T)^{-1} \cdot [\delta\boldsymbol{\phi}^g] , \quad (\text{A.3})$$

$$\boldsymbol{\omega} = (T_T)^{-1} \cdot \boldsymbol{\omega}^g, \quad \dot{\boldsymbol{\omega}} = (T_T)^{-1} \cdot \dot{\boldsymbol{\omega}}^g , \quad (\text{A.4})$$

$$(\mathbf{T}_T)^T = (\mathbf{T}_T)^{-1} . \quad (\text{A.5})$$

According to the principle of virtual work in angular motion, one can write

$$[\delta\phi^g]^T \cdot \mathbf{m}_C^g = [\delta\phi]^T \cdot \mathbf{m}_C . \quad (\text{A.6})$$

By substituting Eqs. (A.2), (A.3), (A.4) and (A.5) into Eq. (A.6),

$$\begin{aligned} & [\delta\phi^g]^T \cdot \mathbf{m}_C^g \\ &= [\delta\phi^g]^T \cdot \left[(\mathbf{T}_T)^{-1} \right]^T \cdot (\mathbf{M}_C \cdot \dot{\boldsymbol{\omega}}_C + \boldsymbol{\omega}_C \times \mathbf{M}_C \cdot \boldsymbol{\omega}_C) \\ &= [\delta\phi^g]^T \cdot \mathbf{T}_T \cdot \left\{ \mathbf{M}_C \cdot \left[(\mathbf{T}_T)^{-1} \cdot \dot{\boldsymbol{\omega}}_C^g \right] + \left[(\mathbf{T}_T)^{-1} \cdot \boldsymbol{\omega}_C^g \right] \times \mathbf{M}_C \cdot \left[(\mathbf{T}_T)^{-1} \cdot \boldsymbol{\omega}_C^g \right] \right\} \\ &= [\delta\phi^g]^T \cdot \left\{ \mathbf{T}_T \cdot \mathbf{M}_C \cdot (\mathbf{T}_T)^{-1} \cdot \dot{\boldsymbol{\omega}}_C^g + \mathbf{T}_T \cdot \left[\left((\mathbf{T}_T)^{-1} \cdot \boldsymbol{\omega}_C^g \right) \times \mathbf{M}_C \cdot \left((\mathbf{T}_T)^{-1} \cdot \boldsymbol{\omega}_C^g \right) \right] \right\} . \end{aligned} \quad (\text{A.7})$$

Thus

$$\mathbf{m}_C^g = \mathbf{T}_T \cdot \mathbf{M}_C \cdot (\mathbf{T}_T)^{-1} \cdot \dot{\boldsymbol{\omega}}_C^g + \mathbf{T}_T \cdot \left\{ \left[(\mathbf{T}_T)^{-1} \cdot \boldsymbol{\omega}_C^g \right] \times \mathbf{M}_C \cdot \left[(\mathbf{T}_T)^{-1} \cdot \boldsymbol{\omega}_C^g \right] \right\} . \quad (\text{A.8})$$

In order to simplify the second part of Eq. (A.8), we would like to prove:

$$\begin{aligned} & \mathbf{T}_T \cdot \left\{ \left[(\mathbf{T}_T)^{-1} \cdot \boldsymbol{\omega}_C^g \right] \times \mathbf{M}_C \cdot \left[(\mathbf{T}_T)^{-1} \cdot \boldsymbol{\omega}_C^g \right] \right\} \\ &= \left[\mathbf{T}_T \cdot (\mathbf{T}_T)^{-1} \cdot \boldsymbol{\omega}_C^g \right] \times \left[\mathbf{T}_T \cdot \mathbf{M}_C \cdot (\mathbf{T}_T)^{-1} \cdot \boldsymbol{\omega}_C^g \right] \\ &= \boldsymbol{\omega}_C^g \times \left[\mathbf{T}_T \cdot \mathbf{M}_C \cdot (\mathbf{T}_T)^{-1} \cdot \boldsymbol{\omega}_C^g \right] . \end{aligned} \quad (\text{A.9})$$

Assuming

$$\mathbf{a} = (\mathbf{T}_T)^{-1} \cdot \boldsymbol{\omega}_C^g; \quad \mathbf{b} = \mathbf{M}_C \cdot (\mathbf{T}_T)^{-1} \cdot \boldsymbol{\omega}_C^g , \quad (\text{A.10})$$

Equation (A.9) can be rewritten as:

$$\mathbf{T}_T \cdot (\mathbf{a} \times \mathbf{b}) = (\mathbf{T}_T \cdot \mathbf{a}) \times (\mathbf{T}_T \cdot \mathbf{b}) . \quad (\text{A.11})$$

The transform matrix \mathbf{T}_T can be expressed as below:

$$\begin{aligned} \mathbf{T}_T &= \begin{pmatrix} \cos \angle x^g ox & \cos \angle x^g oy & \cos \angle x^g oz \\ \cos \angle y^g ox & \cos \angle y^g oy & \cos \angle y^g oz \\ \cos \angle z^g ox & \cos \angle z^g oy & \cos \angle z^g oz \end{pmatrix} \\ &= \begin{pmatrix} \mathbf{l}_1 \\ \mathbf{l}_2 \\ \mathbf{l}_3 \end{pmatrix} , \end{aligned} \quad (\text{A.12})$$

where \mathbf{l}_1 , \mathbf{l}_2 and \mathbf{l}_3 are the space unit vectors with respect to the BS. Therefore

$$\mathbf{l}_1 = \mathbf{l}_2 \times \mathbf{l}_3, \quad \mathbf{l}_2 = \mathbf{l}_3 \times \mathbf{l}_1, \quad \mathbf{l}_3 = \mathbf{l}_1 \times \mathbf{l}_2 . \quad (\text{A.13})$$

Thus

$$\begin{aligned} \mathbb{T}_T \cdot (\mathbf{a} \times \mathbf{b}) &= \begin{pmatrix} \mathbf{l}_1 \cdot (\mathbf{a} \times \mathbf{b}) \\ \mathbf{l}_2 \cdot (\mathbf{a} \times \mathbf{b}) \\ \mathbf{l}_3 \cdot (\mathbf{a} \times \mathbf{b}) \end{pmatrix} \\ &= \begin{pmatrix} (\mathbf{l}_2 \times \mathbf{l}_3) \cdot (\mathbf{a} \times \mathbf{b}) \\ (\mathbf{l}_3 \times \mathbf{l}_1) \cdot (\mathbf{a} \times \mathbf{b}) \\ (\mathbf{l}_1 \times \mathbf{l}_2) \cdot (\mathbf{a} \times \mathbf{b}) \end{pmatrix}. \end{aligned} \quad (\text{A.14})$$

Since it is known from the vector calculus that

$$(\mathbf{d} \times \mathbf{f}) \cdot (\mathbf{g} \times \mathbf{h}) = (\mathbf{d} \cdot \mathbf{g})(\mathbf{f} \cdot \mathbf{h}) - (\mathbf{f} \cdot \mathbf{g})(\mathbf{d} \cdot \mathbf{h}), \quad (\text{A.15})$$

where \mathbf{d} , \mathbf{f} , \mathbf{g} and \mathbf{h} are four randomly defined vectors. Substituting Eq. (A.15) into Eq. (A.14) yields

$$\mathbb{T}_T \cdot (\mathbf{a} \times \mathbf{b}) = \begin{pmatrix} (\mathbf{l}_2 \cdot \mathbf{a})(\mathbf{l}_3 \cdot \mathbf{b}) - (\mathbf{l}_3 \cdot \mathbf{a})(\mathbf{l}_2 \cdot \mathbf{b}) \\ (\mathbf{l}_3 \cdot \mathbf{a})(\mathbf{l}_1 \cdot \mathbf{b}) - (\mathbf{l}_1 \cdot \mathbf{a})(\mathbf{l}_3 \cdot \mathbf{b}) \\ (\mathbf{l}_1 \cdot \mathbf{a})(\mathbf{l}_2 \cdot \mathbf{b}) - (\mathbf{l}_2 \cdot \mathbf{a})(\mathbf{l}_1 \cdot \mathbf{b}) \end{pmatrix}. \quad (\text{A.16})$$

Now developing the right hand side of Eq. (A.11):

$$\begin{aligned} (\mathbb{T}_T \cdot \mathbf{a}) \times (\mathbb{T}_T \cdot \mathbf{b}) &= \begin{pmatrix} \mathbf{i} & \mathbf{j} & \mathbf{k} \\ \mathbf{l}_1 \cdot \mathbf{a} & \mathbf{l}_2 \cdot \mathbf{a} & \mathbf{l}_3 \cdot \mathbf{a} \\ \mathbf{l}_1 \cdot \mathbf{b} & \mathbf{l}_2 \cdot \mathbf{b} & \mathbf{l}_3 \cdot \mathbf{b} \end{pmatrix} \\ &= \begin{pmatrix} (\mathbf{l}_2 \cdot \mathbf{a})(\mathbf{l}_3 \cdot \mathbf{b}) - (\mathbf{l}_3 \cdot \mathbf{a})(\mathbf{l}_2 \cdot \mathbf{b}) \\ (\mathbf{l}_3 \cdot \mathbf{a})(\mathbf{l}_1 \cdot \mathbf{b}) - (\mathbf{l}_1 \cdot \mathbf{a})(\mathbf{l}_3 \cdot \mathbf{b}) \\ (\mathbf{l}_1 \cdot \mathbf{a})(\mathbf{l}_2 \cdot \mathbf{b}) - (\mathbf{l}_2 \cdot \mathbf{a})(\mathbf{l}_1 \cdot \mathbf{b}) \end{pmatrix}. \end{aligned} \quad (\text{A.17})$$

Thus, Eqs. (A.11) and (A.9) have been proved. The equation with respect to the GS can be written as

$$\mathbb{M}_C^g \cdot \dot{\boldsymbol{\omega}}_C^g + \boldsymbol{\omega}_C^g \times \mathbb{M}_C^g \cdot \boldsymbol{\omega}_C^g = \mathbf{m}_C^g, \quad (\text{A.18})$$

where \mathbb{M}_C^g represents the moment of inertia of the rigid body with respect to the GS. It has the following form:

$$\mathbb{M}_C^g = \mathbb{T}_T \cdot \mathbb{M}_C \cdot \mathbb{T}_T^{-1}. \quad (\text{A.19})$$

Appendix B

High Resolution Interface-Capturing Scheme

As mentioned in section 2.3.1, the so-called HRIC scheme has been designed for the convective transport of the scalar quantity c (see Eq. 2.6) to achieve the sharpness of the interface without over- and undershoots. In the following, the basic idea of this scheme will be briefly introduced, more details can be found in Muzafferija and Perić [58].

The scheme is based on limiting the approximation of the cell-face value ϕ_j^* (see Eq. (2.89)) to lie in the shaded area of the so-called Normalized Variable Diagram (NVD) (see Leonard [51]) shown in Fig. B.1. The normalized variable \bar{c} in the vicinity of the cell-center C is defined as:

$$\bar{c}(\mathbf{r}) = \frac{c(\mathbf{r}) - c_U}{c_D - c_U}, \quad (\text{B.1})$$

where the subscripts 'U' and 'D' denote centers of CVs upstream and downstream of the cell-center C. In particular, note that $\bar{c}_U = 0$ and $\bar{c}_D = 1$. The normalized face value \bar{c}_j is

$$\bar{c}_j = \frac{c_j - c_U}{c_D - c_U}. \quad (\text{B.2})$$

The scheme is a non-linear blending of upwind and downwind cell-face values with the normalized face value \bar{c}_j calculated as

$$\bar{c}_j = \begin{cases} \bar{c}_C & \text{if } \bar{c}_C < 0 \\ 2\bar{c}_C & \text{if } 0 \leq \bar{c}_C < 0.5 \\ 1 & \text{if } 0.5 \leq \bar{c}_C < 1 \\ \bar{c}_C & \text{if } 1 \leq \bar{c}_C \end{cases} \quad (\text{B.3})$$

Since the amount of one fluid convected across a cell face during a time step must not be more than the amount available in the donor cell, the calculated value of \bar{c}_j is further corrected according to the local Courant number C_u

$$C_u = \frac{\mathbf{v} \cdot \mathbf{n} S_j \Delta t}{\Delta V_C}. \quad (\text{B.4})$$

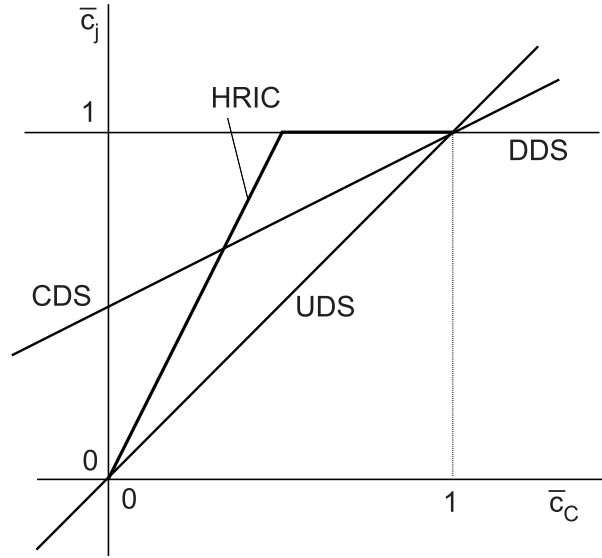


Figure B.1: Normalized Variable Diagram (NVD, see Leonard [51]).

This correction plays a role in transient simulations and is made according to the following expressions:

$$\bar{c}_j^* = \begin{cases} \bar{c}_j & \text{if } C_u < 0.3 \\ \bar{c}_C + (\bar{c}_j - \bar{c}_C) \frac{0.7 - C_u}{0.7 - 0.3} & \text{if } 0.3 \leq C_u < 0.7 \\ \bar{c}_C & \text{if } 0.7 \leq C_u \end{cases} . \quad (\text{B.5})$$

The use of the downwind scheme keeps the interface sharp if the interface is parallel to the cell face and moves in the direction of the cell-face normal; if the interface is perpendicular to the cell face, the convected fluid would be likely of the same composition as in the cell center, so the upwind scheme is appropriate. A final correction is necessary to take this into account:

$$\bar{c}_j^{**} = \bar{c}_j^* \sqrt{\cos \theta} + \bar{c}_C (1 - \sqrt{\cos \theta}) , \quad (\text{B.6})$$

where

$$\cos \theta = \frac{\nabla c \cdot \mathbf{n}_j}{\|\nabla c\|} . \quad (\text{B.7})$$

Here θ denotes the angle between the normal to the interface and the normal to the cell face.

Finally, the cell-face value of c is computed according to Eq. (B.1) as

$$c_j^{\text{HRIC}} = \bar{c}_j^{**} (c_D - c_U) + c_U . \quad (\text{B.8})$$

Appendix C

Derivation of the Rotation Operator \mathbb{T}_t

As stated in Section 2.2.2 (see Eq. (2.129)), \mathbb{T}_t is a rotation operator for the rotational transformation of the body position about a unit axis \mathbf{u} through the origin of the coordinate system. Suppose $\mathbf{u} = (u_x, u_y, u_z)$ and the rotational angle about \mathbf{u} is ϕ , this rotation operator \mathbb{T}_t can be expressed by:

$$\mathbb{T}_t = \begin{pmatrix} u_x^2(1 - \cos\phi) + \cos\phi & u_x u_y(1 - \cos\phi) - u_z \sin\phi & u_x u_z(1 - \cos\phi) + u_y \sin\phi \\ u_x u_y(1 - \cos\phi) + u_z \sin\phi & u_y^2(1 - \cos\phi) + \cos\phi & u_y u_z(1 - \cos\phi) - u_x \sin\phi \\ u_x u_z(1 - \cos\phi) - u_y \sin\phi & u_y u_z(1 - \cos\phi) + u_x \sin\phi & u_z^2(1 - \cos\phi) + \cos\phi \end{pmatrix}. \quad (\text{C.1})$$

The derivation of this operator is performed by the author, as given in the following.

As shown in Fig. C.1, a vector \mathbf{r}_1 rotates about the unit vector \mathbf{u} with a rotational angle ϕ . The plane $\mathbf{u} \cdot \mathbf{r} = 0$ is perpendicular to the unit vector \mathbf{u} and includes the origin of the coordinate system O . Then, the vector \mathbf{r}_1 can be decomposed into two vectors \mathbf{z}_1 and \mathbf{z}_2 , where \mathbf{z}_1 is parallel to \mathbf{u} and perpendicular to the plane $\mathbf{u} \cdot \mathbf{r} = 0$, and \mathbf{z}_2 lies in the plane $\mathbf{u} \cdot \mathbf{r} = 0$ and represents the projection of \mathbf{r}_1 onto this plane. The following relations apply:

Such one can get

$$\mathbf{z}_1 = (\mathbf{u} \cdot \mathbf{r}_1) \mathbf{u}, \quad (\text{C.2})$$

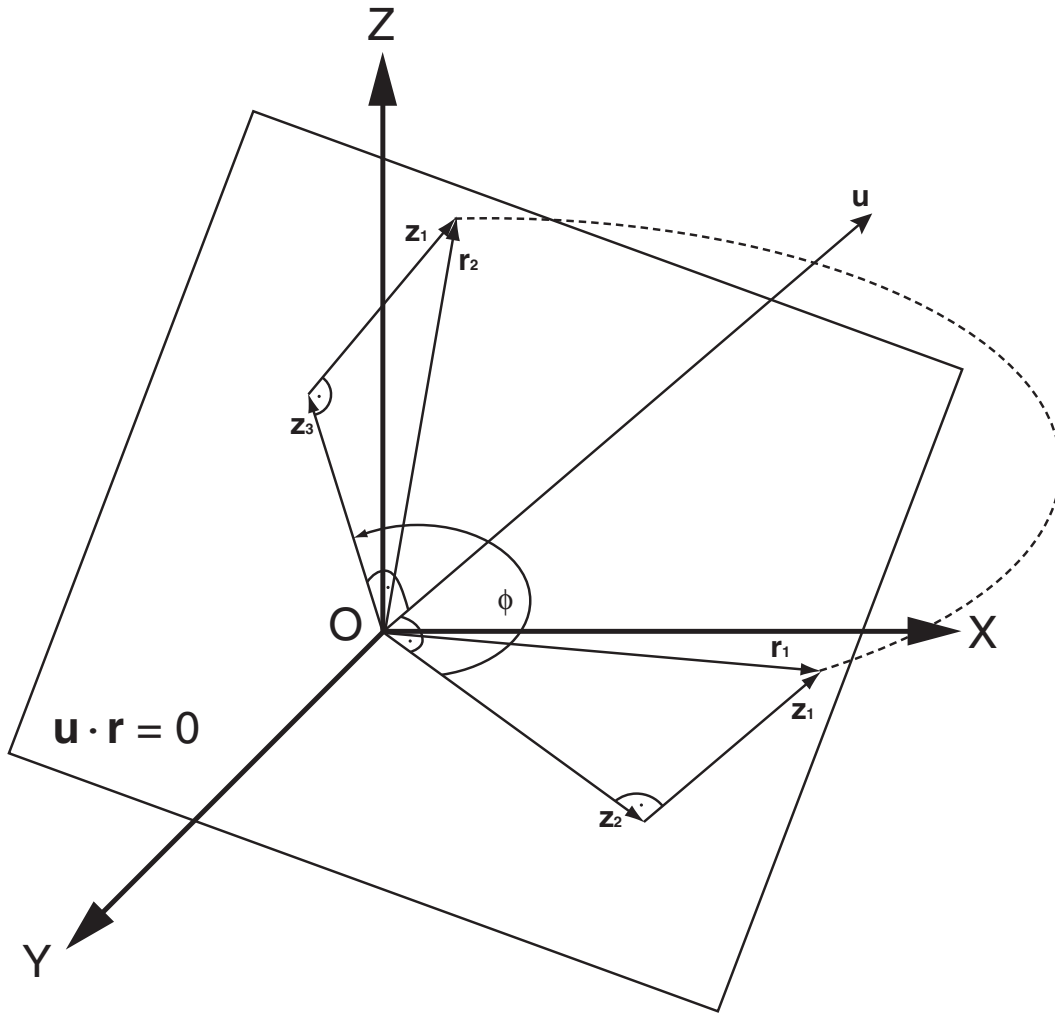
$$\mathbf{z}_2 = \mathbf{r}_1 - \mathbf{z}_1. \quad (\text{C.3})$$

As the vector \mathbf{r}_1 rotates about the unit vector \mathbf{u} with a rotational angle ϕ , only the component \mathbf{z}_2 of \mathbf{r}_1 is altered to \mathbf{z}_3 during the rotation. Therefore the new vector \mathbf{r}_2 can be expressed as

$$\mathbf{r}_2 = \mathbf{z}_1 + \mathbf{z}_3, \quad (\text{C.4})$$

where \mathbf{z}_3 lies in the common plane of \mathbf{z}_2 and $\mathbf{u} \times \mathbf{z}_2$, which is the plane $\mathbf{u} \cdot \mathbf{r} = 0$.

Therefore one can suppose

Figure C.1: Rotation of vector \mathbf{r}_1 about \mathbf{u} .

$$\mathbf{z}_3 = a\mathbf{z}_2 + b(\mathbf{u} \times \mathbf{z}_2) . \quad (\text{C.5})$$

Applying the basic rules of plane geometry, the vector \mathbf{z}_3 can be expressed as

$$\mathbf{z}_3 = \mathbf{z}_2 \cos \phi + (\mathbf{u} \times \mathbf{z}_2) \sin \phi , \quad (\text{C.6})$$

with ϕ as the rotational angle from \mathbf{z}_2 to \mathbf{z}_3 in the plane $\mathbf{u} \cdot \mathbf{r} = 0$.

The vectors \mathbf{u} , \mathbf{r}_1 and \mathbf{r}_2 are expressed through their components:

$$\mathbf{u} = \begin{pmatrix} u_x \\ u_y \\ u_z \end{pmatrix} , \quad (\text{C.7})$$

$$\mathbf{r}_1 = \begin{pmatrix} r_{1x} \\ r_{1y} \\ r_{1z} \end{pmatrix}, \quad (\text{C.8})$$

$$\mathbf{r}_2 = \begin{pmatrix} r_{2x} \\ r_{2y} \\ r_{2z} \end{pmatrix}. \quad (\text{C.9})$$

By substituting Eqs. (C.7) and (C.8) into Eqs. (C.2) and (C.3), it is obtained:

$$\begin{aligned} \mathbf{z}_1 &= (\mathbf{u} \cdot \mathbf{r}_1) \mathbf{u} \\ &= (u_x r_{1x} + u_y r_{1y} + u_z r_{1z}) \begin{pmatrix} u_x \\ u_y \\ u_z \end{pmatrix} \\ &= \begin{pmatrix} u_x^2 r_{1x} + u_x u_y r_{1y} + u_x u_z r_{1z} \\ u_y u_x r_{1x} + u_y^2 r_{1y} + u_y u_z r_{1z} \\ u_z u_x r_{1x} + u_z u_y r_{1y} + u_z^2 r_{1z} \end{pmatrix} \end{aligned} \quad (\text{C.10})$$

and

$$\begin{aligned} \mathbf{z}_2 &= \mathbf{r}_1 - \mathbf{z}_1 \\ &= \begin{pmatrix} r_{1x} \\ r_{1y} \\ r_{1z} \end{pmatrix} - (u_x r_{1x} + u_y r_{1y} + u_z r_{1z}) \begin{pmatrix} u_x \\ u_y \\ u_z \end{pmatrix} \\ &= \begin{pmatrix} r_{1x} - u_x^2 r_{1x} - u_x u_y r_{1y} - u_x u_z r_{1z} \\ r_{1y} - u_x u_y r_{1x} - u_y^2 r_{1y} - u_y u_z r_{1z} \\ r_{1z} - u_x u_z r_{1x} - u_y u_z r_{1y} - u_z^2 r_{1z} \end{pmatrix}. \end{aligned} \quad (\text{C.11})$$

Substituting Eqs. (C.7) and (C.11) into Eq. (C.6) one gets:

$$\begin{aligned} \mathbf{z}_3 &= \cos \phi \mathbf{z}_2 + \sin \phi (\mathbf{u} \times \mathbf{z}_2) \\ &= \cos \phi \begin{pmatrix} z_{2x} \\ z_{2y} \\ z_{2z} \end{pmatrix} + \sin \phi \begin{pmatrix} u_y z_{2z} - u_z z_{2y} \\ u_z z_{2x} - u_x z_{2z} \\ u_x z_{2y} - u_y z_{2x} \end{pmatrix} \\ &= \cos \phi \begin{pmatrix} r_{1x} - u_x^2 r_{1x} - u_x u_y r_{1y} - u_x u_z r_{1z} \\ r_{1y} - u_x u_y r_{1x} - u_y^2 r_{1y} - u_y u_z r_{1z} \\ r_{1z} - u_x u_z r_{1x} - u_y u_z r_{1y} - u_z^2 r_{1z} \end{pmatrix} + \sin \phi \begin{pmatrix} u_y r_{1z} - u_z r_{1y} \\ u_z r_{1x} - u_x r_{1z} \\ u_x r_{1y} - u_y r_{1x} \end{pmatrix} \\ &= \begin{pmatrix} r_{1x} \cos \phi - u_x^2 r_{1x} \cos \phi - u_x u_y r_{1y} \cos \phi - u_x u_z r_{1z} \cos \phi + u_y r_{1z} \sin \phi - u_z r_{1y} \sin \phi \\ r_{1y} \cos \phi - u_x u_y r_{1x} \cos \phi - u_y^2 r_{1y} \cos \phi - u_y u_z r_{1z} \cos \phi + u_z r_{1x} \sin \phi - u_x r_{1z} \sin \phi \\ r_{1z} \cos \phi - u_x u_z r_{1x} \cos \phi - u_y u_z r_{1y} \cos \phi - u_z^2 r_{1z} \cos \phi + u_x r_{1y} \sin \phi - u_y r_{1x} \sin \phi \end{pmatrix}. \end{aligned} \quad (\text{C.12})$$

Finally by substituting Eqs. (C.10) and (C.12) into Eq. (C.4), one can obtain

$$\begin{aligned}
\mathbf{r}_2 &= \mathbf{z}_1 + \mathbf{z}_3 \\
&= \begin{pmatrix} u_x^2 r_{1x} + u_x u_y r_{1y} + u_x u_z r_{1z} \\ u_y u_x r_{1x} + u_y^2 r_{1y} + u_y u_z r_{1z} \\ u_z u_x r_{1x} + u_z u_y r_{1y} + u_z^2 r_{1z} \end{pmatrix} + \\
&\quad \begin{pmatrix} r_{1x} \cos \phi - u_x^2 r_{1x} \cos \phi - u_x u_y r_{1y} \cos \phi - u_x u_z r_{1z} \cos \phi + u_y r_{1z} \sin \phi - u_z r_{1y} \sin \phi \\ r_{1y} \cos \phi - u_x u_y r_{1x} \cos \phi - u_y^2 r_{1y} \cos \phi - u_y u_z r_{1z} \cos \phi + u_z r_{1x} \sin \phi - u_x r_{1z} \sin \phi \\ r_{1z} \cos \phi - u_x u_z r_{1x} \cos \phi - u_y u_z r_{1y} \cos \phi - u_z^2 r_{1z} \cos \phi + u_x r_{1y} \sin \phi - u_y r_{1x} \sin \phi \end{pmatrix} \\
&= \begin{pmatrix} u_x^2 r_{1x} + u_x u_y r_{1y} + u_x u_z r_{1z} + r_{1x} \cos \phi - u_x^2 r_{1x} \cos \phi - u_x u_y r_{1y} \cos \phi - u_x u_z r_{1z} \cos \phi + u_y r_{1z} \sin \phi - u_z r_{1y} \sin \phi \\ u_y u_x r_{1x} + u_y^2 r_{1y} + u_y u_z r_{1z} + r_{1y} \cos \phi - u_x u_y r_{1x} \cos \phi - u_y^2 r_{1y} \cos \phi - u_y u_z r_{1z} \cos \phi + u_z r_{1x} \sin \phi - u_x r_{1z} \sin \phi \\ u_z u_x r_{1x} + u_z u_y r_{1y} + u_z^2 r_{1z} + r_{1z} \cos \phi - u_x u_z r_{1x} \cos \phi - u_y u_z r_{1y} \cos \phi - u_z^2 r_{1z} \cos \phi + u_x r_{1y} \sin \phi - u_y r_{1x} \sin \phi \end{pmatrix}.
\end{aligned} \tag{C.13}$$

that is

$$\mathbf{r}_2 = \mathbb{T}_t \cdot \mathbf{r}_1, \tag{C.14}$$

where \mathbb{T}_t has the form as shown in Eq. (C.1).

Appendix D

Lines Plan of RoRo Ship

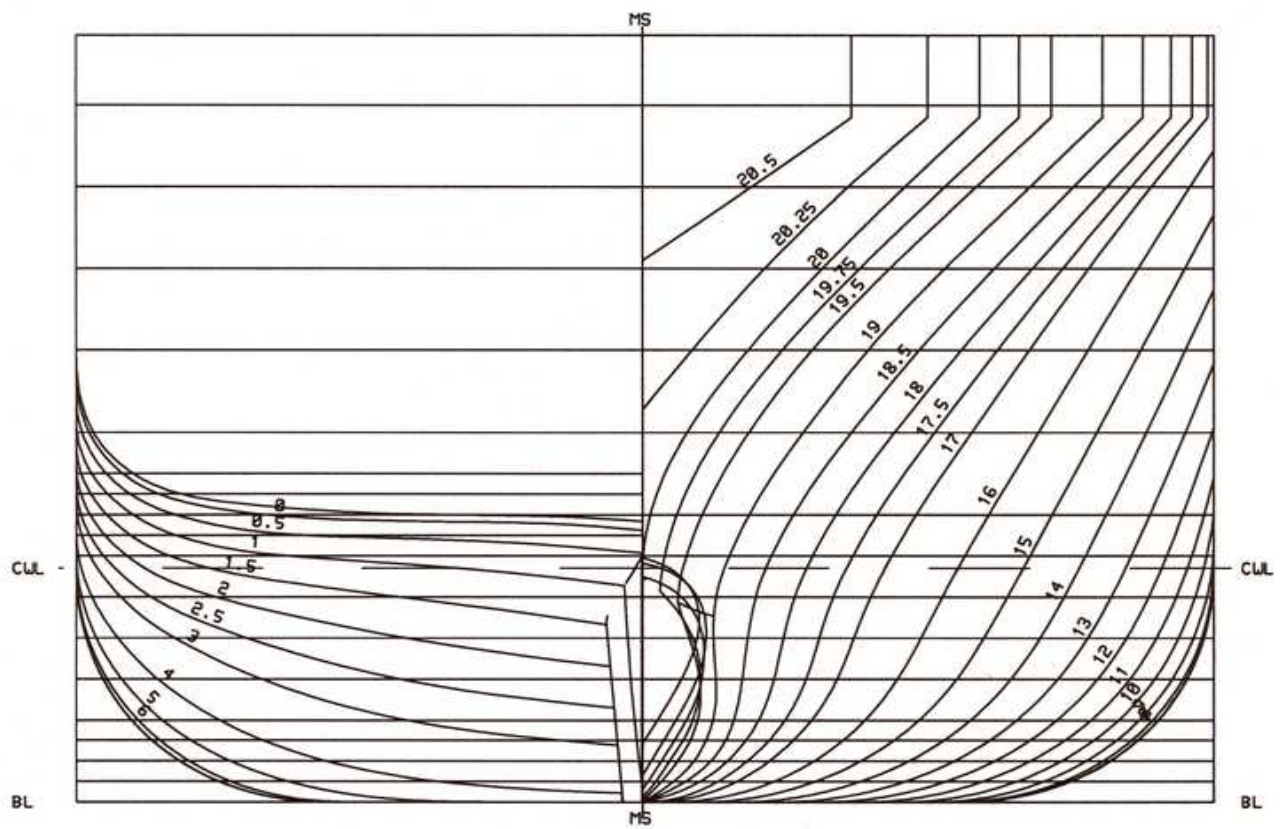


Figure D.1: Transverse sections of RoRo ship.

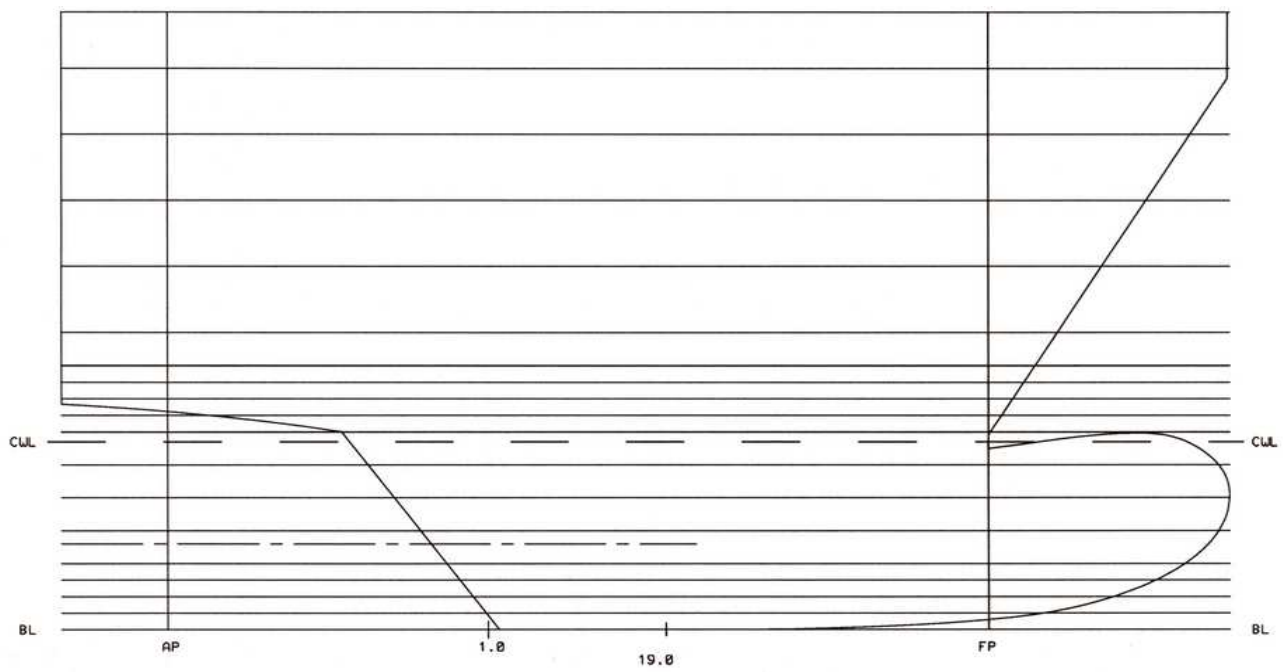


Figure D.2: Profile of RoRo ship.

Appendix E

Lines Plan of CBOX Ship

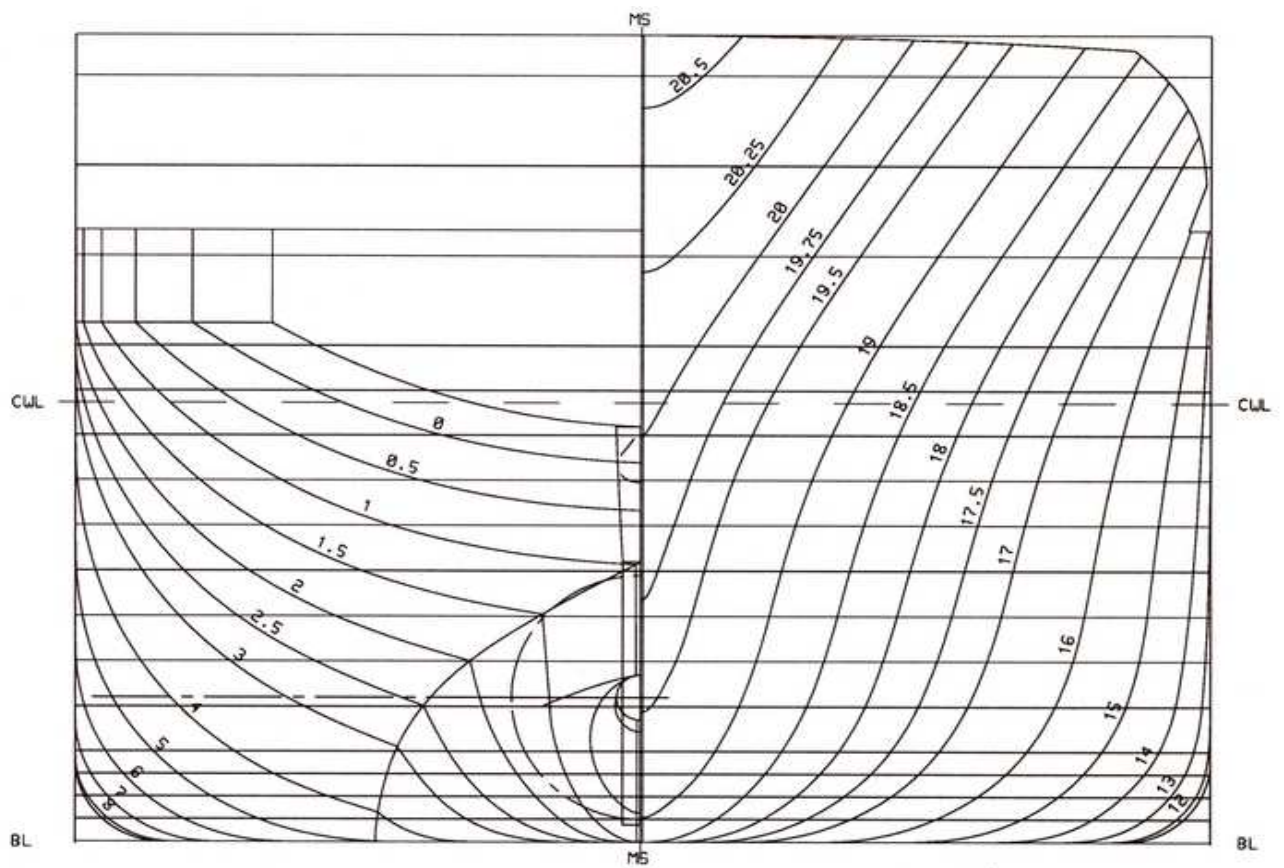


Figure E.1: Transverse sections of CBOX ship.

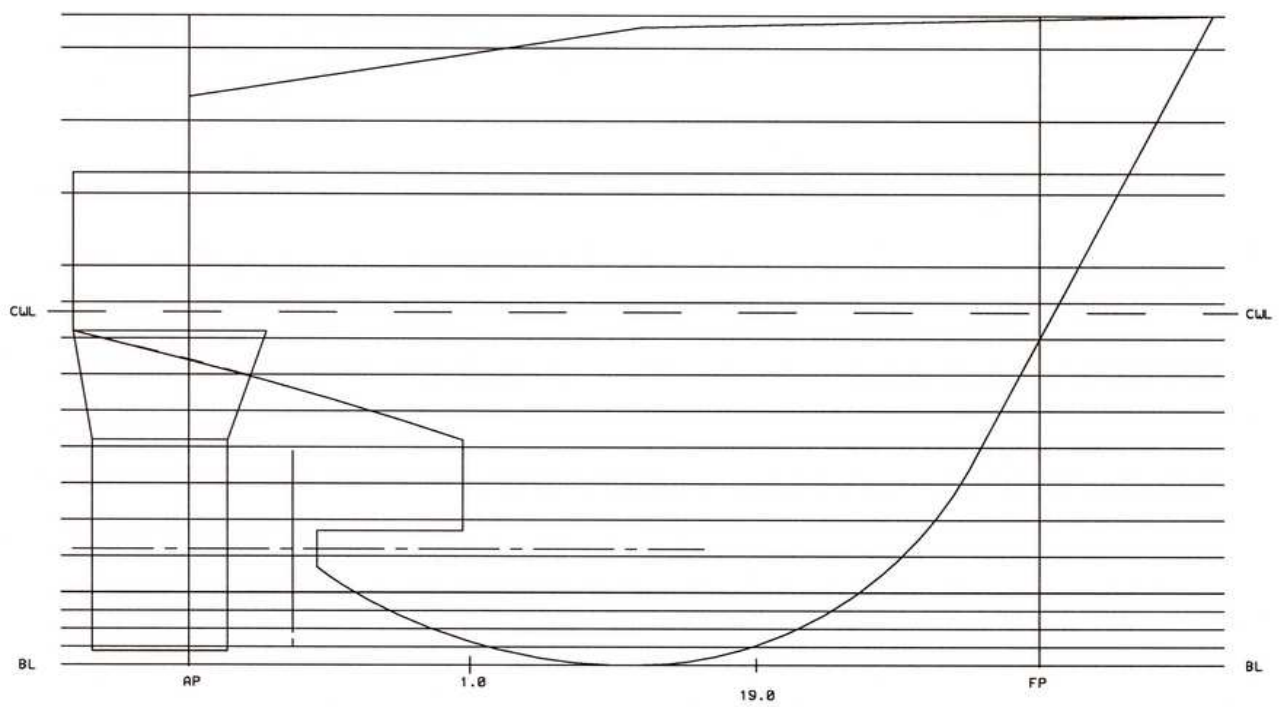


Figure E.2: Profile of CBOX ship.

Appendix F

Definition of Turning Circle Maneuver Test

Turning circle tests are performed to both port and starboard at approach speed with a maximum rudder angle. To determine the main parameters of this trial, it is necessary to continue the maneuver until the ship has turned 540° .

The essential information to be obtained from this maneuver consists of (see Fig. F.1):

- Tactical diameter
- Advance
- Transfer
- Loss of speed on steady turn
- Time to change heading 90°
- Time to change heading 180°

For comparison purpose the following dimensionless variables are used, which are also applied for the Zigzag maneuver (section 6.4.2):

Characteristic maneuvering time:

$$\tau' = \frac{\tau V}{L} . \quad (\text{F.1})$$

Dimensionless yaw rate:

$$\dot{\psi}' = \frac{\dot{\psi} L}{V} . \quad (\text{F.2})$$

Dimensionless advance or transfer (transverse):

$$x' = \frac{x}{L} \quad \text{and} \quad y' = \frac{y}{L} . \quad (\text{F.3})$$

Here τ is time, ψ is yaw angle, L denotes the ship length and V is the ship speed before the outset of the maneuver.

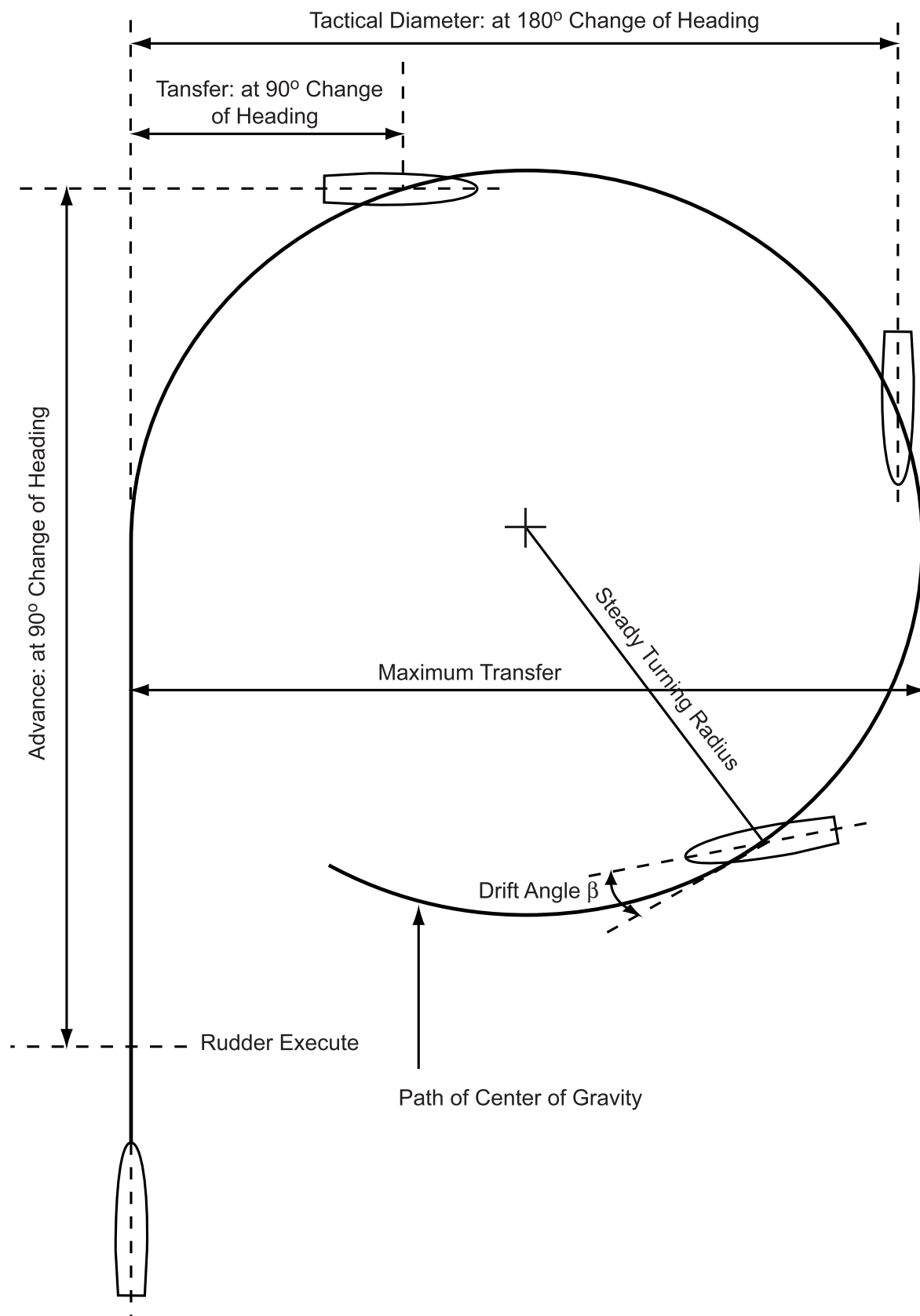


Figure F.1: Turning circle definitions.

Appendix G

Definition of Zigzag Maneuver Test

The typical procedure for conducting a Zigzag maneuver test is as follows:

At the outset of the maneuver the self-propelled model travels on a straight course at a predefined speed. Once a steady speed is established, the engine plant controls, i.e. rate of propeller revolution n , are not altered during the duration of the maneuver. As illustrated in Fig. G.1, the rudder is put over to an angle of $-\delta_R$ (first execute) after a steady approach. When the heading equals $+\psi_s$ off the initial course, the rudder is counter-steered to $+\delta_R$ (second execute). After counter rudder has been applied, the ship continues turning in the original direction with decreasing turning rate until the movement decayed. Then in response to the rudder the turning rate is reversed and later after the time τ_r also the heading reverses. When the heading is $-\psi_s$, the rudder is reversed again (third execute) and this cycle can be repeated through the fourth, fifth, or more executes.

The principle parameters obtained from a standard Zigzag maneuver and those characterizing the steering quantities of the ship model are defined in the following (c.f. Fig. G.1):

- *Switching angle (or execute heading angle) ψ_s [degree]*
Heading ψ_s at which the rudder is reversed, here $\psi_s = 10^\circ$.
- *Time to attain switching value of heading (or initial turning time) τ_a [s]*
The time from the outset of the maneuver (first execute) until the heading is ψ_s off the initial course. At this point the rudder is reversed to the opposite side (second execute).
- *Overshoot angle α_o [degree]*
The difference of heading angle through which the ship continues to turn in the original direction after the application of counter-rudder.
- *Time to check yaw τ_b [s]*
The time from the instant counter rudder is applied to the standstill of the turning movement in the original direction.
- *Reach time τ_r [s]*
The time from the outset of the maneuver (first execute) until the ship, after having completed the starboard turn, passes the initial course. Shortly after this point the transverse deviation y reaches its maximum value (y_{\max}).

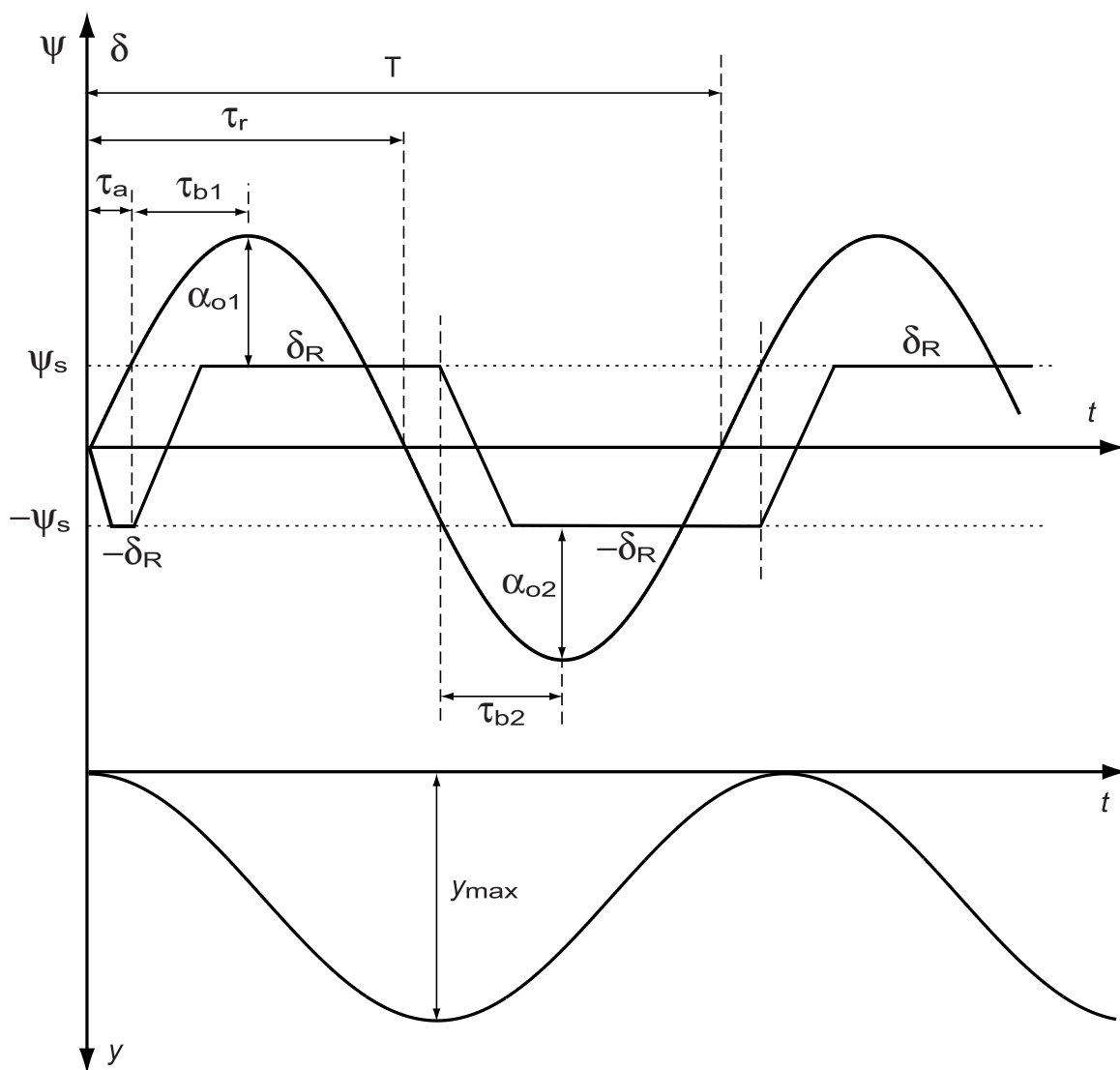


Figure G.1: Scheme of Zigzag maneuver test.

- *Period* T [s]
The time from the outset of the maneuver until one total cycle (yaw to starboard and port) has been completed.
- *Turning speed* $\dot{\psi}_{min}$ [rad/s]
Negative yaw rate approximately when passing the initial course.
- *Transverse deviation* y [m]
The transverse displacement of mass center of the ship.

Bibliography

- [1] Abott IH, von Doenhoff AE. Theory of wing sections. Dover Publications Inc., 1959
- [2] Akimoto H, Miyata H. Finite-volume simulation method to predict the performance of a sailing boat. *J. Mar. Sci. Technol.*, 7:31-42, 2002
- [3] Alessandrini B, Delhommo G. Viscous free surface flow past a ship in drift and in rotating motion. *Proc. 22nd. Symp. on Naval Hydro.*, 1998
- [4] Arai M, Cheng LY, Inoue Y. A Computing Method for the Analysis of Water Impact of Arbitrary Shaped Bodies. *J. Soc. of Naval Arch. of Japan*, Vol. 176, pp. 233-240, 1995
- [5] Azcueta R. Computation of turbulent, free-surface flows around ships and floating bodies. Ph.D thesis, report No. 612, TU Hamburg-Harburg, 2001
- [6] Azcueta R. RANSE simulation for sailing yachts including dynamic sinkage & trim and unsteady motions in waves. *proc. High Performance Yacht Design Conf.*, Auckland, 2002
- [7] Azcueta R, Muzaferija S, Perić M. Computation of breaking bow waves for a very full hull ship. *Proc. 7th. Int. Conf. Numerical Ship Hydrodynamics*, Nantes, pp. 6.2-(1-11), 1999
- [8] Azcueta R, Muzaferija S, Perić M. Numerical simulation of flow around blunt bow model. *Proc. SRI-TUHH Workshop on Numerical Simulation of Two-Phase Flows*, Tokyo, 2001
- [9] Bellevre D, Diaz de Tuesta A, Perdon P. Submarine manoeuvrability assessment using Computational Fluid Dynamics tools. *Proc. 23rd. Symp. on Naval Hydro.*, 2001
- [10] De Bernardis E. Eds. *Proc. 23rd. Int. Towing Tank Conf.*, Venice, 2002
- [11] Bertram V. *Practical Ship Hydrodynamics*. Butterworth-Heinemann, Oxford, 2000
- [12] Brackbill JU, Kothe DB, Zemach C. A continuum method for modelling surface tension. *J. Comput. Physics*, 100: 335–354, 1992
- [13] Breuer M, Jovicic, N, Mazaev, K. Comparison of DES, RANS, and LES for the separated flow around a flat plate at high incidence. *Int. J. for Numerical Methods in Fluids*, Vol. 41, pp. 357-388, 2003

- [14] Brix J. (ed.) *Manoeuvring Technical Manual*, Seehafen-Verlag, 1993
- [15] Caponnetto M. Numerical simulation of planing hulls. Proc. 3rd. Numerical Towing Tank Symp., Tjaerno, 2000
- [16] Chau SW. Numerical Investigation of Free-Stream Rudder Characteristics Using a Multi-Block Finite Volume Method. Ph.D thesis, University of Hamburg, 1997
- [17] Chen HC, Huang E. Validation of a Chimera RANS method for transient flows induced by a full-scale berthing ship. Proc. 22nd. Symp. on Naval Hydro., 1998
- [18] Clauss GF, Kühnlein W.L. Simulation of Design Storm Wave Conditions with Tailored Wave Groups. Proc. 7th. Int. Offshore and Polar Engineering Conf., Hawaii, 1997
- [19] Cura Hochbaum A. Computation of the Turbulent Flow Around a Ship Model in Steady Turn and in Steady Oblique Motion. Proc. 22nd. Symp. on Naval Hydro., 1998
- [20] Cura Hochbaum A, Vogt M. Towards the simulation of seakeeping and manoeuvring based on the computation of the free surface viscous ship flow. Proc. 24th. Symp. on Naval Hydro., 2003
- [21] Demirdžić I, Muzaferija S, Perić M. Computation of turbulent flows in complex geometries. Chap. 7 in G. Tzabiras et al. (eds.), *Calculation of Complex Turbulent Flows*, WIT Press, Southampton, pp. 249-299, 2000
- [22] El Moctar OM. Numerical computations of flow forces on maneuvering ships (in German). Ph.D thesis, report No. 611, University of Hamburg, 2001
- [23] El Moctar OM. Numerical computations of flow forces in ship manoeuvring. *Ship Techn. Res.*, Vol. 48, pp. 98-123, 2001
- [24] Faltinsen O, Kjælland O, Nøttveit A, Vijie T. Water impact loads and dynamic response of horizontal circular cylinders in offshore structures. Proc. Offshore Technology Conf., Houston, pp. 119-126, 1977
- [25] Ferziger JH, Perić M. *Computational method for fluid dynamics*. Springer-Verlag, 3rd ed., Berlin, 2002
- [26] Froude W. On the Part played in the Operation of Propulsion by Differences in Fluid Pressure. *Trans. INA*, Vol. 30, 1889
- [27] García De Jalón J, Bayo E. *Kinematic and Dynamic Simulation of Multibody Systems*. Springer-Verlag, New York, 1994
- [28] Greenhow M, Lin W. Nonlinear free surface effects: experiments and theory. Report No. 83-19, Massachusetts Institute of Technology, 1983
- [29] Greenhow, M. Water-entry and -exit of a horizontal circular cylinder. *Applied Ocean Research*, 10(4), pp. 191-198, 1988
- [30] Hadžić I, Muzaferija S, Perić M, Xing Y, Kaeding P. Predictions of Flow-Induced Motions of Floating Bodies. Proc. 3rd. Numerical Towing Tank Symp., Tjaerno, 2000

- [31] Hadžić I, Xing Y, Muzaferija S, Perić M. Numerical simulation of interaction of a floating body and a free surface flow with waves. Proc. 5th. World Congress on Computational Mechanics, Vienna, 2002
- [32] Hadžić I, Xing Y, Perić M. Simulation of turbulent flow and flow-induced motion of floating bodies (in German). Report No. 618, TU Hamburg-Harburg, 2002
- [33] Hadžić I, Hennig J, Perić M, Xing-Kaeding, Y. Computation of flow-induced motion of floating bodies. *J. Applied Mathematical Modelling*, 29, 1196-1210, 2005
- [34] Harlow FH, Welch JE. Numerical calculation of time-dependent viscous incompressible flow. *J. Phys. Fluids*, 8, 2182, 1965
- [35] Hirt CW, Cook JL, Butler TD. A Lagrangian method for calculating the dynamics of an incompressible fluid with free surface. *J. Comp. Phys.*, 5: 103, 1970
- [36] Hirt CW, Amsden AA, Cook JL. An arbitrary Lagrangian-Eulerian computing method for all flow speed. *J. Comp. Phys.*, 14: 227, 1974
- [37] Hirt CW, Nichols BD. Volume of fluid (VOF) method for dynamics of free boundaries. *J. Comput. Phys.*, 39: 201-221, 1981
- [38] Hino T. Numerical simulation of free surface flow around a blunt bow ship model. Proc. SRI-TUHH Workshop on Numerical Simulation of Two-Phase Flows, Tokyo, 2001
- [39] Jensen G, Klemt M, Xing-Kaeding Y. On the way to the numerical basin for seakeeping and manoeuvring. PRADS, Lübeck-Travemünde, 2004
- [40] Kawamura T, Miyata H. Simulation of nonlinear ship flows by density-function method. *J. Soc. Naval Architects of Japan*, Vol. 176, pp. 1-10, 1994
- [41] Kinoshita T, Kagemoto H, Fujino M. A CFD application to wave-induced floating-bodies. Proc. 7th. Int. Conf. on Numerical Ship Hydrodynamics, Nantes/France, 4.1- (1-20), 1999
- [42] Klemt M. Impact loads on catamarans in waves (in German). Master thesis, TU Hamburg-Harburg, 2000
- [43] Klemt M. Simulation of motion of floating-body in viscous flow (in German). Ph.D thesis, report No. 630, TU Hamburg-Harburg, 2004
- [44] Kodama Y, Takeshi H, Hinatsu M, Hino T, Uto S, Hirata N, Murashige S. Proc. CFD Workshop, Tokyo/Japan, 1994
- [45] Kolk WR. *Modern Flight Dynamics*. Prentice-Hall, Inc. Englewood Cliffs, N.J., 1961
- [46] Korobkin, A. Water impact problems in ship hydrodynamics. *Advances in Marine Hydrodynamics*, Chap. 7, pp. 323-371, 1996
- [47] Lanczos C. *The variational principles of mechanics*. Dover Publications, New York, 1986

- [48] Larsson L. CFD in ship design-prospects and limitations. 18th Georg Weinblum Memorial Lecture. *J. Ship Technol. Research*, Vol. 44, 1997
- [49] Larsson L, Stern F, Bertram V. Benchmarking of computational fluid dynamics for ship flows: The Gothenburg 2000 Workshop. *J. Ship Research*, Vol. 47, No. 1, 2003
- [50] Launder BE, Spalding DB. The numerical computation of turbulent flows. *Comput. Meth. Appl. Mech. Eng.*, 3, pp. 269-289, 1974
- [51] Leonard, BP. Bounded high-order upwind multidimensional finite-volume convection-diffusion algorithms. Chap. 1 in W.J. Minkowycz and E.M. Sparrow (eds.), *Advances in Numerical Heat Transfer*, Taylor and Francis, New York, pp. 1-57, 1997
- [52] Longo J, Stern F. Yaw effects on model-scale ship flows. *Proc. 21st. Symp. on Naval Hydro.*, 1996
- [53] Miyata H, Nishimura S, Masuko A. Finite difference simulation of nonlinear waves generated by ships of arbitrary three-dimensional configuration. *J. Comp. Phys.*, Vol. 60, 1985
- [54] Miyata H, Akimoto H, Hiroshima F. CFD performance prediction simulation for hull-form design of sailing boats. *J. Mar. Sci. Technol.*, Vol. 2, pp. 257-267, 1997
- [55] Miyata H, Zhu M, Watanabe O. Numerical study on a viscous flow with free-surface waves about a ship in steady straight course by a finite-volume method. *J. Ship Research*, Vol. 36, No. 4, pp. 332-345, 1992
- [56] Miyata H. Towards virtual reality by computational physics. 24th Georg Weinblum Memorial Lecture. *J. Ship Technol. Research*, Vol. 50, 2003
- [57] Muzafferija S, Perić M, Sames P, Schellin T. A two-fluid Navier-Stokes solver to simulate water entry. *Proc. 22nd. Symp. Naval Hydro.*, Washington D.C., 1998
- [58] Muzafferija S, Perić M. Computation of free surface flows using interface-tracking and interface-capturing methods. Chap. 2 in O. Mahrenholtz and M. Markiewicz (eds.), *Nonlinear Water Wave Interaction*, WIT Press, Southamton, pp. 59-100, 1999
- [59] Newman JN. *Marine Hydrodynamics*. MIT Press, England, 1978
- [60] Nonaka K, Miyazaki H, Nimura T, Ueno M, Hino T, Kodama Y. Calculation of hydrodynamic forces acting on a ship in manoeuvring motion. *Proc. MARSIM*, pp. 307-317, 2000
- [61] Ohmori T, Fujino M, Miyata H. A study on flow field around full ship forms in manoeuvring motion. *J. Mar. Sci. Technol.*, 3: 22-29, 1998
- [62] Ohmori T. Finite-volume simulation of flows around a ship in manoeuvring motion. *J. Mar. Sci. Technol.*, 3: 82-93, 1998
- [63] Orihara H, Miyata H. CFD simulation of a semi-planing boat in unsteady motion. *Proc. FAST*, Vol. 1, Sydney, 1997

- [64] Orihara H, Miyata H. Evaluation of added resistance in regular incident waves by computational fluid dynamics motion simulation using an overlapping grid system. *J. Mar. Sci. Technol.*, 8: 47-60, 2003
- [65] Orihara H. Validation of numerical method for predicting hydrodynamic characteristics of a high-speed ship. *Proc. 24th. Symp. Naval Hydro.*, Fukuoka, 2003
- [66] Patankar SV, Spalding DB. A calculation procedure for heat, mass and momentum transfer in three-dimensional parabolic flows. *Int. J. Heat and Mass Transfer*, Vol. 15, pp. 1787-1806, 1972
- [67] Pereira R. Simulation of nonlinear sea loads (in German). *Schiffstechnik*, Bd. 35, pp. 173-193, 1998
- [68] Petersson NA. An Algorithm for Assembling Overlapping Grid Systems. *SIAM J. Sci. Comput.*, Vol. 20, pp. 1995-2022, 1999
- [69] Queutey P, Visonneau M. Free-surface capturing RANSE simulations for a ship at steady drift. *J. Ship Technology Research*, Vol. 51, pp. 106-122, 2004
- [70] Rankine WJM. On the Mechanical Principles of the Action of Propellers. *Trans. INA*, Vol. 6, 1865
- [71] Rhie CM, Chow WL. A Numerical Study of the Turbulent Flow Past an Isolated Airfoil with Trailing Edge Separation. *AIAA Journal* Vol. 21, pp. 1525-1532, 1983
- [72] Richardson LF. The approximate arithmetical solution by finite differences of physical problems involving differential equations with an application to the stresses in a masonry dam. *Trans. Roy. Soc. London, Ser. A*, 210: 307-357, 1910
- [73] Sames P, Schellin T, Muzaferija S, Perić M. Application of a two-fluid finite volume method to ship slamming. *Proc. 17th. Conf. Offshore Mechanics and Arctic Engineering (OMAE)*, Lisbon, 1998
- [74] Sato T, Izumi K, Miyata H. Numerical Simulation of Maneuvring Motion. *Proc. 22nd. Symp. on Naval Hydro.*, 1998
- [75] Sato Y, Miyata H, Sato T. CFD simulation of 3-dimensional motion of a ship in waves: application to an advancing ship in regular head waves. *J. Mar. Sci. Technol.*, 4, pp. 108-116, 1999
- [76] Schumacher A. Breaking waves behind a submerged hydrofoil (in German). Master thesis, TU Hamburg-Harburg, 2000
- [77] Schumann C. Volume-of-fluid computations of water entry of bow sections. *Proc. EUROMECH*, Poitiers, 1998
- [78] Söding H. Limits of Potential Theory in Rudder Flow Predictions. *J. Ship Technology Research*, Vol. 45 pp. 141-155, 1998
- [79] Söding H. How to integrate free motions of solids in fluids. *Proc. 4th. Numerical Towing Tank Symp.*, Hamburg, 2001

- [80] Stern F, Kim HT, Patel VC, Chen HC. A viscous-flow approach to the computation of propeller-hull interaction. *J. Ship Research*, vol. 32, no. 4, pp. 246-262, 1988
- [81] Subramani AK, Paterson EG, Stern F. CFD calculation of sinkage and trim. *J. Ship Research*, Vol. 44, No. 1, pp. 59-82, 2000
- [82] Tahara Y, Longo J, Stern F. Comparison of CFD and EFD for the Series 60 $C_B = 0.6$ in steady drift motion. *J. Mar. Sci. Technol.*, 7: 17-30, 2002
- [83] Takada N, Miyata H, Sato T. CFD simulation of 3-dimensional motion of a vehicle with movable wings. *Proc. 7th. Int. Conf. on Numerical Ship Hydro.*, Nantes, 1999
- [84] Telste JG. Inviscid flow about a cylinder rising to a free surface. *J. Fluid Mech.*, Vol. 182, pp. 149-168, 1987
- [85] Travin A, Shur M, Strelets M, Spalart P. Detached-eddy simulations past a circular cylinder. *Flow Turbulence and Combustion*, 63, 293-313, 2000
- [86] Van den Vorst H. BI-CGSTAB: a fast and smoothly converging variant of BI-CG for the solution of non-symmetric linear systems. *SIAM J. Sci. Stat. Comput.*, Vol. 13, pp. 631-644, 1992
- [87] von Karman T. The impact on seaplane floats during landing. *NACA Technical Note 321*, Washington, 1929
- [88] Wagner H. On impact and gliding at the free surface of fluids (in German). *Zeitschrift für Angewandte Mathematik*, Vol. 12, pp. 193-215, 1932
- [89] Wilson R, Peterson E, Stern F. Unsteady RANS CFD method for naval combatants in waves. *Proc. 22nd. Symp. Naval Hydro.*, Washington D.C., 1998
- [90] Wilcox DC. *Turbulence modelling for CFD*. DCW Industries, Inc., La Cañada, California, 1998
- [91] Xing Y, Hadžić I, Muzaferija S, Perić M. CFD Simulation of Flow-Induced Floating-Body Motions. *Proc. 16th. International Workshop on Water Waves and Floating Bodies*, Hiroshima, pp. 169-172, 2001
- [92] Xing Y, Hadžić I, and Perić M. Predictions of Floating-Body Motions in Viscous Flow. *Proc. 4th. Numerical Towing Tank Symp.*, Hamburg, 2001
- [93] Xing Y, Jensen G, Hadžić I, Perić M. An Approach to Ship Manouvering by Simultaneous Computation of Viscous Flow and Ship Motion. *Proc. 5th. Numerical Towing Tank Symp.*, Pornichet, 2002
- [94] Xing-Kaeding Y, Jensen G, Perić M. Simulation of Ship Maneuvering in Viscous Flow with Free Surface. *Proc. 6th. Numerical Towing Tank Symp.*, Rome, 2003
- [95] Xing-Kaeding Y, Jensen G, Hadžić I, Perić M. Simulation of Flow-Induced Ship Motions in Waves using a RANSE Method. *J. Ship Technology Research*, Vol. 51, pp. 56-68, 2004

- [96] Xing-Kaeding Y, Jensen G. RANSE simulation of flow and ship motion in manoeuvring applications. 7th. Numerical Towing Tank Symp., Hamburg, 2004
- [97] Xing-Kaeding Y, Jensen G. A unified approach to ship seakeeping and manoeuvring using a RANSE Method. ICHD, Perth, 2004
- [98] Xing-Kaeding Y, Jensen G, Perić M. Numerical simulation of water-entry and water-exit of a horizontal circular cylinder. ICHD, Perth, 2004
- [99] Yakhot V, Orzag SA. Renormalization group analysis of turbulence. Basic Theory, J. Sci. Comput., Vol. 1, 1986
- [100] Zhao R, Faltinsen O. Water-entry of two-dimensional bodies. J. Fluid Mech., Vol. 246, pp. 593-612, 1993

Curriculum Vitae

Date of birth	1 June 1975
Place of birth	He Bei Province, China
1981 - 1987	Elementary School in He Bei Province, China
1987 - 1993	Secondary School in He Bei Province, China
1993 - 1997	Bachelor Course, Civil Engineering Dalian University of Technology (DUT), China Graduation Project: Design of Dam and Water Power Plant
1997 - 2000	Master Course, Civil Engineering Dalian University of Technology (DUT), China
1998 - 1999	Exchange Student, Structural Mechanics Hiroshima University, Japan Master Thesis: FEM for Reinforced Concrete Frame Bridges under Seismic Loading (in Chinese)
2000 - 2004	Scientific Employee, TUHH
2005 - today	System Engineer, Aerotec Engineering GmbH